DC and AC transport in field-effect controlled LaAlO3/SrTiO3 interface

Alexis Jouan

THÈSE de DOCTORAT de l'UNIVERSITÉ PIERRE ET MARIE CURIE - PARIS VI

Spécialité : Physique

présentée par

Alexis JOUAN

Pour obtenir le titre de DOCTEUR de l'UNIVERSITÉ PARIS VI

DC and AC transport in field-effect controlled $LaAlO_3/SrTiO_3$ interface

---

Soutenue le 14 avril 2017 devant le jury composé de :

M Claude CHAPELIER	CEA (Grenoble)	Rapporteur
M José LORENZANA	Université La Sapienza (Rome)	Rapporteur
M^{me} Sophie GUÉRON	Laboratoire de Physique de Solide (Orsay)	Examinatrice
M^{me} Julia MEYER	Institut Néel (Grenoble)	Examinatrice
M Bernard PLAÇAIS	École Normale Supérieure (Paris)	Examinateur
M Nicolas BERGEAL	ESPCI (Paris)	Co-Directeur de Thèse
M Jérôme LESUEUR	ESPCI (Paris)	Co-Directeur de Thèse

Laboratoire de Physique
et d'étude des Matériaux
ESPCI
10, rue Vauquelin
75005 Paris

École doctorale
Physique en Ile-de-France
4 place Jussieu
75005 Paris

"If you think you understand quantum mechanics,
you don't understand quantum mechanics."
Richard Feynman

Remerciements

Ma thèse s'est déroulée à l'ESPCI au Laboratoire de Physique et d'Etude des Matériaux dans l'équipe PHASME. Je tiens tout d'abord à remercier Nicolas Bergeal, Cheryl Feuillet-Palma et Jérôme Lesueur qui m'ont encadré durant ces trois années. Je garde en mémoire nos précieuses discussions scientifiques aussi bien à l'aube autour d'un café, que le soir autour d'une bière. Merci pour votre disponibilité, votre confiance et la rigueur de votre approche de la physique. Merci Jérôme pour ton optimisme inébranlable, Cheryl pour la justesse de tes paroles, et Nicolas pour ton oeil critique et exigeant. Je remercie Claude Chapelier et José Lorenzana d'avoir accepté d'être rapporteur de ma thèse, ainsi que les autres membres du jury Julia Meyer, Sophie Guéron et Bernard Plaçais pour l'intérêt qu'ils ont porté à mon manuscrit.

Bien sûr ce travail n'aurait pu se faire sans nos collaborateurs qui ont fourni des échantillons de LAO/STO ou donné un cadre théorique solide à nos mesures. Merci à Edouard Lesne et Emmanuel Bibes de Thalès-CNRS pour les échanges fructueux et la qualité des interfaces supraconductrices. Merci au professeur Budhani de l'université de Kanpur ainsi que Gervasi Herranz de l'université de Barcelone d'avoir envoyé de multiples échantillons depuis l'Inde et l'Espagne. Merci à Sergio Caprara, Marco Grilli et Lara Benfatto de l'université La Sapienza à Rome qui ont accompagné les discussions théoriques sur tous les sujets. Je veux remercier tout spécialement Lara Benfatto pour le temps qu'elle a pris pour répondre à mes nombreuses questions sur l'électrodynamique des supraconducteurs bidimensionnels. Je remercie enfin Johan Biscaras de l'UPMC d'avoir partagé si souvent son savoir sur l'interface LAO/STO et sur les méthodes de calcul numériques.

L'équipe PHASME ne serait rien sans les autres doctorants et post-doctorants. Simon, tout d'abord, qui m'a appris à travailler avec madame Patience et monsieur Amour. J'étais heureux de partager avec toi tous ces joyeux moments en musique et en rire. Merci à toi Rémi avec qui j'ai traversé ces trois années de thèse en toute fraternité. Merci à Maxime d'avoir pris le temps de me parler de lithographie électronique et de pompage optique. Gyanendra thank you for every discussions, and the long measurements which always start to work in August when no one is in the lab. I also thank you Aleksei for the fruitful discussions on Josephson array dynamics. Evidemment je souhaite bon courage à Paul dans sa quête de photons uniques, à Francois pour faire résonner les jonctions Josephson, et à Shanru pour continuer d'explorer les propriétés de cette heterostructure d'oxyde si riche et si passionnante.

Mes années en thèse n'aurait pas pu aboutir à ce résultat sans le concours des responsables de toutes les salles blanches et ateliers mécaniques dans lesquels j'ai travaillé. Je remercie José Palomo et Michaël Rosticher de la salle blanche de l'ENS de m'avoir fait passer tous les permis dont j'avais besoin pour travailler et de leur nombreux conseils. Merci à Ludovic Olanier de ses conseils pour la confections des plans et la réalisation des pièces. Mais surtout un immense merci à toi Christian d'avoir gardé espoir même quand on se retrouvait la veille de Noël dans la salle blanche déserte du LPN, à chercher les croix d'or une par une.

Merci à tous les membres du LPEM pour les déjeuners du midi qui ont rythmé ces trois années de thèse sur fond de discussions politiques passionnées. Merci à Sophie et Marie-Claude d'avoir veillé à mon style vestimentaire, à Francis de nous dépanner au quotidien, à Ricardo notre directeur présent aussi bien pour une signature qu'une question sur les phonons, à Kamran pour débats sur le Titanate de Strontium, à Dimitri pour qui la supra 2D n'a pas de secret, à Sergio qui déménage aussi vite qu'il diagonalise, à Stéphane pour son regard acerbe sur l'actualité et son expertise sur le spin-orbite, à Hervé de nos discussions sur les Fermions de Majorana et autres états exotiques, à Sandrine d'avoir été une marraine aussi formidable, mais aussi Guillaume, Benoît, Lionel, Alexandre, Lucas, Nicolas, David, Wilhelm, Mathilde... et beaucoup d'autres que je prie de m'excuser de ne pas avoir cité.

Je remercie Hervé Guillon et ses précieux conseils en Latex. Un immense merci à Pierre Lundahl, qui a eu la gentillesse et le courage de relire ce manuscrit du début à la fin. Merci pour votre relecture attentive qui m'a permis d'éviter bon nombre d'étourderies et de fautes d'anglais.

Je veux évidemment remercier les professeurs qui m'ont donné envie de faire de la physique jusqu'au plus haut niveau. Merci donc à Monsieur Fleckinger et Monsieur Barnier (Lycée Condorcet), Monsieur Lumediluna (Lycée Louis-Le-Grand), et tous les professeurs de l'ENS parmis lesquels Jean-François Allemand qui a cru en moi, Monsieur Jean-Michel Raimond avec qui j'ai découvert la physique quantique, mais aussi Gwendal Fève, Erwann Bocquillon, Thomas Salez et tous les autres. J'en profite au passage pour remercier tous mes amis de l'ENS qui continue de m'apporter énormément à tous points de vue.

Merci à mes parents qui m'ont donné leur amour. Mon goût pour la physique vient certainement entre autres de ces week-ends prolongés au festival des sciences de Chamonix où ils m'ont emmené depuis tout petit. Merci à vous.

Merci à Sophie, ma bien aimée, d'être là tous les jours et de rendre ma vie si belle.

List of frequently used symbols

The equation in this manuscript are given in MKS units. The following list details all abreviations and physical constants present in this manuscript.

$\mathbf{A}$	Potential vector	V s/m
A_K	Köler coefficient	T^{-2}
B	Magnetic field	10^4 G =1 T =1 Vs/m^2
C	Capacitance	F
c	Velocity of light	2.998×10^8 m/s
D	Diffusion Constant	m^2/s
e	Electron charge	1.602×10^{-19} C
$\mathbf{E}$	Electric field	V/m
E_F	Fermi Energy	J
ϵ_0	Dielectric permittivity of vacuum	8.854×10^{-12} F/m
ε_r	Relative dielectric constant	
G	Conductance	S
G_0	Quantum of conductance $2e^2/h$	S
h	Planck constant	6.626×10^{-34} J.s
J_s	Superfluid stiffness	J
k_B	Boltzmann constant	1.380×10^{-23} J/K
l_e	Mean free path	m
l_ϕ	Inelastic scattering length	m
l_{so}	Spin diffusion length	m
L_k	Kinetic Inductance	H
λ_L	London penetration length	m
λ_F	Fermi wavelength	m
μ_0	Permeability of vacuum	$4\pi \times 10^{-7}$ H/m
μ	Mobility	m^2/(V.s)
m_e	Mass of electron	9.107×10^{-31} kg
n_{2D}, n_s	2D electron density	e$^-$/m^2
n_{3D}	3D electron density	e$^-$/m^3
R_s	Sheet resistance	$\Omega/\square$
σ	Conductivity	S

$\tan(\delta)$	Loss tangent	
τ_e	Elastic scattering time	s
τ_ϕ	Inelastic scattering time	s
τ_{so}	Spin diffusion time	s
T	Temperature	K
T_c	Critical temperature of a superconductor	K
T_{KT}	Kosterlitz-Thouless transition temperature	K
v_F	Fermi velocity	$\mathrm{m.s}^{-1}$
V_{BG}	Back Gate Voltage	V
V_{TG}	Top Gate Voltage	V
ξ	Superconducting coherence length	m

List of abbreviations

The list of the abbreviations used throughout this thesis

$2D$	Two-Dimensional
$2DEG$	Two Dimensional Electron Gas
$3D$	Three-Dimensional
BKT	Beresinsky Kosterlitz Thouless
DOS	Density Of States
HMC	High Mobility Carriers
JJA	Josephson junctions Array
LMC	Low Mobility Carriers
LAO	Lantanum Aluminate $LaAlO_3$
MF	Maekawa-Fukuyama
MB	Mattis-Bardeen
QPC	Quantum Point Contact
RF	Radio-Frequency
$RSOC$	Rashba Spin-Orbit Coupling
SIT	Superconductor to Insulator Transition
SOC	Spin-Orbit Coupling
STO	Strontium Titanate $SrTiO_3$

Introduction

Interfaces in semiconducting heterostructures are at the heart of some of the major developments of the last fifty years, both in fundamental science and applied technology. Benefiting from the fruitful interaction between experimentalists and theoreticians, this field of research has lead to the discovery of new electronic states of matter such as integer and fractional quantum Hall effects, and the emergence of revolutionary technologies including MOSFET transistors and laser diodes for instance. In this context, the realization of similar heterostructures involving materials hosting more complex orders, has attracted a great deal of attention. This is the case of oxides heterostructures since this familly of materials displays a wide variaty of quantum orders such as high-T_c superconductivity, ferro and antiferro-magnetism, ferroelectricity, Mott orders etc.

In 2004, the discovery of a two-dimensional electron gas at the interface between two insulating oxides (Strontium Titanate and Lantanum Aluminate) paved the way for a new area of research. Among its most interesting physical properties, this interface hosts together superconductivity, magnetism, and a strong spin-orbit coupling. Such unique combination of properties makes the $LaAlO_3/SrTiO_3$ interface one of the most exotic electronic system in condensed matter physics. In addition, the possibility to tune superconductivity and spin-orbit coupling by electric-field effect offers an unprecedented level of control on the system. Applications in the field of spintronics are foreseen since the interface also appears as an ideal platform for spin propagation and spin manipulation.

From the theoretical point of view, this interface has raised a lot of questions that need to be addressed. In the superconducting phase, the exact nature of the pairing mechanism, as well as the non-monotonic variation of the critical temperature with carrier density, are hotly debated. In addition, the role of spatial inhomogeneities must also be clarified. The observation of localized magnetic moments and their possible coexistence with superconductivity also deserve attention. As far as the spin-orbit coupling is concerned, it is expected that the symmetry breaking at the interface should lead to a Rashba type interaction. However, the experimental signatures of such interaction are scarce. In addition, its interplay with superconductivy raises some exciting questions related to the possible existence of topological states. To address these questions, theoretical predictions push forward the realization of nanodevices that would enable to probe this system at the characteristic length scales (mean free path, superconducting coherence length, spin diffusion length...). It is therefore desirable to fabricate nanodevices both for

fundamental and applied perspectives.

The main goal of this thesis is to explore the transport properties of $LAlO_3/SrTiO_3$ interfaces both at DC and finite frequency, and to realize mesoscopic field-effect devices. The first chapter is dedicated to an introduction on $LAlO_3/SrTiO_3$ interfaces, starting from the properties of the bulk materials, to the electronic properties of the two-dimensional electron gas. In this chapter, we also present a numerical simulation of the band structure inside the interfacial quantum well, which was developed during this thesis. It contains key ideas that will be useful to analyze the results reported in experimental chapters. The second chapter describes the fabrication processes of the samples, from epitaxial growth performed by our collaborators to the realization of micro and nano-scale devices. It also introduces the different experimental setups, both for standard DC transport measurements and microwave AC conductance measurements.

In chapter 3, we first report an experiment where we use the disorder generated by Cr substitution of Al atoms in LaAlO3 as a tool to explore the nature of superconductivity and spin-orbit coupling in these interfaces. In particular, we analyze the evolution of the spin-orbit coupling strength with carrier density and we address the important question of the spin relaxation mechanism. In the second part, we describe the realization of a field-effect $LaAlO_3/SrTiO_3$ device, whose physical properties, including superconductivity and spin-orbit coupling, can be tuned over a wide range by a top-gate voltage.

Chapter 4 presents an introduction to dynamical conductivity in two-dimensional superconductors based on Mathis-Bardeen theory. The second part of this chapter is devoted to the dynamical response of vortices in the framework of Berezinsky-Kosterlitz-Thouless (BKT) phase transition theory. The specific case of a Josephson junctions array, which is of particular relevance in our system, is discussed. In chapter 5, we report on the AC conductivity of the LAO/STO interface measured by a resonant technique. We extract the superfluid stiffness of the 2DEG, i.e. the energy scale which determines the cost of a phase twist in the superconducting condensate, as a function of electrostatic gating and temperature. The results are compared with predictions from the Bardeen-Cooper-Schrieffer theory and from the BKT phase transition one.

Finally, in chapter 6, we describe the realization of a quantum point contact (QPC) in a split gate geometry whose conductance displays quantized steps. The number of conducting channels can be tuned either by changing the shape of the confinement potential with the split gates or by changing the Fermi energy of the 2DEG with the back-gate. The effect of a perpendicular magnetic field is investigated and a comparison with standard GaAs QPC is made.

Contents

Chapter 1

The $LaAlO_3/SrTiO_3$ Interface

"God made the bulk; surfaces were invented by the devil. "
Wolfgang Pauli
as cited in *Growth, Dissolution, and Pattern Formation in Geosystems* (1999)

Contents

The conducting $LaAlO_3/SrTiO_3$ interface is a complex and rich system which attracts much attention in the scientific community. Since the discovery of a high-mobility electron gas at the interface by Ohtomo and Hwang in 2004 [1], many interesting features have been studied. In 2007, the group of J-M Triscone at University of Geneva and the group of Mannhart at the University of Augsburg reported the existence of 2D superconductivity below 300mK [2]. One year later, field effect tuning of the electronic properties, including superconductivity was demonstrated [3]. Finally tunable spin-orbit coupling interaction was evidenced by magneto-transport measurements [4], and signs of magnetism were reported to coexist with superconductivity [5]. The combination of all these properties in the same 2D electronic system is unique. Their tunability by electric field effect opens new perspectives for the study of fundamental properties of 2D superconducting systems and paves the way for a new generation of electronic devices.

In this chapter, we give an overview of this promising new field of research. Starting from $SrTiO_3$ (STO) structural and electronic properties and the polar characteristics of $LaAlO_3$ (LAO), we introduce the key factors that are at play at the interface. We focus mainly on STO, because the electronic properties of the two-dimensional electron gas (2DEG) are governed by this exotic dielectric material. Section 1.2 briefly presents the different scenarii that explain the presence of a conducting 2DEG at the interface and detail its band structure. Special attention is devoted to spin-orbit coupling. The last section gives an overview on the properties of this 2D superconductor and highlights the role of disorder. Some of the results are still under debate and are questioned throughout this thesis.

1.1 Perovskites

The first Perovskite ($CaTiO_3$) was discovered in the Ural mountains in 1839 by a German mineralogist, Gustave Rose. The name comes from the Russian mineralogist Lev Alexeïevitch Perovski. Their crystalline ABO_3 structure is cubic at 300K. At the centre of the unit cell, the B atom is surrounded by an octahedral cage of oxygen while the A atoms are placed at the corners as represented in figure 1.1.

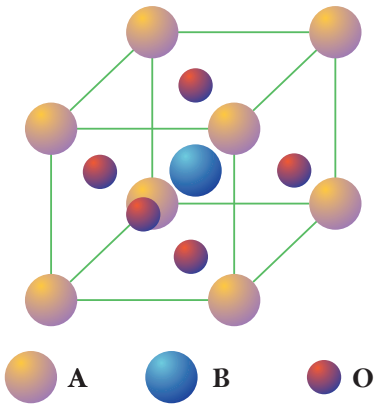

Figure 1.1 – Perovskite crystalline structure ABO_3 unit cell. Oxygen atoms are represented in red. They form a cage around the B atom, while A atoms are placed on the corners of this cubic lattice.

At lower temperatures, the cubic structure is often unstable and perovskites display less symmetric crystallographic structures. Perovskite's electronic properties are greatly affected by the different temperature driven structural transitions. Ferroelectricity in $BaTiO_3$, ferromagnetism in $YTiO_3$ or antiferromagnetism in $LaTiO_3$ [6, 7, 8] arise from the successive symmetry breakings that occur upon cooling. Nowadays, Perovskite thin films are widely used in advanced technologies to fabricate ferroelectric memories, optical or piezoelectric devices. Recently, perovskites have proven to have a good conversion efficiency in solar cell technologies [9]. Up-coming applications in microwave devices based on the electric-field tunable dielectric constant of $BaMg_xNb_{1-x}O_3$ and $Ba_xSr_{1-x}TiO_3$ also offer a promising future to this large family of materials [10].

1.1.1 Strontium Titanate

Strontium titanate is at the centre of our study, because in the $LaAlO_3/SrTiO_3$ interface, the 2DEG extends in the STO side [11]. Hence most of LAO/STO 2DEG properties are inherited from one of the most exotic materials in the Perovskite family. STO has been continuously studied for more than sixty years but it remains a subject of controversy. As detailed below, after undergoing a tetragonal transition when the temperature is lowered, STO avoids a ferroelectric transition by entering in a so-called quantum paraelectric phase. Understanding these transitions is crucial in order to characterize the transport properties of this material both in the normal and the superconducting states.

1.1.1.1 Tetragonal transition

At 300K, the lattice parameter of STO ($a_{SrTiO_3} = 3.905$ Å) matches the value observed in many other perovskites, such as $YBa_2Cu_3O_7$ or $LaAlO_3$, allowing the growth of various heterostructures. At 105K, a cubic to tetragonal transition occurs. It can occur in any one of the three directions of space with equal probabilities, leading to the coexistence of domains with different orientations as shown in figure 1.2 [12]. After each cooling the domains may align in a different way, leading to a different macroscopic dielectric constant. However, the domains can be oriented along a specific direction by repeated electric field [13] or thermal cycling [14]. This transition is accompanied by an antiferro-distortion of the oxygen octahedra [15] (see figure 1.3), which affects the phonon's spectrum and the electronic properties as we will see in the next section.

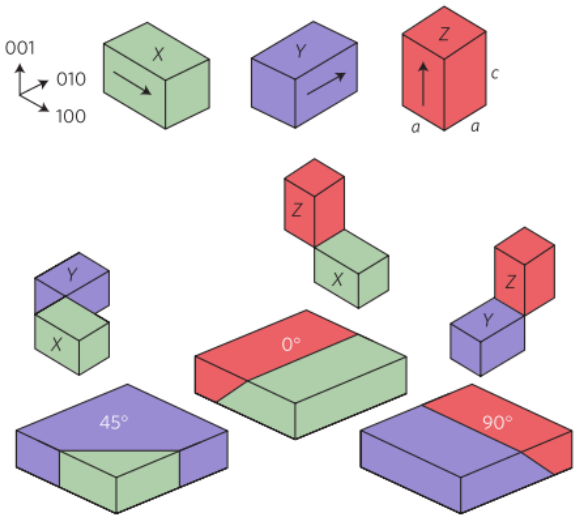

Figure 1.2 – Below 105K, the cubic cell acquires a tetragonal form. The c-axis along which the cell elongates can be oriented in either the x, y or z direction. In $SrTiO_3$ tetragonal domains are thus formed in three directions of space as represented with three different colours (green along x, purple along y and red along z). Figure from [13]

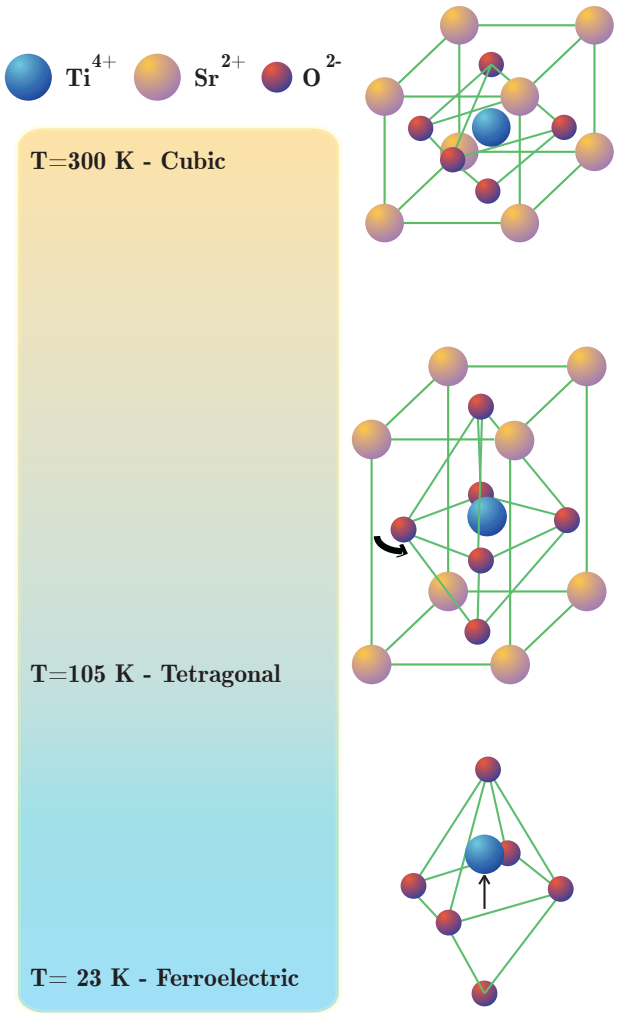

Figure 1.3 – STO structural transitions : The first symmetry breaking occurs at 105K with lengthening along the c-axis and a rotation of the oxygen octahedra. At T=23K, the Ti atom shifts from its position at the centre of the cage, leading to a quantum paraelectric transition.

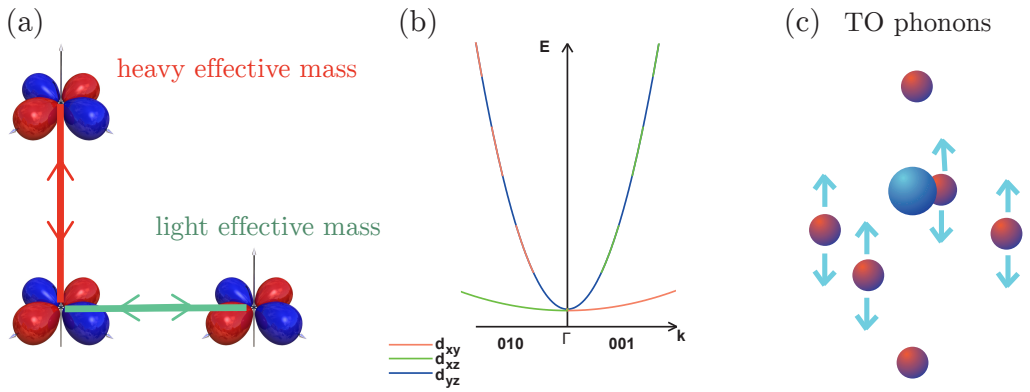

Figure 1.4 – STO electronic structure : (a) The overlap of d_{xy} orbitals is higher in the plane than out of the plane. (b) STO band structure at high temperature without spin-orbit coupling. (c) Transverse optical phonon (TO) at the ferroelectric transition.

1.1.1.2 Quantum paraelectricity

Below 23K, the position of titanium atoms shifts from the centre of the cell (see fig.1.3), creating two equilibrium positions for oxygen atoms [16]. These atoms are light enough to avoid the ferroelectric transition by quantum tunnelling in symmetric positions across the titanium atom. In 1979, Müller et al. demonstrated the quantum paraelectric nature of STO [14]. Instead of diverging upon cooling, the dielectric constant saturates below ∼10 K at a very high value $\varepsilon_{STO} \simeq 23000$. This very fragile state of matter can be broken in different ways :

- **Isotope doping** : Doping STO with oxygen 18 by annealing also favours a ferroelectric state [17]. This effect is due to the fact that $^{18}0$ are too heavy to spread their wavefunction in the two minima of the electric potential formed below 23K.
- **Calcium doping** : Another way to induce a ferroelectric transition in STO is to replace a few strontium atoms by calcium [18]. The precise origin of the induced ferroelectricity in this case is still under debate.
- **Stress** : When stress is applied along both (001) and (110) directions, the system recovers a ferroelectric transition [19].
- **Electric field** : Neville et al. have reported [20] that the dielectric constant decreases with the absolute value of the electric field $F = |\mathbf{E}|$, according to the relation

$$\varepsilon_{STO}(F) = \varepsilon(F = \infty) + \frac{1}{A + BF} \tag{1.1}$$

where A and B are two temperature dependent parameters. This can be understood as a perturbation equivalent to applying stress given the piezoelectric properties of STO at low temperature [21]. This electric field dependence is a key ingredient to understand the shape of the potential well that confines the 2DEG at the LAO/STO interface.

1.1.1.3 Band structure of STO and electronic mass

STO is a band insulator with a gap of 3.2 eV. The conduction band is mainly built on the t_{2g} orbitals (d_{xy},d_{xz} and d_{yz}) of the titanium atom, while the valence band is mostly formed by the $2p$ orbitals of the surrounding oxygens [22]. The t_{2g} orbital anisotropy leads to an anisotropic dispersion relation (fig. 1.4(a)). On the one hand, the strong overlap of the d_{xy} orbitals in the plane gives rise to a light in-plane mass $m_t^{xy} = m_l = 0.7 \times m_e$. In the z direction, the mass of the d_{xy} band is heavy $m_z^{xy} = m_h = 14 \times m_e$. On the other hand, the $d_{xz/yz}$ bands are light in the z direction $m_z^{xz/yz} = m_l$ and the in-plane masses are anisotropic ($m_x^{xz} = m_y^{yz} = m_l$ and $m_y^{xz} = m_x^{yz} = m_h$) (fig. 1.4(b)).

Near the Γ point, the cubic symmetry implies that the three bands are degenerated (fig. 1.4 (b)). The tetragonal transition at 105 K lifts this degeneracy together with atomic spin-orbit coupling [23]. The tetragonal transition is accompanied by a softening of the transverse optical (TO)and longitudinal optical (LO) phonons. The oxygen octahedron is indeed moving relatively to the titanium at its centre, inducing a polarity (fig. 1.4(c)). The strong interaction of electrons with these polar phonons results in the formation of a polaronic liquid in the normal

state. The electrons coupled to the TO4 phonons[1] are described by a Frölich Hamiltonian [24]. Measurements of the optical conductivity show that in polar crystal, the effective mass of electrons is increased [22, 25]. The light mass obtained by ARPES measurements on a cleaved surface is around 0.6 m_e [26], while quantum oscillation in doped bulk STO gives values of 1.12 to 1.56 m_e [27].

1.1.1.4 Superconductivity in doped bulk STO

Doping strontium titanate with electrons (n-doping) can be achieved by replacing titanium atoms Ti^{4+} by Niobium Nb^{5+} or strontium atoms Sr^{2+} by Lanthanum La^{3+}, or by creating oxygen vacancies. Once the conduction band is filled, doped STO becomes a good conductor with mobilities of up to 10 000 $cm^2V^{-1}s^{-1}$ at low temperature, depending on the doping and type of impurities introduced [28]. STO undergoes a superconducting transition with a maximum critical temperature $T_c \sim 0.3$K. The carriers density at which this superconductivity is observed (down to 5.5 10^{17} cm^{-3}) makes it the most dilute superconductor ever measured [29]. Contrary to most superconductors where the Fermi energy E_F is much higher than the Debye frequency ω_D, at low doping STO is within the anti-adiabatic limit $E_F \simeq 1meV << \hbar\omega_D$. The critical temperature dependence on doping was first measured by Koonce et al. (see fig. 1.5) and revisited recently by X. Lin et al. [30, 29]. The superconducting critical temperature,T_c, follows a dome shape that extends over more than two orders of magnitude in doping.

The first mechanisms proposed to explain the attractive interaction between electrons responsible for superconductivity in this compound, was based on a multi-valley scenario; it has now been proven that this scenario is wrong [31, 30]. Appel was the first to propose that soft phonon modes would be responsible for pairing [32]. Along similar lines, a mechanism involving the exchange of two optical phonons was later proposed [33]. None of these theories was able to predict the critical temperature from first principles, and they could not explain the effect of applied stress on T_c either [34]. In the 80s, Takada was able to reproduce the dome of T_c by introducing a dynamical dielectric constant based on the polar phonon and plasmon mechanisms [35]. However, J. Ruhman and P. Lee recently suggested that in Takada's calculation, the anti-adiabatic limit was uncontrolled [36].

Recently, the interest in the origin of superconductivity in STO was renewed after the discovery of 2D superconductivity in the LAO/STO interface. In 2015, Edge et al. proposed a scenario based on DFT calculations, where quantum ferroelectric fluctuations are responsible for the pairing. In the overdoped regime, they are suppressed by antiferro-distortive fluctuations [37]. As the elementary excitations associated with ferroelectric fluctuations are $q = 0$ optical phonon modes, they give rise to a conventional s-wave superconducting gap. The following year, a measurement of the isotope effect demonstrated an increase of the critical temperature in ^{18}O doped STO, supporting this scenario [38]. More recently new mechanisms involving plasmons [36] and longitudinal optical phonons [39] have been proposed to account the presence of super-

1. One of the polar phonon mode created by the vibration of Ti atoms and oxygen octahedra as represented on figure 1.4(c)

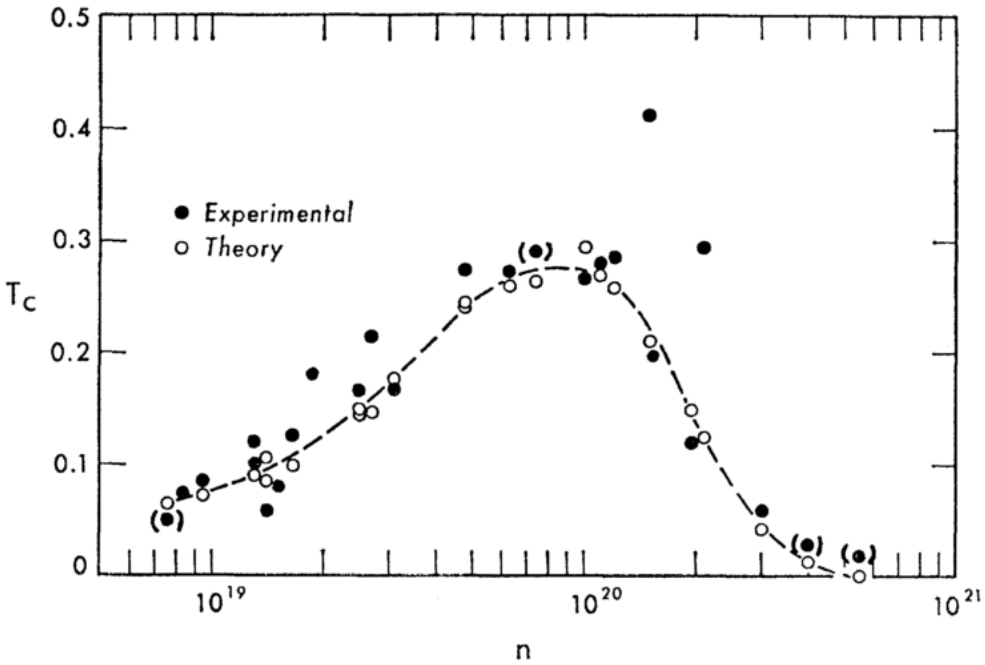

Figure 1.5 – STO critical temperature as a function of doping, taken from [30]

conductivity in the underdoped region. The origin of superconductivity in STO is still hotly debated. Nevertheless, we would like to emphasize here that the exotic dielectric behaviour of STO is at the heart of most of the proposals.

1.1.2 Lanthanum Aluminate

Before discussing the origin of the 2DEG, we summarize here the main properties of Lanthanum aluminate. LAO is also a band insulator perovskite with a band gap of 5.6 eV and a lattice parameter $a_{LaAlO_3} = 3.79$ Å[40]. Below 800 K, it undergoes a structural transition and becomes rhombohedric [41]. It is a polar material with alternating $La^{3+}O^{2-}$ planes having a +1 total charge, and $Al^{3+}O_2^{4-}$ planes with -1 total charge. This polarity may be one of the key ingredients to building a conducting two-dimensional electron gas at the interface between LAO and STO [42].

The value of the static dielectric constant found in the literature for the crystalline form is $\varepsilon_{LAO} = 24$ [43]. Since the 2DEG lies in the STO side in LAO/STO heterostructures, LAO appears as an insulator on top of it. It is therefore tempting to use it to make a capacitor and apply an electric field to the 2DEG through the LAO barrier. However, producing an effective field effect from the LAO side has remained a challenge for many years. When a layer of this oxide with a thickness of few unit cells is used to create a capacitance, any pinholes or other defects in the atomic structure quickly lead to leakage currents. This question will be addressed in chapter 2 section 2.1.3.

1.2 Electronic Properties of the LAO/STO Interface

Using the pulsed laser deposition (PLD) technique, LAO can be grown on a TiO_2 terminated STO substrate as described at the beginning of chapter 2. Depositing a few unit cell of a band insulator onto an other insulator would, in principle, give rise to a trivial insulating heterostructure. However, the polar nature of LAO and the exotic properties of the quantum paraelectric STO create a metallic interface which is still challenging to fully understand. Moreover, this conducting region happens to behave like a two-dimensional system. If the system is cooled down to very low temperatures (below 300mK), superconducting transition takes place. In the next two sections we present the theoretical and experimental state-of-the-art on this interface.

1.2.1 Origin of the 2DEG

It has been shown experimentally that the conducting 2D gas is formed only when the thickness of the LAO exceeds a critical value of 4 u.c. [44]. Different theoretical scenarii that can explain this experimental result are still debated in the community : we review them in the following pages.

1.2.1.1 Polar catastrophe scenario

Two different cases have to be considered depending on the ions at the interface. In the first case, STO is TiO_2 terminated, the first LAO atomic plane is $La^{3+}O_2^{4-}$ with a +1 effective charge and the second atomic plane is $Al^{2+}O_2^{4-}$ with a -1 effective charge. As sketched on Figure 1.6 (a), this alternate charge density in the growth direction gives rise to an increasing and diverging potential V. Above a critical threshold of 4 unit cells, the electric potential at the surface of LAO is so high (fig. 1.6 (a)) that transfering half an electron per unit cell down to the TiO_2 plane lowers the total electrostatic energy (fig. 1.6 (c)). In the second case $LaAlO_3$ is deposited on a SrO terminated STO. In this case, the boundary conditions are exactly opposite because the first atomic plane of lanthanum aluminate is negatively charged. Instead of transferring half an electron per unit cell, LAO will take out half an electron from the interface and bring it to the top. This second situation is described on figure 1.6 (b) and (d).

In the case of a TiO_2 termination (n-type), above a critical thickness of LAO, the STO substrate is thus forced to accept electrons, which corresponds to experimental observations [44]. The polar catastrophe scenario predicts that it is energetically favourable to transfer half an electron per unit cell of LAO at the interface. In this case, the expected 2D electron density is $n_{2D} = 3.3 \times 10^{14} e^- cm^{-2}$. However, the carrier densities measured experimentally usually fall short of this value by an order of magnitude. In addition, the polar catastrophe also does not explain why p-type interfaces are insulating.

1.2.1.2 Alternative doping mechanisms

The polar catastrophe scenario is not fully convincing because it does not take into account other possible sources of doping. For instance, the pressure of oxygen in the chamber has a

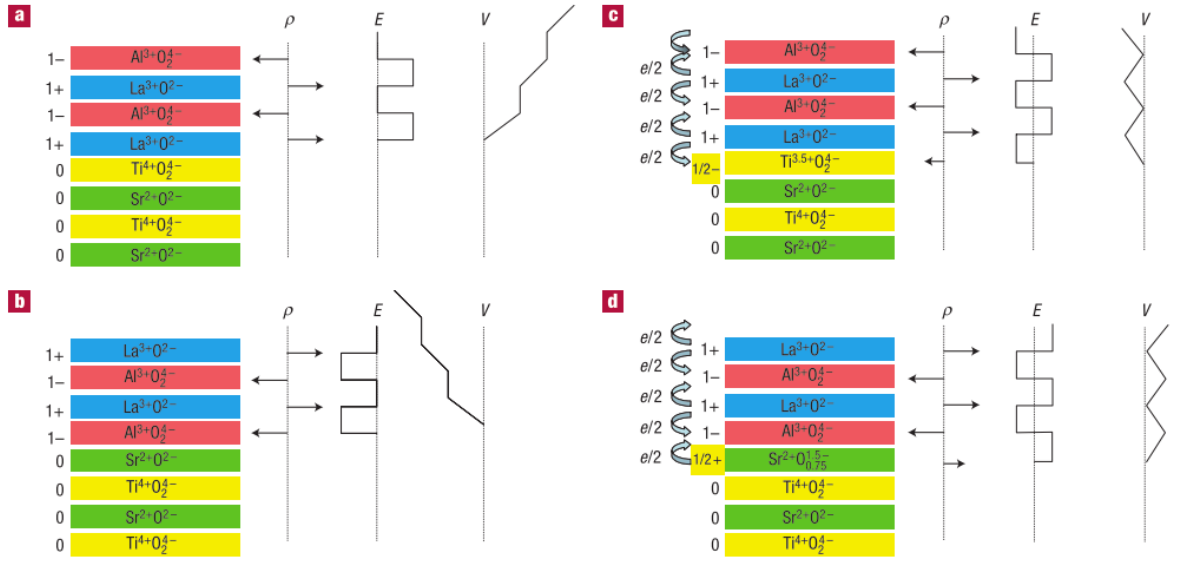

Figure 1.6 – Polar catastrophe scenario schematics. (a) and (b) correspond to the n-type and p-type situations respectively below the 4 u.c. limit. We see the diverging potential due to the polarity of LAO. (c) and (d) show the transfer of electrons above 4 u.c. Taken from [42]

strong effect on the stoichiometry of each compound. Residual oxygen vacancies in both LAO and STO could also be responsible for the presence of the 2DEG [45, 46]. In this section, after presenting in detail the fundamental role of oxygen vacancies, we will introduce the polarity induced defect mechanism.

Oxygen vacancies, cation vacancies and cation intermixing

During the growth of LAO/STO heterostructures, the low partial pressure of oxygen in the chamber of the PLD and the high deposition temperature induce oxygen vacancies. A systematic study of the role of the oxygen partial pressure during the deposition of LAO was done by Brinkman et al. [47]. For oxygen pressure $P_{O_2} > 10^{-4}$mbar, the resistance of the heterostructures displays signs of weak-localisation at low temperature (upturn below 20K) which is a clear indication of the 2D nature of the conducting gas. However, some oxygen vacancies are inevitably created during the growth. For lower oxygen pressure ($P_{O_2} = 10^{-5}$ mbar) many vacancies are generated and the resistance displays a more 3D behavior with a lower value and no signs of weak localization (fig. 1.7 (a)).

Even when relatively high oxygen pressure ($P_{O_2} = 10^{-4}$ mbar) is used during the growth, it is necessary to perform a post-annealing treatment with a high pressure (typically 200mbar) of oxygen to suppress as many oxygen vacancies as possible. Basletic et al. [48] compared the resistivity measured by a conductive tip AFM on the sample side with and without annealing (fig. 1.7 (b) and (c)). With a post-annealing, a clear 2D gas extending typically on 10 nm is clearly seen at the interface between the 2 insulating materials (region in red in fig. 1.7 (c)). With-

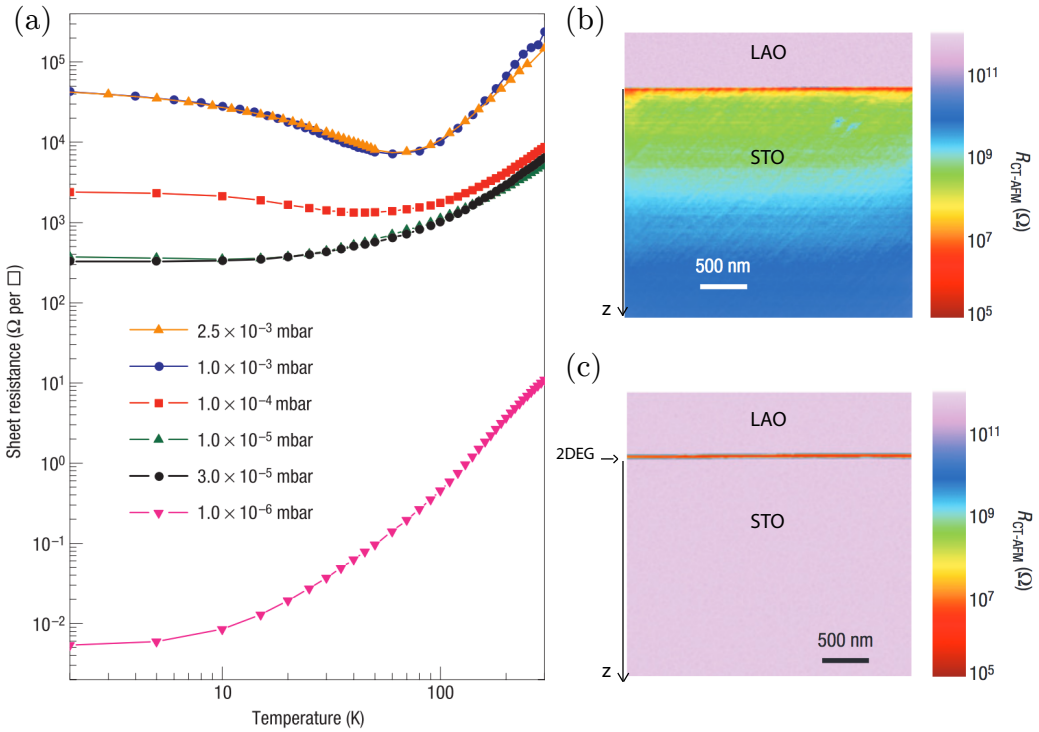

Figure 1.7 – (a) Resistance as a function of temperature for different partial pressures of oxygen. Figure taken from [47] (b) LAO/STO 001 as grown sample measured with Conductive Tip AFM (P_{O_2}=10^{-5}mbar) without annealing; (c) Same with annealing at 200 mbar of O_2 ((b) and (c) were adapted from [48]

out post-annealing, the STO substrate is doped by oxygen vacancies and the 2D confinement is lost. The lack of oxygen in the structure leads to electron doping, whereas symmetrically, cation vacancies can result in doping with holes. Another possible issue raised in [42] is the exchange of cations at the interface. Typically, Ti-Al exchange can occur but it does not cancel out the divergence of the potential [49]. Moreover, oxygen vacancies and cation intermixing do not explain the observation of a critical thickness of LAO. A recent proposal involves both the electrostatic effect and the creation of oxygen vacancies [45] : we describe it in the next paragraph.

Polarity-induced defect mechanism

A polarity-induced mechanism was recently proposed to try to reconcile the various experimental observations. Yu and Zunger calculated the energy cost of every possible defect both at the interface and at the surface of LAO using DFT calculations [45]. By comparing the electric potential developed in LAO with the energy needed to create oxygen vacancies at the surface of LAO ΔH_0, they proposed a scenario combining the polar catastrophe and the doping by oxygen vacancies. Oxygen vacancies are created in LAO when the electrostatic energy developed in this polar material is higher than ΔH_0.

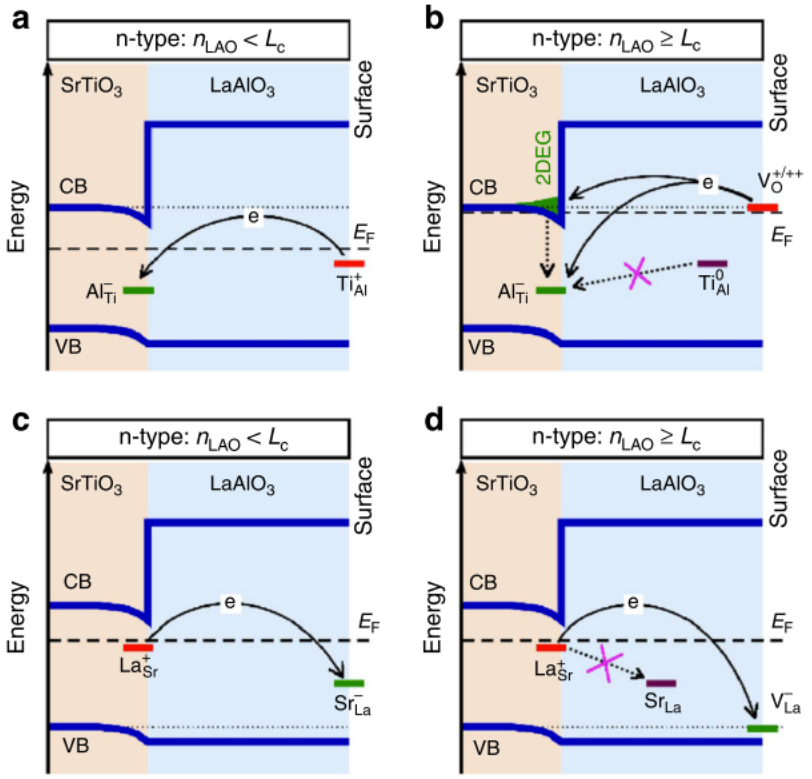

Figure 1.8 – Polarity induced defect mechanism schematics (a) represents an n-type situation below the 4 u.c. critical thickness where no 2DEG is formed. In (b), 2DEG is formed due to oxygen vacancies created in LAO (c-d) show the situation in the p-type case. Figures taken from [45]

ΔH_0 happens to be of the same order of magnitude as the critical energy predicted by the polar catastrophe scenario. Below 4 u.c. of LAO, the conduction band of STO is empty (fig. 1.8 (a)). Above the 4 u.c. critical thickness, it becomes favorable to create oxygen vacancies on top of LAO. Electrons compensate the rising electric field, either by localizing on defects, or by contributing to the free electron gas formed at the interface as plotted on fig. 1.8 (b). This alternative scenario also explains why the p-type interface is insulating. (figures 1.8 (c) and (d)). According to this theory, the creation of oxygen vacancies due to the polar nature of LAO could participate to the formation of a quasi two dimensional electron gas between two insulating perovskites.

1.2.2 Band Structure

The purpose of this section is to provide a framework for the understanding of the band structure in a self-consistently defined confining potential. At the LAO/STO interface, free carriers move in STO [50, 51, 48]. After building a Hamiltonian on the d states of the Ti electrons, we show how to account for the STO non-linear dielectric properties in a semi-classical model.

1.2.2.1 Nearly free electron in a 2D system

As the system is confined in the z direction, each band of bulk STO is split in multiple quantized 2D subbands. In the plane, electrons behave as nearly free electrons with a kinetic energy $\hbar^2 k_x^2/2m_x + \hbar^2 k_y^2/2m_y$. The bottom of each band E_i is inversely proportional to the effective mass along the confinement direction m_z^i.

We start from the 3D bulk STO conduction band built on the t_{2g} orbitals presented in section 1.1.1.3. Near the Γ point, tranport at the interface can be modeled using a nearly free electrons gas in the basis $\Psi_{\mathbf{k}} = {}^t(c^{xy}_{\mathbf{k},\uparrow}, c^{xy}_{\mathbf{k},\downarrow}, c^{xz}_{\mathbf{k},\uparrow}, c^{xz}_{\mathbf{k},\downarrow}, c^{yz}_{\mathbf{k},\uparrow}, c^{yz}_{\mathbf{k},\downarrow})$. The Hamiltonian reads $H = \sum_{\mathbf{k}} \Psi^\dagger_{\mathbf{k}} \mathcal{H}_0 \Psi_{\mathbf{k}}$ with

$$\mathcal{H}_0 = \begin{pmatrix} \frac{\hbar^2 k_x^2}{2m_l} + \frac{\hbar^2 k_y^2}{2m_l} & 0 & 0 \\ 0 & \frac{\hbar^2 k_x^2}{2m_l} + \frac{\hbar^2 k_y^2}{2m_h} + \Delta_I & 0 \\ 0 & 0 & \frac{\hbar^2 k_x^2}{2m_h} + \frac{\hbar^2 k_y^2}{2m_l} + \Delta_I \end{pmatrix} \otimes \sigma_0 \tag{1.2}$$

where σ_0 is the identity matrix in spin space and $\Delta_I = E^{xz/yz} - E^{xy}$ is the energy difference between the d_{xy} band and the $d_{xz/yz}$ bands. The d_{xy} electrons presented on figure 1.9 (a) have a light in-plane mass $m^z_{xy} \sim 0.7 \times m_e$. Their out-of-plane effective mass is much higher than the effective mass of $d_{xz/yz}$ electrons. Consequently, the d_{xy} bands are lower in energy than the anisotropic $d_{xz/yz}$ band represented on figure 1.9 (b). This energy difference Δ_I depends on the confinement potential which can be calculated self-consistently using the Schrödinger-Poisson method adapted from semi-conductor models.

1.2.2.2 Quantum confinement

If a quantum well is described by a potential $\phi(z)$, any electron of mass m at energy E is described by a wavefunction which is a solution of the simple one dimensional Schrödinger equation. In the free electron approximation, the eigenvectors of the Hamiltonian $\mathcal{H} = \mathcal{H}_0 \otimes \mathcal{H}_z$ where $\mathcal{H}_z$ is the Hamiltonian in the z direction, can be written $\Psi(x, y, z) = \psi(z) e^{i\theta(k_x, k_y)} e^{i(k_x x + k_y y)}$ with ψ solution of

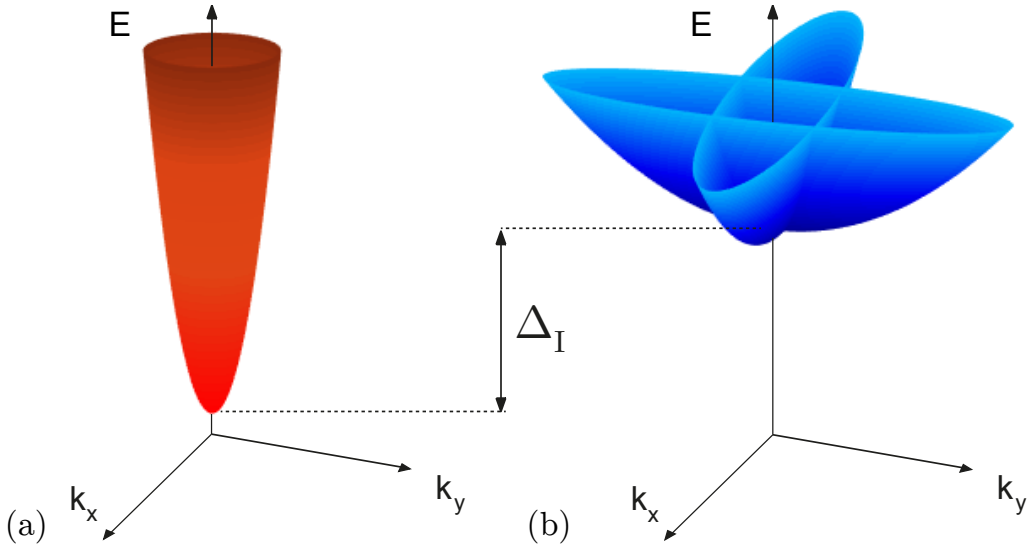

Figure 1.9 – (a) Schematic representation of the free electron dispersion of the d_{xy} band (b) Anisotropic bands d_{xz} and d_{yz} shifted from the last d_{xy} band by an energy Δ_I

$$\frac{d^2\psi_{xy}}{dz^2}+\frac{2m_z^{xy}}{\hbar^2}\left[E^{xy}+e\phi(z)\right]\psi_{xy}(z)=0 \tag{1.3}$$

$$\frac{d^2\psi_{xz/yz}}{dz^2}+\frac{2m_z^{xz/yz}}{\hbar^2}\left[E^{xz/yz}+e\phi(z)\right]\psi_{xz/yz}(z)=0 \tag{1.4}$$

where E^{xy} are the energies of the d_{xy} electrons, and $E^{xz/yz}$ is the energy of the $d_{xz/yz}$. The equations are coupled with a classical equation of the electrostatic potential. The dielectric constant of STO is described in equation (1.1). Knowing the density of charge $n_{3D}^{tot}(z)$, the shape of the electric potential ϕ can be deducted by means of the Poisson equation :

$$\nabla(\varepsilon_0\varepsilon_r(F(z))\nabla(\phi(z)))=-n_{3D}^{tot}(z) \tag{1.5}$$

$$\varepsilon_r(F)=\varepsilon_r(F=\infty)+\frac{1}{A+B|F|} \tag{1.6}$$

with the electric field $F=-\nabla\phi$. The value of $\varepsilon_R(F=\infty)$ is unknown. It has to be between 1 and 300 which is the lowest value ever measured in STO [52]. Charge density $n_{3D}^{tot}(z)=N_{trap}(z)+n_{3D}(z)$ includes all possible charges present at the interface, including trapped charges (N_{trap}) in order to account for the existence of the 2DEG (see appendix B). The contribution of each band to the carrier density depends on their respective filling. Each band has a density of state $N_{2D}^i=m_t^i/\pi\hbar^2$ where m_t^i is the in-plane mass of the ith band. The 3D electron density in one subband is given at $T=0$ by

$$n_{3D}(z)=\sum_i\frac{m_t^i}{\pi\hbar^2}\times(E_F-E^i)\times|\psi_i(z)|^2 \tag{1.7}$$

where E^i is the energy of the bottom of the i$^{\text{th}}$ subband.

By solving self-consistently equations (1.5) and (1.3), the filling and the confinement of each subband are determined. In figure 1.10, is plotted an example of a numerical resolution of the problem for two different situations : one corresponding to low carrier density resulting from the application of a back gate voltage of -100V (depletion of carriers), and one corresponding to high carrier density resulting from the application of a back gate voltage of +100V (addition of carriers). In both cases, the total carrier density of around $n = 10^{13}$ e^-/cm^2 corresponds to typical values measured experimentaly in these situations.

In the first situation, the negative back gate localized the electrons close to the interface and only two d_{xy} subbands are populated. In the second situation, a $d_{xz/yz}$ band is also filled and the Fermi energy is located close to the top of the well. Electrons of the $d_{xz/yz}$ band having a much lighter mass in the z direction, they are more extended in the STO substrate (around 10 nm). Therefore they recover properties closer to the bulk ones. In particular, they experience a dielectric constant whose value is much higher than the one close to the interface. The Lifschitz transition between the situation one where electrons are strongly confined and fill only dxy bands, and situation two where electrons fill a more delocalized dxz/yz band, will be important for our analysis of the 2DEG properties. More details of the Schrödinger-Poisson simulations are given in appendix B.

1.2.3 Spin-Orbit Interaction

Based on DFT calculations, a tight binding model was proposed recently to describe the effect of atomic spin-orbit (ASO) and Rashba spin-orbit coupling (RSOC) in the LAO/STO interface [53]. The ASO couples the spin of the electron to its own momentum via the electric field created by the ionic network. In the basis of t_{2g} bands (as in equation (1.2)), it appears as follows in the Hamiltonian [54]

$$\mathcal{H}_{ASO} = \Delta_{ASO} \begin{pmatrix} 0 & i\sigma_z & -i\sigma_y \\ -i\sigma_z & 0 & i\sigma_x \\ i\sigma_y & -i\sigma_x & 0 \end{pmatrix} \tag{1.8}$$

where σ_i are the Pauli matrices and Δ_{ASO} is the atomic spin orbit energy. Such interaction does not break inversion symmetry ($E(\mathbf{k}) = E(-\mathbf{k})$) but mixes the states where the different bands cross each other (fig. 1.11)

On the contrary, the electric field created by the accumulation of electrons at the interface breaks the inversion symmetry. The electric field tends to polarize the Ti orbitals, giving rise to asymmetric $d_{xy} - p_x - d_{xz}$ hopping in the y direction. On top of this, the tilt of the oxygen octahedra also plays a role as explained in [55]. This intrinsic breaking of inversion symmetry is modeled by :

$$\mathcal{H}_{RSO} = \alpha(F) \begin{pmatrix} 0 & 0 & 2ik_x \\ 0 & 0 & 2ik_y \\ -2ik_x & -2ik_x & 0 \end{pmatrix} \otimes \sigma_0 \tag{1.9}$$

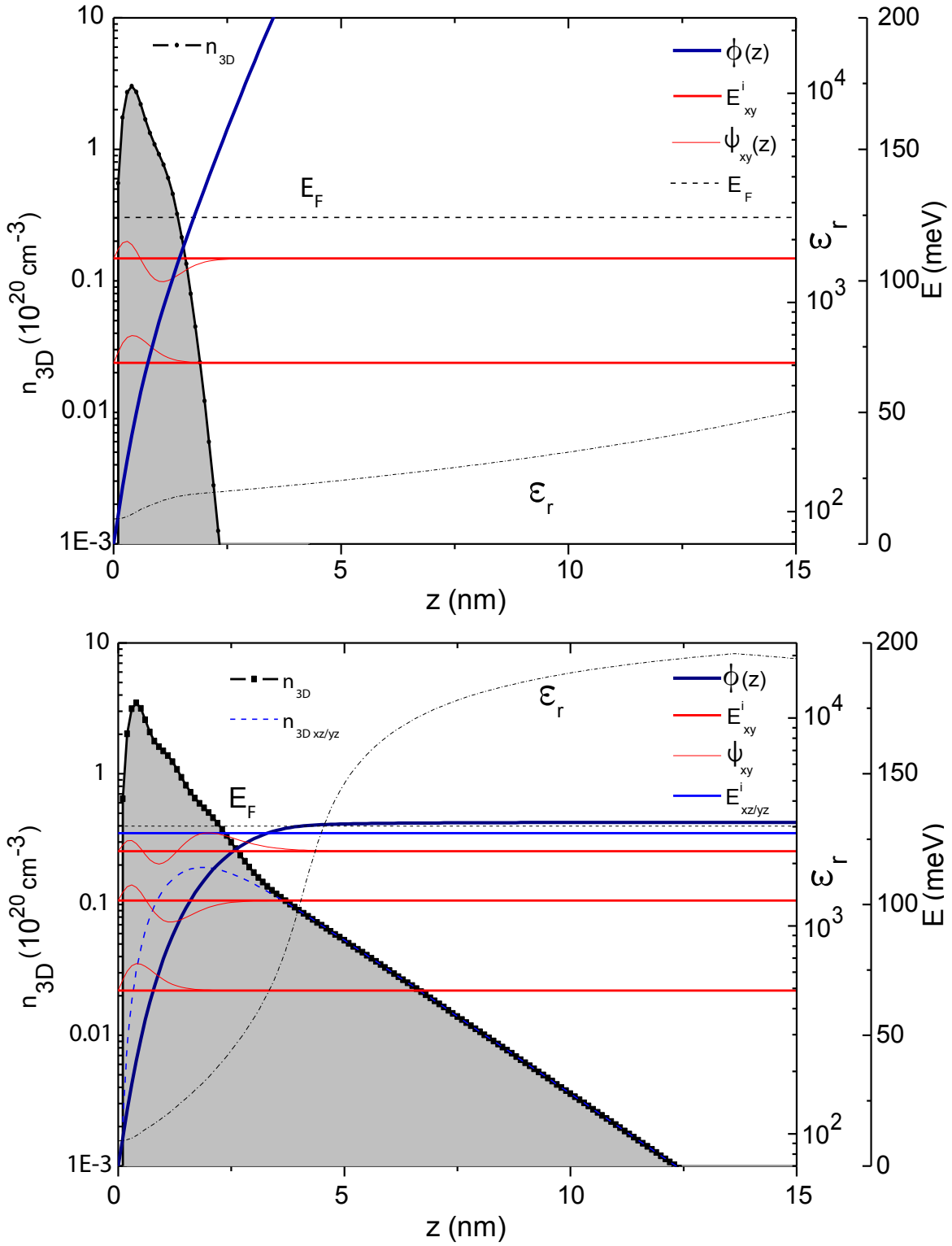

Figure 1.10 – Simulation of the potential well calculated self-consistently with both xy and xz/yz bands using Schrödinger-Poisson simulations. On the graph, E_F is the Fermi level, the 3D density and energy levels of the xy band are plotted in red, and the energy level of the xz/yz is plotted in blue. For $V_{BG} = -100$ V (upper panel), two d_{xy} bands are populated. The extension of the gas is 2.5 nm. The calculated dielectric constant ε_r is low in the quantum well, much lower than the bulk value. For $V_{BG} = 100$ V (lower panel), three d_{xy} bands and one $d_{xy/yz}$ band are populated. The gas extends to 12 nm, thanks to the $d_{xz/yz}$ bands as shown by the dashed blue line. ε_r recovers a bulk value in a region where the 2DEG density is non zero.

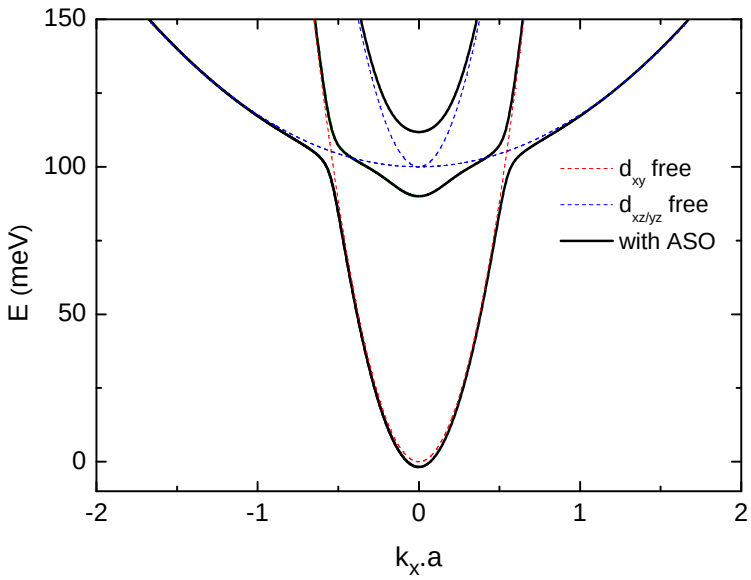

Figure 1.11 – In red and blue the dotted curves represent the free d_{xy} and $d_{xz/yz}$ bands respectively. Dispersion relation with atomic spin-orbit $\Delta_{ASO} = 10$ meV and in-plane mass $m_l = 0.7 \times m_e$ and $m_h = 14 \times m_e$ are presented in black. Here we have considered only one d_{xy} subband.

where α, the Rashba spin-orbit coupling constant, is directly proportional to the electric field. This last term in the Hamiltonian lifts the spin degeneracy and thus the spin is no longer a good quantum number (fig. 1.12 left). Near $k = 0$, the effective interaction in the orbital basis is Rashba-like [54] :

$$\left\langle k, d_{xy}, \sigma' \right| H_{RSO} \left| k, d_{xy}, \sigma \right\rangle = \alpha_1 (\mathbf{k} \times \boldsymbol{\sigma}).\mathbf{z} \qquad \text{where} \quad \alpha_1 \simeq \frac{\Delta_{ASO} \times \Delta_{RSOC}}{\Delta_I} a \tag{1.10}$$

where a is the lattice constant, α_1 is the effective spin-orbit coupling constant, $\Delta_{RSOC} = 2\alpha k_F$ is the spin-splitting energy and Δ_I the distance between the bottom of d_{xy} and $d_{xz/yz}$ bands. This relation between band structure and effective Rashba spin-orbit coupling constant will be crucial for the understanding of our results. The density of states in the presence of both atomic spin-orbit and Rashba spin-orbit coupling is presented on figure 1.12. The presence of these interactions tends to smooth the Lifschitz transition by mixing the d_{xy} and $d_{xz/yz}$ bands. In this sweet spot, the spin splitting energy is up to 20 meV for $\alpha = 4 \times 10^{-12}$ eV.m (indicated in grey on fig. 1.12 right) and an anisotropic spin texture is formed.

Experimentally, the presence of Rahba spin-orbit coupling was first identified by Cavilgia et al. and Ben Shalom et al. by measuring the magneto-conductance of the 2DEG [56, 4]. However, more experiments are needed to fully confirm the exact nature ot the spin-orbit interaction from magneto-transport experiment. This question will be addressed in chapter 3. More recently, E. Lesne et al. demonstrated an efficient spin to charge conversion in LAO/STO thanks to the Rashba spin-orbit coupling [57].

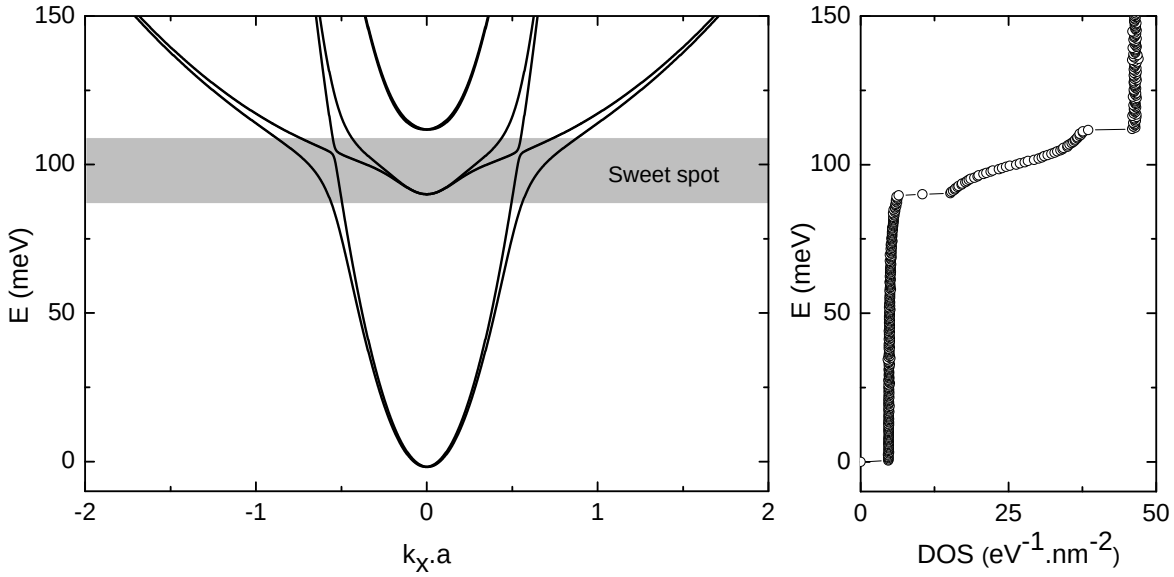

Figure 1.12 – (Left) Dispersion relation in the presence of both atomic spin-orbit and Rashba spin-orbit coupling as described by equation (1.8) and (1.9) for $\Delta_{ASO} = 10$ meV, $\alpha = 4.10^{-12}$ eV.m, $m_l = 0.7 \times m_e$ and $m_h = 14 \times m_e$ (Right) The density of state (DOS) corresponding to the dispersion on the left.

1.2.4 Typical Energy and Length Scales

When cooling a LAO/STO heterostructure, the resistance shows a Fermi liquid behaviour from 100K to 10K followed by a weak localization at lower temperature (chapter 3). The resistivity of as grown samples (ie non-gated sample) at 500mK is typically 300 $\Omega/\square$. Here is a list of the characteristic transport properties of the $LaAlO_3/SrTiO_3$ interface :

- **Mobility** is in the range of 100-1000 $cm^2/(V.s)$ for the samples studied in this thesis, depending on the intrinsic disorder and the band filling. It can be up to $\mu \simeq 10^4$ $cm^2/(Vs)$ for non superconducting samples under different growth conditions [1].
- **Fermi energy** is around $E_F \sim 100$ meV as previously mentioned. This value is small compared to the typical value for a metallic thin film like Pb (around 500 meV [58]). Assuming an in-plane effective mass of $0.7 \times m_e$, the Fermi wavelength is around $\lambda_F \simeq$ 10nm.
- **Scattering length** : the mean free path is short compared to those in clean semiconductors. By estimating it within a one band model the elastic scattering length is $l_e < 50$ nm. Below 10K the resistance starts to increase slowly due to weak localization (see chapter 3 for more details).
- **Electron-Phonon interaction** : there is a strong lattice-electron coupling with TO phonons [59, 24]
- **Coherence length** : the 2DEG is superconducting with a maximum critical temperature T_c of 300 mK. The coherence length, $\xi \simeq 70$ nm extracted from critical fields

measurements, is larger than the thickness of the superconducting layer $d < 10$ nm [2]. We are dealing with a 2D superconductor.

Magnetism The presence of magnetism was measured by torque magnetometry in the group of Mannhart from 300mK up to 40K [5]. Bert et al. reported clear localized magnetic dipoles oriented in the plane using scanning SQUID magnetometry (fig. 1.13) [60]. However, it is hard to discriminate between magnetism that may be due to impurities far from the interface and magnetism related to the 2DEG.

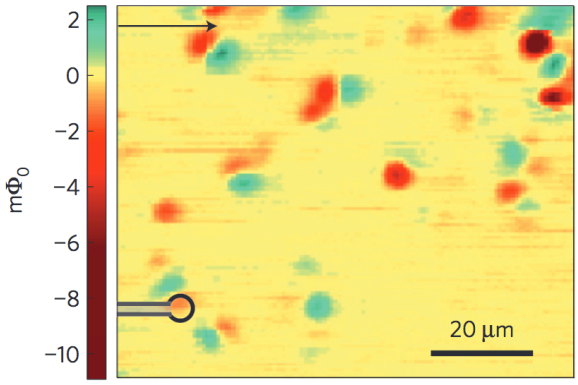

Figure 1.13 – Localized magnetic dipoles measured with SQUID. The dipoles are mostly oriented in-plane. Figure is taken from [60]

The presence of magnetism at the LAO/STO interface was also demonstrated by transport measurement, by showing hysteretic behaviour of the critical temperature and sheet resistance upon magnetic field sweeping at the lowest temperature [61]. This is surprising because neither STO nor LAO have magnetic properties. However, these results remain controversial as this hysteretic behavior is not seen by many groups (includind our group). Different scenarios could explain the existence of ferromagnetism at the interface. The first one is that localized d_{xy} states of titanium close to the interface create magnetic moments [62]. The second is that such magnetic moments are due to oxygen vacancies created during the growth or due to polar catastrophe. In all cases, the possible coexistence between superconductivity and magnetism is quite surprising and hotly debated.

1.3 2D Superconductivity

1.3.1 Superconducting properties

As the 2DEG is standing on the STO side of the interface [48], it is expected that the LAO/STO superconductivity mechanism originates from it. Close to the interface the electric field breaks inversion symmetry and affects the dielectric constant. A few nanometers deeper, the dielectric constant recovers bulk values as seen in our numerial simulation of the interfacial band structure (see fig. 1.10). Assuming that ferroelectric soft modes are responsible for attractive pairing [37], the superconducting gap of LAO/STO would have a s-wave symmetry. With a critical temperature comparable to the critical temperature of bulk STO ($T_c \sim 0.3$K), and within BCS theory, the gap of LAO/STO is around $\Delta = 1.76 k_B T_c \sim 40$ μeV.

Superconductivity was first measured by Reyren et al. in 2007 [2]. By applying a perpendicular magnetic field, they estimated the superconducting coherence length $\xi(T = 0) \simeq 70$ nm using the Ginzburg-Landau critical magnetic field $B_{c\perp}(T) = \phi_0/2\pi\xi^2(T)$ (figure 1.14). Together with the in-plane critical magnetic field $B_{c\parallel} = \frac{\sqrt{3}\phi_0}{\pi\xi_\parallel d}$, it gives an upper bound for the 2DEG thickness of $d < 10$ nm $< \xi$ [2, 4]. This upper bound shows that LAO/STO 2DEG is a two dimensional superconductor, where Beresinsky-Kosterlitz-Thouless (BKT) physics is expected to take place [63]. This is developed in chapters 4 and 5.

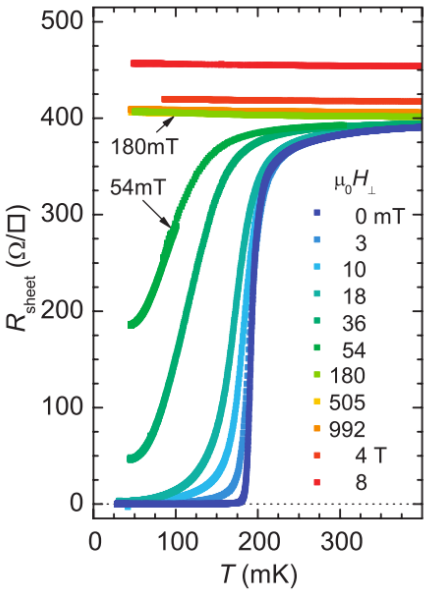

Figure 1.14 – Resistance as a function of temperature for different perpendicular magnetic fields [2]

Surprisingly $B_{c\parallel}$ can be up to four times higher than the Chandrasekhar limit corresponding to the energy needed to break a Cooper pair in a singlet state $\Delta \sim g\mu_B B_{c\parallel}$, where g is the Lande factor (usually $g \sim 2$), μ_B is the Bohr magneton and $B_{c\parallel}$ the critical in-plane magnetic field. This result has remained unexplained up to now.

1.3.2 Dome shape of T_c with doping by electric field effect

Using field effect through a back gate, Caviglia et al. [3] were able to tune the density of carriers at the LAO/STO interface. Figure 1.15 (a) shows R(T) curves as a function of the gate voltage. By applying a negative gate voltage and therefore removing electrons, they were able to completely suppress superconductivity. Figure 1.15(b) represents the typical phase diagram of LAO/STO. The transition at T=0 from a metal to an insulator by tuning an internal parameter

of the Hamiltonian is called a Quantum Phase Transition (QPT). When increasing the gate voltage and consequently the electron density, the critical temperature reaches a maximum before decreasing. The maximum T_c is obtained for an optimal doping which allows to define an underdoped region (gate lower than the optimal doping) and an overdoped region (gate higher than the optimal doping). This dome shape behavior is similar to superconductivity in STO but takes place on a much smaller doping range. Indeed, for a 10 nm thick 2DEG, the 3D carrier density range where superconductivity is observed is $\sim 10^{20}$ e^-/cm^3, as compared to a few 10^{21} in bulk STO.

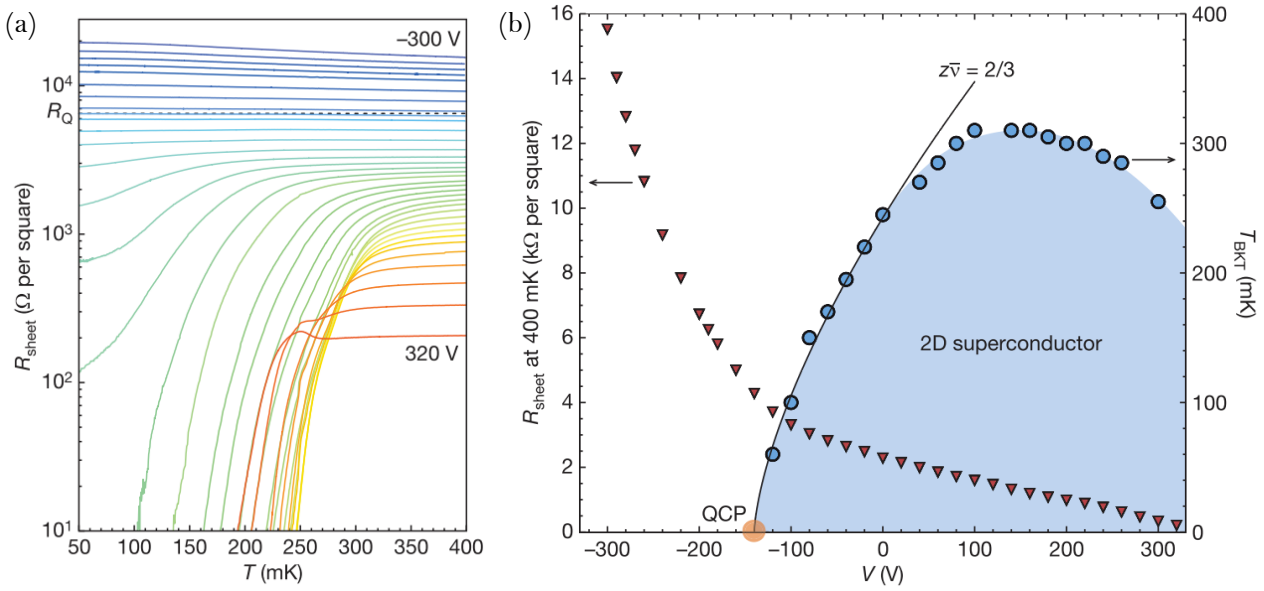

Figure 1.15 – (a) Resistance as a function of temperature for different back gate voltages. At negative gate voltage superconductivity slowly decreases until the system reaches a weakly localizing metal state. The effect of applying a positive gate voltage is to add electrons to the system, lowering the resistance and changing the critical temperature. (b) Phase diagram with temperature and back gate voltage extracted from R(T) curves; the quantum critical point is indicated in orange. The figures were adapted from [3]

Several scenarii were proposed to explain this dome behaviour at the LAO/STO interface. Gariglio et al. proposed to explain it by a sudden extension of the 2DEG for high doping levels leading to a decrease in 3D carrier density [64]. Maniv et al. proposed a scenario where electronic correlations leads to a non monotonic filling of the $d_{xz/yz}$ band [65]. Mohanta and Taraphder included spin-orbit interaction and magnetism in a tight binding numerical calculation to account for the dome shape in T_c [66]. Finally, Klimin et al., following recent theoretical predictions of the possible origin of superconductivity in bulk STO, proposed a mechanism based on optical phonons at the LAO/STO interface [67, 68]. As of today there is still no consensus about the origin of the decrease of T_c in the overdoped region.

1.3.3 Inhomogeneous superconductivity in LAO/STO

In addition to the superconducting microscopic properties developed above, an ingredient has to be included for a full understanding of the LAO/STO interface electronic properties. For instance, tunneling [69, 70], atomic force microscopy [71] and SQUID magnetometry [72] experiments provide clear evidence for the existence of spatial inhomogeneities at mesoscopic scales. The origin of such inhomogeneities could be related to materials properties (ferroelectric domains for instance) but could also be the result from an intrinsic mechanism. N. Scopigno et al. proposed a phase separation mechanism based on the negative compressibility of the 2DEG [73]. Spin-orbit coupling could also favour such a phase separation mechanism where small regions with higher densities are embedded in a more diluted phase [74].

1.3.3.1 R(T) with tails

When the superconducting transition is plotted using a linear scale, one can not ignore the tails in the resistance as a function of temperature that occurs. Above T_c, the downward rounding of the transition can be attributed to Aslamasov-Larkin fluctuations of the amplitude of the superconducting order parameter. However, the tail of the R(T) curves is too broad to be be fitted using a standard BKT approach for an homogeneous superconductor [75]. Moreover, in the underdoped region, signs of superconductivity are present but the resistance often saturates at a finite value. This implies that superconductivity can not percolate through the sample and that some regions of the sample are not superconducting. In order to explain such result, S. Caprara et al. proposed a Random Resistor Network (RRN) model [76]. Within a mean field theory, the RRN is called Effective Medium Theory (EMT) and has an analytical expression.

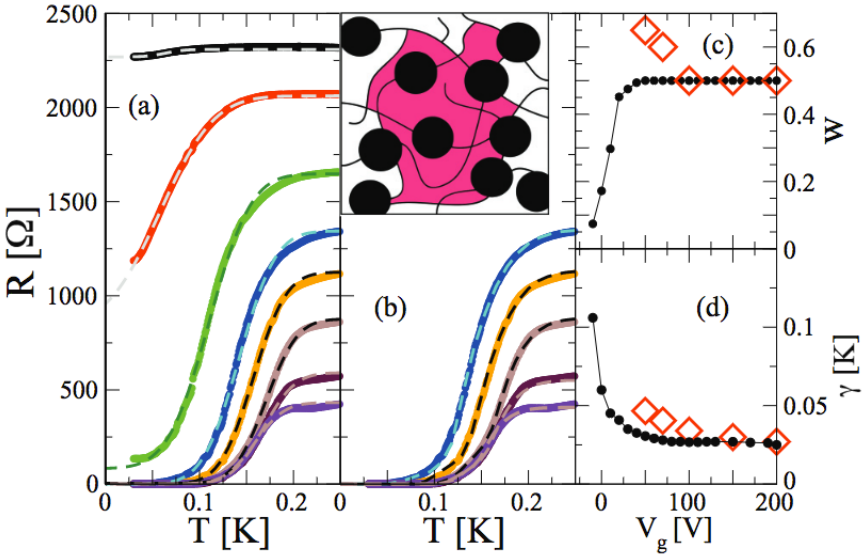

Figure 1.16 – (a) Fit of R(T) curves as a function of doping with EMT model (b) and with RRN model (c) and (d) are the superconducting fraction w and the width of the gaussian distribution of T_c γ as a function of the gate voltage. Inset : scheme of the filamentary structure (see text). Figure taken from [76]

In these models, puddles of different sizes and different critical temperatures are randomly organized on a 2D array. When the temperature is lowered, they progressively switch to zero resistance. It is interesting to note that in both models shown on figure 1.16), the width of the Gaussian distribution of the T_c of the puddles suddenly increases when the 2DEG is depleted with a negative gate voltage. In addition, it has been found that a filamentary structure of the network has to be taken into account to get the best fits, reminiscent of the calculation by Ioffe-Mezard [77] and Castellani et al. [78].

1.3.3.2 Superconductor-Insulator Transition driven by a magnetic field

Superconductor-to-insulator transition (SIT) driven by magnetic field was studied in our group by Biscaras et al. in 2013 [79]. They demonstrated the existence of multiple critical fields which were interpreted as reflecting the non homogeneous nature of the system. They considered the situation of superconducting puddles (islands) coupled by Josephson effect through a metallic 2DEG.

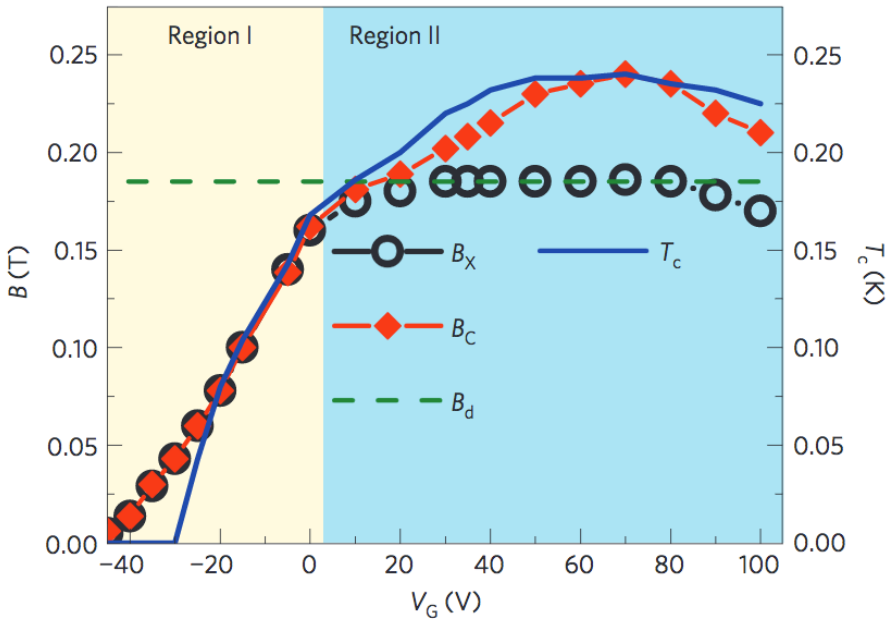

Figure 1.17 – Two critical magnetic field B_x and B_c obtained from finite scale analysis performed in two different ranges of temperature are plotted as a function of back gate voltage. At low doping, they coincide with the T_c versus V_G curve, but at high doping, B_x saturates whereas B_c keeps following T_c. Figure taken from [79]

Using finite-size scaling analysis, they showed that above a certain temperature, the dynamics corresponds to clean superconductivity inside individual puddles, while at low temperature, the dynamics reveals superconducting fluctuations of the whole arrays of puddles (see fig. 1.17). The size of these puddles can be estimated from the value of the critical field B_x in the overdoped region. Assuming this field corresponds to a dephasing magnetic field $B_d \sim \phi_0/L_d^2$, they estimated the size of the puddles to be around $L_d \simeq 100$ nm.

1.3.3.3 Josephson-like behaviour

More recently, measurements performed on Hall bars reported unusual I(V) curves [46]. While a non-hysteretic behaviour is usually expected for a homogeneous superconductor, the current-voltage I(V) characteristics shows a strong hysteresis most commonly encountered in Josephson junctions.

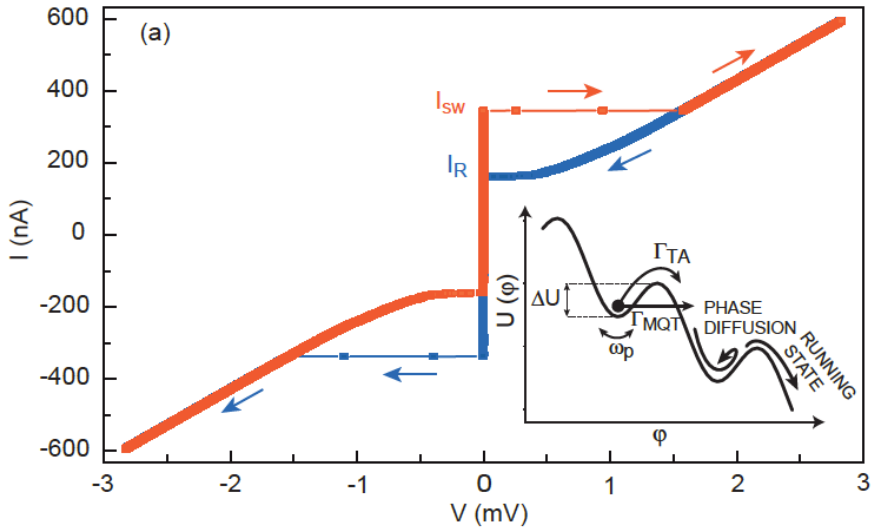

Figure 1.18 – I(V) curve of a LAO/STO Hall bar obtained by ramping the current up and down. When the current is increased, at $I = I_{sw}$, the system suddenly switches into a resistive state. When the current decreases, the Hall bar recovers a superconducting state at a lower intensity called the return current I_R. The inset presents the dynamic of the phase of a single Josephson junction in the underdamped regime.

Figure 1.18 shows a typical I(V) curve for a Hall bar device in LAO/STO measured by S. Hurand [80]. When the current is progressively increased, starting from the superconducting state, a sudden switching to the normal state occurs at I_{sw}. When the current decreases starting at $I > I_{sw}$, the 2DEG recovers a superconducting state at a current I_R significantly smaller than I_{sw}. Hurand et al. did a systematic study of the switching current distribution as a function of doping and temperature and showed that the dynamics was consistant with the behaviour of an array of Josephson junctions in the underdamped regime. Prawiroatmodjo et al. showed that the critical current depends on the magnetic field in a way which is similar to a Josephson junction [46] : $J_c(B) \propto 1/(1 + B/B_0)^{\beta}$, where $\beta \simeq 1$. They estimated the typical size of the mesoscopic Josephson junction in the array as $\sim 100 - 200$ nm.

Chapter 2

Devices Fabrication and Experimental Setup

"Ce n'est qu'en essayant continuellement que l'on finit par réussir. Autrement dit : plus ça rate, plus on a de chance que ça marche."
Devise Shadok

Contents

The aim of this chapter is to introduce the technical details of devices fabrication and measurement setups. In section 1, we explain how the different devices were manufactured, from the pulsed laser deposition of LAO on a STO substrate to the realization of field-effect devices. In section 2, we describe the different experimental setups which have been used for DC and high-frequency transport measurements.

2.1 Devices Fabrication

The recent progress in the fabrication of epitaxial interfaces with complex oxide materials has opened new possibilities to engineer artificial heterostructures where new phenomena take place. The first LAO/STO heterostructures presenting a two-dimensional electron gas were made in

the group of H. Hwang at Bell Labs by using Pulsed Laser Deposition [81]. This powerful technique allows to build atomically flat structures with a lot of different materials (cuprates, manganites, transition metal oxides...). In the case of the LAO/STO interface the growth is sensitive to many parameters such as oxygen partial pressure, temperature, the orientation and the terminated surface of the substrate, or the fluence of the laser. For this reason, it is difficult to fabricate reproducible samples with good electronic properties. In this section we describe the fabrication procedure employed by our different collaborators.

2.1.1 Sample growth

Samples studied in this thesis were grown by E. Lesne, at the Thales-CNRS lab, in the group of M. Bibes and A. Barthélémy and by P. Kumar at NPL New Delhi in R. Budhani group. Although each group has its own receipe, the overall fabrication process is rather similar. We report here the one used in the Thales-CNRS lab. First a commercially available 0.5 mm thick STO monocrystal is TiO_2-terminated by HF [1] treatment. The horizontal miscut creates atomically flat terraces with a typical width of 300 nm (see fig. 2.1(a)). The substrate is pasted at the center of a vacuum chamber with silver epoxy and heated to a high temperature (T=650-800°C) with an infrared laser.

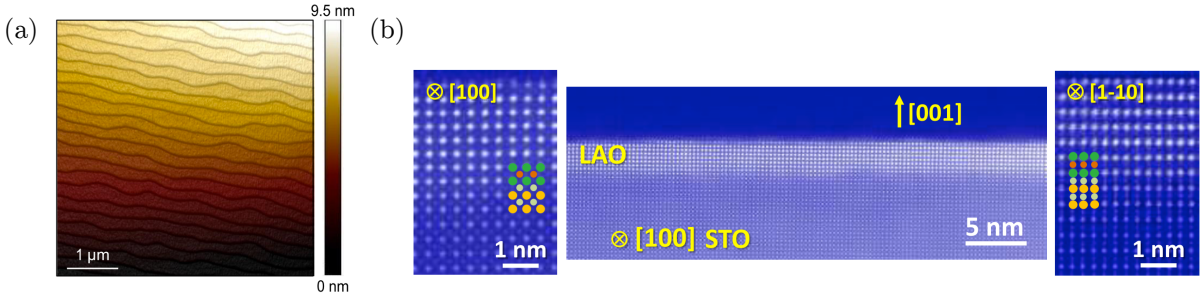

Figure 2.1 – (a) AFM image of a LAO/STO sample with terraces. This image was measured by E. Lesne (UMR CNRS-Thalès) (b) HAADF-STEM images of a (001) oriented $LaAlO_3/SrTiO_3$ interface. Zooms in 100 and 1-10 directions are presented on the left and on the right. Adapted from [82]

A target of LAO is then ablated at a laser fluence of 1 J.cm^{-2} and a repetition rate of 1Hz under a partial oxygen pressure of $P_{0_2} = 2 \times 10^{-4}$ mbar. The power of the laser is sufficient to expel a stoichiometric quantity from this LAO target. The atoms meet the surface of the STO sample and organize themselves epitaxially. This is possible only because the STO and LAO lattice parameters are close to each other ($a_{LAO} = 3.79$ Å and $a_{STO} = 3.905$ Å). If the fluence is well calibrated, one layer of LAO crystal is created at each step. During the process, the number of unit cells deposited is monitored by high energy electronic diffraction (RHEED). After the deposition, the sample is cooled down to 500°C with a 10^{-1} mbar oxygen pressure. In order to avoid the creation of oxygen vacancies, the sample is finally annealed for 30 minutes under a pressure of oxygen of 400 mbar and then slowly brought back to room temperature.

1. Hydrofluoric acid

2.1.2 Patterning the LAO/STO interface

In this thesis, we tested two different methods to pattern the 2DEG at the LAO/STO interface. The first which was developed in the group of J-M Triscone at Geneva University, uses an amorphous LAO layer as a template. The second was developped in our group over the past years and requires an irradiation with high-energy oxygen ions : it is called the irradiation technique. The results obtained with this second technique are not presented in this manuscript [83]. All the processes used for devices fabrication can be found in appendix D.

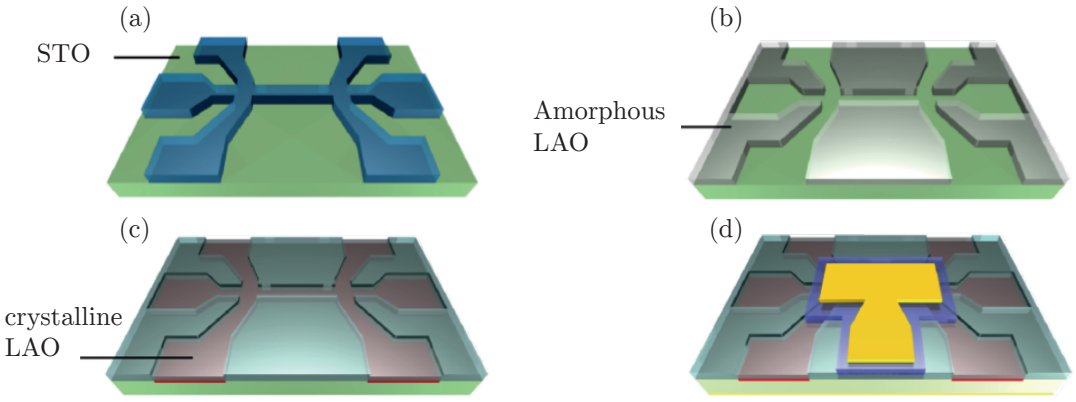

Figure 2.2 – Amorphous LAO technique (a) A resist with Hall bar shape is deposited on top of a TiO_2 terminated STO. (b) Amorphous LAO template after lift-off (c) Deposition of a few crystalline LAO layers (d) Deposition of a top gate separated by a dielectric with optical lithography and liftoff technique

Amorphous LAO technique : The main idea of the amorphous LAO technique is to deposit a thick amorphous LAO template on a TiO_2 terminated STO substrate. First, a 2.1 μm thick negative resist (AZ2021) with a Hall bar shape is deposited on the STO substrate using optical lithography technique (fig. 2.2 (a)). Second, a 50 nm thick amorphous LAO layer is deposited at room temperature, followed by a lift-off to obtain the amorphous LAO template as shown on figure 2.2 (b). Under the right condition of oxygen pressure, this step does not modify the properties of the STO substrate which remains insulating. Third, a 4 to 12 u.c. thick LAO layer is then deposited at high temperature such that a crystalline epitaxial growth is realized on the uncovered area of the STO substrate (fig.2.2 (c)). Growth on amorphous layer is not epitaxial, and the top layer is insulating. Therefore, the 2DEG takes place in the uncovered part in a shape of a Hall bar. Detailed recipes are given in appendix D. A picture of this Hall bar is shown on figure 2.3 (a).

2.1.3 Top Gate and Back Gate fabrication

The final step represented on figure 2.2 (d) consists in depositing an insulating Si_3N_4 dielectric layer and a gold top gate by lift-off to control electrostatically the number of electrons in the system. One of the main difficulties is to avoid current leakage between the gate and the 2DEG when applying a voltage.

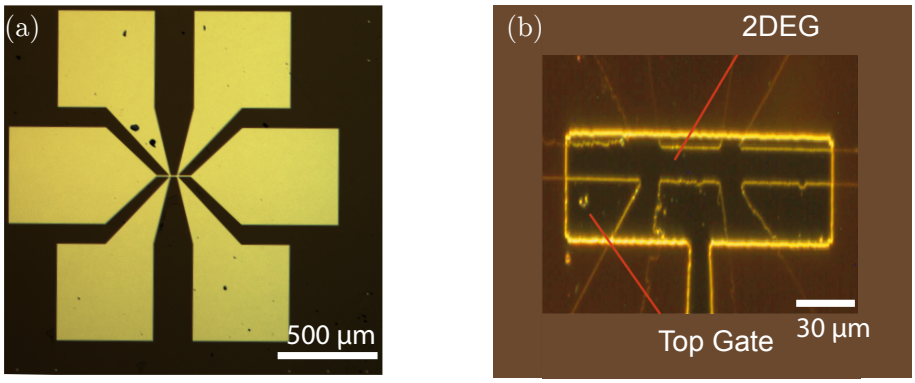

Figure 2.3 – (a) Optical picture of the Hall bar defined by amorphous LAO technique on the sample studied in chapter 6 before the deposition of QPC top gates shown on fig 6.3. (b) Dark field optical microscope picture of the center of the Hall bar, on the top of which the global top gate studied in chapter 3 is deposited.

In order to avoid leakage, we had to find a dielectric material with good insulating properties. In addition, we needed a dielectric that did not affect the polar catastrophe which occurs in the LAO layer. Si_3N_4 and HfO_2 were both tested. They both preserve the LAO/STO properties. Our global top gate is separated from $LaAlO_3/SrTiO_3$ by a 500 nm thick Si_3N_4 layer. The Si_3N_4 was deposited at relatively low temperature ($< 80°C$) using a RF magnetron sputtering technique at minimum power (200 W) for five hours. A maximal partial pressure (67.5% of Ar, 32,5% of N_2) of P=1.10^{-2} mbar was chosen to avoid the formation of cracks which could weaken the insulating properties of Si_3N_4. This top gate could hold a 100 V voltage without current leakage, despite its large area ($\sim 1000\ \mu m^2$). Figure 2.3 (a) shows an enlarged view on the Hall bar before the deposition of top gates.

A back gate was also deposited on the back side of the STO substrate by e-beam evaporation. Unlike the top gate, this gate is far from the interface as the thickness of the substrate is 0.5 mm. However, the high-value of the dielectric constant in STO (24000) enables the production of an efficient electric field effect despites the thickness of the STO. Back gating is now commonly used in the community. Irreversible effects occurs when the gas is extremely overdoped. This was studied in details by Biscaras et al. [84]. In order to perform reversible measurements, a first polarization with a positive back gate voltage is done at 4K before each measurement presented in this manuscript.

2.1.4 Quantum Point Contact Fabrication

With optical lithography, it is possible to design structures down to the micrometer scale but not much below. Reaching scales orders of magnitude smaller is achievable by electron beam lithography. In this last paragraph, we give the details of the fabrication of a quantum point contact with split gates. These structures were fabricated at Center for Nanoscience and Nanotechnology in collaboration with Christian Ulysse (C2N-Marcoussis).

It was recently shown that the electronic lithography technique can be used to fabricate sub-micrometer devices in LAO/STO without altering their properties [85]. In order to design the quantum point contact experiment, one needs to reach an appropriate scale of the order of $\lambda_F \simeq 10$nm. Our gates were realized with an electronic masking device RAITH-VISTEC EBPG 5000 plus.

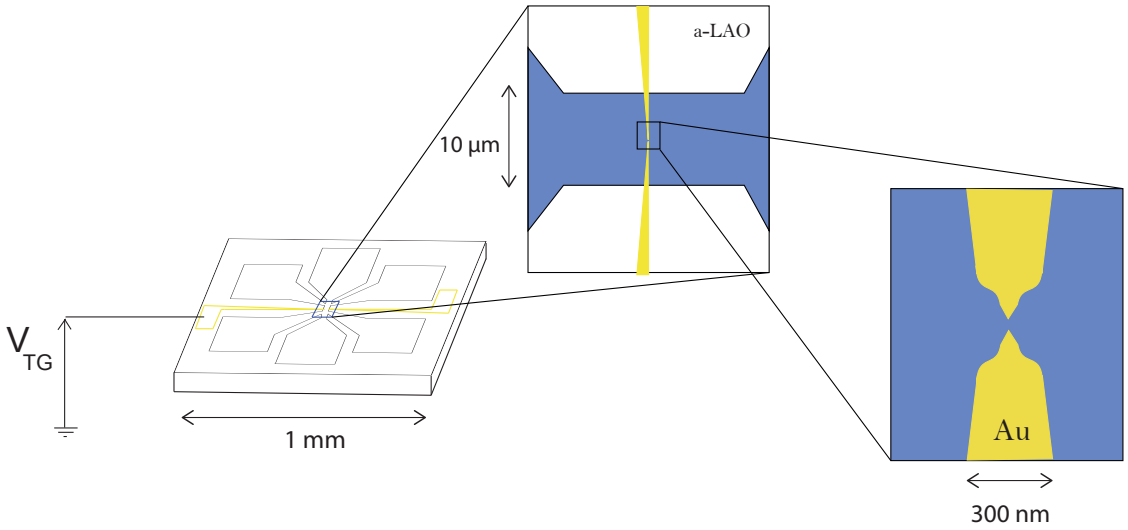

Figure 2.4 – Schematic of the QPC with the two split gates deposited on a the Hall bar designed by amorphous LAO technique shown on fig. 2.3 (a). A top gate voltage V_{TG} is applied simultaneously on each split gate. The arms of each gate are large (300 nm) to ensure that the current is only flowing in the region of interest.

Figure 2.4 shows a SEM image of one of the devices measured in this thesis (chapter 6). It consists of a 10 micron wide Hall bar as (described above) covered at the center by two split gates. Unlike the global top-gate described previously, this top gate is not separated from the sample by a thin dielectric layer. For this experiment, we needed the gates to be as close as possible to the 2DEG in order to produce a sharp confining potential in the transverse direction. A thicker LAO layer (5 nm) was deposited during the PLD process and the gold layer is thus deposited directly on the top of the Hall bar. In the sample shown on figure 2.5, the distance between the two split gates is approximately 26 nm. Despite the weak thickness of the LAO layer, no leakage current was measured on this sample between -3 V and 3 V, showing the good quality of the crystalline LAO layer.

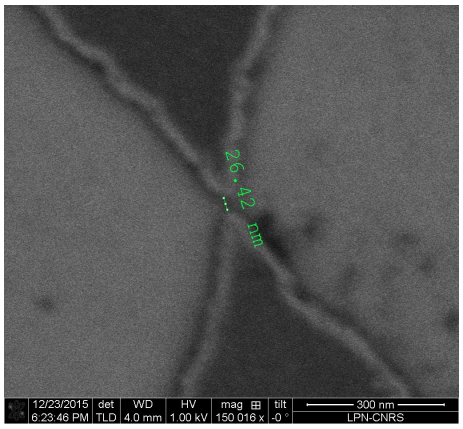

Figure 2.5 – SEM image of the split gates with a gap of 26 nm. The results obtained on this device are given in chapter 6.

2.2 Measurement Setups

In this section, we explain briefly how transport measurements were done both at low and high frequency. All the measurements were performed at very low temperatures in a dilution refrigerator manufactured by Cryoconcept, a french company. The goal of this section is to present the different experimental techniques used during this thesis. First, in sub-section 2.2.1 we explain how the sample is cooled down to low temperature, then, in 2.2.2, we discuss the different types of wiring that enable measurements in different frequency ranges. The final part of the section 2.2.2 is dedicated to the microwave reflection measurement setup used in chapter 5.

2.2.1 ^{3}He/^{4}He Dilution refrigerator

This dilution refrigerator showed in figure 2.6 is a closed-cycle cryostat which does not require the use of liquid ^{4}He to reach 4 K, as opposed to the previous generation of 'wet' fridge. Instead the ^{3}He/^{4}He mixture cooled down to 3 K by a two stages pulse tube (PT415 Cryomech model), using Joule-Thomson cycles. The first stage (PT1) has a 40 W cooling power, while the second one (PT2) has a cooling power of 1.5 W at 4.2 K (see schematic on fig. 2.6). The fridge is equipped with a system which protects the lower plates from mechanical vibrations while ensuring the heat transfer.

The last step is to enter into the dilution regime. At 2 K, ^{4}He and ^{3}He are in the liquid state. In the mixing chamber, below 800 mK, the mixture separates into two phases. The lower one is the heavier with a majority of ^{4}He in the superfluid state. It is called the dilute phase. The upper one is the concentrated phase, it is made of almost pure ^{3}He. ^{3}He is pushed towards the mixing chamber via the condenser. On the other side of the circuit, a pump extracts ^{3}He gas out of the mixture. The ^{4}He superfluid phase is represented in grey on figure 2.6. Finally, a heat flow transfer represented by an arrow occurs between the downgoing, and the upgoing pipes. By forcing the ^{3}He to go into the dilute phase, the entropy of the system is lowered. For the sake of energy conservation, the mixing chamber absorbs heat energy. Pumping on the dilute phase cools down the base plate attached to the mixing chamber.

The schematic on the right of figure 2.6 shows how ^{3}He circulates. The cooling power of our DR is 250 μW at 100 mK and its base temperature can reach 15-20 mK, depending on the exact experimental configurations (DC or RF, B field...). The cryostat is also equipped with a 7 T superconducting magnet (in red on fig 2.6). For more details on dilution refrigerators, see ref. [86].

2.2.2 Electronic transport

Measurements at low temperature require some precautions. First one needs to make sure that no electromagnetic noise from outside reaches the sample. Second, electrons must be well thermalized to the fridge's temperature.

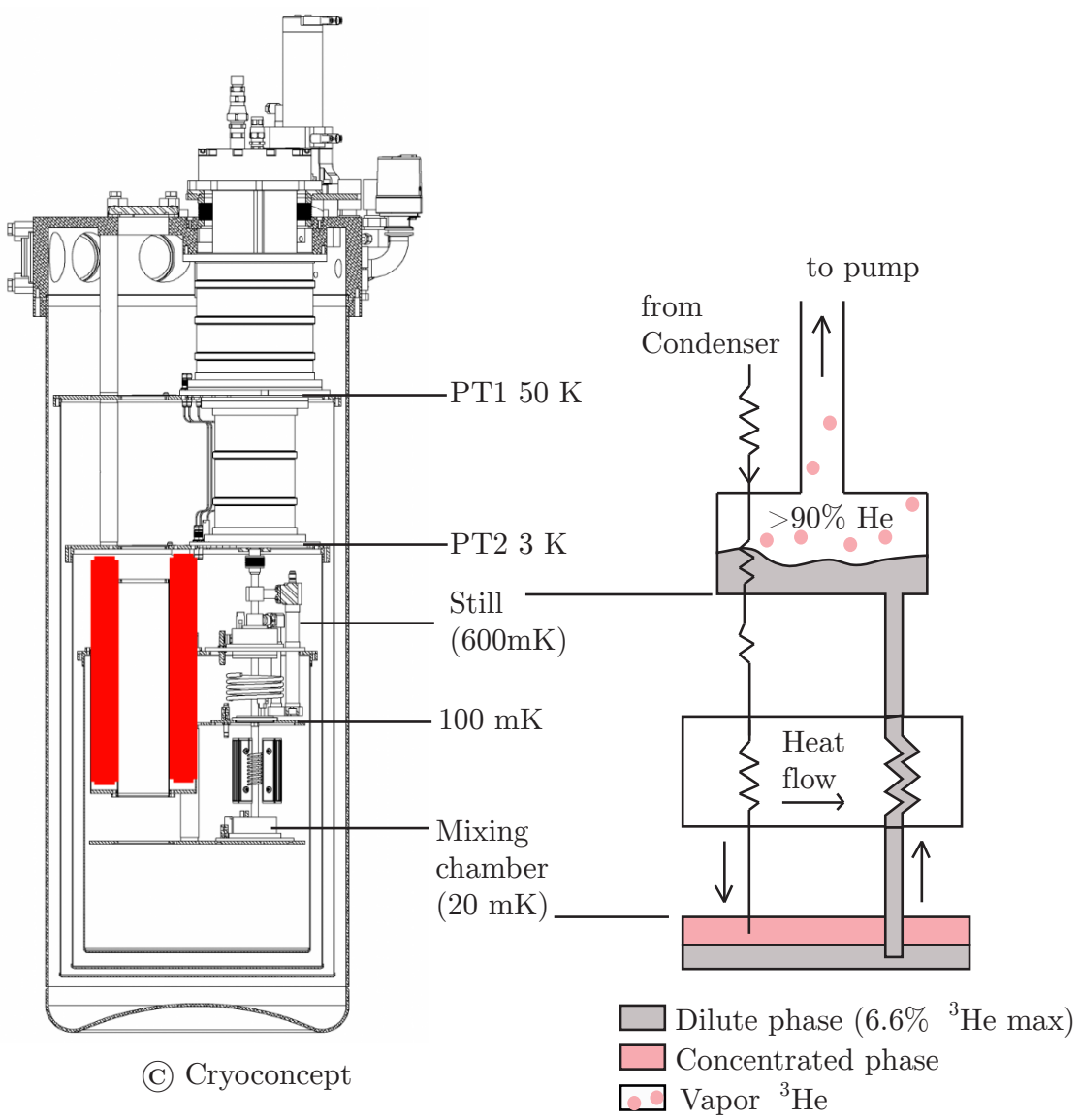

Figure 2.6 – Dilution Refrigerator schematic. A sectional view of the DR is represented on the left. The 7 T coil is shown in red. A detailed schematic of the last step of the cooling where ^{3}He is forced to enter the dilute phase is shown on the right.

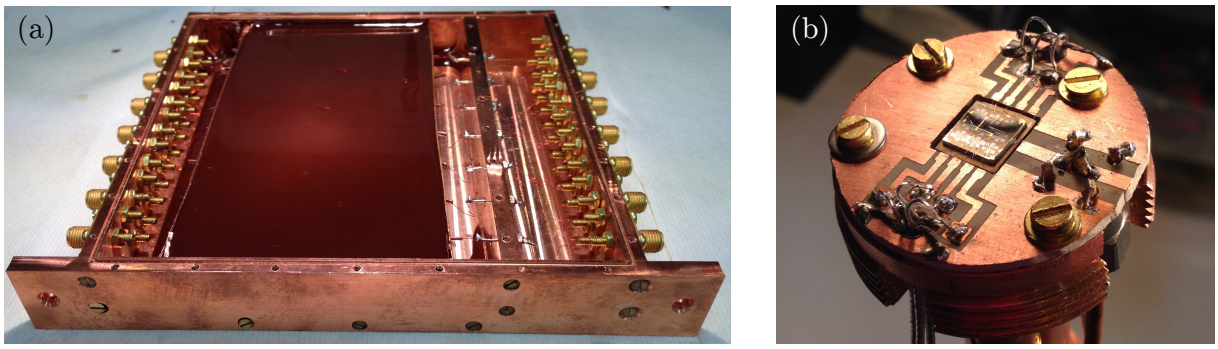

Figure 2.7 – (a) Homemade copper powder filter in series with a low pass filter. The region in brown in the center is a mix of copper powder and Stycast. The box is closed by a cap of copper tightly screwed with a thin wire of Indium to protect from external noise. (b) Picture of the sample holder with a RF connector and DC coaxial lines. On top of this sample, a cap made of copper protects it from electromagnetic noise.

2.2.2.1 Low pass filters for low noise measurements

The sample has to be protected from noise of the environment such as radio frequency and Wi-Fi signals for instance. Depending on the sensitivity of the measurement, two different setups were used. The first one consists of 24 manganite wires in twisted pairs which are thermalized through 3 cm long gold lines on Kapton at each stage, and filtered at the top of the fridge by low pass filters (Pi filters) with a 1.9 MHz cut-off frequency. The second set of cable for DC transport is comprised of 7 coaxial cables in stainless steel, thermalized at every stage (except the 100 mK) by a feed-through connector. These cables are filtered at 300 K and 20 mK by Pi filters with a cut-off frequency of 1.9 MHz. Finally, the copper powder filter presented on fig. 2.7(a) was added to suppress microwave frequency noise.

In order to fabricate the handmade filter, copper powder was mixed with Stycast 1266 and poured around a 10 m long DC wire. The small metallic spheres act like scatterers for the RF signals on a frequency range from 1 GHz to hundreds of gigahertz, leading to a strong attenuation. Figure 2.8 shows a comparison of the transmission of the line with and without the copper powder filter demonstrating a clear attenuation on the whole spectrum. This last filtering step also guarantees a good thermalization at the lowest temperature, because the filter is anchored on the 20 mK plate. Finally, the sample holder (see fig. 2.7 (b)) is mounted with a metallic cap in order to protect the last unshielded part of the circuit from the high-frequency noise in the fridge. The coaxial cables and the copper powder filter setup were mounted on the fridge for the QPC experiment reported in chapter 6. The measurements described in chapter 3 were made on the first set of cables. The second set was used in chapter 6.

2.2.2.2 Four-point measurement

Most of the DC measurements were performed on Hall bar shaped devices in LAO/STO samples, as described in section 2.1.2. Figure 2.9 schematically represents the measurement. A

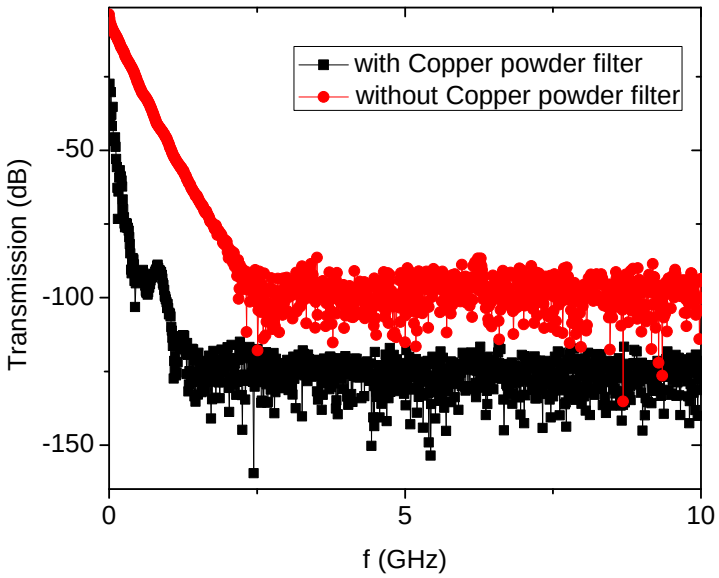

Figure 2.8 – Transmission through the whole setup from top to bottom with and without the copper powder filter.

Yokogawa 7565 voltage source is used to generate a DC bias current through a large resistance $R_{\text{Polar}} = 10$ MΩ, which is much higher than the sample's resistance. This current is measured in a resistance $R_I = 100$ kΩ by means of a voltmeter (Keithley 2000 or Lock-In amplifier). Each signal is amplified and filtered using Stanford SR 560 low noise amplifier. In order to compensate the gradient of temperature created by parasitic offset voltages due to thermoelectric effect, the resistance was measured both for positive (+I) and negative current (-I) and averaged.

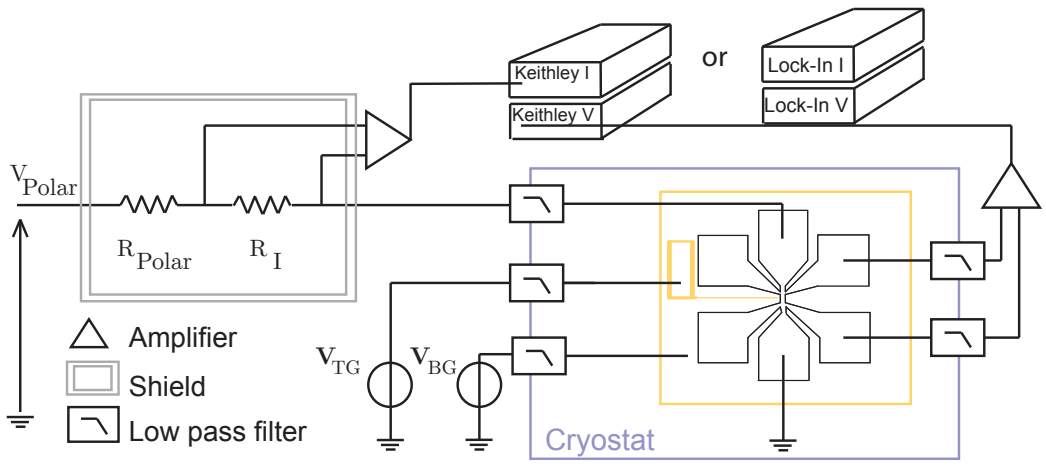

Figure 2.9 – Four points measurement schematic. The cryostat is represented by a shield at 20 mK. A polar resistance R_{Polar} is placed in a box at 300 K in series with a small resistance R_I (typically 100 kΩ).

2.2.2.3 Conductance measurement

A precise measurement of the dynamical conductance as a function of the voltage is fundamental in order to study the transport properties through a quantum point contact. This can be obtained by adding an low frequency AC signal $V_{\rm ac}$ on top of the DC voltage $V_{\rm dc}$.

Let us consider a total current consisting of a large DC current $I_{\rm dc}$ and a small AC signal $I_{\rm ac}$

$$I = I_{\rm dc} + I_{\rm ac} = I_{\rm dc} + i\cos(\omega t) \tag{2.1}$$

For $i << I_{\rm dc}$ a first order expansion of the current gives

$$V(I) = V(I_{\rm dc}) + \underbrace{\left.\frac{dV}{dI}\right|_{I=I_{\rm dc}}}_{R_{\rm ac}} i\cos(\omega t) \tag{2.2}$$

Two Lock-In amplifiers measure the small AC signals at the frequency $f_{ac} = \omega/2\pi$. The first, reads the bias current I_{ac}, while the second detects the resulting voltage V_{ac} between source and drain. One can calculate the dynamical conductance with the ratio of these two quantities.

$$G_{\rm ac} = 1/R_{\rm ac} = I_{\rm ac}/V_{\rm ac} \tag{2.3}$$

The setup illustrated on figure 2.10 (a) allows the simultaneously measurement of the DC and AC conductances. An Agilent oscillator generates (via a transformer) a periodic signal at frequency $f_{ac} = 13.29573$ Hz. The DC conductance is measured with a Keithley 2000.

2.2.2.4 Capacitance measurement

In order to know the carrier density added by gating, a measurement of the capacitance between the back gate and the 2DEG as a function of gate voltage is needed (chapters 3 and 5). This capacitance can be measured by a complex impedance method. A transformer is used to add a small AC voltage on a fixed voltage V_G applied to the back gate. The complex impedance is given by :

$$Z_{ac} = \frac{v_{ac}}{i_{ac}} = \frac{1}{j\omega C_{STO}} \tag{2.4}$$

The Lock-In amplifier detects the AC voltage $v_{\rm ac}$ between the 2DEG and the back gate in quadrature with the input current $i_{\rm ac}$, as shown on fig. 2.10 (b).

This setup allows the measurement of the capacitance as a function of the back gate voltage once the parasitic capacitance of the cable has been extracted. Figure 2.11 shows a typical measurement of the capacitance as a function of the back gate. As the STO dielectric constant is electric field dependent, the capacitance varies symetrically around $V_{BG} = 0$ V.

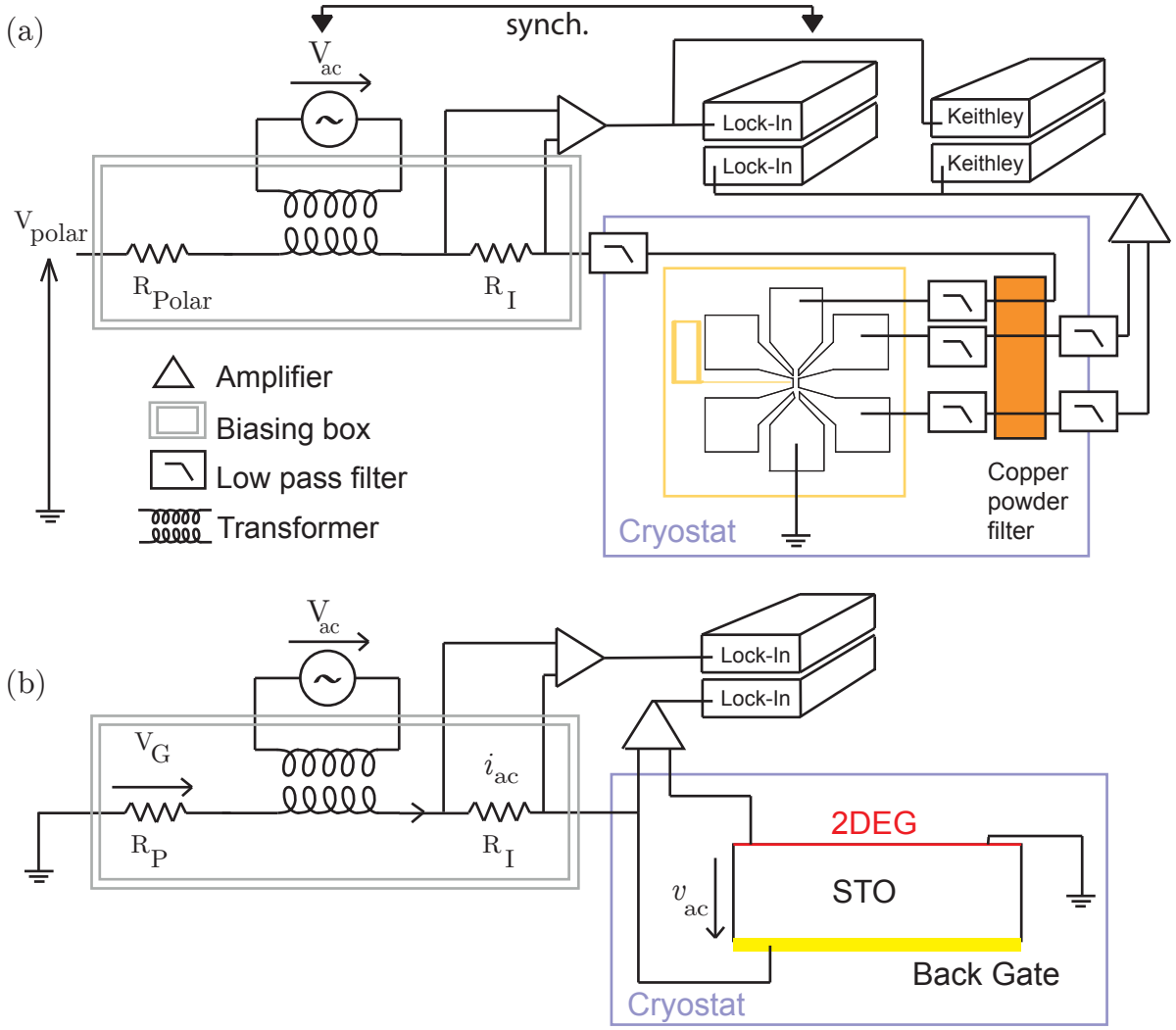

Figure 2.10 – (a) G(V) measurement setup (b) Capacitance measurement setup

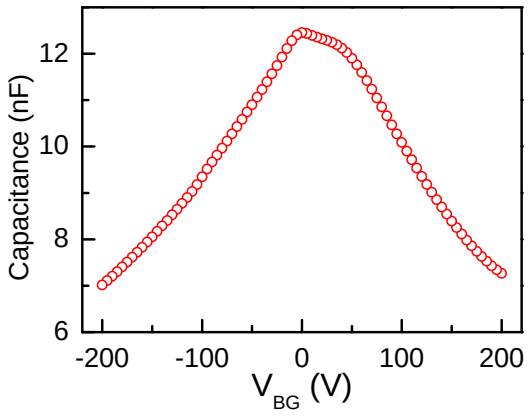

Figure 2.11 – Capacitance of the sample as a function of back gate voltage measured on the sample of chapter 3.

2.2.3 RF measurements

An RF setup was built to measure the complex conductance $G(\omega)$ of a resonant RLC circuit at around 300 MHz. The results obtained for the LAO/STO interface are analyzed in chapter 5. The complex impedance at low temperature is obtained by measuring the reflexion coefficient $\Gamma(\omega)$ with an input line and a return line as shown on figure 2.12 (respectively port 1 and port 2). A directional coupler is used to decouple the incoming wave from the outgoing one. In the following we describe the different parts of the RF setup. All the measurements were performed using a vector network analyzer (VNA) from the Rohde and Schwarz company.

2.2.3.1 Input Line

The coaxial lines are made of Cu-Ni which has a low thermal conductivity so that each stage of the refrigerator stays thermally decoupled from the other one. Their attenuation is 8 dB/m at 10 GHz. Cables at the lowest stage are made of copper which has much higher conductivity and less attenuation. Attenuators are placed along the input line at the different temperature stages in order to prevent 300 K noise to reach the sample and to thermalized the cables. The total attenuation of the input line is around 60 dB at 1 GHz.

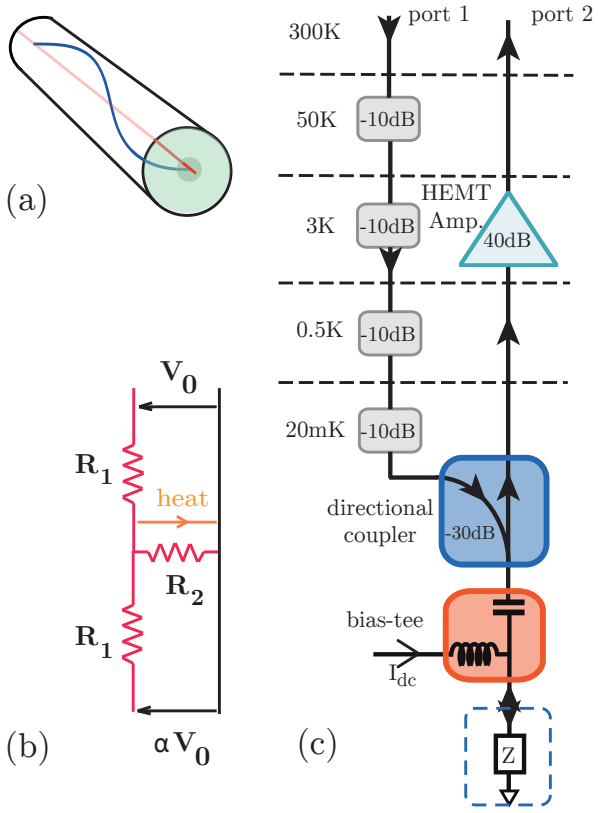

Figure 2.12 – (a) Schematic of a coaxial cable with an electromagnetic wave propagating (b) Schematic of a -10 dB attenuator. They are placed at each stage to allow thermalization of the cables. (c) RF lines in the cryostat. Each grey rectangle corresponds to an attenuator.

The external part of the coaxial cables is easy to thermalize, but the central pin is isolated

by a dielectric layer which poorly conducts heat as indicated in green on figure 2.12 (a). Cooling progressively the whole cable is allowed by putting an attenuator on each plate of the dilution fridge. Indeed, an attenuator works like a voltage divider, represented on figure 2.12 (b). Two different resistances R_1 and R_2 are tuned to match the characteristic impedance Z_0 and reduce the incident power by a certain factor $\alpha = 10^{-Loss/20}$. The presence of the resistance R_2 allows the thermalization of the central pin.

2.2.3.2 Directional coupler

A directional coupler is used to separate the incoming wave from the reflected one in blue in figure 2.12 (c). This device has 4 ports. One of them is terminated with an impedance matched with the characteristic impedance $Z_0 = 50\ \Omega$, such that no reflectivity is expected. A small fraction (-30 dB) of the incoming signal on the input port is transmitted to the coupled port while the rest of the signal is fully transmitted to the output.

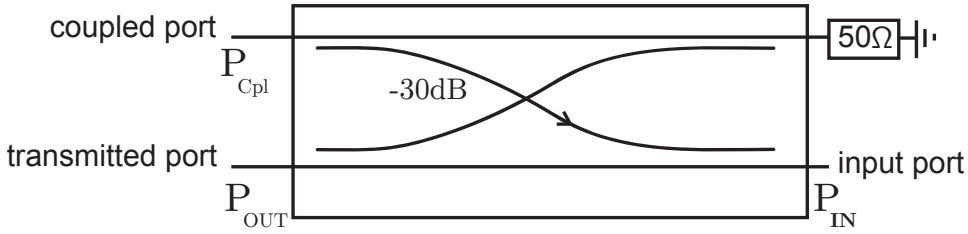

Figure 2.13 – Directional coupler schematic

The directionnal coupler used in this thesis has a bandwith 0.3-8GHz and is characterized by the following parameters

$$C = -10\ \log\frac{P_{Cpl}}{P_{IN}} \simeq -30\ \text{dB} \tag{2.5}$$

$$I = -10\ \log\frac{P_{OUT}}{P_{IN}} \simeq 1\ \text{dB} \tag{2.6}$$

$$D = -10\ \log\frac{P_{Cpl}}{P_{IN}} \simeq -50\ \text{dB} \tag{2.7}$$

Sending a strong power (typically in the range of [-20 dBm,-10 dBm]) through the input line allows us to induce a small free of noise signal in the direction of the sample. The signal reflected by the sample is mainly transmitted to the output port (see transmitted port on figure 2.13).

2.2.3.3 Cryogenic HEMT amplifier

A High Electron Mobility Transistor (HEMT) placed on the 3 K stage is used to amplify the signal on the return line. It operates on the 0.1-12 GHz band with a 4 K noise (fig. 2.12). It is a heterojunction made of multiple layers such as GaAlAs, GaAs or GaInAs. In order to allow a broad band amplification, the setup has to be optimized by impedance matching and fine tuning of all the parameters. Schematic 2.14 shows the basic principle of a low noise amplifier matched

in impedance thanks to two inductances L_S and L_G. More details are given in chapter 12 of [87].

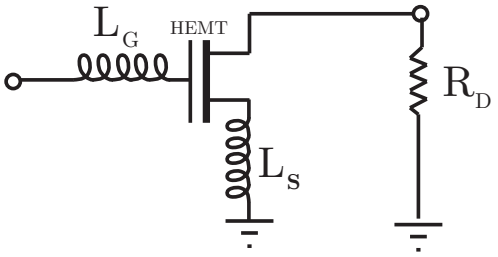

Figure 2.14 – Schematic of low noise amplifier. R_D is the load resistance.

Usually an isolator is placed in the chain to minimize the back action of the amplifier on the sample. However, these microwave elements offer only a limited bandwidth (one octave) which was not sufficient for our experiment. In addition, the back-action noise was negligible compared to the signal used to probe the system.

2.2.3.4 Bias tee

Finally, in order to perform DC measurements without disturbing the high frequency signal, we placed a bias tee between the directional coupler and our sample as indicated on figure 2.12(c) in orange. It is a three ports device. The DC current is sent through an inductance L such that $X_L = \omega L >> Z_0$. The RF signal cannot flow through such a high impedance. The second port is filtered by a capacitance C, chosen so that $X_C = 1/\omega C << Z_0$. The RF signal can easily flow through this low capacitance but the DC signal is stopped. Thanks to the bias tee we are able to perform simultaneously DC and RF measurements, which was crucial for the setup calibration.

2.3 Summary of Studied Samples

A list of the samples studied in this thesis is shown below. Samples C0, C1 and C2 are un-patterned samples that were used in chapter 3 for DC measurements. Sample A was patterned into 10 μm wide and 30 μm long Hall bar, shaped using the amorphous LAO technique (chapter 3). Sample B is an un-patterned sample that was used in chapter 5 for complex conductance measurement of the 2DEG. Finally, sample D was patterned with split gates in quantum point contact geometry (chapter 6).

Name	Institution	u.c.	Specifics	Top gate	Back Gate
A	CNRS-Thalès	8	Hall bar with a-LAO	Top gate + Si_3N_4	yes
B	Kampur	8	3×3 mm^2	No	yes
C0,C1,C2	Kampur	10	3×1 mm^2 (Cr doped)	No	yes
D	CNRS-Thalès	14	Hall bar with a-LAO	QPC	yes

Chapter 3

DC Transport

"In our endeavor to understand reality we are somewhat like a man trying to understand the mechanism of a closed watch. He sees the face and the moving hands, even hears its ticking, but he has no way of opening the case."

Albert Einstein

The Evolution of Physics (1938)

Contents

This chapter is dedicated to the study of the DC transport and magneto-transport properties of the LAO/STO interfaces both in the normal and superconducting states. By measuring longitudinal and transverse conductivities, we extract intrinsic parameters such as the mobility μ, density n, elastic τ_e and inelastic τ_ϕ scattering times and the spin diffusion time τ_{so}, as a function of electrostatic doping. However, it is sometimes difficult to disentangle the respective contributions of doping, disorder and carrier density changes to the electronic properties of the interface. For this reason, in addition to the gate voltage, we use microscopic disorder induced by Cr doping as a tuning parameter to probe the 2DEG properties.

In the first section, we show that substituting Cr for Al atoms in the LAO layer, affects essentially the elastic scattering time of the 2DEG without changing the carrier density nor the

confinement conditions. By comparing the transport properties of three samples having different level of Cr doping, we are able to study microscopic mechanisms such as superconductivity and Rashba spin-orbit coupling (SOC), and to clarify the specific role of disorder.

Most of the results that appear in the literature published to date have been obtained by using a back-gate to tune the carrier density of the interface. In the perspective of making local changes to electron doping and studying mesoscopic samples, we developed a technique to make top gates. In the second part of this chapter, we discuss the realization of top-gated devices where the superconductivity and the SOC can be tuned over a wide range.

3.1 Effect of Controlled Disorder on Superconductivity and Rashba Spin-Orbit Coupling

The influence of atomic disorder on electronic transport properties in two dimensions has been described by the weak localization theory, including electron-electron interactions effects [88]. Corrections to Drude conductivity and magneto-conductivity have been calculated. A comparison between experimental data and the theory gives access to various scattering times and diffusion lengths in the system. Increased scattering and its correlated enhancement of electron-electron interactions lower the critical temperature T_c in disordered superconductors, as proposed by Finkelstein for example [89]. It is therefore interesting to chemically dope oxide interfaces to further explore their electronic properties. Doping the STO substrate with Mn quenches electron density and mobility [90, 91, 92]. It was also recently observed that 2% doping with rare earth ions Tm and Lu at the La site of $LaAlO_3$ does not significantly affect the electronic transport [93]. An increase of SOC in δ doped $LaTiO_3/LaCrO_3/SrTiO_3$ interfaces was demonstrated by Das et al. [94]. However, all those results are not sufficient to disentangle the respective roles of doping, disorder and carrier density on the fundamental properties of interfaces such as Rashba SOC and superconductivity.

We first study the effect of Cr doping on the elastic scattering time for different gate voltages. We then present superconducting properties as a function of disorder. Finally, magneto-conductance measurements give an insight on the spin-orbit coupling mechanism at the LAO/STO interface.

3.1.1 Effect of Cr doping on the resistance

For this study three 10 u.c. $LaAl_{1-x}Cr_xO_3$ films were grown on 3×1 mm^2 TiO_2 terminated substrates, with doping parameters of x=0 (sample C0), x=0.1 (sample C1) and x=0.2 (sample C2). Details on growth conditions are given in ref. [95]. We deposited back gates on the back side of the 500 μm thick STO substrate as explained in chapter 2, section 2.1.3.

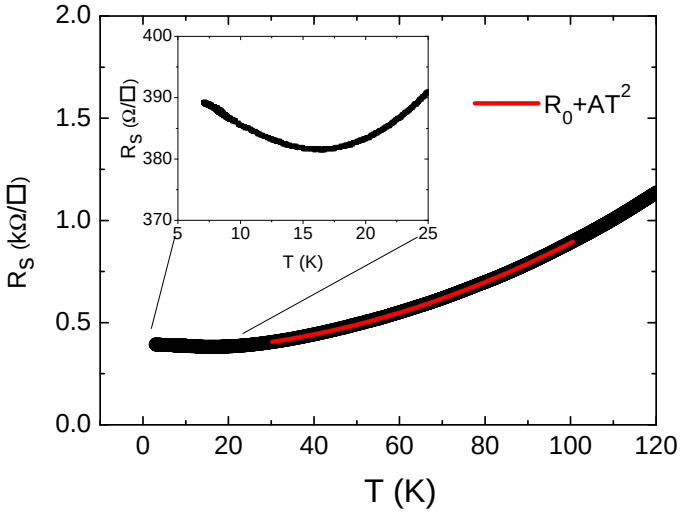

Figure 3.1 – Sheet resistance measured from 300K to 3K on sample C0. The current applied is 1μA at a frequency f=17.37Hz. The fit of equation (3.1) is indicated in red. (inset) Upturn of the R(T) curve below 20K, corresponding to weak localization effect.

3.1.1.1 R(T) curve as grown

The samples were anchored to the mixing chamber of the dilution refrigerator. We first measured the resistance in a four-probes geometry from 300 K to 3 K, using lock-in amplifiers. For the undoped sample (C0), the resistance is of the order of 5 kΩ at room temperature, and decreases by a factor roughly ten at 3 K (fig. 3.1). Above 100 K, electron-phonon scattering dominates transport properties, while a typical Fermi liquid behaviour is observed at lower temperatures. Indeed, R(T) varies according to the square of temperature :

$$R(T) = R_0 + AT^2 \tag{3.1}$$

Assuming a thickness of 10nm for the 2DEG we find $A = 5.3 \times 10^{-8}$ Ω.cm/K^2, which is comparable to the value found in bulk doped STO for similar doping. For instance, this can be compared with the value observed in STO doped with Lanthanum where $A = 2.6 \times 10^{-8}$ Ω.cm/K^2 [96]. This is in agreement with the idea that electrons are located in the STO side of the interface. Van Der Marel et al. have proposed that this T^2 behaviour can be explained by a nearly non-retarded polaron-polaron interaction [25]. Below 20K the resistivity exhibits an upturn ($\partial R/\partial T < 0$, inset of figure 3.1). This behaviour is expected as it reflects the weak localization theory for two-dimensional disordered metals. We will come back to this point later.

3.1.1.2 Doping with a Back Gate

After cooling the sample to 3K, the back-gate voltage was first swept to its maximum value (+200V) while keeping the 2DEG at the electrical ground, to ensure that no hysteresis would take place upon further gating. During this operation, electrons are added in the quantum well, increasing the Fermi energy to its maximum value (i.e., close to the top of the well) [84].

When the gate voltage is decreased, electrons are removed from the confinement well and the sheet resistance of the three samples increases (Fig 3.2 (a)). The main effect of Cr doping is to increase the resistance. In a Drude model, the conductivity σ is proportional to the elastic scattering time τ_e and to the density of carriers n.

$$\sigma = ne^2\tau_e/m^* \tag{3.2}$$

Cr doping has either created more elastic scattering (leading to a decrease of the elastic scattering time τ_e), or modified the density of electrons in the system.

To determine the carrier density, we performed Hall effect measurements for different back gate voltages. In the depleted regime ($V_{BG} < 0$) the Hall resistance increases linearly with the magnetic field (inset fig. 3.2 (b) for sample C0). On the contrary, a non-linear dependence is observed in the doped region : this is a sign of a multiband system. J. Biscaras et al. identifed two populations of carriers at the interface : a majority of low-mobily ones (LMC) that are always present in the quantum wells and a minority of high-mobility ones (HMC) which only appear for strong electrostatic doping [1] ($V_{BG} > 0$) [97]. In the limit of weak magnetic field ($B \to 0$), the extracted carrier density $n_H = IB/eV_H$ (I is the bias current) gives the correct carrier density for $V_{BG} < 0$ (single band) but decreases in the overdoped region (two bands) which is unphysical. In order to obtain the correct carrier density directly from Hall effect for $V_{BG} > 0$, one must performed a two-band analysis as described in appendix A and ref. [97]. However, such analysis is difficult here as the non-linearity of Hall effect is weak due to relatively low magnetic field (7 T). Alternatively, the total carrier density can be determined by combining gate capacitance and Hall effect measurements (fig. 3.2 (b)). We obtain

$$n_{tot}(V_{BG}) = n(V_{BG} = -200V) + \frac{1}{eS}\int_{-200V}^{V_{BG}} dV(C_{BGmeas}(V)) \tag{3.3}$$

where S is the surface of the plane capacitance formed between the 2DEG and the back gate and C_{BGmeas} is the measured capacitance. To recover the absolute variation of the carrier density with gate voltage, we match the value of n_{tot} at $V_{BG} = -200V$ to the one measured by Hall effect since in the underdoped region, only one type of carrier is present (fig. 3.2(b)). One can see that Cr doping does not change significantly the total number of electrons in the 2DEG for the whole range of doping. The main effect of Cr doping is thus to reduce the elastic scattering time τ_e. One therefore expects the ratio $R(x)/R(x = 0) = \tau_e(x = 0)/\tau_e(x)$ to be constant as a function of gate voltage and to increase with Cr doping. This behaviour is indeed observed experimentally as can be seen in figure 3.2 (c).

A first simple conclusion is that Cr doping increases the atomic disorder in the system, and, at first order, only modifies the elastic scattering time τ_e. The carrier density is the same for the three samples within experimental marging errors. This remarkable property will allow us to study for the first time the effect of a controlled homogeneous disorder on LAO/STO properties.

1. In chapter 5, we will propose to relate the LMC and HMC to the populations of the different t_{2g} bands.

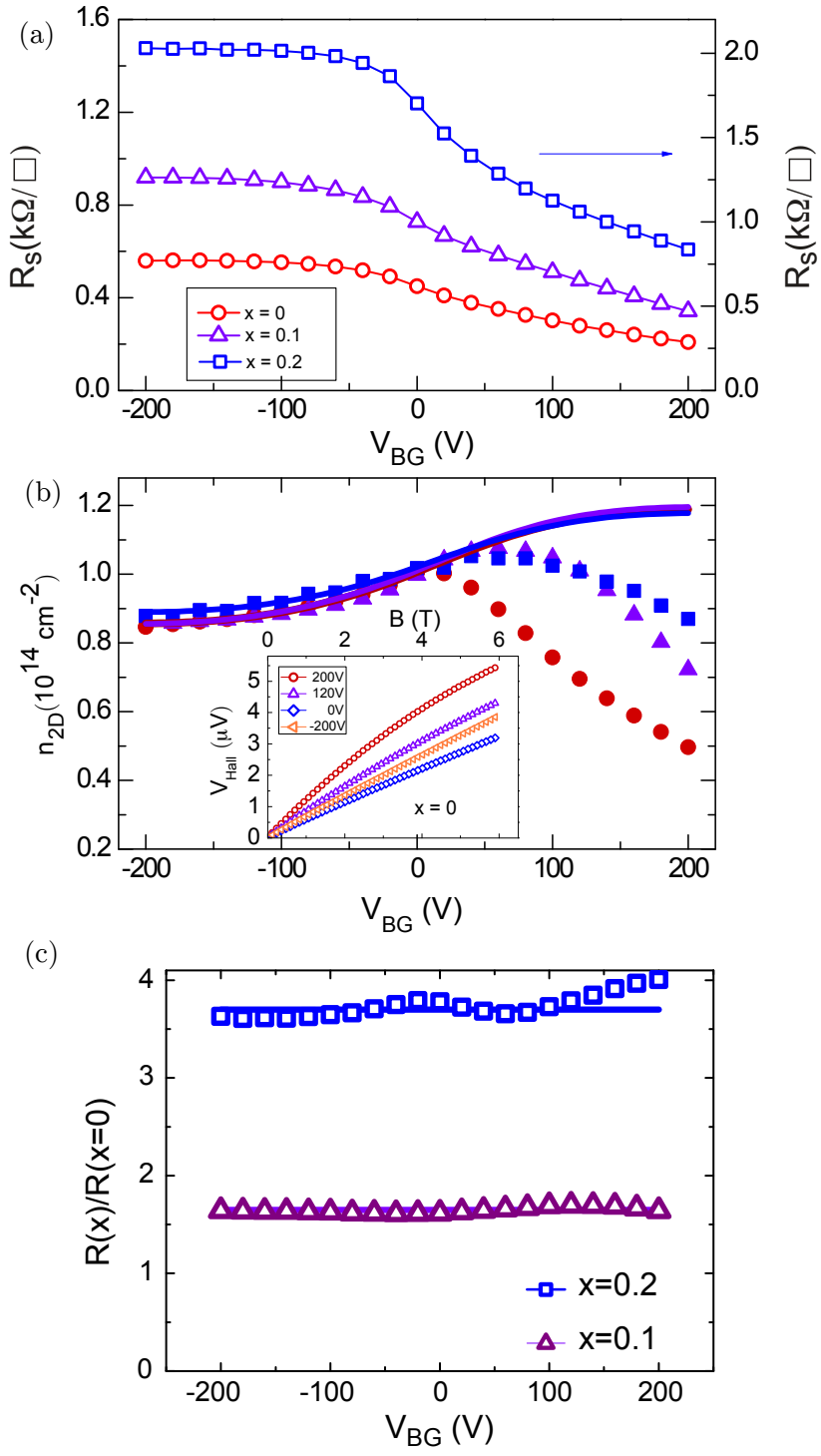

Figure 3.2 – (a) Sheet resistance R_s at T=3K as a function of V_{BG} for three $LaAl_{1-x}Cr_xO_3/SrTiO_3$ samples corresponding to doping levels x=0, x=0.1 and x=0.2 (b) Carrier density extracted at T=3K by matching capacitance measurements (full lines) with low-magnetic field Hall effect measurements for $V_{BG} < 0$(filled symbols, same color code). Inset : Hall voltages V_H as a function of the magnetic field B measured for different V_{BG} in sample C0. The Hall voltage is linear with B for negative gate voltages (single band) and non-linear for positive gate voltages (two bands). (c) Sheet resistance of the x=0.1 and x=0.2 samples normalized by the sheet resistance of the x=0 sample. The straight lines are guides for the eye.

3.1.2 Effect of Cr doping on superconductivity

3.1.2.1 Gate voltage dependence of T_c

The undoped sample C0 presents a complete superconducting transition whose T_c follows a dome shape as a function of gate voltage with a maximum value around 170 mK (Fig. 3.3 (a) and (d)). The same measurement was performed on C1 (x=0.1) and C2 (x=0.2). A superconducting transition can be seen on figure 3.3 (b) for the C1 sample for positive V_{BG} although the R(T) curve saturates to a finite value of resistance at 20 mK. At the highest disorder level (C3 sample), superconductivity is completely suppressed (Fig. 3.3 (c)). One can plot a phase diagram by extracting the critical temperatures (50% of the resistance at T=350mK criterion) as a function of gate voltage for all the samples (Fig 3.3 (d)). The intermediate doping sample (x=0.1) follows the same dome like trend as the undoped one.

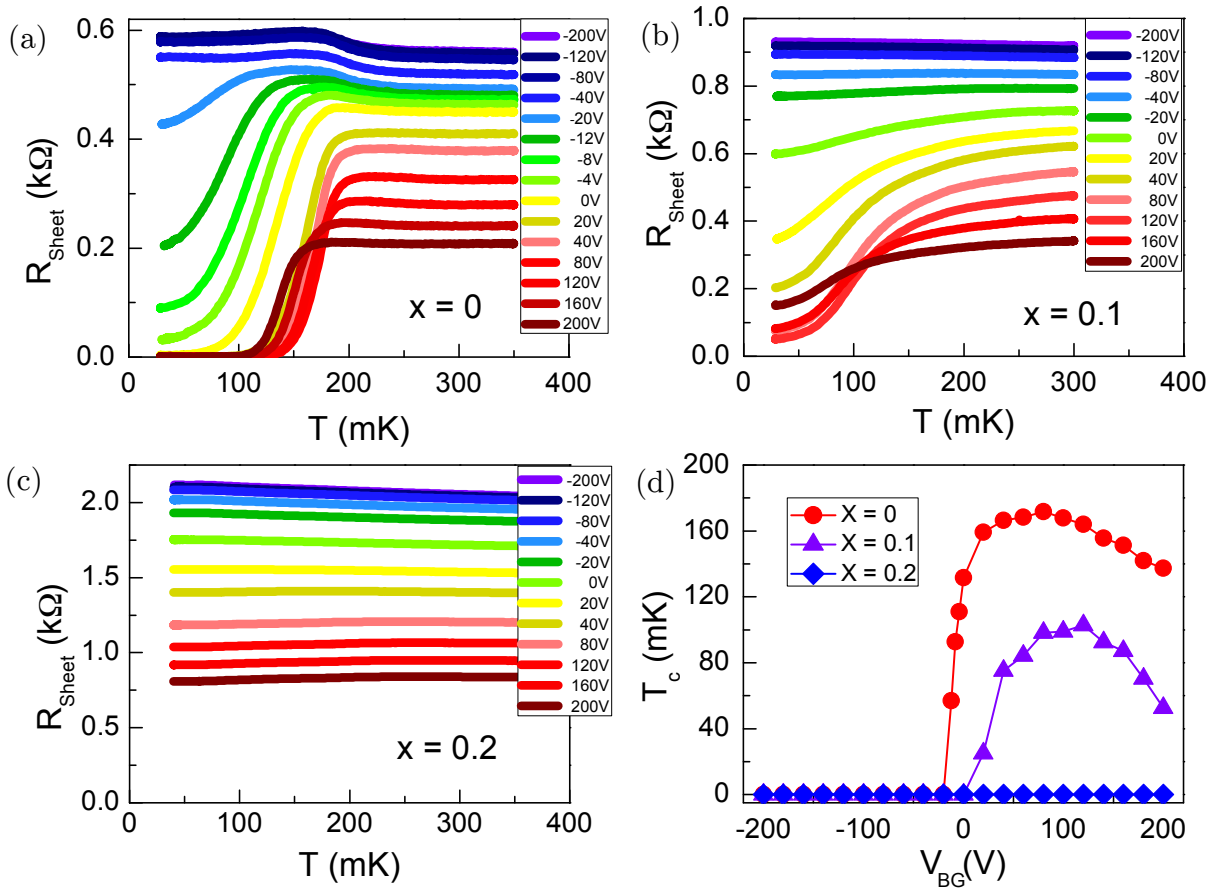

Figure 3.3 – (a),(b) and (c) R(T) curves for different back gate voltage in sample C0, C1 and C2 respectively (d) Critical temperature (50% of the normal resistance at T=350mK) as a function of back gate voltage for the three samples

3.1.2.2 Optimally doped superconducting transition

We now focus on the optimally doped region. Figure 3.4 shows the sheet resistance as a function of temperature at optimal doping ($V_{BG} = 80V$). The 2DEG undergoes a supercon-

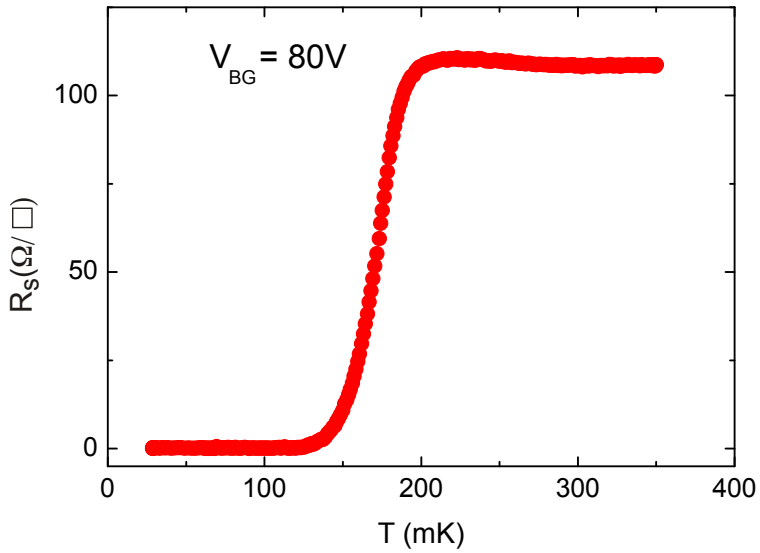

Figure 3.4 – R(T) curve of C0 at optimal doping $V_{BG} = 80$ V. The measurement was done with a Lock-in amplifier at frequency f=17.31Hz and current $I = 20$ nA

ducting transition with a critical temperature of around 150 mK.

The transition is rather broad, indicating the presence of spatial inhomogeneities. In order to explain the relatively broad transition in the optimally doped region, M. Grilli et al. proposed an inhomogeneous repartition of critical temperature with a Gaussian probability distribution (see chapter 1 paragraph 1.3.3)[76]. The larger is the width of the transition, the higher are the fluctuations of T_c around a mean value $\bar{T_c}$. Such systems would behave as a disordered array of superconducting puddles coupled through a metallic 2-DEG by proximity effect [98, 76, 79, 73]. In the underdoped region, the number of superconducting puddles is not sufficient to enable even one percolating path. Tunneling spectroscopy [69] reveal that in the optimally doped region, the zero temperature gap energy is in agreement with BCS predictions ($\Delta \simeq 1.76 k_B T_c$). This indicates that at optimal doping : (i) the puddles are well connected despite a broad transition, and (ii) the T_c is controlled by pairing interaction and not phase fluctuations.

3.1.2.3 Role of homogeneous disorder on superconductivity

Increasing homogeneous disorder by Cr doping leads to a decrease of the elastic time τ_e, which has two distinguishable effects. Firstly, it explains why the superconducting transitions are broader in the C1 sample than in C0. The coupling of superconducting islands is controlled by the normal coherence length $\xi_n = \sqrt{\frac{\hbar D}{k_B T}}$ where the electronic diffusion constant D is proportional to τ_e. If ξ_n becomes shorter, the number of connected superconducting paths for a given temperature is reduced, and the resistance higher. This is why the transition appears broader. The second effect concerns the strengh of superconductivity inside each puddle. Superconductivity is made possible by an attractive electron-electron interaction. As disorder increases, screening is less and less efficient, and the Coulomb interaction starts to compete with the attractive interaction. Moreover in dirty systems, the density of states at the Fermi level

is reduced. Following the work of Anderson, Maekawa and Fukuyama [99] proposed to include electron-electron interaction in the BCS calculation. In this case, the loss of superconducting properties is caused by a progressive and homogeneous destruction of Cooper pairs. For even higher disorder levels, Finkelstein's theory predicted [89] a universal law where T_c depends on the sheet resistance R and on the parameter $\gamma = \ln\frac{1}{T_{c0}\tau_e}$

$$T_c = T_{c_0}\exp\left[\gamma + \frac{1}{\sqrt{2r}}\ln\left[(1/\gamma + r/4 - \sqrt{r/2})/(1/\gamma + r/4 + \sqrt{r/2})\right]\right] \tag{3.4}$$

where $r = Re^2/(\pi h)$ and T_{c_0} is the value of T_c in absence of disorder. Such high disorder can be found in granular systems as well as homogeneous systems. The effect of atomic disorder is to homogeneously reduce the gap energy to zero. The system is no longer made of Cooper pairs : it is simply a dirty metal. In our case, the decrease in elastic time leads to the weakening of superconductivity inside each island.

Fig. 3.5 shows the fitting of T_c at optimal doping ($V_{BG} = 80$V) as a function of R_s with the Finkelstein's function (equation (3.4)). A quantitative agreement is obtained, with a limit T_{c_0} of 350 mK for null disorder, close to the T_c of doped bulk STO. The fitting parameter $\gamma = 10.5$ is consistent with its theoretical expression. This shows that the enhanced disorder through Cr doping can explain the suppression of superconductivity in doped samples. This is valid both for as grown disorder (x=0) and built-in disorder (x=0.1 and x=0.2) and could explain the spread in T_c observed in the literature for sample grown in various institutions. Note that we considered here only the T_c at optimal doping since in the underdoped region, phase fluctuations which are not described by Finkelstein theory, play an important role in the suppression of T_c.

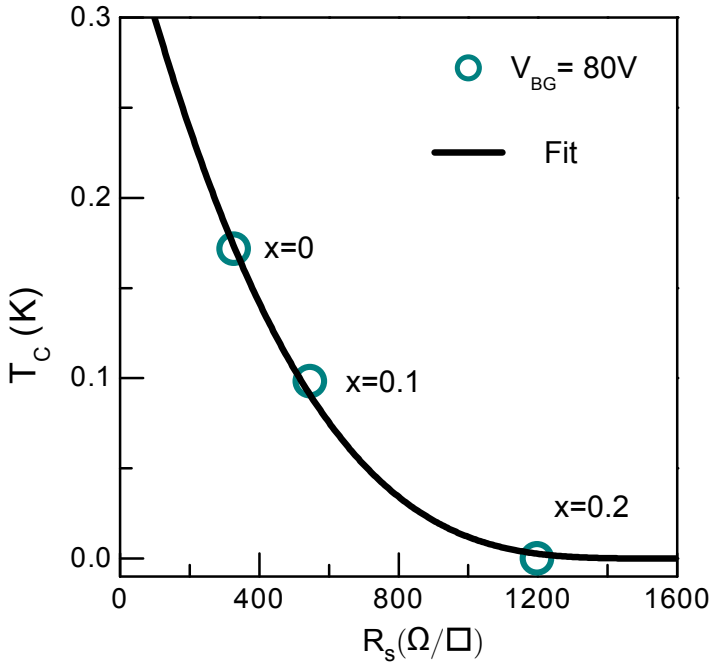

Figure 3.5 – Finkelstein fit (equation (3.4)) for the critical temperature at optimal doping.

3.1.3 Effect of disorder on spin-orbit coupling and inelastic scattering length

When electrons are confined in two dimensions, their quantum wavelike behaviour is unveiled. In the 80s, the diagrammatic technique was applied to the calculation of macroscopic observables in condensed matter systems : this is the so-called weak localization theory [100]. Maekawa and Fukayama calculated the probability for an electron to cross a 2D region with randomly distributed defects as a function of the magnetic field in presence of spin-orbit coupling [101]. After summarizing the different phenomena which characterize the transport in 2D interfaces, we study them through magneto-conductance measurements.

3.1.3.1 Weak localization

In order to compute the amplitude probability for an electron to be transmitted or reflected on randomly distributed scatterers, the quantum mechanics description adds all the amplitudes A_i of each of the paths between point M and point N. The probability for the particle to go from M to N is then :

$$\mathcal{P}_{M\to N} = \left|\sum_i A_i\right|^2 \tag{3.5}$$

In a quasi two-dimensional electron gas, the thickness d is usually smaller than the in-plane mean free path. This is the case for the LAO/STO interfaces where $d \simeq 10$ nm and $l_e \simeq 20$ nm. Elastic processes create loops as shown on figure 3.6. The probability for an electron to return to point M by following either one direction on the loop (A_1) or the other (A_2) is then $\mathcal{P}_{M\to M} = |A_1 + A_2|^2 = 4A^2$, which is twice the classical probability. Those closed paths interfere constructively and increase the probability of back scattering, thus decreasing the longitudinal conductance of the sample. This phenomenon is called weak localization [102]. It is illustrated on figure 3.6.

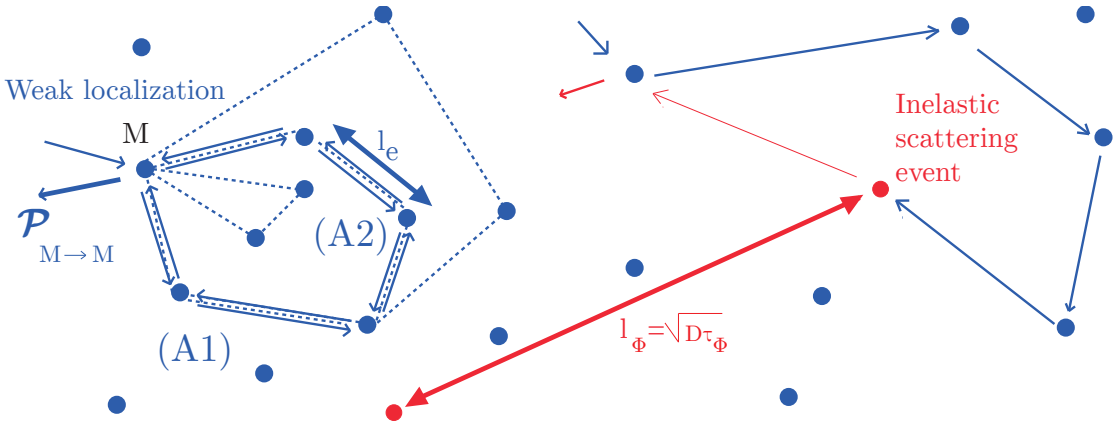

Figure 3.6 – Weak localization schematic. Closed path due to elastic scattering are presented (in blue) on the left; Scatterers are separated by a typical distance l_e. On the right, an inelastic event occurs (in red).

On the contrary, inelastic scattering events destroy the interference. Indeed an inelastic scattering event does not preserve the phase of the particle wave function. When summing the amplitude probabilities they average to zero and quantum interferences are destroyed. All the loops with a diameter larger than $l_\phi = \sqrt{D\tau_\phi}$ do not participate in weak localization. In the inelastic length l_ϕ, τ_ϕ is the typical time between two inelastic collisions ($\tau_\phi >> \tau_e$). Up to now, we have considered spin-less particles. However, spin-orbit interaction, which generates spin relaxation, should also be included in our analysis.

3.1.3.2 Spin-orbit coupling time

When electrons scatter close to a high electric field $\mathbf{E}$, they experience an effective magnetic field $\mathbf{B}_{soc} = \mathbf{E} \times \mathbf{v}/c^2$, where $\mathbf{v}$ is the velocity of electrons. Spin-orbit interaction defines a typical time called the spin diffusion time. Physically it represents the time it takes for a spin to flip while the electron is experiencing the effective spin orbit magnetic field $\mathbf{B}_{soc}$.

There are mainly two kinds of spin-orbit interaction encountered in metallic or semiconducting systems. The first one is called atomic spin-orbit coupling. This interaction is due to the presence of a strong electric field close to the nucleus as represented schematically in figure 3.7 (a). Each time electrons approach a nucleus they have a finite probability of undergoing a spin flip. Atomic spin-orbit (ASO) leads to an Elliot-Yafet type of mechanism [102]. The more scattering occurs, the shorter is the time needed to flip the spin. Hence, the characteristic spin relaxation time is proportional to the elastic scattering time $\tau_{so} \propto \tau_e$.

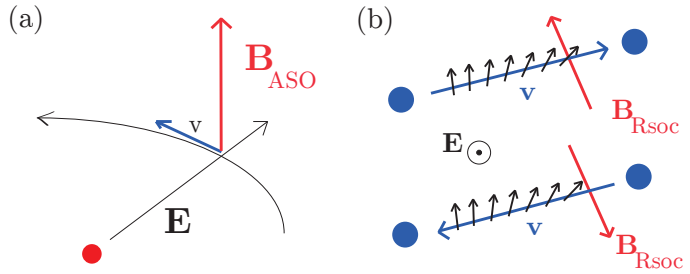

Figure 3.7 – (a) ASO mechanism. (b) RSOC mechanism. Between two scattering events represented by blue points, the spin of the electron tends to align in the direction of B_{so}

The second kind of spin-orbit coupling we consider here is called Rashba spin-orbit coupling (RSOC) which is relevant in the case of LAO/STO as already discuss in chapter 1. It leads to a D'Yakonov-Perel spin relaxation mechanism and occurs when inversion symmetry is broken [102]. The electrons experience an electric field during their ballistic trajectory between two scattering events. The longer is the time between to elastic collisions, the higher is the probability to flip the spin with RSOC. The characteristic spin relaxation time in this case is expected to be inversely proportional to τ_e. We can therefore write

$$\tau_{so} \propto 1/\tau_e \tag{3.6}$$

As shown in figure 3.7 (b) Rashba spin-orbit interaction does not destroy time reversal

symmetry since the direction of $\mathbf{B}_{RSOC}$ changes with the sign of $\mathbf{v}$. However, the constructive interference between loops (A1) and (A2) (shown on figure 3.6) are partially suppressed by spin-orbit interaction. This effect is called weak antilocalization.

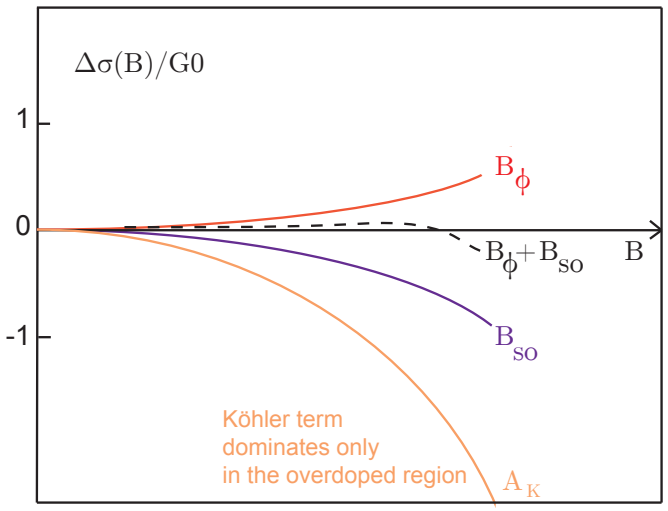

Figure 3.8 – Magneto-conductance in a 2D metallic system in the weak localization framework : Each curve represents the contribution of a specific scattering event.

3.1.3.3 Magneto-conductance : Maekawa-Fukuyama Formalism

The Maekawa-Fukuyama (MF) formula describes the evolution of the conductance of a 2D system as a function of the magnetic field in the presence of weak localization and including a spin-orbit term. It is valid only for negligible Zeeman splitting [101, 103]

$$\frac{\Delta\sigma(B)}{\tilde{G}_0} = -\Psi\left(\frac{1}{2}+\frac{B_{tr}}{B}\right)+\frac{3}{2}\Psi\left(\frac{1}{2}+\frac{B_\phi+B_{so}}{B}\right)-\frac{1}{2}\Psi\left(\frac{1}{2}+\frac{B_\phi}{B}\right) - \left[\ln\left(\frac{B_\phi+B_{so}}{B_{tr}}\right)+\frac{1}{2}\ln\left(\frac{B_\phi+B_{so}}{B_\phi}\right)\right]-A_K\frac{\sigma_0}{\tilde{G}_0}B^2 \quad (3.7)$$

Here Ψ is the digamma function, $\tilde{G}_0 = e^2/\pi h$ the quantum of conductance and B_{tr}, B_ϕ and B_{so} are the elastic, inelastic and spin-orbit effective magnetic fields respectively. They are related to the elastic scattering time τ_e, the inelastic scattering time τ_ϕ and the spin-orbit relaxation time τ_{so} by the expression $B_{tr} = \hbar/2el_e^2$, $B_\phi = \phi_0/2\pi D\tau_\phi$ and $B_{so} = \phi_0/2\pi D\tau_{so}$ where $D = v_F l_e/2$ is the electronic diffusion constant in two dimension (v_F is the Fermi velocity). The term $A_K B^2$ is the regular orbital magneto-resistance in a metal (Köhler law's [104]).

On figure 3.8 is represented the effect of spin-orbit coupling on the variation of the magneto-conductance. Applying a magnetic field perpendicular to the 2DEG induces a dephasing between the two opposite trajectories of a given loop $\delta\phi = 2\pi BS/\phi_0$, where $\phi_0 = h/2e$ is the flux quantum. The probability of backscattering becomes

$$\mathcal{P}_{M\to M} = 2A^2\left[1+\cos\left(\frac{2\pi BS}{\phi_0}\right)\right] \quad (3.8)$$

As already mentioned, $l_\phi = \sqrt{D\tau_\phi}$ is the maximum diameter over which constructive interference leading to enhanced backscattering takes place, and $D\tau_\phi$ the corresponding surface. The dephasing effect of the magnetic field is effective when it occurs on a surface S smaller than $D\tau_\phi$. We call $B_\phi = \phi_0/2\pi D\tau_\phi$ the corresponding magnetic field. When the magnetic field reach $B_{tr} = \hbar/2el_e^2$ the electrons are dephased on the smallest loop possible and no weak localization can occur anymore. The presence of spin-orbit interaction tends to suppress constructive interference which favours back scattering. Therefore, when spin-orbit coupling dominates the electronic transport, the conductance at zero magnetic field is increased due to weak antilocalization effect. When a magnetic field is applied, weak antilocalization effects disappear. Hence, a sign inversion in $\Delta\sigma(B)$ is a signature of spin-orbit coupling.

The last term of equation 3.7 proportional to B^2 at low field accounts for the classical orbital magneto-conductance where A_K is the Köhler coefficient. This classical effect scales like the square of the mobility for small magnetic field [104]. It starts to dominate the transport in the highly doped region where mobility is high and makes difficult the correct determination of τ_{so}. When the Köler term A_k is relatively low, one can extract reliably the characteristic scattering times τ_{so} and τ_ϕ.

3.1.3.4 Magneto-conductance : Measurements

We performed magneto-conductance measurements up to 6T at T=3K. Fits of $\Delta\sigma$ with the Maekawa-Fukuyama equation 3.7 are presented in figure 3.9 for samples C0, C1 and C2 for different back gate voltages. A very good agreement is obtained between the experimental data and the theory over the whole electrostatic gating range. For large negative V_{BG}, a positive magneto-conductance is observed in agreement with weak localization in the presence of a weak SOC. When V_{BG} is increased, the magneto-conductance becomes negative because of enhanced SOC. For $V_{BG} = 200$ V, the classical magneto-conductance dominates the transport. As far as the longitudinal conductance is close to $\tilde{G}_0$, weak localization and antilocalization theory are at play. The elastic scattering time is too small in our case to contribute. Therefore we fit only B_ϕ, B_{so} and A_K parameters.

Inelastic scattering Figure 3.9 (b) shows the inelastic magnetic field obtained from MF fits. Inelastic scattering processes are extracted via the parameter defined in the previous section

$$B_\phi = \frac{\hbar}{4eD\tau_\phi} = \frac{\hbar}{2ev_F^2\tau_e\tau_\phi} \tag{3.9}$$

Hence B_ϕ is inversely proportional to $\tau_e \times \tau_\phi$ as stated in equation 3.9. Assuming that τ_ϕ is not affected by Cr doping, the ratio $B_\phi(x)/B_\phi(x=0)$ should only depend on the ratio of elastic scattering times $\tau_e(x=0)/\tau_e(x) = R(x)/R(x=0)$. For x=0.1 and x=0.2 this is qualitatively verified experimentally (Figure 3.10), which confirms that the main effect of Cr doping is to reduce the elastic scattering time τ_e. It shows the consistency between zero magnetic field resistivity measurement and the MF analysis of magneto-conductance.

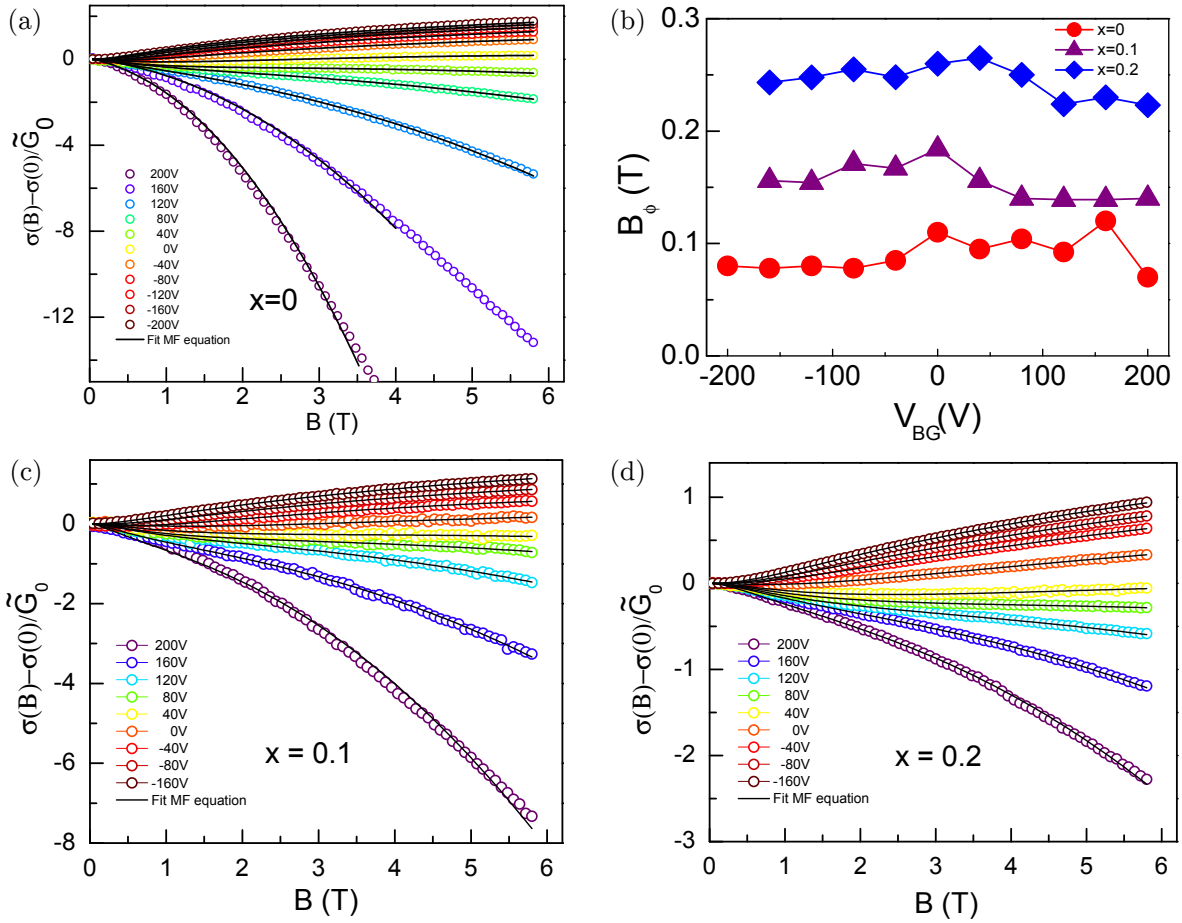

Figure 3.9 – (a,c,d) Normalized magneto-conductance as a function of out-of-plane magnetic field B at T=3K in Cr doped samples C0, C1 and C2 for different back gate voltage V_{BG} (b) Inelastic magnetic field B_ϕ as a function of back gate voltage for the three samples.

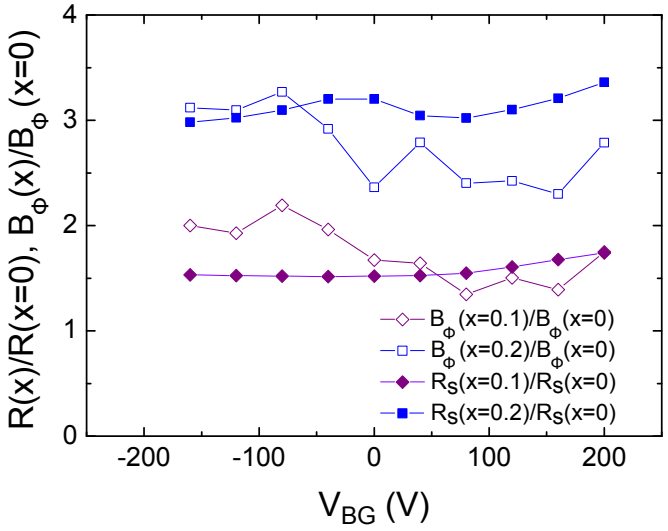

Figure 3.10 – Ratio $B_\phi(x)/B_\phi(x=0)$ and $R_s(x)/R_s(x=0)$ as a function of gate voltage at T=3K

Spin-orbit coupling Figure 3.11 (a) and (b) shows the spin-orbit magnetic field B_{so} and the Köler term A_K obtained from the MF fit. In the depleted region the conductance increases with the magnetic field, which is consistent with a low spin-orbit interaction. In this case the transport is dominated by weak localization. When the back voltage is increased, a sign inversion of $\Delta\sigma(B)/\tilde{G}_0$ indicates the presence of spin-orbit interaction. Above $V_{BG} = 150V$, the 2DEG acquires a high-mobility (due to HMC) that reinforces the classical contribution $\sigma \propto -\mu^2 B^2$ as represented by the Köler coefficient on figure 3.11(b). The shadow region corresponds to a region of gate voltage where the determination of B_ϕ and B_{so} becomes less and less accurate. According to the D'yakonov-Perel mechanism, the spin relaxation time τ_{so} is expected to be inversely proportional to the elastic scattering time τ_e. The product $D \times \tau_{SO}$ is therefore independent of τ_e, and we expect the spin-orbit field not to be affected by a reduction of τ_e due to Cr doping. This is indeed what is extracted from the fitting as shown on figure 3.11(a) where B_{so} is the same for the three samples over the whole phase diagram.

The elastic scattering time τ_e can be calculated in the Drude model with a single band approximation assuming $m^* \simeq 0.7 \times m_e$. Figure 3.12 (left) shows the spin-orbit relaxation time τ_{so} extracted from B_{so}, as a function of τ_e^{-1}. A clear linear dependence is observed for all the gate voltages validating the DP spin-relaxation mechanism. We have demonstrated that Cr doping was only decreasing the elastic scattering time without changing other intrinsic parameters. On the contrary, back gating modifies the carrier density, the confinement potential and the band occupancy. This behaviour of spin-orbit coupling relaxation time is a strong indication that a Rashba mechanism is at play in the LAO/STO interface.

Gate dependence of the spin-orbit coupling In the following, we propose to explain the increase of the spin-orbit strength with the gate voltage. The Hamiltonian representing the Rashba spin-orbit coupling in LAO/STO interface has been introduced in chapter 1 section 1.2.3. It takes the general forms :

$$H_{RSOC} = \alpha(\mathbf{k} \times \boldsymbol{\sigma})_z \tag{3.10}$$

where $\mathbf{k}$ is the electron wave vector, $\boldsymbol{\sigma}$ are the Pauli matrices and α is the coupling constant. This latter characterizes the strength of the spin-orbit interaction and is expected to be directly proportional to the electric field F. Through Maxwell-Gauss equation, F at $z = 0$ can be directly related to the carrier density of the 2DEG

$$F = \frac{e}{\varepsilon_0 \varepsilon_r (F = \infty)}(n + N_{trap}) \tag{3.11}$$

where N_{trap} is the density of trapped charges and ε_r is the dielectric constant at the interface. Considering a 2D system with Rashba spin-orbit coupling in the diffusive limit, ie when $a = \Delta_{SO}\tau/\hbar < 1$ one can express spin-orbit time as [105]

$$\frac{1}{\tau_{so}} = \frac{1}{2\tau}\frac{a^2}{1+a^2} \simeq \frac{2\alpha^2 k_F^2 \tau}{\hbar^2} \tag{3.12}$$

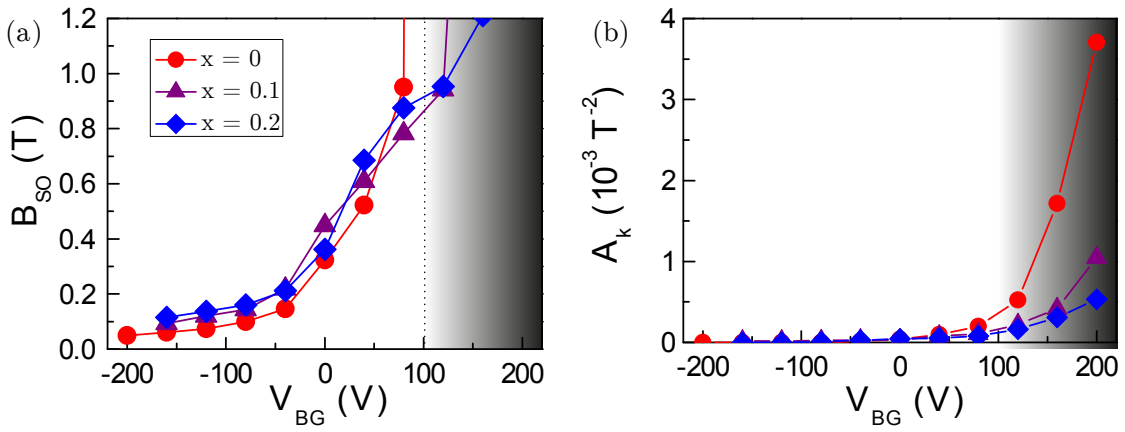

Figure 3.11 – (a,b) B_{SO}, and A_K parameters extracted from Maekawa-Fukuyama fit as a function of gate voltage for the three Cr doping x=0, x=0.1 and x=0.2. The shadow region on the right delimits the part of the phase diagram where Köler term is dominating.

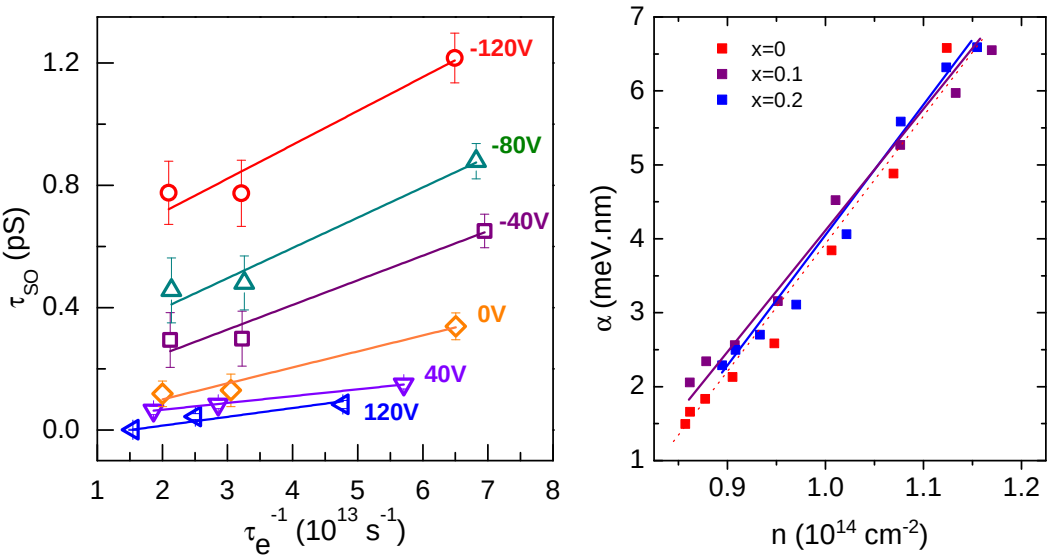

Figure 3.12 – (Left) Linear dependence of τ_{so} as a function of τ_e^{-1} and gate voltage. (Right) Spin-orbit coupling constant α as a function of carrier density.

From this expression we obtain an expression of the spin-orbit coupling constant as a function of B_{SO}

$$\alpha = \sqrt{e\hbar^3 B_{SO}} \tag{3.13}$$

Figure 3.12 (right) shows the gate dependence of α determined from the experimental values of B_{so}. For the three samples, the coupling constant increases linearly with n, and correspondingly with $F(z = 0)$, in agreement with a Rashba spin-orbit interaction.

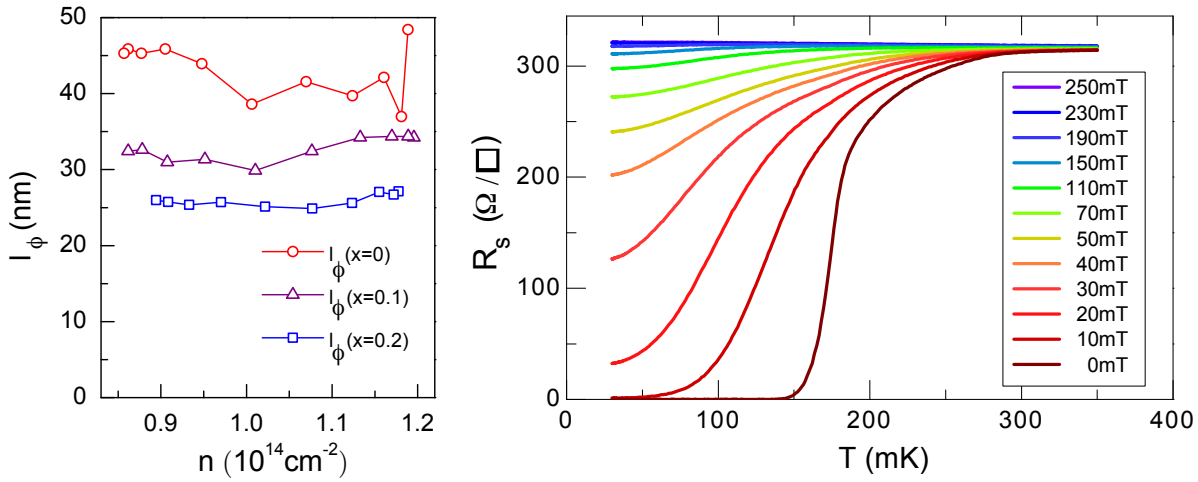

Figure 3.13 – (Left) Dependence of spin diffusion length as a function of the density of carriers for samples C0, C1 and C2. (Right) Resistance as function of temperature under a perpendicular magnetic field in sample C0.

3.1.3.5 Inelastic scattering lengths versus superconducting length

One can finally compute the inelastic lengths l_ϕ within the one band approximation (fig. 3.13 (a)). They only weakly depend on the gate voltage indicating that the variation of $v_F^2 \times \tau_\phi$ compensates approximately the one of τ_e (fig. 3.13 (left)). C0 has an inelastic length $l_\phi \sim 50$ nm. At higher disorder (C2 sample), $l_\phi \sim 25$ nm is approximately twice shorter. This inelastic scattering length represents the length over which the phase is lost. Superconductivity is suppressed if the coherence length ξ (size of a Cooper pair) is larger than the inelastic length [106]. Measuring the out-of-plane critical field, it is possible to estimate the coherence length ξ within the Ginzburg-Landau theory $B_c^\perp = \frac{\phi_0}{2\pi\xi^2}$. Figure 3.13 (right) shows the R(T) curves in the C0 sample as a function of the out-of-plane magnetic field. The critical field is $B_c \simeq 200$ mT corresponding to a Ginzburg-Landau coherence length $\xi \simeq 40$ nm. In sample C2, where superconductivity has completely disappeared, the inelastic coherence length l_ϕ becomes comparable or shorter than ξ. This is another way to explain how superconductivity is suppressed by inelastic disorder.

This first study gave us the typical microscopic lengths over which electrons interact with their environment. Replacing Cr by Al modifies the typical elastic scattering length without changing the total number of carriers, which is consistent with the extracted inelastic scattering length. The systematic study of the magneto-conductance as a function of back gate voltage provided important informations about the spin-orbit coupling. Its evolution with gate voltage and Cr doping evidences a D'Yakonov-Perel mechanism of spin relaxation in the presence of a Rashba-type spin-orbit interaction. ($\tau_{so} \propto \tau_e^{-1}$). Finally, we compared the critical temperature in the optimally doped region to the values obtained with the Finkelstein model and we observe a quantitative agreement.

3.2 Top-Gating Control of Superconductivity and Spin-Orbit Coupling

The back-gating technique on LAO/STO has now become a standard tuning parameter. Unfortunately, the STO substrate is too thick (0.5mm) to address characteristic mesoscopic scales such as the superconducting coherence length ξ, the Fermi wave length λ_F or the spin diffusion length. On the other hand, in the LAO/STO structure, the 2DEG is buried a few nanometers under the insulating crystalline LAO layer; this is a natural geometry for top-gating. However, the realization of top-gating devices has proven to be more challenging than expected in the community. The first reason is that any defect or pinholes in the heterostructure will inevitably lead to leakage currents. The second reason is that the 2DEG is sensitive to any material deposited on it, because of the polar catastrophe. For sake of charge conservation, any electron at the interface must have a positive counterpart on top of LAO. Depositing a material (residues of resist for example) will therefore modify the potential and sometimes annihilate the 2DEG. The first top-gated devices were fabricated in 2011 to measure the effect of negative compressibility of the 2DEG on the gate capacitance [107]. This was followed two years later by the first demonstration of top-gate control of Tc in a superconducting sample, but only for a limited range of gate voltage due to leakage current [108]. Instead of depositing metallic gates, the ionic liquid technique was also adapted to realize top gates [109, 110]. Here we propose a study of the effect of top gating on superconductivity and spin-orbit coupling. In particular, we demonstrate for the first time the continuous control of the superconductor-insulator transition with a top-gate.

3.2.1 Sample's structure

The following study was done on sample A (see chapter 2 section 2.3). The Hall bar was patterned with the amorphous LAO technique and a 8 u.c. crystalline LAO layer was deposited. The top gate shown on schematic 3.14 covers the three squares of the Hall bar and is separated from the 2DEG by a 500nm thick layer of Si_3N_4 in order to avoid leakage as indicated on figure 3.14.

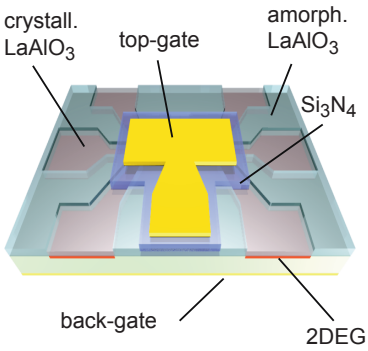

Figure 3.14 – Schematic of sample A with back gate deposited on the back of the STO substrate. A 500nm Si3N4 layer is deposited on top of the LAO layer to avoid gate leakage. V_{BG} and V_{TG} are the voltages applied respectively on the back gate and the top gate respectively.

The results presented in the following section were obtained together with S. Hurand and were published in 2015 [111]. Similar results were obtained on an ion-implanted sample having same growth parameters and identical dimensions [83], but they will not be reported here for the sake of clarity.

3.2.2 Carrier doping with a top-gate

By applying a voltage δV between a metallic gate of surface S and the 2DEG separated by a distance d, charges $\pm\delta q$ appear on the top gate and the grounded 2DEG respectively according to the following relation

$$\delta Q = C\delta V \tag{3.14}$$

where $C = \varepsilon_0\varepsilon_r\frac{S}{d}$ is the capacitance (assuming a plane capacitance geometry) of the dielectric in between the metallic parts. Contrary to back gating through STO whose dielectric constant depends on the applied electric field, carrier doping with a top gate should depend linearly on V_{TG} since both LAO and Si3N4 are regular dielectric materials. A sketch of the electrical configuration that we used to perform these experiments is displayed in Figure 3.15

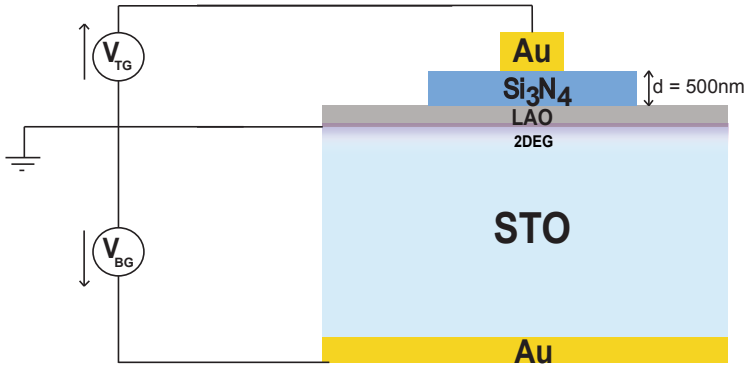

Figure 3.15 – LAO/STO schematic top gate and back gate

The sample is cooled to 3 K where a first polarization to a maximum back gate voltage (+20V) is done in order to avoid any hysteretic behaviour due to electrons escaping from the potential well. A second forming step of the 2DEG with the top gate voltage V_{TG} = 110V at $V_{BG} = 20V$ is performed for the very same reasons [84]. At 3K, we perform Hall measurements as a function of the top gate voltage. At $V_{BG} = 0V$, similarly to what we measured in sample C0, the presence of two types of carriers (LMC and HMC) leads to a non-linear Hall voltage similarly to what we measured in sample C0. The carrier density n_H extracted from Hall measurements $n_H = -IB/eV_h$ suddenly decreases when the top-gate voltage is increased as indicated by the open blue squares on figure 3.16. In order to test the linear relation between the top gate voltage and the carrier density, we drive the system in the depleted region with a back gate where only low mobility carriers (LMC) are present and where Hall effect is linear ($V_{BG} = -15V$). On figure 3.16, the open red circles show the carrier density variation with top-gating in this region. The relation is linear as expected. A similar dependence was reproduced by COMSOL numerical

simulation (fig. 3.16) assuming a dielectric constant of 5 for the Si_3N_4 which is close to the value reported in the literature for a similar layer. We obtain the following linear relationship between top gate voltage and carrier density

$$n(V_{TG}, V_{BG}) = n(V_{TG} = 0, V_{BG}) + \frac{dn}{dV_{TG}} V_{TG} \tag{3.15}$$

where $\frac{dn}{dV_{TG}} = 5.0 \times 10^{10}$ e$^-$/cm^2 and $n(V_{TG} = 0, V_{BG}) = 1.69 \times 10^{13}$ e$^-$/cm^2. In this device, the carrier density can be modulated by a factor two with a top gate without leakage current.

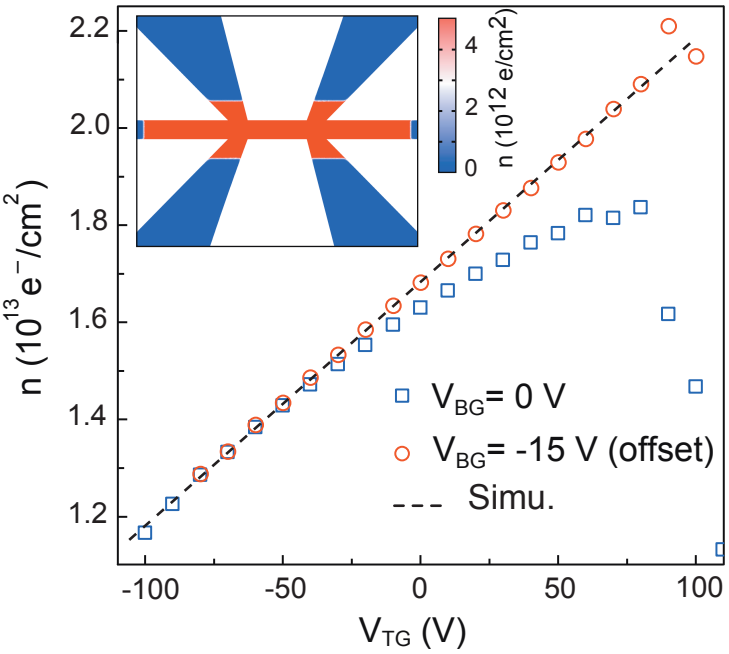

Figure 3.16 – Figure 2. Hall effect and carrier density. Carrier density (n) extracted from the slope of the Hall voltage (V_H) at 4 T as a function of V_{TG} for two different back-gate voltages (V_{BG}). The curve at V_{BG}= 15 V is offset to match the curve at $V_{BG} = 0$ V at negative top-gate voltages. The dashed line was obtained from numerical simulations of the carrier density, assuming a dielectric constant of $\varepsilon_{Si_3N_4} = 5$ for the Si_3N_4 layer. Inset: example of a numerical simulation of the charge carrier distribution in the device for $V_{BG} = 0$ V and V_{TG}= 10 V.

3.2.3 Gate dependence of T_c and phase diagram

Figure 3.17 shows the resistance of the sample measured in dc in a four contacts geometry (see chap 2 section 2.2.2.2). The resistance in the normal state is around $R_s(T = 350mK) = 700\Omega/\square$. When cooling the as grown [2] sample down to 20mK, the resistance increases slowly due to weak localization. Signs of paraconductivity start to appear at around 400 mK due to Aslamasov-Larkin fluctuations. A full superconducting transition takes place at 200mK indicating that the fabrication process has not degraded significantly the 2DEG properties. The current-voltage (I(V)) characteristic shown on the inset in figure 3.17 displays a strong hysteresis. The critical current around $I_c = 460$ nA is indeed much higher than the return current $I_r \simeq 100$ nA. This

2. ie before the first positive polarization is applied.

shape of I(V) was analyzed in detail by S. Hurand et al. [80] and its dynamics was compared to the dynamics of underdamped Josephson junctions [3].

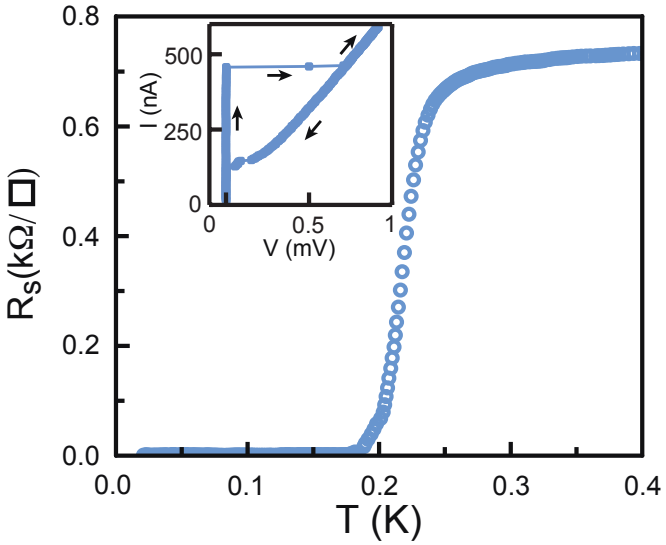

Figure 3.17 – As grown resistance as a function of temperature in sample A (inset) As grown I(V) curve with switching behaviour ($I_c = 460$ nA) and overdamped regime ($I_r \simeq 100$ nA)

Figure 3.18 (a) displays a systematic measurement of resistance as a function of temperature when the carrier density is tuned with a top gate. When carriers are removed from the potential well, the normal resistance increases by two orders of magnitude while T_c is changed significatively. Figure 3.18 (b) represents a phase diagram otained by plotting the normalized resistance R/R(T=350mK) as a function of temperature and top gate voltage. The corresponding carrier density is indicated on the top axis.

When electrons are removed from the potential well, superconductivity is suppressed smoothly showing sharp transitions in the optimally doped region, and much broader ones saturating at a finite resistance in the underdoped one. The broad transitions in the underdoped regime suggest the presence of inhomogeneities as mentioned in chapter 1. A superconductor to insulator transition (SIT) takes place around $V_{TG} = -90V$ with a critical sheet resistance $R_s \simeq 8$ kΩ which is close to the universal conductance value in the bosonic scenario $R_Q = h/4e^2 \simeq 6.5$ kΩ [112]. Surprisingly, once every trace of paraconductivity has disappeared, the resistance does not increase sharply at low temperatures which is unusual for an insulator. Rather than a true superconductor-insulator transition, we have here a transition between a superconductor and a weakly localizing metal. As for back-gating, the critical temperature presents a dome behaviour upon top-gating with a decrease of T_c on the overdoped region. In figure 3.18 (b), three different criteria for T_c are shown. Explaining the dome shape in back-gating or top-gating has remained a challenge from a theoretical point of view.

3. Appendix E give some general properties on Josephson junction in the RCSJ model

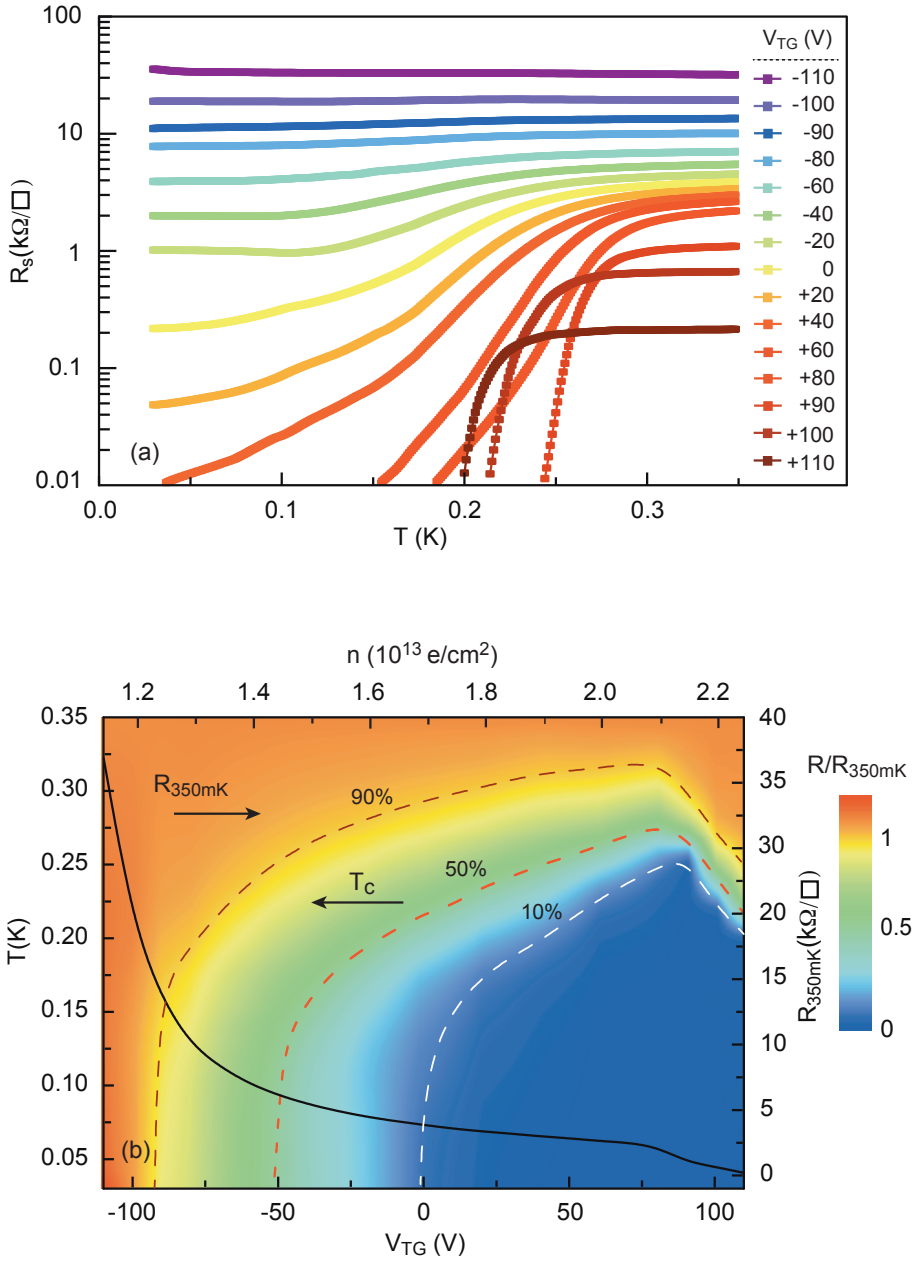

Figure 3.18 – (a) Sheet resistance of sample A as a function of temperature for different top gate voltage. (b) Color plot of the sheet resistance normalized with respect to its value at T=350mK as a function of temperature (left axis) and top gate voltage. The associated carrier densities are plotted on the top axis. The sheet resistance at T=350mK is represented in black on the right axis. Three different criteria for T_c are proposed : 10%, 50% and 90% of the normal resistance at 350mK

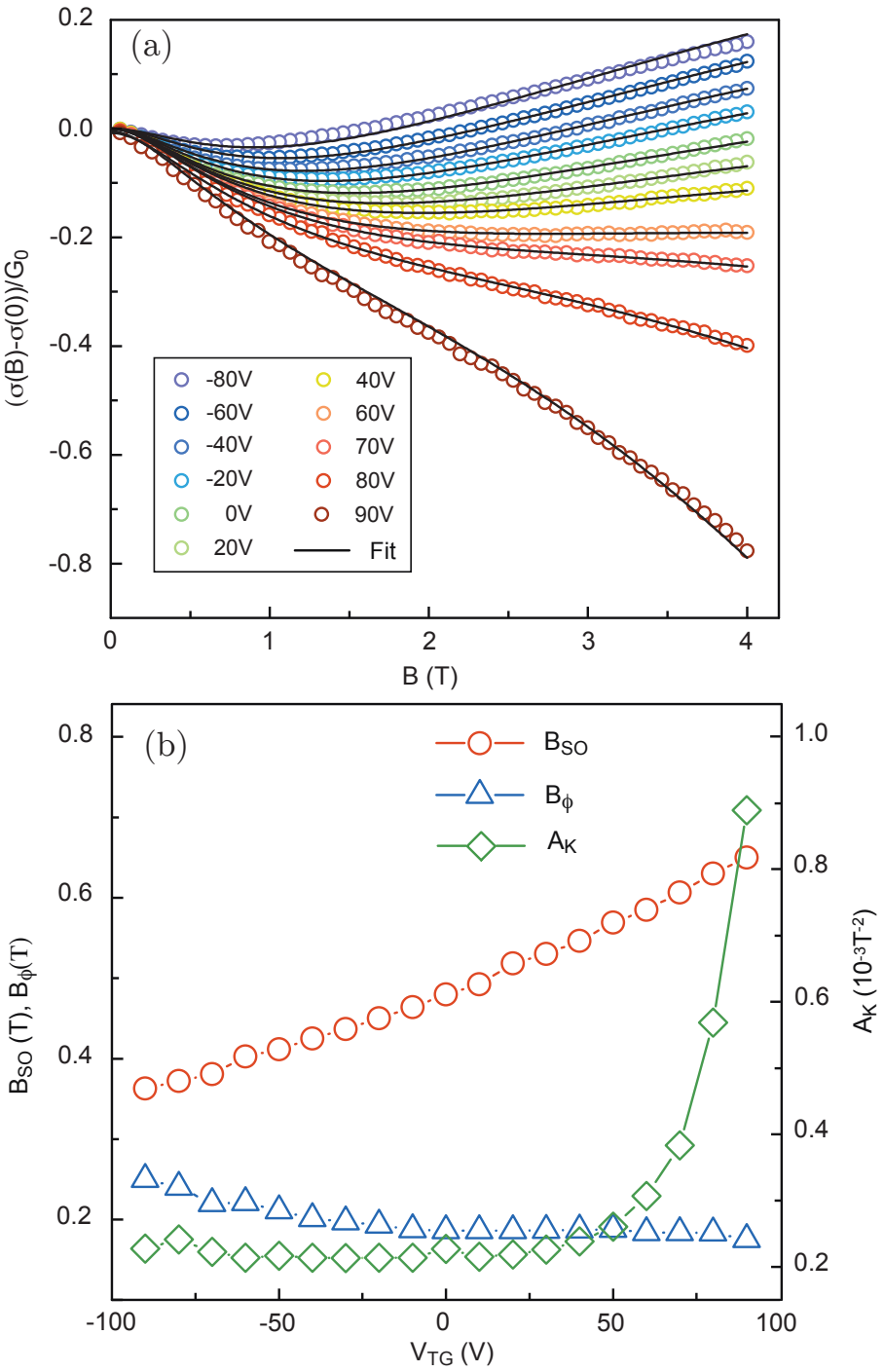

Figure 3.19 – (a) Fitting of the magneto-conductance with Makeawa-Fukuyama formula for different top gate voltages (b) B_ϕ, B_{so} and A_K parameters extracted at T=3K in sample A

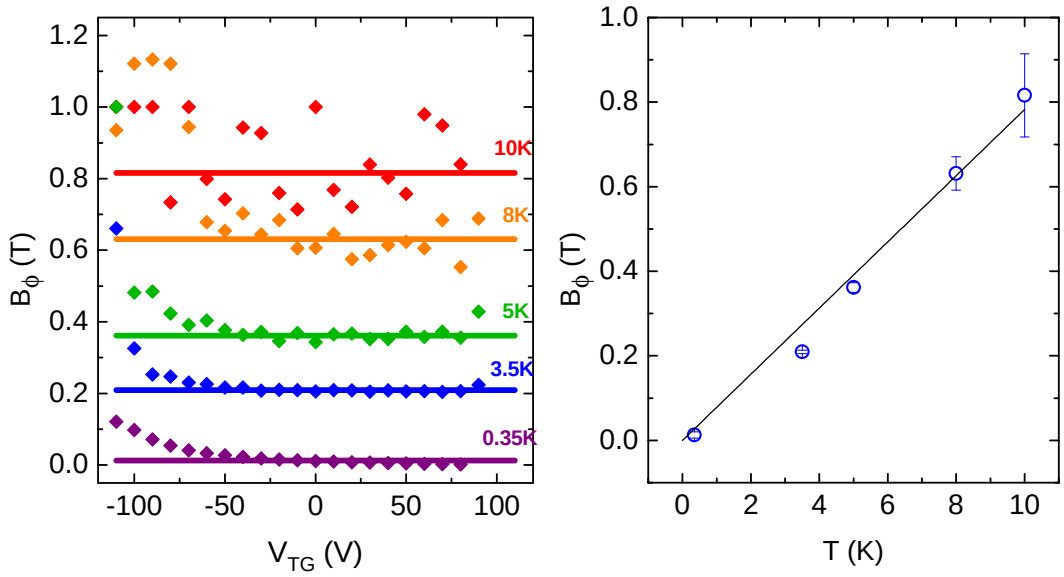

Figure 3.20 – (left) B_ϕ parameter extracted from the longitudinal magneto-conductance as a function of top-gate voltage for different temperatures. (Right) B_ϕ as a function of temperature for $V_{TG} = 50$ V.

3.2.4 Magneto-conductance measurements

We now present magneto-transport measurements and analysis to extract the spin-orbit interaction strength as a function of top-gating. Magneto-resistance measurements were performed as a function of temperature and top gate voltage. The parameters obtained with the fit of Maekawa-Fukuyama formula (equation 3.7) are presented in figure 3.19 (a) in the whole range of top gate voltage. As explained in the previous section, we obtain three parameters B_ϕ and B_{so} and A_K. The Köler term dominates in the overdoped region as in the case of Cr doped samples (fig. 3.19 (b)).

In the framework of the weak localization, the inelastic inelastic scattering time follows a power law as a function of temperature

$$\tau_\phi \propto T^{-p} \tag{3.16}$$

where p depends on the dominant mechanism of inelastic scattering (p=3 for electron-phonon interaction and p=1 for electron-electron interaction [113, 88]). Figure 3.20 shows that B_ϕ is a linear function of temperature. $B_\phi = \phi_0/2\pi D\tau_\phi$ being inversely proportional to τ_ϕ, we immediately find p=1 which demonstrates that electron-electron interaction dominate the inelastic process. This is consistent with the logarithmic temperature dependence of the conductivity in LAO/STO interfaces [97].

The spin-orbit magnetic field obtained from the fits is represented in open red circles on figure 3.19 (b). [4]. It continuously increases with gate voltage and correspondingly with carrier density as already observed with back-gating. As opposed to B_ϕ, B_{SO} is temperature independent since

the confinement conditions are not modified (for $T < 10$ K) (Inset fig.3.21). If we assume that the spin relaxation is dominated by the D'Yakonov-Perel mechanism, based on a Rashba spin-orbit interaction we obtain a linear variation of α with carrier density (Figure 3.21). As already discussed for the Cr doped sample, this linear variation is in agreement with the linear variation of α with the interfacial electric field as expected for Rashba spin-orbit coupling. Assuming a Fermi energy $E_F = 100$ meV, and neglecting the variation of k_F on this small range of doping, we can also calculate the spin splitting energy $\Delta_{so} = 2\alpha k_F \simeq 10$ meV. The order of magnitude is a few meV, which is much larger than in most semiconductors.

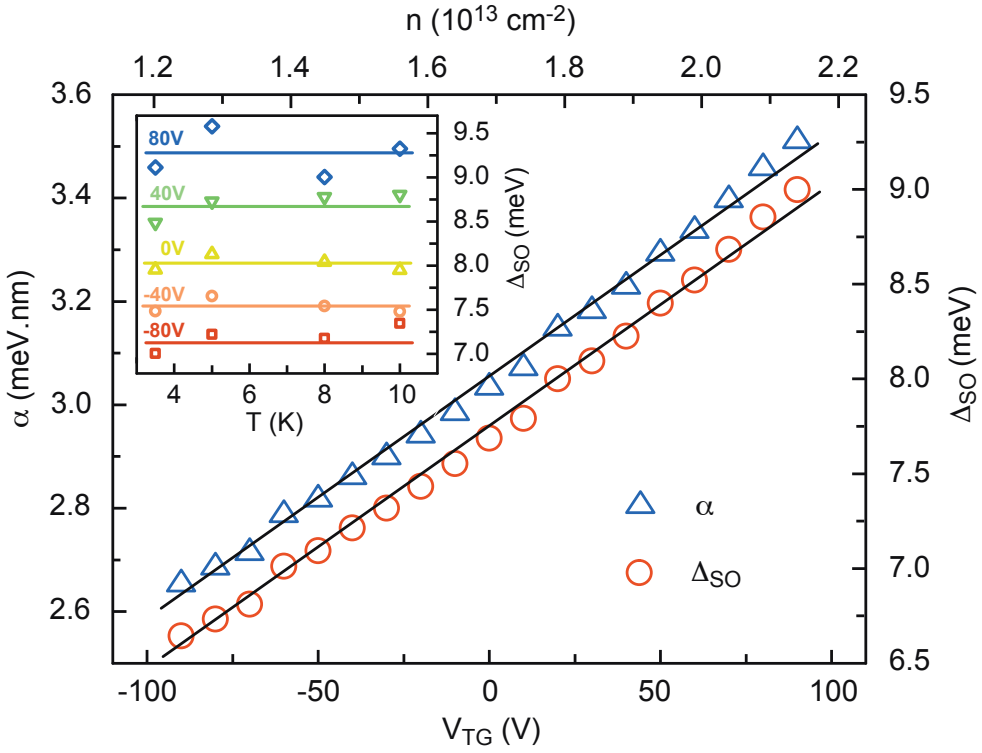

Figure 3.21 – Spin-orbit coupling constant (left axis) and spin splitting energy (right axis) as a function of the top gate voltage obtained from spin-orbit magnetic field. The spin splitting energy is calculated by assuming a Fermi energy $E_F = 100$ meV with the expression $\Delta_{SO} = 2\alpha k_F$. The corresponding total carrier density is plotted on the top axis. (inset) Δ_{so} as a function of temperature

3.2.5 Conclusion

In the first section of this chapter we have investigated the effect of the substitution of Al by Cr on superconductivity and spin-orbit coupling in $LaAl_{1-x}Cr_x$ O_3 /$SrTiO_3$ interfaces. The main effect of Cr doping is to induce disorder in the interfacial quantum well which leads to a decrease of the electronic elastic scattering time of the 2DEG, without significant modification of the carrier density. A suppression of superconductivity was observed by increasing the Cr doping consistent with a Finkelstein's reduction of T_c induced by disorder and electron-electron interactions. By analyzing the magneto-conductance of the 2DEG as a function of magnetic

field, we showed that the spin relaxation occurs according to a D'Yakonov-Perel mechanism. In addition, we found that the spin-orbit coupling constant α increases linearly with the interfacial electric which is controlled by the gate voltage, as expected for a Rashba spin-orbit interaction. In the second section, we studied a LAO/STO top-gated field effect devices fabricated using the amorphous $LaAlO_3$ template method. The superconductivity was electrostatically modulated over a wide range by a top-gate voltage, without any leakage, and a superconductor-to-insulator quantum phase transition was induced when the quantum well is strongly depleted. By analyzing the magneto-transport measurements, the presence of strong spin-orbit coupling that could be controlled with the top-gate voltage was demonstrated. The spin-spliting energy of the order of a few meV was also found to increase linearly with the interfacial electric field as for the experiments described in the first section. These results represent an important step toward the realisation of new mesoscopic devices such as the ones that will be discussed in chapter 6.

Chapter 4

2D Superconductors Electrodynamics

"It must be borne in mind that mean field approximations are notoriously bad in predicting the form of the singularities in specific heats etc, since such a theory ignores fluctuations in the internal field."

J M Kosterlitz and D J Thouless

Ordering, metastability and phase transitions in two-dimensional systems (1973)

Contents

The superfluid stiffness, which is the energy cost to twist the phase of a superconductor, and the superconducting gap are two intrinsic energy scales that can be probed at high frequency. In the previous chapter, we demonstrated the possibility to tune spin-orbit coupling and superconductivity in $LaAlO_3/SrTiO_3$ by field effect either with a top gate or a back gate. Transport at finite frequency reveals other properties of electronic systems. Measuring the complex conductivity with AC radio frequency techniques as a function of temperature and gate voltage provides a complementary description of superconductivity at this interface. The role of this chapter is to introduce both basic concepts on disordered 2D superconducting and the standard

Mattis-Berdeen theory of electrodynamics of dirty superconductors.

First we present theoretical predictions of the response of a superconductor to an electromagnetic excitation at high frequency. Starting from London equations and the two-fluid model, we establish the response of a BCS superconductor in the presence of homogeneous disorder. Then we describe how the strength of superconductivity can be controlled by phase fluctuations in case of a high disorder or in the presence of inhomogeneities. In the specific case of inhomogeneities at a mesoscopic scale, we propose a description based on the Josephson effect in coupled superconducting islands, which is relevant to understand the properties of $LaAlO_3/SrTiO_3$ interfaces. Most of the concepts developed here play a fundamental role in the explanation of the behaviour of superfluid stiffness upon field effect doping as developed in chapter 5.

4.1 Superconductivity : the basics

In 1935, Heinz and Fritz London proposed an empirical description of the electrodynamics of a superconductor by a perfect diamagnetic current $\mathbf{j}_s$. In this seminal paper, they introduced for the first time a concept that will later be called the gap energy : *"But now suppose the electrons to be coupled by some form of interaction. Then the lowest state of the electrons may be separated by a finite distance from the excited one and the disturbing influence of the field on the eigenfunctions can only be appreciable if it is of the same order of magnitude as the coupling forces."* [114]. The estimated value of the superconducting gap of $LaAlO_3/SrTiO_3$ is $\Delta = 50\ \mu\text{eV} = 10$ GHz, which is much higher than the typical frequency used in the experiments made in this thesis $f \simeq 300$ MHz. Within this limit, the RF photons do not have enough energy to break Cooper pairs. At low temperature, the system can therefore be modelled by two conducting channels in parallel, namely the two-fluid model. One channel accounts for the superfluid electrons, while the other one describes all thermally activated quasiparticles.

4.1.1 Drude Model

First, let us consider a system of electrons with a density n having a mass m and a characteristic relaxation time τ. The Drude model gives a probability per unit time $p = 1/\tau$ for one electron to be scattered. The electron mean velocity under an applied electric field $\mathbf{E}$ is governed by Newton's second law :

$$m\frac{d\mathbf{v}}{dt} = e\mathbf{E} - m\frac{\mathbf{v}}{\tau} \tag{4.1}$$

The Drude response to a time-dependent field in the complex notation $\mathbf{E}e^{j\omega t}$ follows from equation (4.1). The complex conductance defined such that $\mathbf{j} = \sigma\mathbf{E}$ where $\mathbf{j}$ is the current reads

$$\sigma = \sigma_1 - j\sigma_2 = \frac{ne^2\tau/m}{1+j\omega\tau} = \frac{ne^2\tau/m}{1+\omega^2\tau^2} - j\frac{ne^2/m \times \omega\tau^2}{1+\omega^2\tau^2} \tag{4.2}$$

For normal electrons, the relaxation time is $\tau = \tau_e \simeq 10^{-13}$ s. In the limit $\omega << 1/\tau_e$, equation (4.2) becomes $\mathbf{j}_n = \sigma_n\mathbf{E}$ with

$$\sigma_n = \frac{n_n e^2 \tau_e}{m} \tag{4.3}$$

This very simple formula was used in the previous chapter to calculate the elastic scattering time from the normal state conductivity.

4.1.2 London equations and the superfluid stiffness

Using this classical description, the London brothers proposed the following empirical description of the superfluid state. Cooper pairs are not sensitive to scattering, which corresponds to an infinite relaxation time. By taking $\tau \to \infty$ in (4.1), the scattering term disappears in equation 4.1 which becomes the first London equation [115] $d\mathbf{j}_s/dt = (n_s e^2/m)\mathbf{E}$ where $\mathbf{j}_s = e n_s \mathbf{v}$ ($\mathbf{v}$ is the velocity of electrons and n_s the density of superconducting electrons). Accordingly equation (4.2) becomes

$$\sigma_s(\omega) = \frac{\pi n_s e^2}{m}\delta(\omega) - j\frac{n_s e^2}{m\omega} \tag{4.4}$$

In the two-fluid model we have to consider two channels in parallel. In the limit $\omega << 1/\tau_e$, the total conductance is simply the sum of the conductances in the normal and superconducting states

$$\sigma = \sigma_n + \sigma_s = \frac{1}{R_n} + \frac{\pi}{L_k}\delta(\omega) + \frac{1}{j\omega L_k} \tag{4.5}$$

where $L_k = \frac{m}{e^2 n_s}$ is called the kinetic inductance of the superconducting gas and $R_n = 1/\sigma_n$ is the resistance of the quasiparticle channel. The superconducting state can be seen as a coherent state of electrons forming Cooper pairs. Each Cooper pair has a mass 2m, a charge 2e and an energy $E_k = \sqrt{\Delta^2 + \xi_k^2}$ where $\xi_k = \varepsilon(k) - \mu$ is the kinetic energy of the electrons with respect to the chemical potential μ. The pairs have a common phase ϕ which means they respond as one unique state when the system is probed with an energy smaller than the gap Δ. A superconductor is then fully described by a wave function $\Psi = |\Psi|e^{i\phi}$, where $|\Psi|^2 = n_s$ is the superfluid density. The kinetic inductance can thus be seen as a retarded response due to the inertia of a coherent macroscopic quantum state. The London brothers had already grasped the physics underneath this macroscopic behaviour. Their empirical theory can be summarized by the following relations (London equations)

$$\mathbf{j}_s = -\frac{n_s e^2}{m}\mathbf{A} = -\frac{1}{L_k}\mathbf{A} = -\frac{1}{\mu_0 \lambda_L^2}\mathbf{A} \tag{4.6}$$

where λ_L, the London penetration depth, is the typical size over which a magnetic field can penetrate the superconductor ($\mathbf{A}$ is the vector potential).

4.1.3 Characteristic lengthscales

A superconductor is characterized by two typical lengths ξ the superconducting coherence length and λ the penetration length. **The coherence length** $\xi = \hbar v_F/\pi\Delta$ is the length over which the wave function ψ can be bent without killing superconductivity. It is related to the

pairing energy Δ. In some sense it is the minimal size of a Cooper pair. It has to be compared with the elastic scattering length l_e. If $l_e >> \xi$ the superconductor is in the so called clean limit. In the case where $l_e << \xi$ the superconductor is in the dirty limit. In case $l_\phi << \xi$, that is $\Delta/h >> 1/\tau_\phi$, the phase coherence of the superconductor is decreased, and so is the superfluid density as calculated by Ambegaokar and Smith [106], The LAO/STO interface has a rather low pairing potential and is in the limit $1/\tau_\phi < \Delta/h$ where the Mattis-Bardeen approximation that we derive in section 4.2 is still valid.

The penetration length λ: In a 2D sample of thickness $d < \lambda$, one has to make the difference between magnetic field applied parallel or perpendicular to the layer. In the first case, the field penetrates the superconductor. In the second one, screening currents are confined within a thickness d, and the corresponding penetration depth $\lambda_\perp$ reads :

$$\lambda_\perp = \lambda^2/d \tag{4.7}$$

The radius of a vortex formed in a quasi-two-dimensional system is fixed by the Pearl's length $\lambda_\perp$ [116]. In the last section of this chapter, we'll see how these vortices can contribute to the dynamical response of a quasi-2D system even in the absence of a magnetic field.

In general, the superfluid density, the kinetic inductance and the London penetration length are not simply related as in equation (4.6). In a 2D superconductor, phase fluctuations dominate the superconducting state. A Beresinsky-Kosterlitz-Thouless transition (BKT) is predicted to occur in quasi-2D superfluid system. The London model we discussed is not sufficient to capture the physics anymore. We can still consider it as a toy model which gives an intuitive understanding of the electrodynamical response of a superconductor. In the next sections we develop more accurate models where temperature and frequency dependence of complex conductivity are calculated within the BCS theory. We then discuss the effects of disorder and topological phase transitions in 2D superconducting systems.

4.2 Mattis-Bardeen theory

After a brief introduction on the main properties of the complex conductivity of a many-body quantum system in the linear approximation, we detail the Mattis-Bardeen theory of a s-wave BCS superconductor in the dirty limit.

4.2.1 Kubo formalism

The Kubo formalism allows us to derive the conductivity of a system described by a BCS Hamiltonian at any frequency. The most general Hamiltonian is given by $H = H_0 + H_{int} + H_{ext}(t)$ where H_0 is the Hamiltonian of free electrons relative to the chemical potential μ and $H_{ext} = -e \int d\mathbf{rj}(\mathbf{r})\mathbf{A}_{ext}(\mathbf{r}, t)$ describes the time dependent coupling to an electromagnetic excitation. In our case $H_{int} = H_{BCS}$ corresponds to the attractive interaction responsible for superconductivity as defined in appendix E. For small excitations, the Kubo formula relates the current-current correlation function to the conductivity.

One can first express the current created by the electromagnetic field within the gauge $\phi = 0$ and $\mathbf{E} = -\partial_t \mathbf{A}$. The Noether theorem [1] applied to our Hamiltonian using minimal coupling ($\mathbf{p} \to \mathbf{p} - e\mathbf{A}$) leads to the following expression for the current in the direction α $j_\alpha(r) = j^p_\alpha(r) + j^d_\alpha(r)$ with paramagnetic and diamagnetic contributions for the current

$$j^p_\alpha(r) = \frac{i\hbar}{2m} \sum_\sigma (\partial_{r_\alpha} c^\dagger_{r_\sigma}) c_{r\sigma} - c^\dagger_{r\sigma} (\partial_{r_\alpha} c_{r\sigma}) \tag{4.8}$$

$$j^d_\alpha(r) = -\frac{e}{m} \sum_\sigma A_\alpha(r) c^\dagger_{r\sigma} c_{r\sigma} \tag{4.9}$$

where $c^\dagger_{r\sigma}$ and $c_{r\sigma}$ are the creation and annihilation operators of electron at position $\mathbf{r}$ with spin σ. The paramagnetic current is the result of the strain applied by the electromagnetic excitation on the wave function [117]. The diamagnetic current screens the external magnetic field, and is responsible for the Meissner effect when the system is superconducting.

Starting from a ground state $|\phi_0\rangle$, and using the linear response formula $\chi^R_{j^p_\alpha j^p_\beta}(\mathbf{r}-\mathbf{r}', t-t') = -i\theta(t-t') \langle\phi_0| [j^p_\alpha(r,t), j^p_\beta(r',t')] |\phi_0\rangle =_{def} \Pi_{\alpha\beta}(\mathbf{r}-\mathbf{r}', t-t')$ we find the following expression for the current

$$\begin{aligned} J_\alpha(\mathbf{r},\omega) &= e\langle j_\alpha(r,\omega)\rangle && (4.10)\\ &= e\langle j^p_\alpha(r,\omega)\rangle + e\langle j^d_\alpha(r,\omega)\rangle && (4.11)\\ &= -e^2 \int d\mathbf{r}' \sum_\beta \Pi_{\alpha\beta}(\mathbf{r},\mathbf{r}',\omega) A_\beta(\mathbf{r}',\omega) - \frac{e^2}{m} \langle n(r)\rangle A_\alpha(\mathbf{r},\omega) && (4.12)\\ &= \int d\mathbf{r}' \sum_\beta \underbrace{-\frac{e^2}{i\omega} \left(\delta_{\alpha\beta}\delta(\mathbf{r}-\mathbf{r}') \frac{n(r)}{m} + \Pi_{\alpha\beta}(\mathbf{r},\mathbf{r}',\omega) \right)}_{\sigma_{\alpha\beta}(\mathbf{r},\mathbf{r}',\omega)} E_\beta(\mathbf{r}',\omega) && (4.13) \end{aligned}$$

In a translation invariant system, we Fourier transform this expression of conductivity

$$\sigma_{\alpha\beta}(\mathbf{q},\omega) = \frac{ie^2}{\omega} \left(\frac{n}{m}\delta_{\alpha\beta} + \Pi_{\alpha\beta}(\mathbf{q},\omega) \right) \tag{4.14}$$

where the first term corresponds to the diamagnetic response of Cooper pairs and $\Pi_{\alpha\beta}$ accounts for paramagnetic currents. The Kubo formula tells us that the dynamical conductivity gives a measure of correlations inside the material. In the case of a metal in the limit $q = 0$ and $\omega \to 0$ equation (4.14) leads to the Drude formula (4.3). A general relation, independent of temperature and of the interaction, is derived from Kramers Kronig relations [118]. It is named the sum rule :

$$\int_0^\infty \mathrm{Re}\sigma_{\alpha\beta}(\omega) d\omega = \frac{\pi}{2} \frac{ne^2}{m} \delta_{\alpha\beta} \tag{4.15}$$

In a superconductor, this rule says that the spectral weight below the gap should condense in a delta function at zero frequency, with a weight of $\pi n_s e^2/2m$ [119].

1. The Noether theorem relates symetries and conservation laws. Charge conservation in this context gives a current $j_\alpha(r) = -1/e \frac{\delta H}{\delta A_\alpha}$

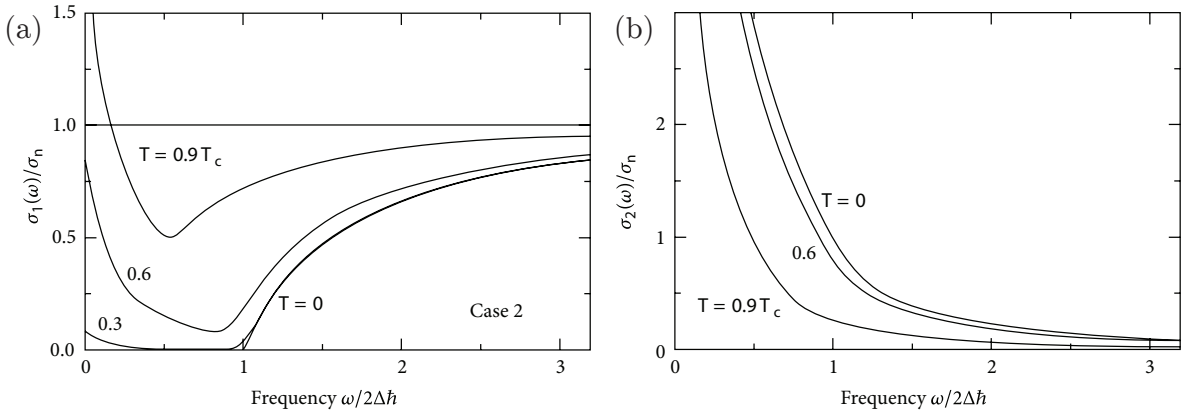

Figure 4.1 – (a) Mattis Bardeen formula real part of the conductance σ normalized by the conductivity in the normal state σ_n as a function of frequency. (b) The imaginary part of the conductance σ normalized by the conductance in the normal state. Each curve is calculated for different temperatures between 0 and T_c. Figures come from [121]

4.2.2 Mattis Bardeen

At T=0, for a clean BCS superconductor $\Pi_{\alpha\alpha}(\omega = 0, \mathbf{q} \to 0) = 0$ as a result of the phase rigidity of the superconducting wavefunction [120]. Using equation (4.14), we obtain a purely imaginary conductivity as in equation (4.4). In a more general case, for arbitrary values of $T < T_c$ and $\hbar\omega$, Mattis and Bardeen calculated the electrodynamical response of a BCS superconductor in the dirty limit $\Delta << \Gamma = \hbar/\tau_e$. The real and imaginary parts of the complex conductance $\sigma_s(\omega, T)$ are given by the following formulas [122]

$$\frac{\sigma_{1s}}{\sigma_n}(\omega,T) = \frac{\pi n_s}{m\sigma_n}\delta(\omega) + \frac{2}{\hbar\omega}\int_{\Delta}^{\infty} dE(f_D(E) - f_D(\hbar\omega + E))g(E) + \frac{\Theta(\omega - 2\Delta)}{\hbar\omega}\int_{\Delta-\hbar\omega}^{-\Delta} dE(1 - 2f_D(\hbar\omega + E))g(E) \tag{4.16}$$

$$\frac{\sigma_{2s}}{\sigma_n}(\hbar\omega,T) = \frac{1}{\hbar\omega}\int_{max(-\Delta,\Delta-\hbar\omega)}^{\Delta} dE(1 - 2f_D(\hbar\omega + E))g(E)\frac{E(E+\hbar\omega)+\Delta^2}{\sqrt{\Delta^2 - E^2}\sqrt{(E+\hbar\omega)^2 - \Delta^2}} \tag{4.17}$$

with

$$g(E) = \frac{E(E+\hbar\omega)+\Delta^2}{\sqrt{E^2 - \Delta^2}\sqrt{(E+\hbar\omega)^2 - \Delta^2}} \tag{4.18}$$

and f_D is the Fermi-Dirac distribution.

The real part σ_1 accounts for dissipative processes. The first integral in (4.16) comes from thermally activated quasiparticles while the second term represents the photon-excited quasiparticles. At $T = 0$ no quasiparticle is created, and thus the dissipative part σ_1 is zero for $\hbar\omega < 2\Delta$ as shown on figure 4.1(a). In figure 4.1(b) the imaginary part recovers its inductive

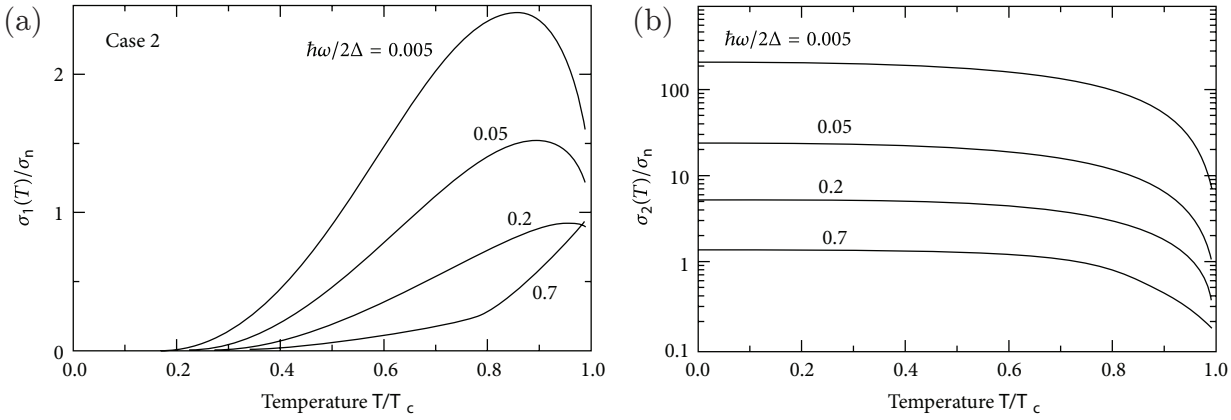

Figure 4.2 – (a) Mattis Bardeen formula real part of the conductance σ normalized by the conductivity in the normal state σ_n as a function of temperature. (b) Corresponding imaginary part of the conductance σ normalized by the conductance in the normal state. Each curve is calculated for frequencies varying between $0.005 \times 2\Delta$ and $0.7 \times 2\Delta$. Figures come from [121]

evolution in $1/\omega$ at a frequency much lower than the gap. Figure 4.2 shows the evolution of the real and imaginary parts as a function of temperature. At low frequency $\hbar\omega << 2\Delta$ a peak is visible on σ_1 just below T_c (fig. 4.2(a)). This coherence peak corresponds to the excitation of quasiparticles populating the levels above the gap where the density of state is maximum. Their probability to be scattered is given by the coherence factor as calculated in the BCS theory.

The expression (4.17) which describes the contribution of the Cooper pairs is plotted on figure 4.2(b). In the limit $\hbar\omega << 2\Delta$ this non-dissipative response simplifies as follows [115] (for a demonstration see appendix C.2)

$$\frac{\sigma_2(\omega \to 0, T)}{\sigma_n} \simeq \frac{\pi\Delta}{\hbar\omega}\tanh(\beta\Delta/2) \tag{4.19}$$

where $\beta = 1/k_B T$. Using the Drude expression for conductivity (4.3)

$$\sigma_2(\omega \to 0, T \to 0)\omega = \frac{n_s e^2}{m} = \frac{\pi\Delta\sigma_n}{\hbar} = \frac{ne^2\tau}{m}\frac{\pi\Delta}{\hbar} = \frac{ne^2}{m}\frac{l}{\xi} \tag{4.20}$$

where $\xi = \hbar v_F/\pi\Delta$ is the coherence length and $l = v_F\tau_e$ is the mean free path. In the London picture at $T = 0$, $n_s = n$, which means that all electrons condense in Cooper pairs, and the penetration depth λ is $\sqrt{m/n_s e^2}$. In the dirty limit, only the spectral weight below Δ/h of the Drude peak condense in the superconducting state.

The London superfluid stiffness $J_s = \hbar^2 \times n_s/4m$ is now related to the normal state conductance σ_n and the superconducting gap Δ through equation (4.20). It comes

$$J_s = \frac{R_0}{R_n}\frac{\Delta}{4} \tag{4.21}$$

where $R_n = 1/\sigma_n$ the normal state resistance and R_0 the quantum of resistance h/e^2. In two dimensions, R_n is just replaced by the square resistance $R_\square$.

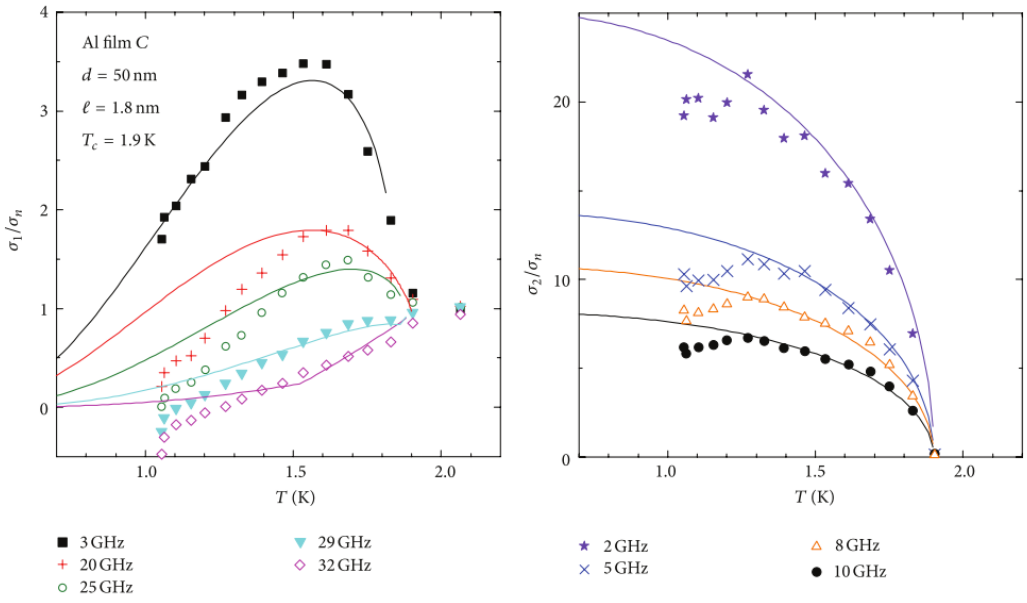

Figure 4.3 – Temperature dependence of real and imaginary parts of Al thin films conductance from [123]

The Mattis-Bardeen theory has been very successful in describing electrodynamics properties of superconductors in the dirty limit as shown in the following example. Disordered 50 nm thick Al thin films have been measured as illustrated on figure 4.3. A good agreement has been found with the Mattis Bardeen theory for a large range of frequencies and temperature, for both the real and imaginary parts of the conductivity. Most of the time however, 2D systems depart from this theory. Now that we have described the general theory in any dimension, let us address the specific case of a 2D superconductor.

4.3 Dissipation and transport in disordered 2D systems

We now describe the specific signatures of the dynamical response of a 2D superconductor in the presence of disorder. In 1959, Anderson predicted that s-wave superconductivity should not be affected by the presence of disorder [124]. In fact, he demonstrated that in the dirty limit, usual BCS pairing is protected by time reversal symmetry. In other words, the critical temperature is not affected by increasing elastic disorder. Nevertheless, in lower dimension the electrons are much more sensitive to any kind of disorder. A 2D superconductor is always in the dirty limit as $\xi >> d \simeq l_e$, because the thickness d sets the mean free path. The Mattis-Bardeen theory is therefore appropriate to describe 2D superconductors. But when disorder increases, superconducting properties can be more affected, Anderson theorem falls down and a superconductor to insulator transition (SIT) is observed. Depending on the interactions, on the nature of superconductivity (symmetry of the gap, number of bands, etc.), and taking into account different degrees of disorder (strong disorder, spatial inhomogeneities, quantum phase fluctuations etc.), different scenarii are proposed to explain it.

As we have seen, superconductivity can be suppressed by enhanced Coulomb interactions in the presence of strong disorder. Finkelstein's theory that is based on the competition between pairing and electron-electron interactions, describes quantitatively this phenomena, and explains our data on Cr-doped samples (see chapter 3 section 3.1.2) [89]. Another way to destroy superconductivity is related to the phase of the order parameter. After presenting phase fluctuations in 2D superconductors, we will describe vortex excitations using BKT theory.

4.3.1 Phase fluctuations

In 2D superconducting films, disorder can be so strong that the Anderson theorem falls down. In a seminal paper Ma and Lee explained how the validity range of the Anderson theorem is given by the following condition [125] :

$$N\Delta_0 L^d >> 1 \tag{4.22}$$

where N is the density of state (DOS) averaged over $\pm\Delta_0$ (the bulk value for the gap), L is the localization length and d the dimension of the system. On the contrary, if Cooper pairs are localized on scale such that $N\Delta_0 L^d \sim 1$, superconductivity has to be described in a different way. Under these extreme disorder conditions, pairs are localized, until they form a bosonic insulator. A phase diagram (figure 4.4) was established by Fisher [112] after exploring the disorder-driven superconducting to insulator transition in the case where phase fluctuations dominate.

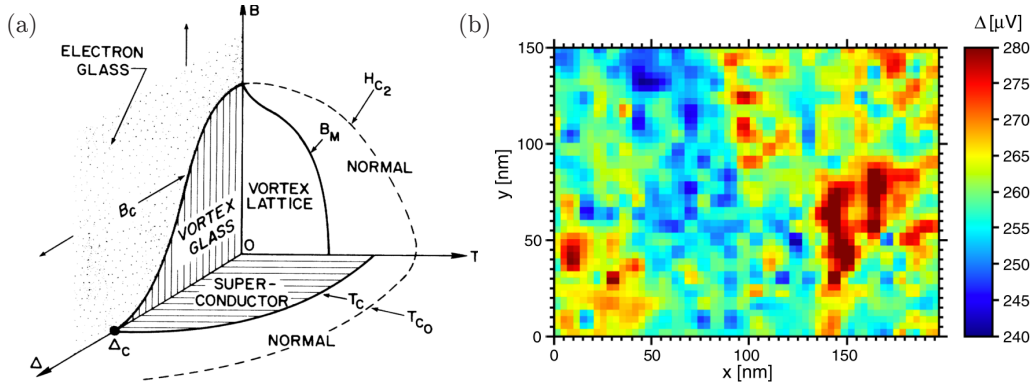

Figure 4.4 – (a) Phase diagram of disordered two-dimensional superconductor [112]. Here Δ quantifies the disorder. (b) Spatial fluctuations of the superconducting gap Δ in a titanium nitride thin film. Adapted from [126]

In order to simulate low energy excitations when Cooper pairs are localized, one can map the Hubbard Hamiltonian to a quantum spin on a lattice one calls the Ma-Lee model. It was recently proven that the strong disorder can induce spatial inhomogeneities in the sample [127, 77]. Such inhomogeneities lead to a lowering of the superfluid stiffness and to the transfer of some spectral weight below 2Δ [128, 129]. In this case, the superfluid stiffness is lower than the gap energy and drives the SIT [130]. Tunneling measurements were performed on homogeneously disordered superconducting titanium nitride thin films [126]. Clear spatial inhomogeneities of the superconducting gap are visible on figure 4.4 (b).

4.3.2 BKT transition

In 2016, Thouless and Kosterlitz received the Nobel prize together with D. Haldane for their major contribution in the field of topological physics. They studied topological excitations in a 2D spin lattice model with $U(1)$ symmetry called the XY model. The Hamiltonian of such a system is given by

$$H_{XY} = -J \sum_{\langle ij \rangle} \cos(\phi_i - \phi_j) \tag{4.23}$$

where classical spins $\mathbf{S}_i = S_i e^{i\phi_i}$ are coupled to their neighbours via an Heisenberg interaction $J\mathbf{S}_i.\mathbf{S}_j$.

4.3.2.1 Free vortices

This description of a two-dimensional superconductor allows a mapping to the XY model where J in equation (4.23) corresponds to the superfluid stiffness and the phase ϕ is mapped to the angle of the spins. Superconductivity in two dimensions is believed to be controlled by phase fluctuations. For small excitations, the XY model can be simplified $H_{XY} \simeq J/2 \int d^2\mathbf{r}[(\nabla\theta)^2]$. Within this model, vortices and antivortices naturally arise as low energy excitations. A vortex winds the phase by $\pm 2\pi$, depending on its vorticity $\varepsilon_i = \pm 1$ so that any closed path around its centre gives

$$\oint \nabla\phi dl = 2\pi\varepsilon_i n \qquad \text{with} \quad n \in \mathbb{N} \tag{4.24}$$

A vortex configuration $\bar{\phi}$ satisfies the equation

$$\nabla^2\bar{\phi}(\mathbf{r}) = 2\pi\delta(\mathbf{r} - \mathbf{r}_0) \tag{4.25}$$

For a vorticity of $\varepsilon_i = +1$, a solution in the xy plane is given by

$$\bar{\phi}(x, y) = \arctan(\frac{y - y_0}{x - x_0}) \tag{4.26}$$

The energy associated with this topological excitation is

$$E = \frac{J}{2} \int d\mathbf{r}(\nabla\phi(\mathbf{r}))^2 = \frac{J}{2} \int_a^L dr 2\pi r \frac{1}{r^2} = \pi J \ln(\frac{L}{a}) \tag{4.27}$$

with a being the lattice parameter and L the size of the 2D superconductor. The entropy is calculated by counting the number of possible vortices in the system.

$$S = k_B \ln(\frac{L^2}{a^2}) \tag{4.28}$$

Finally, the free energy of vortices in a 2D superconductor is given by

$$F = E - TS = (\pi J - 2k_B T) \ln(\frac{L}{a}) \tag{4.29}$$

Above $T_{KT} = \pi J/2k_B$ vortices start to proliferate and destroy the long-range order of the superconducting state. Using the renormalization group (RG) method, Kosterlitz and Thouless

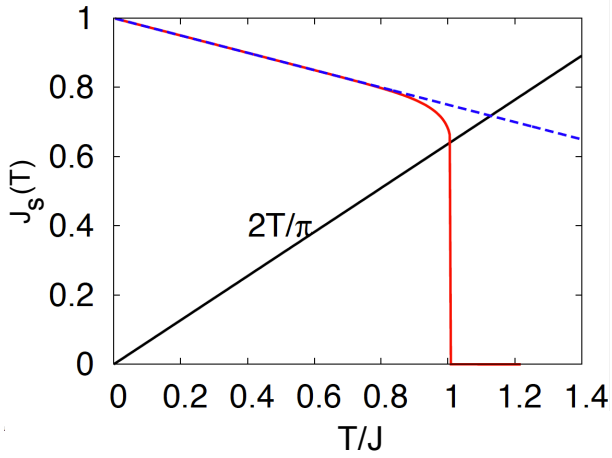

Figure 4.5 – Jump of the superfluid stiffness in BKT theory. From [132]

demonstrated [131] that when the interactions between vortices, which we neglected so far, are taken into account, the critical temperature $T_{KT} = \pi J/2k_B$ still holds. The RG also takes into account the cost of creating a vortex, which is described by the vortex core energy μ. In this new frame, vortices and anti-vortices are paired below T_{KT} and bound (fig. 4.6(a)). Above T_{KT}, it becomes favourable for vortex-antivortex pairs (figure 4.6(b)) to unbind leading to a sudden drop in the superfluid stiffness (see fig. 4.5).

4.3.2.2 BKT contribution to transport

Zero frequency Below T_{KT}, the vortices pairs do not dissipate; the system is thus fully superconducting. The vortex coherence length $\xi_+(T)$ which gives the distance above which interaction between vortices is infinite at T_{KT} and decreases exponentially :

$$\xi_+(T) = \frac{\xi_0}{A} \exp\left\{ b \frac{T_C - T_{KT}}{T - T_{KT}} \right\} \tag{4.30}$$

In this equation A and b are two parameters close to 1. This length can also be seen as the typical distance between two vortices. The vortex density n_f is thus

$$n_f = \frac{1}{2\pi\xi_+^2} \tag{4.31}$$

The physics of vortices can be mapped onto a Coulomb gas model, where the vorticity ε_i corresponds to the charge. Vortices and anti-vortices attract each other, while vortices of the same sign repel each other. If these pairs are broken (above T_{KT}), applying a current creates a transverse force similar to the Lorentz force called the Magnus force (figure 4.6 (c)) :

$$\mathbf{F} = \varepsilon_i \mathbf{j}_s \times \mathbf{z}\phi_0 \tag{4.32}$$

Vortices acquire a drift velocity $v_L = \mu_V \mathbf{F}$ where $\mu_V = D/k_B T$ is the vortex mobility and D the diffusion constant. Once they reach the edge of the system, they disappear. Each vortex crossing the edge induces a 2π variation of the phase. During a time Δt, the number of vortices

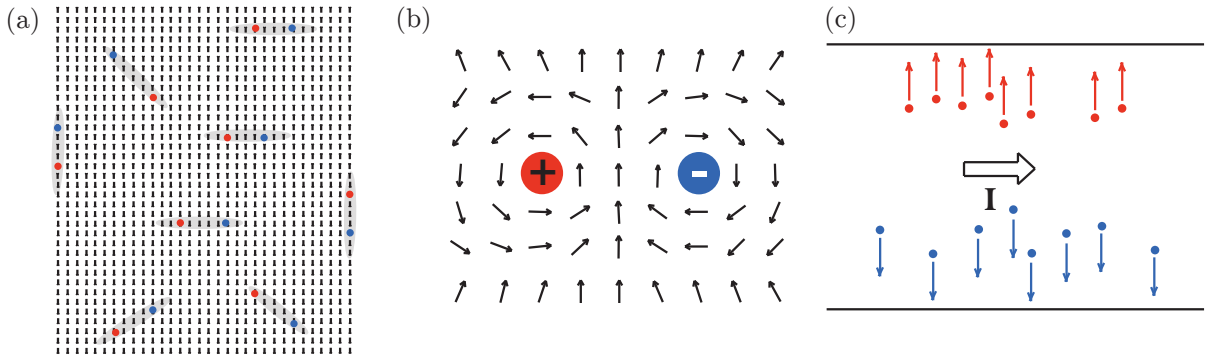

Figure 4.6 – (a) 2D superfluid below T_{KT} where vortex-antivortex pairs are bound (b) Zoom on a vortex-antivortex pair. (c) Magnus force : red dots correspond to vortices with vorticity $\varepsilon_i = +1$ and blue ones to vorticity $\varepsilon_i = -1$.

crossing the edge is thus $n_f v_L \Delta t$ where n_f is the vortex density and v_L their drift velocity in the transverse direction. The total phase variation during a time Δt is

$$\Delta\phi = 2\pi n_f v_L L \Delta t \tag{4.33}$$

The variation of $\Delta\phi$ with time corresponds via the Josephson equation [2] to a voltage $\Delta V = (\phi_0/2\pi)\Delta\phi/\Delta t$. The resulting electric field and resistivity of a system of size L are

$$E_x = \frac{\Delta V}{L} = \phi_0 n_f v_L \tag{4.34}$$

$$\rho = \frac{E_x}{j_s} = \phi_0^2 n_f \mu_V \tag{4.35}$$

Usually they are related to the normal resistivity, but their value can also be affected by the presence of inhomogeneities.

BKT physics changes current-voltage characteristic I-V below T_{KT} in a non-trivial way. Indeed, it can be expected that before the critical current is reached, vortices will be generated, giving rise to a non-linear I-V characteristics

$$V \propto I^{a(T)} \qquad \text{with} \quad a(T) = \frac{\pi J_s(T)}{T} + 1 \tag{4.36}$$

A sudden jump of a from 3 to 1 is expected at T_{KT}. In a recent experiment on LAO/STO, I-V curves were analyzed within this model [133] but the expected jump in the critical exponent a is not present, which can be explained by the presence of inhomogeneities. This interface could still be a good candidate to show the features of a 2D superconductor in the BKT regime, as we will see next, when we consider that inhomogeneities form a Josephson Junction array (JJA).

2. A derivation of Josephson equation is given in appendix E.

Finite frequency At finite frequency two typical length scales are important : the penetration length λ and the equivalent of the skin depth of a Coulomb gas δ. The first is related to the imaginary part of the conductivity σ_2

$$\lambda^{-2} = \mu_0 \omega \sigma_2 \tag{4.37}$$

The second instrinsic length is associated with the real part of the conductivity and is a measure of the dissipation due to vortex fluctuations

$$\delta^{-2} = \mu_0 \omega \sigma_1 \tag{4.38}$$

This length has to be compared with the typical length r_ω over which vortices are displaced when an AC current is applied at a frequency ω

$$r_\omega = \sqrt{\frac{14D}{\omega}} \tag{4.39}$$

where D is the diffusion constant introduced in equation (4.50).

We now want to derivate the electromagnetic response of a superfluid film. Originally, Ambegaokar et al. [134] calculated the electromagnetic response of a superfluid helium thin film which is also described by BKT physics. Then, Halperin and Nelson applied this approach to a charged superconductor [135]. We have outlined in the previous section the analogy between the BKT physics and a Coulomb gas. An additional step in this analogy, is to take into account a frequency dependent dielectric function $\epsilon(\omega)$. The complex conductivity in a BKT model is given by

$$\sigma(\omega) = -\frac{d}{i\omega L_k \epsilon(\omega)} \tag{4.40}$$

In this equation $L_k = m/n_s e^2 = 1/J$ and d is the thickness of the system. The vortex dielectric function $\epsilon(\omega)$ can be computed using the RG method and depends on two parameters. The first one is related to the superfluid stiffness $K = \pi J_s/T$, and the second to the fugacity $g = 2\pi e^{-\beta\mu}$. The latter accounts for the Vortex core energy μ. Contrary to the calculation presented in section 4.3.2.1, RG allows the computing of the physics of interacting vortices. From equation (4.40), the two typical scales can be expressed as

$$\lambda^{-2} = \frac{J_s}{d\alpha} \mathrm{Re} \frac{1}{\epsilon} = \frac{J_s}{d\alpha} \frac{\epsilon^{'}}{\epsilon^{'2} + \epsilon^{''2}} \tag{4.41}$$

$$\delta^{-2} = -\frac{J_s}{d\alpha} \mathrm{Im} \frac{1}{\epsilon} = \frac{J_s}{d\alpha} \frac{\epsilon^{''}}{\epsilon^{'2} + \epsilon^{''2}} \tag{4.42}$$

with $\alpha = \hbar^2/4e^2\mu_0$ and where $\epsilon^{'}$ and $\epsilon^{''}$ are the real and imaginary parts of the dielectric constant respectively. Only vortices smaller than r_ω will contribute to the imaginary part of the vortex dielectric constant $\epsilon^{''}$. It was demonstrated that it can be computed from the static dielectric constant of vortices [135]

$$\epsilon^{''}(\omega) = \epsilon(r_\omega) \simeq \frac{Dn_f}{\omega} \tag{4.43}$$

As for the real part of the dielectric constant, r_ω also sets a length at which the RG flow should be stopped. Instead of sending $l \to \infty$, it is stopped at $l_\omega = \ln(r_\omega/\xi)$ where ξ is the superconducting coherence length.

$$\epsilon^{'}(\omega) \simeq \frac{J_s(0)}{J_s(l_\omega)} \tag{4.44}$$

4.3.3 Network of Josephson junctions

It was demonstrated in our team [80], that the LAO/STO interface behaves as a network of Josephson junctions. By measuring IV curves as a function of back voltage, we were able to extract typical values of Josephson energy $E_J = \phi_0 I_c/2\pi$, charging energy $E_c = e^2/2C$ and dissipation energy V^2/R. The charging energy is very small compared to the Josephson energy.

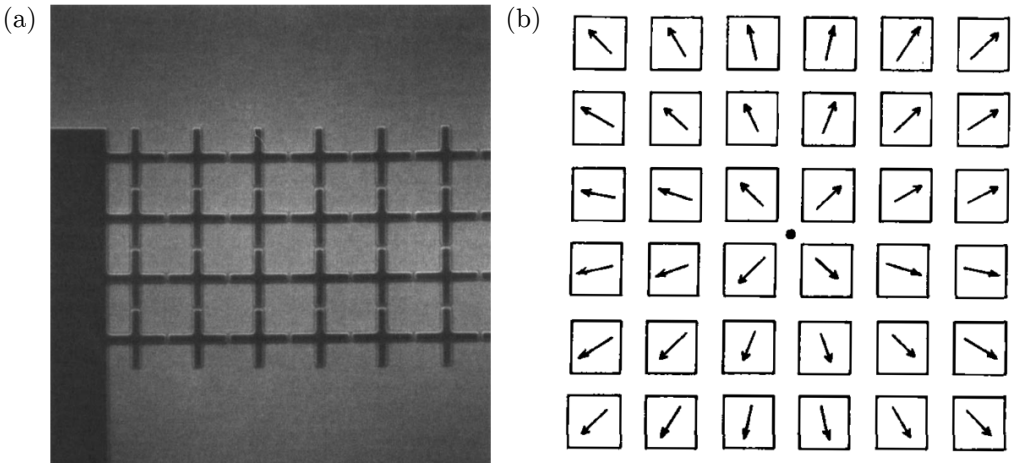

Figure 4.7 – (a) Electron micrograph of a square JJA made from Nb crosses (dark region) with a center to center spacing of 10 μm and 1.5 μm large crossarms. (b) Schematic of a square JJA where each square represents a superconducting island and each arrow a phase ϕ_i. Both figures come from [136]

During the 70s, technological progress allowed the realization of macroscopic devices made of millions of Josephson junctions as shown on figure 4.7 (a) [137] creating Josephson Junctions Arrays (JJA). Such arrays of Josephson junctions described with a RCSJ model [3] are well characterized below T_c by the following Hamiltonian

$$H_J = -\sum_{\langle ij \rangle} E_J \cos(\phi_i - \phi_j) \tag{4.45}$$

In this equation $E_J = \hbar I_c/2e$ is the Josephson energy, I_c the critical current of each Josephson junction, and ϕ_i the phase of each superconducting island. If the charging energy is negligible

3. Notes on RCSJ model are available in appendix E

compared to the Josephson energy, the Hamiltonian looks exactly the same as for a 2D superconductor with $E_J \simeq J$. The low energy excitations of this system are called Josephson vortices. Figure 4.7 (b) represents schematically a Josephson vortex. As we will see, Josephson-vortex dynamics is much slower than usual Abrikosov vortices.

Transport properties : As well demonstrated in a review by Newrock et al. [136], the phase dynamics of a Josephson junction can be mapped onto the one of Josephson vortices in a 2D network. In the ground state, a Josephson vortex has its centre in the middle of a cell. When the current is zero, and the temperature sufficiently low, vortices are trapped in a 2D Peierls-Nabarro potential U_{NP} ($k_BT << U_{NP}$). This potential has an egg box's shape. The energy needed for a vortex to jump across a junction is approximately $U_{NP} \sim \gamma E_J$ [138], where γ depends on the precise geometry of the network ($\gamma = 0.2$ for a square array). By applying a current in the x direction, Josephson vortices are subject to a Magnus force described in equation (4.32). The total potential energy seen by the vortex is given by

$$U(y) = -\frac{1}{2}\gamma E_J(T)\cos(2\pi y/a^2) - \phi_0 I y/a^2 \tag{4.46}$$

Where I is the source-drain current. The first term represents the cost for a Josephson vortex to overcome the Navarro potential and the second represents the Lorentz force described in equation (4.32).

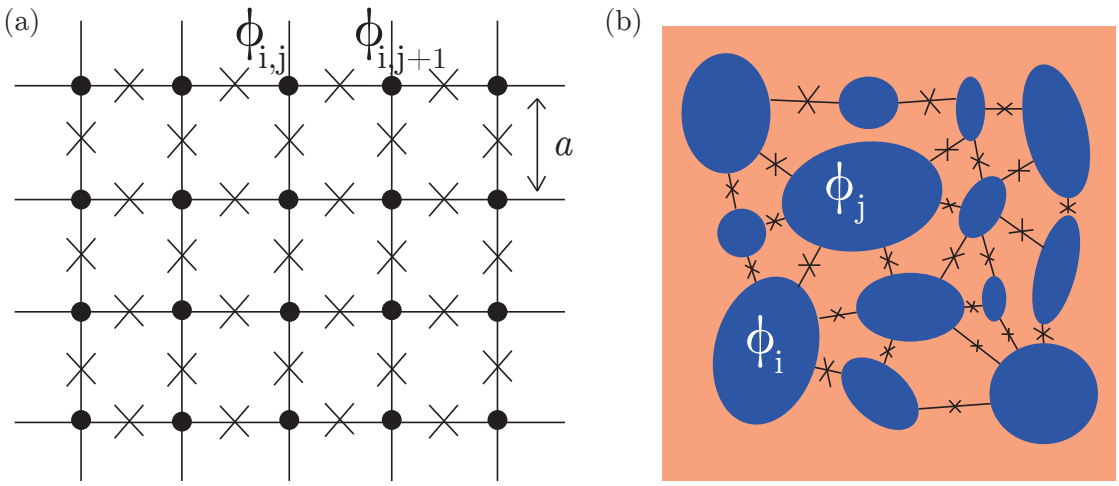

Figure 4.8 – (a) Squared Josephson-junction array (JJA) with a lattice parameter a. Each cross represents the Josephson coupling between each island (black dot), ϕ_i is the phase of the i^{th} puddle (b) Scheme of a 2D Josephson-junction network due to phase separation at the LAO/STO interface.

The presence of a resistance R in parallel to the Josephson junction dissipates power, resulting in a damping force $-\eta \mathbf{v}_V$ with $\mathbf{v}_V$ the vortex velocity. Any vortex crossing a junction will create

a $\pi-$shift of the phase. Using the Josephson relation $\frac{\partial\phi}{\partial t} = \frac{2e}{\hbar}V$, we find that the voltage drop is

$$V_{ij} = \frac{\phi_0}{2a}\langle v_V \rangle \tag{4.47}$$

The dissipated energy is the sum of all the dissipation across all the junctions

$$\eta \mathbf{v}_v^2 = \sum_{\langle ij \rangle} \frac{V_{ij}^2}{R} \tag{4.48}$$

In a square array, the effective resistance is $R/2$, giving rise to a viscosity

$$\eta = \left(\frac{\phi_0}{a}\right)^2 \frac{1}{2R} \tag{4.49}$$

The vortex diffusion constant $D = k_B T/\eta$ is thus

$$D = \frac{2Ra^2 k_B T}{\phi_0^2} \tag{4.50}$$

In the presence of a non-negligible capacitance between superconducting islands (RCSJ model provided in appendix E), energy is also stored in the junctions. The movement of a vortex in the 2D array in the y direction when a current I is applied in the x direction, is summarized by the following formula [136]

$$I = \underbrace{I_{cV} \sin\left(\frac{2\pi y}{a}\right)}_{\text{PN potential}} + \underbrace{\frac{\Phi_0}{4\pi R}\frac{d(2\pi y)/a}{dt}}_{\text{Dissipation due to R}} + \underbrace{\frac{\Phi_0 C}{4\pi}\frac{d^2(2\pi y/a)}{dt^2}}_{\text{Energy stored in C}} \tag{4.51}$$

According to equation (4.50), the diffusion of Josephson vortices is limited by the resistance of the array. The lower the resistance, the more they will dissipate. In the next chapter, we will compare this model to our experimental results. If homogeneous 2D superconductors and JJA are both related to BKT physics, the dissipation in both cases are different. In the first case, it is related to the movement of regular vortices ; in the second one to the jump of Josephson vortices accross barriers. We are now ready to study the AC transport at LAO/STO interface. Dynamical measurements of this disordered 2D array of Josephson junctions will provide crucial information on the superconducting properties of this system.

Chapter 5

AC Transport

"When we have to explain in a word what superconductivity means, the answer might be that the quantum mechanical phase of the electron system becomes "solid" as if it were a rigid body, and gains rigidity."
Naoto Nagaosa, *Quantum Field Theory in Strongly Correlated Systems* (1995)

Contents

Since the discovery of a high-mobility electron gas at the LAO/STO interface in 2004, the transport properties of this interface have been intensively studied at zero (or quasi-zero) frequency. Such measurements are nowadays relatively simple to implement at dilution refrigerator temperatures but they only give access to a limited number of static parameters such as the superconducting T_c or the critical magnetic fields B_c for instance. In this chapter, we present an AC transport experiment that consists in sending a microwave signal to a LAO/STO sample embedded into a resonant circuit and measuring the reflected signal. After a proper calibration, the measured reflection coefficient allows extracting the complex conductance of the interface at a frequency of around 0.5 GHz, as a function of temperature and back-gate doping. This gives us access to two important energy scales that control the superconducting phase diagram : the superfluid stiffness J_s, and, indirectly, the energy gap Δ through the BCS theory. J_s can be converted into a superfluid density n_s, which has to be discussed within the context of the peculiar $LaAlO_3/SrTiO_3$ band structure.

In the first part of this chapter, we describe the propagation of an electromagnetic plane wave in a general lossy medium. We also examine the specific case of the propagation of such wave in a coplanar waveguide terminated by a complex impedance Z_L which corresponds to the experimental situation. Then, we introduce the calibration method that has been developed for this specific experiment. Finally, we present, analyze and discuss the results obtained on the complex conductance of the LAO/STO interface in the framework of the different theories developed in previous chapters.

5.1 Electromagnetic wave propagation

In this section we first describe the propagation of a monochromatic transverse electromagnetic (TEM) plane wave in a lossy medium. The second part of this section is devoted to the lossless terminated transmission line.

5.1.1 Lossy medium

Let us consider a medium with a conductivity σ, a dielectric permittivity ϵ and a magnetic susceptibility μ. In the complexe notation [1] ($\mathcal{E}(x,y,z,t) = \mathrm{Re}\{\mathbf{E}(x,y,z)e^{j\omega t}\}$), Maxwell equation are given by :

$$\nabla \times \mathbf{E} = -j\omega\mu\mathbf{H} \tag{5.1}$$

$$\nabla \times \mathbf{H} = j\omega\epsilon\mathbf{E} + \sigma\mathbf{E} \tag{5.2}$$

which leads to the following wave equation

$$\nabla^2\mathbf{E} + \omega^2\mu\epsilon(1 - j\frac{\sigma}{\omega\epsilon})\mathbf{E} = 0 \tag{5.3}$$

If we consider a simple one dimensional problem with propagation in the z direction, the equation becomes

$$\frac{\partial^2 E_x}{\partial z^2} - \gamma^2 E_x = 0 \quad \text{where} \quad \gamma = \pm j\omega\sqrt{\mu\epsilon}\sqrt{1 - j\frac{\sigma}{\omega\epsilon}} \tag{5.4}$$

where $E_x = \mathbf{E}.\mathbf{e}_x$. The solution of this second order differential equation is well known : $E_x(z) = E^+e^{-\gamma z} + E^-e^{\gamma z}$. The real part of γ describes the exponential attenuation of the electromagnetic waves due to the losses, and its imaginary part is the wave number. Losses due to the medium can be included in the definition of a complex dielectric permittivity $\epsilon = \epsilon' - j\epsilon''$ where the imaginary part describes the dissipative part. With this notation (5.4) becomes

$$\gamma = j\omega\sqrt{\mu\epsilon'(1 - j\tan\delta)} \quad \text{where} \quad \tan\delta = \frac{\omega\epsilon'' + \sigma}{\omega\epsilon'} = \frac{\epsilon'' + \sigma/\omega}{\epsilon'} \tag{5.5}$$

In order to send microwave signals to the sample, we need to guide the propagation of the electromagnetic wave. This is achieved by using coaxial cables in the refrigerator, which are connected at the base temperature to a 2D waveguide made in a printed circuit board that hosts the sample.

1. $\mathcal{E}$ is the time dependent electric field.

5.1.2 Terminated lossless transmission line

The transport of a TEM electromagnetic wave through coaxial lines is described by the telegrapher equation which is presented in Appendix C. In this geometry, the system can be modeled by a 1D line (see fig. 5.1). Along the z direction, the voltage between the two conductors and the current can be written as the sums of the incident and reflected waves

$$V(z) = V_0^+ e^{-j\beta z} + V_0^- e^{j\beta z} \tag{5.6}$$

$$I(z) = I_0^+ e^{-j\beta z} - I_0^- e^{j\beta z} \tag{5.7}$$

We introduce a characteristic impedance $Z_0 = V_0^+/I_0^+$. In the case of a coaxial line, this characteristic impedance reads

$$Z_0 = \frac{V_0^+}{I_0^+} = \frac{E_\rho \ln(b/a)}{2\pi H_\phi} = \sqrt{\frac{\mu}{\epsilon}}\frac{\ln(b/a)}{2\pi} \tag{5.8}$$

where a and b are the radius of the external and internal conductors respectively as indicated on figure 5.1(a).

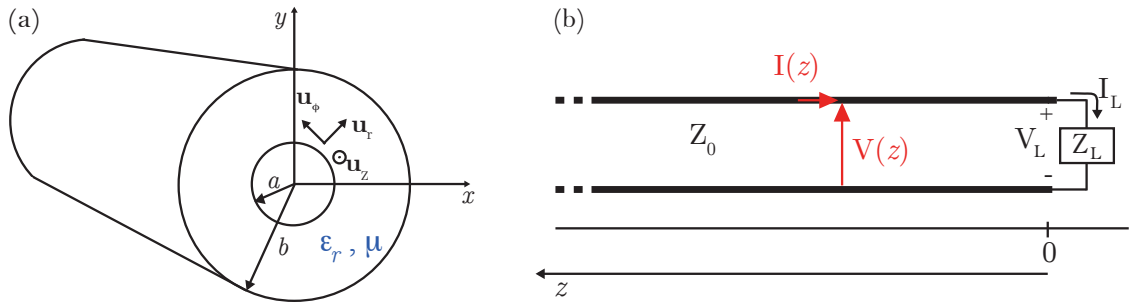

Figure 5.1 – (a) Coaxial cable geometry with an inner radius a and outer radius b. The two conducting cylinders are separated by a material with a dielectric constant ε_r and a permeability μ. (b) Schematic of a terminated lossless transmission line in a 1D model. A voltage $V(z)$ and a current $I(z)$ can be locally defined.

We now consider the case of a transmission line terminated by a load of impedance Z_L at $z = 0$ (see fig. 5.1(b)). The wave is partially reflected since the effective medium suddenly changes. At z=0, the ratio between the voltage and current is imposed by Z_L

$$Z_L = \frac{V(0)}{I(0)} = \frac{V_0^+ + V_0^-}{V_0^+ - V_0^-} Z_0 \tag{5.9}$$

The reflection coefficient $\Gamma_L = V_0^-/V_0^+$ can be easily calculated from (5.9)

$$\Gamma_L = \frac{Z_L - Z_0}{Z_L + Z_0} \tag{5.10}$$

This is a complex quantity whose real and imaginary parts, or alternatively amplitude and phase, can be directly measured with a Vector Network Analyzer (VNA). When $|\Gamma_L| = 1$, corresponding to Z_L=0 (short) or $Z_L = \infty$ (open), the wave is entirely reflected. For a matched

impedance ($Z_L = Z_0$) all the power is absorbed into the load. With a perfect knowledge of the line impedance, it is possible to measure the frequency dependence of Z_L from the reflection coefficient Γ_L. Unfortunately, parasitic capacitances and impedance mismatches between the different components of a circuit (amplifier, directional coupler, bias Tee...) make this determination difficult. Between each component of a RF circuit, waves can be partially reflected creating complicated interference patterns. Losses through the transmission line also contribute to a frequency dependent decrease of the power along the lines. The problem is usually circumvented by doing a calibration of the lines using three different loads.

5.2 Resonant sample circuit for complex conductance measurement

The microwave set-up designed for this experiment is shown on figure 2.12 and has been introduced in details in chapter 2 section 2.2.3.1. A directional coupler allows sending the microwave signal from port 1 to the sample circuit through a bias-tee, and separating the reflected signal which is amplified by a low-noise cryogenic HEMT amplifier before reaching port 2. In the first part of this section, we describe the resonant sample circuit which involves the LAO/STO heterostructures and Surface Mounted Devices (SMD). In the second part we introduce the calibration method and apply it to the normal state data.

5.2.1 Sample circuit

The sample is placed at the end of a CPW line (coplanar wave guide) whose characteristic impedance was chosen to be 50 Ω to match the impedance of the cable (fig. 5.2). This geometry is convenient as it allows connecting SMD (surface mounted device) components and bringing the RF signal to the sample in a controlled way. One can easily solder them since the ground is available all along the central line. Such planar wave guide provide a quasi-TEM transport [87]. Hence, the theory developed in the previous section is applicable to our setup. The dimensions of the central line were chosen to be close to the sample size (S=3mm). Given the dielectric constant of the PCB $\epsilon_r = 10.7$ and the characteristic impedance $Z_0 = 50\Omega$, there is only one set of parameters that satisfies all the conditions (see fig. 5.2). The wide central line and the large gap between the central line and the ground guarantee that the intrinsic capacitance and inductance of the CPW line are negligible compared to those of the SMD and the sample.

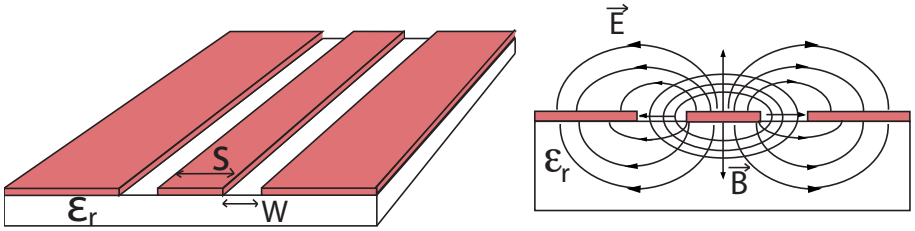

Figure 5.2 – (Left) CPW line : $\epsilon_r = 11$, S=3 mm and W=1 mm. (Right) quasi-TEM mode.

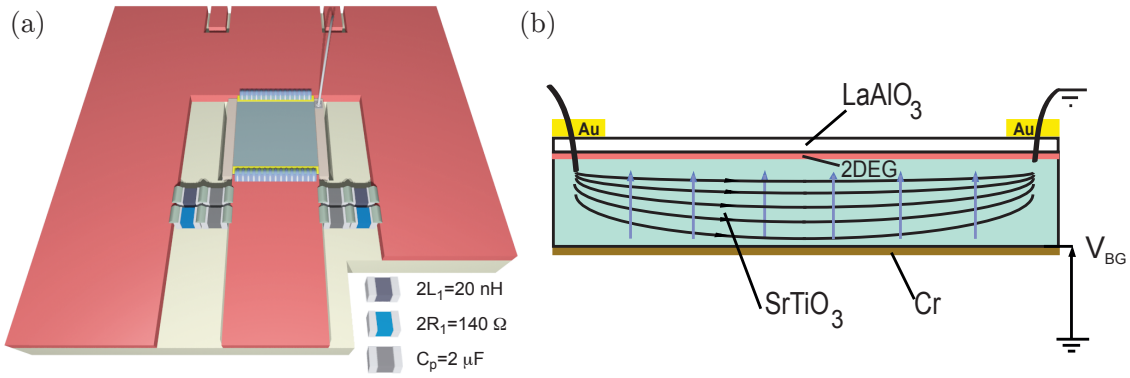

Figure 5.3 – (a) Schematic of the LAO/STO sample embeded in a RLC circuit with SMD components. (b) Cross section of the LAO/STO sample.

Figure 5.3 (a) shows how the CPW line is terminated. The LAO/STO heterostructure is inserted between the central line and the ground of the CPW. One thin strip of gold is deposited on each side of the sample through which many wirebonds connect electrically the 2DEG to the rest of the circuit. The combination of the gold strips (capacitive coupling) and the bondings (resistive coupling) ensures that the contacts impedance is much lower than 1 Ω in the range of frequency considered here (from DC to 0.6 GHz). After the growth, a weakly conducting metallic back gate of resistance 100 kΩ (to avoid a microwave shortcut of the 2DEG) was deposited on the backside of the 100 μm thick $SrTiO_3$ substrate. The sample is glued on a MgO substrate with an electrically insulating varnish (GE varnish) that ensures a good thermalization of the sample. Cooling also occurs through the ground of the CPW which is strongly thermalized.

The high dielectric constant of the $SrTiO_3$ substrate at low temperature (i.e. $\varepsilon_{STO} \simeq 23000$) generates a sizable capacitance C_{STO} in parallel with the 2DEG (fig.5.3 (b)). At the frequencies considered here (0.3-0.6 GHz), the corresponding impedance can be of the same order of magnitude or even lower that the impedance of the 2DEG (including in the superconducting state). This leads to a paradoxical situation where for frequencies higher than 1 GHz, the AC current circulates mainly in the insulating STO and not in the superconducting 2DEG. In addition, as the dielectric constant of STO depends on the electric field, the value of the capacitance depends on the applied gate voltage [2]. This capacitance must therefore be correctly measured and subtracted in order to extract correctly the dynamic transport properties of the 2DEG.

This problem can be overcome by embedding the $LaAlO_3/SrTiO_3$ heterostructure in an RLC resonating circuit which inductor $L_1 = 10$ nH and resistor $R_1 = 70$ Ω are Surface Mounted microwave Devices (SMD), and which capacitor C_{STO} is the STO substrate in parallel with the 2DEG (fig. 5.3 (b)). In order to balance the circuit in the CPW geometry, we chose to use one inductor and one resistor on each side of the central line. We also placed large protective

2. As seen in figure 5.3 (b), the RF electric field is mostly parallel to the interface (100), whereas the static electric field created by the gate is perpendicular (001). Despite this unusual orientation, the in-plane dielectric constant is still slightly gate-dependent [23].

capacitors C_p that prevent DC current from flowing through L_1 and R_1 without influencing the microwave response of the circuit. Figure 5.4 shows the equivalent electrical circuit where the SMD part is separated from the sample part. G_{STO} represents the losses of the STO substrates that are discussed in appendix C.2. Given that the circuit is much smaller than the wavelength $\lambda = c/f$ of TEM waves, circuit theory is sufficient to model it. In the normal state, the 2DEG can be described by a simple resistor (in the limit $f << 1/\tau_e$) in parallel with the capacitance of STO and the SMD. This defines a RLC circuit whose resonant frequency is given by $f_0 = \frac{1}{2\pi\sqrt{LC}}$. In practice, f_0 is in the frequency range 0.3-0.6 GHz, depending on the temperature and the gate voltage.

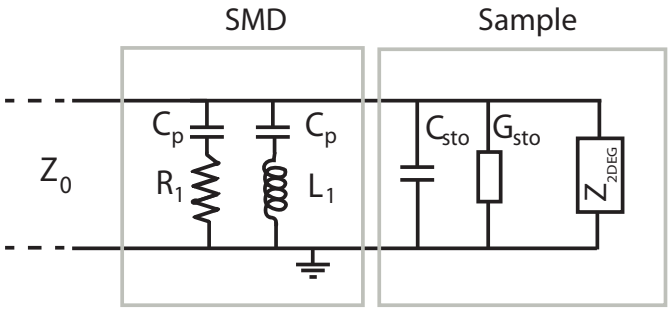

Figure 5.4 – Equivalent circuit of the resonant sample circuit. $R_1 = 70\ \Omega$ and $L_1 = 10$ nH are obtained by two balanced SMD resistors and SMD inductors. $C_p = 2\ \mu$F are protective SMD capacitors. C_{STO} and G_{STO} represent the capacitance and the losses of STO substrate in parallele with the impedance of the 2DEG (Z_{2DEG}).

SMD were first tested in different circuits to ensure that their properties were not affected at low temperature. The total complex conductance $G_L = 1/Z_L$ of the circuit in the normal state is

$$G_L = \frac{1}{j\omega L_1} + j\omega C_{STO} + \underbrace{\frac{1}{R_1} + \frac{1}{R_s} + G_{STO}}_{G_{tot}} \tag{5.11}$$

Much below f_0, the system is dominated by the inductance $Z_L = j\omega L_1$. Well above the resonance frequency the current circulates mainly in the STO substrate with an impedance $Z_C = 1/j\omega C_{STO}$. At the resonance frequency, the RLC circuit behaves as a pure resistor because the inductive and capacitive contributions compensate each other. From the expression of the reflection coefficient in equation (5.10), we can calculate the electrodynamical response of our system of impedance $Z_L = 1/G_L$. Figure 5.5 shows the theoretical reflection coefficient for a RLC circuit corresponding to our experimental situation. The resistance R_1 of 70 Ω was chosen in order to ensure that the total resistance of the circuit $1/G_{tot}$ (including G_{STO} and R_s) remained always close to 50 Ω. At $f \simeq f_0$, the circuit load is therefore almost matched to Z_0 and the energy is absorbed in the sample circuit. As a result, an absorption dip is observed in the amplitude of Γ_L. The resonance is also associated to a 2π phase shift. We see that f_0 can be clearly evidenced both in the modulus and phase of the reflection coefficient. This will allow us to determine unambiguously the value of C_{STO} as a function of gate voltage.

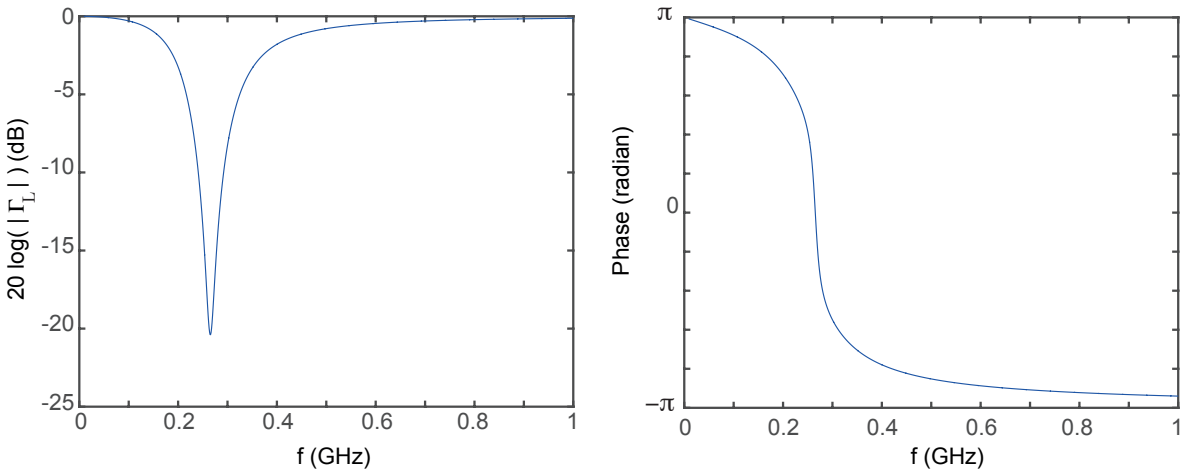

Figure 5.5 – Amplitude and phase of Γ_L for $L_1 = 10$ nH, $C_{STO} = 36$ nF, $R_1 = 70\ \Omega$ and $R_s = 449\ \Omega$ (STO losses are neglected here).

5.2.2 Calibration of the microwave setup

So far, we have only considered the reflection coefficient Γ_L at the discontinuity between the CPW line and the sample circuit. However, this quantity is not directly accessible experimentally since the signals are sent and measured from outside the cryostat. We therefore need to relate the transmission coefficient Γ_{in} between port 1 and 2 measured with the VNA to the reflection coefficient Γ_L. This is done through a calibration procedure.

5.2.2.1 Scattering matrix

Any N-ports network can be completely defined by its scattering matrix S, whose coefficients S_{ij} relate the incoming wave at port i to the outgoing wave at port j, when the other ports are terminated by a matched load. This matrix S is defined by

$$S_{ij} = \left.\frac{V_i^-}{V_j^+}\right|_{V_k^+=0 \text{ for } k\neq j} \tag{5.12}$$

A reciprocal network is described by a symmetric scattering matrix $S = S^t$ [87]. A lossless network will have a unitary matrix $S.S^{*t} = 1$. Rather than voltage or current, RF signals are usually described by the ingoing and outgoing power waves that are respectively defined as :

$$a_i = \frac{V_i^+}{\sqrt{Z_0}} \tag{5.13}$$

$$b_i = \frac{V_i^-}{\sqrt{Z_0}} \tag{5.14}$$

with these definitions, the power delivered to the load is $\mathrm{Re}\{VI^*\} = 1/2(|a|^2 - |b|^2)$. With these notations, the reflection coefficient Γ_i at port i is given by

$$\Gamma_i = \frac{b_i}{a_i} \tag{5.15}$$

5.2.2.2 Calibration method

A simplified version of the RF set-up introduced in chapter 2 is shown in figure 5.6 (a). It can be described within the scattering matrix formalism as represented in figure 5.6 (b). The vector network analyzer measures the reflection coefficient $\Gamma_{in} = b_3/a_1$. α, β, γ et δ represent the complex transmission and reflection coefficients in the circuit. They satify the following relations[3]:

$$a_3 = \delta b_3 + \alpha a_1 \tag{5.16}$$

$$b_2 = \gamma a_1 + \beta b_3 \tag{5.17}$$

Solving these two equations, we obtain the relation between $\Gamma_L = b_3/a_3$ and $\Gamma_{\text{in}} = b_3/a_1$

$$\Gamma_{in} = \gamma + \frac{\overbrace{\alpha\beta}^{\tilde{\alpha}}\,\Gamma_L}{1 - \delta\Gamma_L} \tag{5.18}$$

We see that Γ_L is related to the Γ_{in} coefficient measured with the VNA through three coefficients ($\tilde{\alpha} = \alpha\beta$, δ and γ). Therefore, a calibration procedure requires measurements at three known impedances of Z_L^i (and therefore known values of Γ_L^i) to obtain these three coefficients.

In a standard microwave experiment, an open, a short and a match standard are usually employed for the calibration. In practice, changing loads at low temperature is far from easy. Indeed, it is nearly impossible to reproduce the exact same experimental configuration from one run to another. High frequency waves are sensitive to tiny details, such as the tightening of RF connectors, or the presence of wire bondings. A calibration at 300K is not possible, since the properties of the RF set-up varies with the temperature (losses of lines and RF components, gain of the amplifier....)

Instead of using different loads, we took advantage of the temperature and gate dependence of the LAO/STO properties. The microwave set-up was calibrated by using the impedances of the sample circuit at three different gate voltage or alternatively at three different temperature values. The first method is used to fully calibrate the setup at 500 mK and obtain the capacitance of STO as a function of gate voltage. The second method is used to extract the temperature dependence of the 2DEG conductance in the superconducting state.

3. A generalization of this result in any RF system is given by the signal flow graph theory [87].

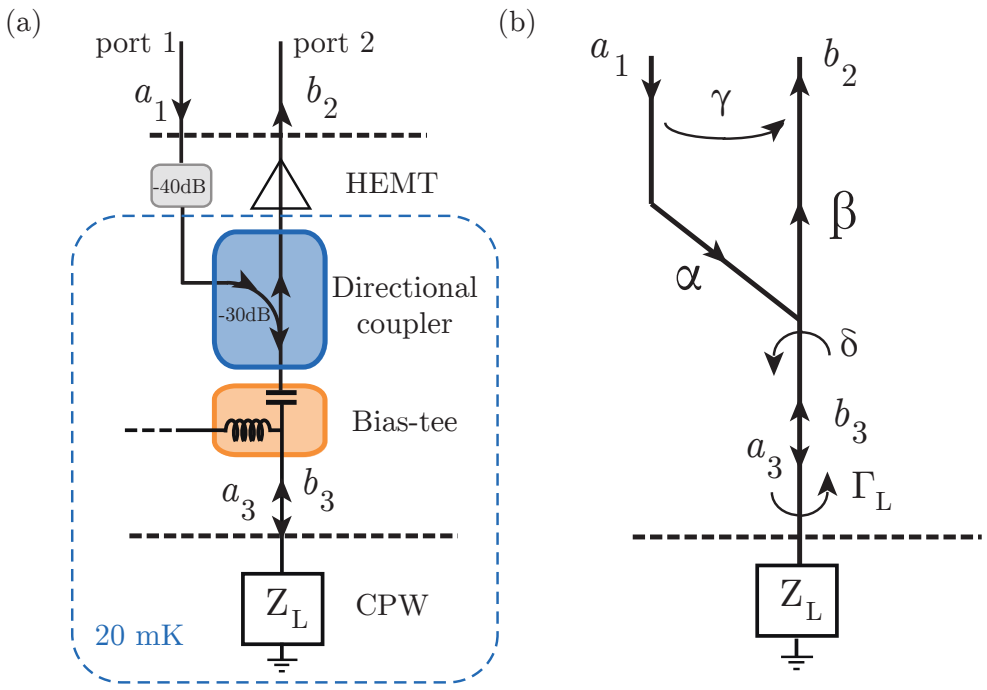

Figure 5.6 – (a) Schematic of the experimental setup. (b) Schematic representing the complex wave amplitudes at different locations in the set-up. α, β, γ, δ represent the various reflection and transmission coefficients.

5.2.2.3 Calibration in the normal state

We first record the complex coefficient $\Gamma_{in}(\omega)$ as a function of frequency for three different gate values corresponding to three well separated resonance frequencies. The absorption dip in the amplitude can be identifed clearly from the raw data (see fig. 5.7). As the value of the inductance L_1 is known, the resonance frequency gives directly the value of C_{STO}. In addition, as the 2DEG resistance R_s is obtained from dc transport measurements, the only missing quantity in equation (5.11) is G_{STO} that accounts for the losses in the substrate. However, it can be determined for each gate value from the amplitude of the absorption dip at the resonance frequency [4]. Once the value of Z_L is known for three different data points, we obtain the error coefficients ($\tilde{\alpha}$, δ and γ) from expression (5.18). The relation is then inverted to obtain Γ_L as a function of the measured Γ_{in} coefficient for any gate value

$$\Gamma_L = \frac{\gamma - \Gamma_{in}}{\delta(\gamma - \Gamma_{in}) - \tilde{\alpha}} \tag{5.19}$$

where $\tilde{\alpha} = \alpha\beta$. Such a calibration procedure is only valid in the range of frequency covered by the three calibrating points. Figure 5.7 shows the comparison between the raw data (Γ_{in}) and the calibrated data (Γ_L) for the same gate value ($V_{BG} = 50$ V) in the normal state.

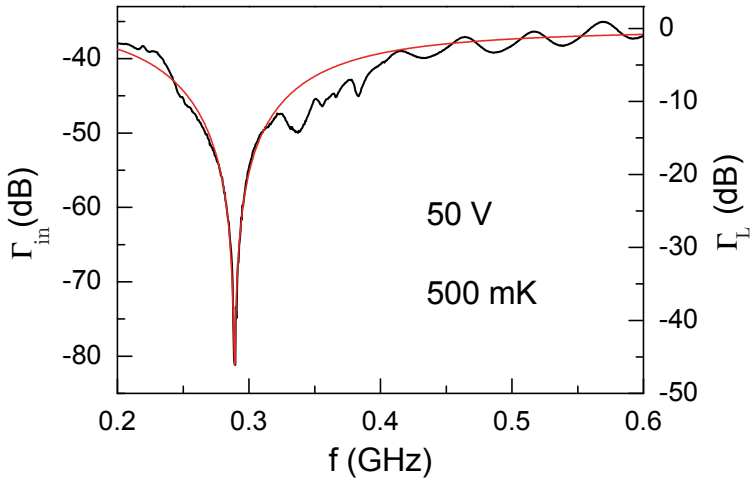

Figure 5.7 – Comparison at $V_{BG} = 50$ V and $T = 500$ mK, between the amplitude (in dB) of the measured reffection coefficient Γ_{in} (black, left axis) and the coefficient Γ_L (red, right axis) imposed in the calibration.

The calibration procedure was applied to obtain all the data measured in the normal state at $T = 500$ mK after a first positive polarization at a maximum gate value of 50 V. Note that, as the STO substrate is thinner in this experiment (nominally 100 μm) than in a standard back-gating experiment (500 μm), we used a reduced gate range [-34V,50V] to obtain a similar

4. In practice, it is deduced from the fit of the amplitude and phase of the Γ_{in} coefficient by the theoretical reflection coefficient of a RLC circuit.

carrier density modulation. Figure 5.8 (a) shows on a color scale the evolution of the amplitude of Γ_L (after calibration) as a function of frequency and gate voltage while figure 5.8 (b) shows the amplitude and phase of the resonance at $V_{BG} = +24$ V. C_{STO} extracted from the resonance frequency f_0, decreases with gate voltage, with a symmetry around zero (fig. 5.8 (c)).

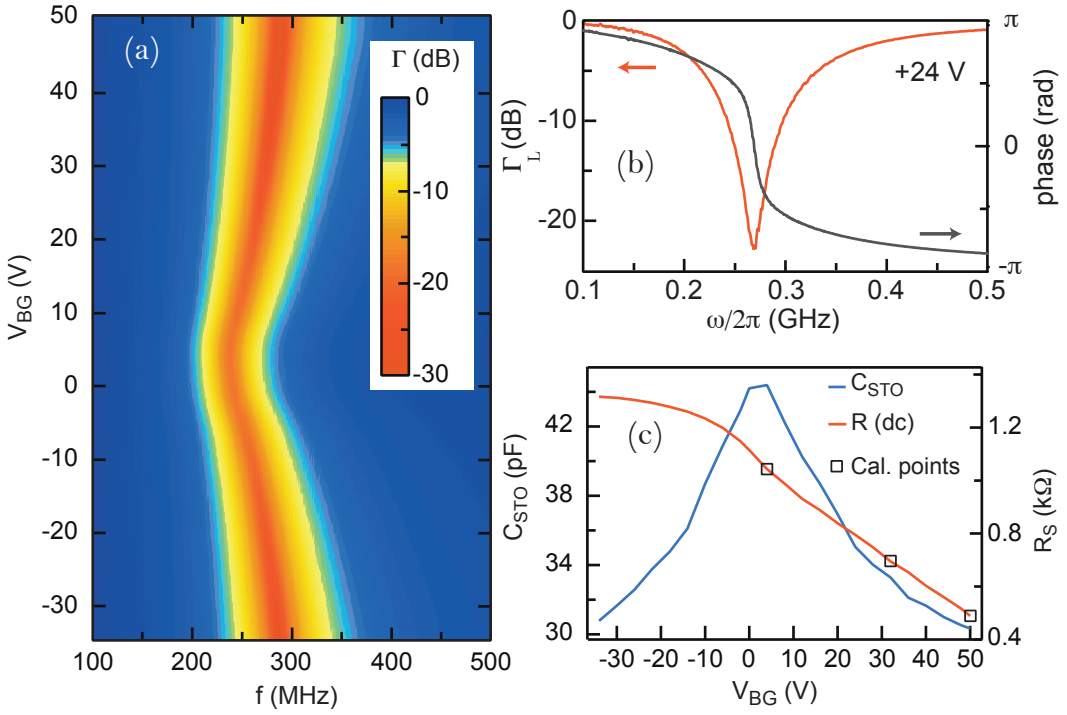

Figure 5.8 – Field effect tuning of capacitance : (a) color plot representing the reflection coefficient Γ_L in dB as a function of frequency and gate voltages at 500mK. On figure (b) the amplitude and phase at $V_{BG} = 24$ V. (c) Capacitance and 2DEG resistance as a function of gate voltage.

5.3 $LaAlO_3/SrTiO_3$ complex conductance

After having applied the calibration method to the normal state data, we now present the measurement of the complex impedance of the 2DEG in the superconducting state. In the first part of this section, we determine the superfluid stiffness of the 2DEG as a function of gate voltage and compare it with the BCS theory prediction. In the second part, we convert the superfluid stiffness into a superfluid density and discuss it within the interfacial band structure. Finally, we analyze the temperature dependence of both the real and imaginary parts of the complex conductance.

5.3.1 Superfluid Stiffness

5.3.1.1 Resonance shift

In the superconducting state the total conductance of the circuit is given by :

$$G_L = \frac{1}{j\omega L_1} + j\omega C_{STO} + \frac{1}{R_1} + \sigma(\omega, T) + G_{STO} \tag{5.20}$$

$$= \frac{1}{j\omega L_1} + j\omega C_{STO} - j\sigma_2(\omega, T) + \frac{1}{R_1} + \sigma_1(\omega, T) + G_{STO} \tag{5.21}$$

where σ_1 and $\sigma_2 = 1/\omega L_k$ are the real and imaginary part of the 2DEG complex conductance, and L_k is its kinetic inductance (cf equation (4.5)).

We measured the frequency-dependent reflection coefficient Γ_L as a function of gate voltage and temperature. The VNA imput power was set to -14bBm corresponding to approximately 0.04 mW. Taking into account the attenuation of all the cables, the coupling factor of the directionnal coupler and the various impedances of the sample circuit, the typical current flowing into the 2DEG is in the range 1-5 nA which is much lower than the superconducting critical current ($I_c = 5\ \mu$A).

When the sample is cooled below T_c, a shift in the resonance frequency is expected because of the inductive behavior of the superconductor :

$$L_{tot}(T) = \frac{L_1 L_k(T)}{L_1 + L_k(T)} \tag{5.22}$$

This decrease of the total inductance L_{tot} leads to a shift of the resonance frequency $f_0 = 1/\sqrt{L_{tot}C_{STO}}$ toward higher values. The same calibration procedure described in the previous section for the normal state can be applied to the data. However, as in the superconducting state, the resonance frequencies span a range which is wider that in the normal state, the calibration may be inaccurate for some gate values. Instead, we used here the impedance of the circuit at three different temperatures for the calibration at each gate voltage. The value of C_{STO} is known from the normal state calibration and the total inductance of the circuit is determined from the resonance frequency. The dissipative part G_{tot} is inferred from the absorption dip like for the normal state calibration. However, while in the normal state the resistance of the 2DEG could be determined from DC measurement, in the superconducting state σ_1 is unknown. Nevertheless,

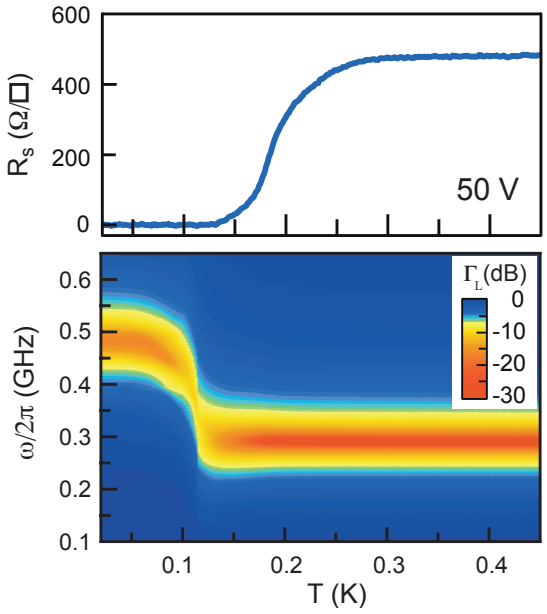

Figure 5.9 – (Upper panel) DC resistance as a function of temperature in the overdoped region $V_{BG} = 50$ V. (Lower panel) The corresponding modulus of the reflection coefficient $|\Gamma_L|$ as a function of temperature and frequency after calibration.

we will see in the last section of this chapter that σ_1 can still be qualitatively determined by making reasonable assumptions on the frequency dependence of STO losses (G_{STO}). Figure 5.9 shows simultaneously the DC and the calibrated RF measurement of the superconducting transition as a function of temperature for $V_{BG} = 50$ V. A clear shift of the resonance frequency is observed which allows the determination of L_k or equivalently, σ_2. On the contrary, in the absence of superconductivity (for $V_{BG} < 0$) no shift is observed.

From the inductive part of the complex impedance $\sigma_2(\omega) = 1/\omega L_k$, we can deduce an experimental value of the superfluid stiffness (chapter 4 section 4.2.2) :

$$J_s^{exp} = \frac{\hbar^2}{4e^2 L_k} \tag{5.23}$$

In the previous chapter, we derived the superfluid response of a BCS superconductor as a function of temperature (equation (C.30)). For a single band BCS superconductor in the dirty limit ($2\Delta < \hbar/\tau_e$)

$$J_s(T \simeq 0) = \frac{R_0}{R_n}\frac{\Delta(T \simeq 0)}{4} \tag{5.24}$$

where $R_n = R(T \geq T_c)$ is the normal state resistance and $R_0 = h/e^2 = 25.813$ kΩ. At the lowest temperature ($T \simeq 20$ mK) we can compare the theoretical stiffness given by equation (5.24) and the values obtained by our resonant technique.

5.3.1.2 Gate dependence

The figure 5.10 upper panel shows the superfluid stiffness and critical temperature measured as a function of the back gate voltage. T_c is defined by the temperature where the DC resistance

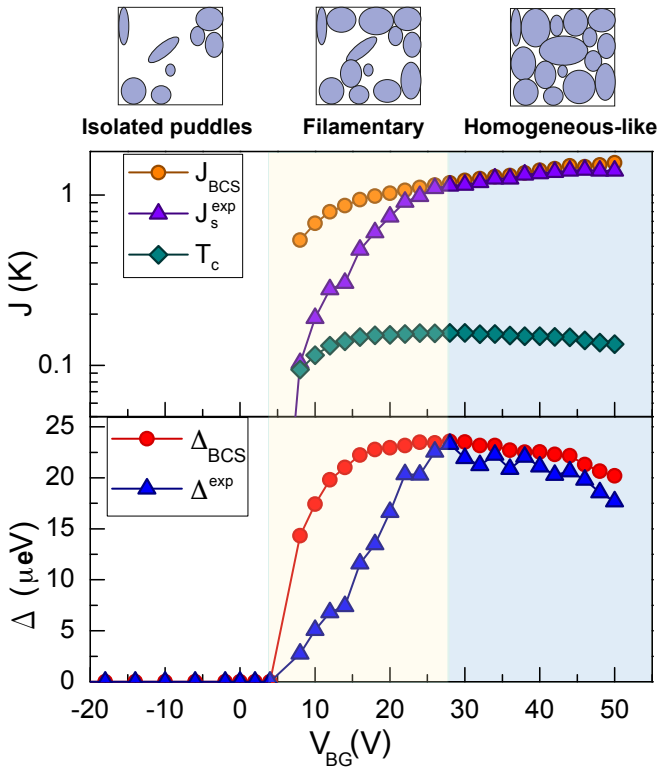

Figure 5.10 – (Upper panel) Experimental superfluid stiffness J_s^{exp} compared with the BCS prediction J_{BCS} expressed in Kelvin units. (Lower panel) Gap energy Δ_{ex} converted from J_s^{exp} (eq. (5.24)) compared with the BCS gap energy $\Delta = 1.76 k_B T_c$ where T_c corresponds to $R_s = 0$.

R_s reaches zero. In the overdoped region (above the optimal doping gate voltage $V_{BG} = 27$ V) the experimental data (J_s^{exp}) coincide with the dirty BCS estimate (J_{BCS}) assuming a simple BCS gap energy $\Delta(T \simeq 0) = \Delta_{BCS} = 1.76 k_B T_c$ in equation (5.24). In this region, the superfluid stiffness is much higher than the gap energy as expected for a homogeneous superconductor in the BCS limit. On the underdoped side, the superfluid stiffness J_s^{exp} drops significantly while T_c and J_{BCS} evolve smoothly before vanishing only when closely approaching the quantum critical point where T_c =0 (V_{BG} = 4V). This indicates that the global phase coherence of the superconducting condensate is partially lost in the 2DEG. Such behavior is likely due to strong phase fluctuations in presence of spatial inhomogeneities. As discussed in chapter 1, the 2DEG behaves like a disordered array of superconducting islands coupled by Josephson effect [79, 46]. Starting from a well connected 2D array of Josephson junctions in the overdoped region (homogeneous-like), the depletion of the 2DEG progressively decouples the superconducting islands. On the one hand, a T_c can be measured in DC transport as far as a percolating path allows the superconducting current to flow between the two sides of the samples. On the other hand, the superfluid stiffness obtained through RF measurement gives a macroscopic response of a less and less rigid network of superconducting puddles.

Using equation (5.24) we can convert the stiffness into a characteristic gap energy Δ^{exp} which we compare with the BCS gap $\Delta = 1.76 k_B T_c$ obtained from the critical temperature. Interestingly, the gap is following the T_c dome while the superfluid stiffness in monotonic when

the number of carriers increases. In the overdoped region, the agreement with the BCS theory implies that T_c is controlled by the pairing energy, while in the underdoped region, T_c seems to be dominated by phase fluctuations enhanced by the disappearance of the superconducting islands. In the optimally doped region, the gap energy is $\Delta^{exp} = 23\ \mu$eV. By using tunneling spectroscopy on planar $Au/LaAlO_3/SrTiO_3$ junctions, Richter et al. have reported an energy gap in the density of states of 40 μeV for optimally doped $LaAlO_3/SrTiO_3$ interfaces [69], which, taking into account their T_c, corresponds to $\Delta \simeq 1.76 k_B T_c$ in agreement with our results. However, the tunneling gap was found to increase in the UD regime, which is different from the behaviour we reported here. This apparent contradiction with our results can be reconciled by the fact that contrary to superfluid stiffness that probes the global phase coherence of the superconducting state, tunneling experiments measure a one-particle density of state which is not sensitive to phase coherence.

5.3.2 Superfluid density and band structure

One of the main challenges that need to be addressed in order to elucidate superconductivity in the LAO/STO interface is to understand the role of the occupancy of the different bands. Figure 5.11 shows a schematic of the band structure in the confinement well. At low carrier densities, we expect several d_{xy} sub-bands to be populated, whereas at higher densities ($V_{BG} > 0$ V), the Fermi energy should enter into the $d_{xz/yz}$ bands. The emergence of superconductivity at an intermediate carrier density ($V_{BG} \simeq 0$ V) naturally suggests that it could be intrinsically related to the filling of the $d_{xz/yz}$ bands. In addition, Biscaras et al. [97] noticed that the appearance of high-mobility carriers leading to a multiband Hall effect was concomitant with the emergence of superconductivity. The presence of high-mobility carriers was recently confirmed by quantum oscillations at high magnetic field. The in-plane mass was found to be $m_t = 1.9 \times m_e$ which is close to the in-plane mass of the $d_{xz/yz}$ bands. It is therefore crucial to compare the superfluid density extracted from RF experimental data and the carrier density measured by Hall effect.

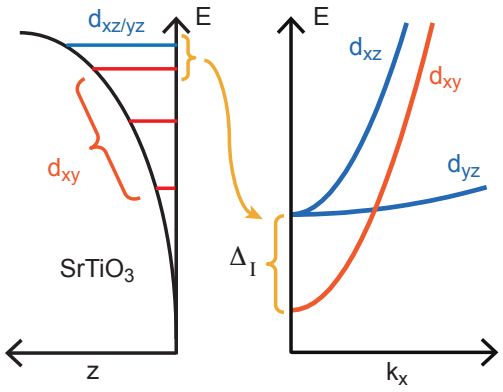

Figure 5.11 – The energy levels due to the confinement in the z direction are represented on the left. On the right, the corresponding in plane dispersion relation of xy bands and xz/yz bands are represented in red and blue respectively.

We measured the Hall effect for different gate voltages. Whereas the Hall voltage is linear in

magnetic field in the underdoped regime, corresponding to one-band transport, this is not the case in the overdoped regime because of the contribution of high-mobility carriers (fig. 5.12 (a)). Such behaviour has already been discussed in chapter 3 for the Cr doped samples. The Hall carrier density measured in the limit $B \to 0$ shows a sudden decrease when high-mobility carriers are injected by gating. We performed a two-band analysis of the Hall effect data combined with gate capacitance measurements to determine the contribution of the two populations of carriers to the total density n_{tot} [5] (fig. 5.12 (b)). A majority of low mobility carriers (LMC) is always present whatever the gate voltage (green open symbols on fig. 5.12(b)). HMC density n_{HM}, presented on figure 5.12 (c), appears at the same time as superconductivity for $V_{BG} > 0$. HMC represent only 2% of the total carrier density at maximum gating. In consistency with quantum oscillation measurements, we identify LMC and HMC as coming from the d_{xy} and $d_{xz/yz}$ subbands respectively.

The simultaneous appearance of HMC and superconductivity suggests a scenario where, doping with a back gate would progressively fill a new band more prone to host superconductivity. In order to outline the link between HMC and superconductivity, we extract the superfluid density n_s from J_s^{exp} assuming a mass $m_{t,xz/yz} = \sqrt{m_l m_h} = 3.13 \times m_e$ for the electrons.

$$n_s = \frac{4mJ_s}{\hbar^2} \tag{5.25}$$

The result is compared with the HMC density on figure 5.12 (c). n_s increases continuously to reach $n_s^{2D} \simeq 2 \times 10^{12}$ e$^-$.cm^{-2} at $V_{BG} = 50$ V. This is comparable to the density observed by scanning SQUID experiments [139]. The superfluid density and HMC density have the same trend, occur at the same time and almost coincide numerically, suggesting that the emergence of the superconducting phase is indeed related to the filling of $d_{xz/yz}$ bands. This is consistent with the observation of a gate-independent superconductivity in (110) oriented $LaAlO_3/SrTiO_3$ interfaces for which the $d_{xz/yz}$ bands have a lower energy than the d_{xy} subbands and are therefore always filled [82].

From the point of view of superconductivity, the $d_{xz/yz}$ band has three favorable properties. First, their 2D density of state is almost five times larger than the density of d_{xy}. Second, at the top of the potential well the $d_{xz/yz}$ electrons are less confined due to their lower mass in the z-direction (see numerical simulations figure 1.10 in chapter 1). Therefore, they extend deeper in STO where scattering is reduced. Finally, STO slowly recovers its bulk properties far from the interfaces, in particular a high dielectric constant, which, according to most of the scenarii is favorable to superconducting pairing (see chapter 1). A high density of state and a high dielectric constant also tend to enhance superconductivity in a BCS picture. Indeed, the gap energy is enhanced when the DOS at Fermi energy increases as illustrated by the following equation

$$\Delta \propto \omega_D e^{-\frac{1}{N(E_F)V}} \tag{5.26}$$

where ω_D is the Debye frequency, V the attractive interaction and $N(E_F)$ the density of state at the Fermi level [6]. Increasing the gate voltage progressively fills the superconducting

5. For more detail about the fitting procedure, see appendix A
6. See appendix E for more details on BCS theory

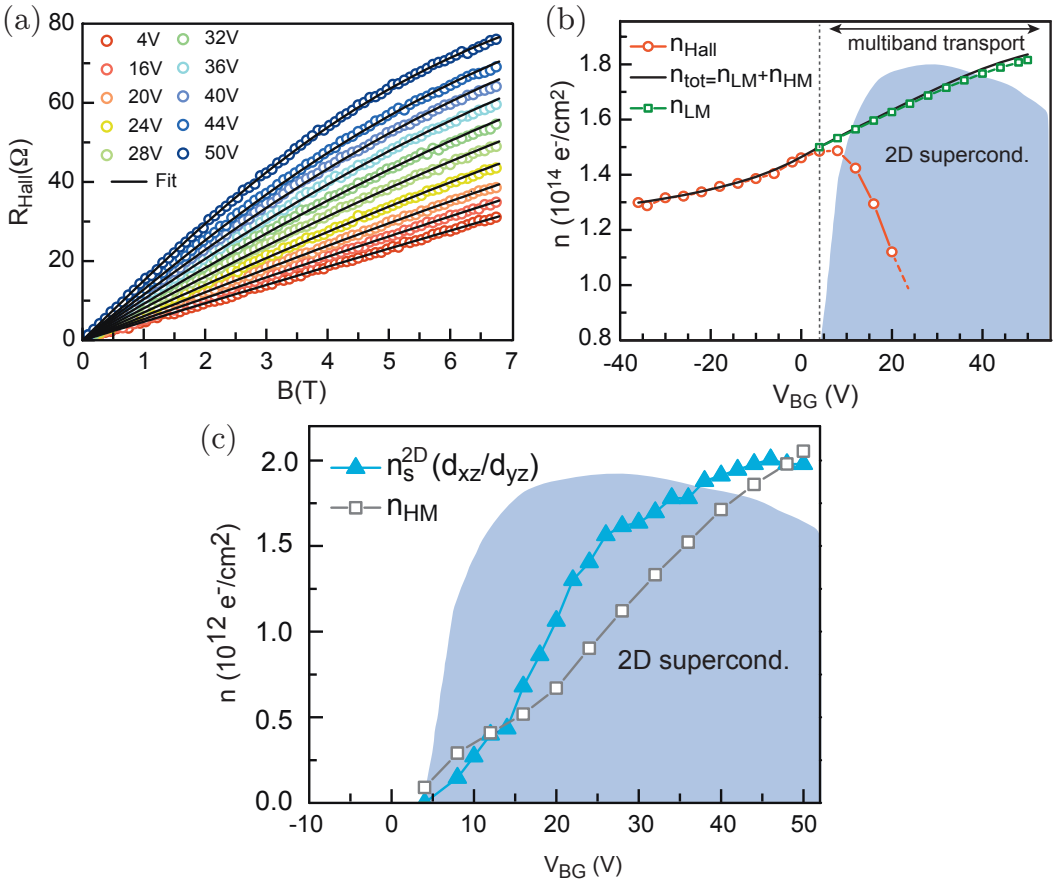

Figure 5.12 – (a) Hall resistance as a function of perpendicular magnetic field for different back gate values measured at $T = 3$K. (b) Hall density of carrier is plotted in red. The sudden fall off is due to apparition of high mobility carriers. The total carrier density n_{tot} is obtained by combining Hall effect and capacitance measurement (see appendix A). The LMC represents the majority of the carriers. (c) Comparison between the density of HMC extracted from the two-carrier analysis and the superfluid density n_s calculated from J_s assuming a mass corresponding to $d_{xz/yz}$ electrons.

band leading to a system with a higher and higher superfluid density. The superconducting state is well defined when the number of electrons in the ground state is large.

To complete this section, we would like to mention that the fact that $n_s = n_{HM}$ is rather intriguing as the dirty limit that we used in Eq. (5.24) implies that n_s should correspond to a fraction of the total normal carrier density (approximately $2\Delta * \tau_e/h$, where τ_e is the scattering time) and not to n_{HM}. To understand such an apparent discrepancy, we need to go beyond single-band superconductor models that cannot account correctly for the unusual t_{2g}-based interfacial band structure of the $LaAlO_3/SrTiO_3$ interfaces. Our theoretician collaborators at La Sapienza university (L. Benfatto, M. Grilli and S. Caprara) are actively working to provide an appropriate framework to address this question.

5.3.3 Temperature dependence of the complex conductance

The study of the superconducting transition in temperature should give us information on the nature of superconductivity. A simple BCS model, or equivalently a Mattis-Bardeen model, is not suitable to describe correctly the superconducting transition. Indeed, in 2D superconductors the transition is expected to belong to the Berezinsky-Kosterlitz-Thouless (BKT) type of phase transitions driven by the dissociation of vortex-antivortex pairs. First, we study qualitatively the DC resistance as a function of temperature. Second, the superfluid stiffness is compared with BCS and BKT predictions and the role of disorder is analyzed. Finally, we describe the temperature dependence of σ_1, in particular the high dissipation peak that occurs near the jump in the superfluid stiffness.

5.3.3.1 R(T) measurement

After a first polarization up to $V_{BG} = 50$ V in the normal state (as described in section 5.2.2.3), a systematic measurement of the complex conductance as a function of back-gate voltage and temperature was performed. Figure 5.13 displays the DC resistance and the amplitude of the reflection coefficient Γ_L as a function of temperature for a selection of gate voltages spaning the whole phase diagram. In the superconducting state the 2DEG conductance leads to a shift of the resonance frequency as described in section 5.3.1.1 (see fig. 5.13 (c,d,e and f)). However, the shift occurs only when a complete transition is observed, indicating that at least one superconducting path percolates. When the DC resistance shows only a partial transition (fig 5.13 (b)), the phase is not rigid over the whole sample and the macroscopic stiffness is zero. A similar behaviour has been observed in granular aluminum films [140]. In the insulating state (fig 5.13 (a)), the resonance frequency is not shifted as expected.

The broad transition observed in the DC resistance at $V_{BG} = 10$ V (fig. 5.13 (c)) indicates the presence of strong inhomogeneities. This is consistent with the measurement of a reduced stiffness at $T = 0$ (section 5.3.1.2). Indeed, this gate voltage corresponds to the underdoped region of the phase diagram where $J_s(0)$ is lower than the BCS estimate because of the presence of non-superconducting regions. As a consequence, the shift of the resonance is very weak, while the critical temperature remains higher than 100mK. On the contrary, at optimal doping corresponding to $V_{BG} = 24$ V (fig. 5.13 (e)), the transition is sharper and a clear shift of the resonance occurs. However, it seems that this shift takes place at temperatures lower than T_c. There must therefore be a mechanism that delays the establishment of the macroscopic phase coherence. At the end of the previous chapter, we discussed the effect of Josephson vortices in an array of Josephson junctions. The existence of such a type of excitation could explain this behaviour by setting a second critical temperature T_{KT} above which vortices would start to dissipate. In our case, the nature and the dynamics of the vortices could be explained by the intrinsically inhomogeneous nature of superconductivity. In the following section, we will analyze in details the imaginary part and the real part of the conductance as a function of temperature.

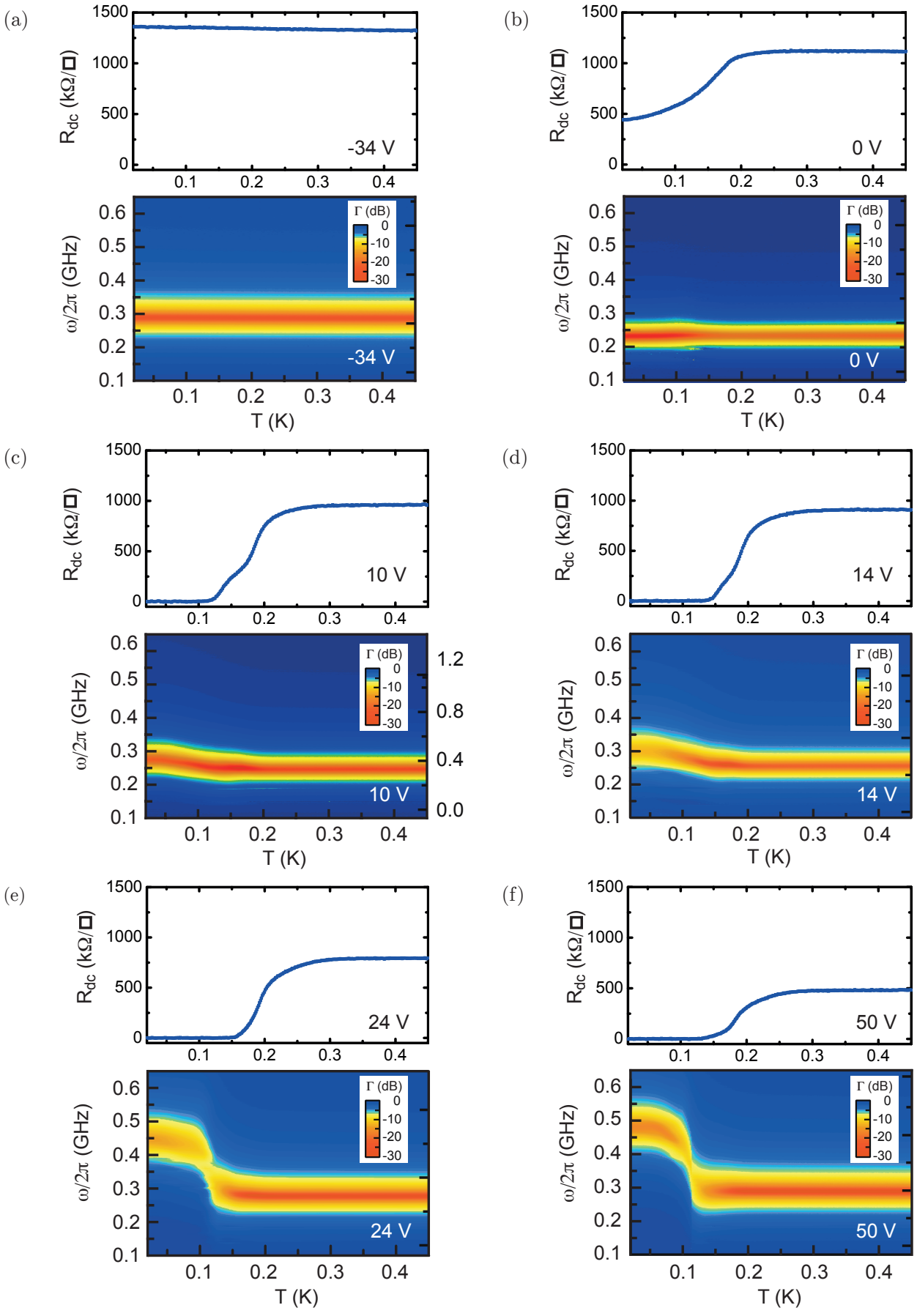

Figure 5.13 – Temperature dependence of the DC resistance and of Γ_L (dB in color scale) as a function of frequency for selected gate voltages.

5.3.3.2 Temperature dependence of J_s

We now compare the temperature dependence of the superfluid stiffness of the LAO/STO interface with the BCS prediction. $J_s(T)$ is determined from the kinetic inductance $L_k(T) = 1/(\sigma_2\omega)$ (eq. (5.24)) which is extracted from the resonance frequency. Figure 5.14 shows the normalized stiffness obtained after calibration, at frequency $f = 500$ MHz and for a gate voltage $V_{BG} = 50$ V. It is fitted by the BCS expression [115]

$$\frac{J_s(T)}{J_s(0)} = \frac{\Delta(T)}{\Delta(0)}\tanh\left(\frac{\Delta(T)}{2k_BT}\right) \quad \text{with} \quad \Delta(T) \simeq \Delta(0)\tanh\left(1.74\sqrt{\frac{T_c}{T}-1}\right) \tag{5.27}$$

A good agreement between experimental data and equation (5.27) is obtained for the low temperature part of the curve. At $T = T_{KT} \simeq 110$ mK, a clear jump of J_s occurs whereas the BCS fit indicates a mean field T_c of $\simeq 150$ mK. Such a jump is usually the hallmark of a Kosterlitz-Thouless transition. This type of transition is expected to take place at the temperature of vortex-antivortex dissociation which is given by $J_s = 2k_BT_{KT}/\pi$ (i.e. the point of intersection between $J_s(T)$ and a straight line with a slope of $2k_BT/\pi$) as shown in the previous chapter (eq. (4.29)). As indicated in figure 5.14 T_{KT} defined by the intersection with the slope $2k_BT/\pi$ is close to the temperature where the DC resistance reaches zero but is, however, significantly higher than T_{KT} defined by the jump.

The presence of inhomogeneities could explain such a discrepancy. When the temperature is decreased, puddles switches to the superconducting state at different temperatures. At $T = 130$ mK, the connectivity between puddles allows the supercurrent to percolate in the sample and zero resistance is observed in DC transport. However, this simple path is not sufficient to confer a finite superfluid stiffness to the 2DEG. When the temperature is further reduced, the number of superconducting puddles increases connectivity, leading to a sudden jump in Js. As seen in the previous section, at $T = 0$, the 2DEG recovers the stiffness predicted by the BCS theory (for the overdoped regime only).

5.3.3.3 Temperature dependence of σ_1

In the previous chapter, we described the peculiar dynamics of Josephson vortices. As opposed to regular BKT vortices, Josephson vortices are considerably slower. We therefore expect their contribution to the dissipation (i.e. to σ_1) to be significant in LAO/STO interfaces. The temperature dependence of σ_1 can be directly extracted from the real part of the total conductance G_L (eq. (5.21)) entering into the expression of Γ. The main difficulty here consists in subtracting the contribution of STO losses G_{STO}.

STO losses : The losses of STO (G_{STO}) can be extracted in the normal state at the resonance frequency since the other dissipative contributions entering into G_L are $R_1 = 70\ \Omega$ and R_s which is measured by DC transport. In practice, for the calibration of the RF set-up, we assumed that

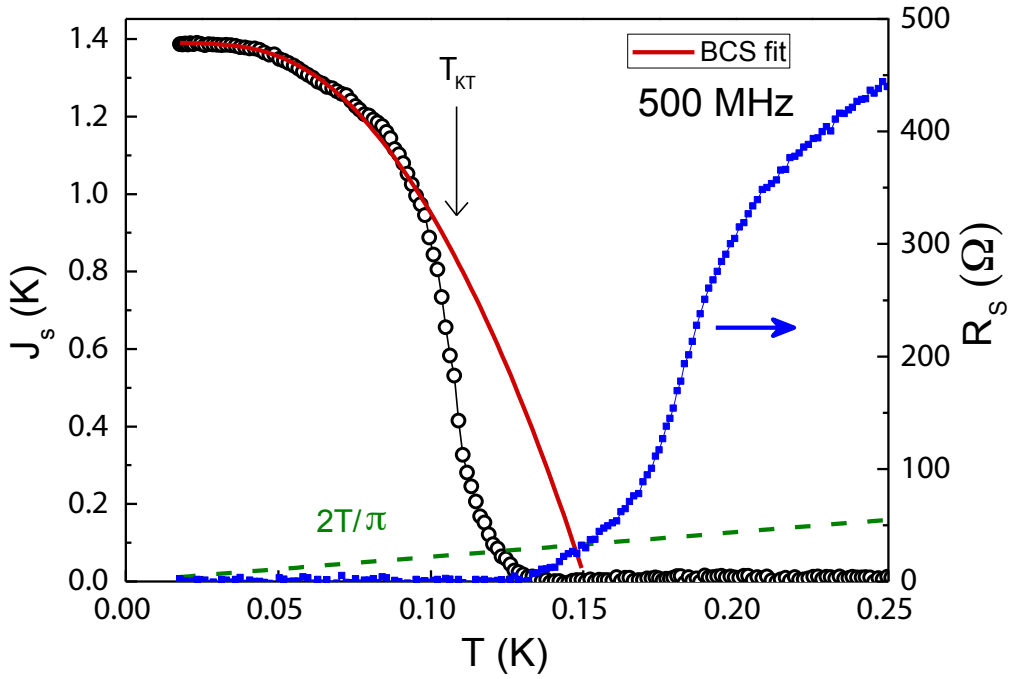

Figure 5.14 – Temperature dependence of $J_s(T)$ at $V_{BG} = 50$ V and f=500MHz.

G_{STO} is frequency independent around f_0 for any given gate value. When the temperature is lowered, this assumption is acceptable as long as the resonance frequency is not shifted (note that, in this temperature range, the properties of STO are temperature independent). However, this is no longer the case when the 2DEG is superconducting as a large shift of f_0 occurs. We therefore need to estimate the frequency dependence of G_{STO} in the range corresponding to $f_0(T = 0\text{K}) - f_0(T = 500\text{mK})$. In appendix C, we derived the losses in STO due to the quasi-Debye mechanism which we assumed to be the only relevant frequency dependent contribution here. We obtained (eq (C.17)) :

$$G_{STO} = A \overbrace{\frac{C_{STO}(0) - C_{STO}(V_{BG})}{C_{STO}(0)}}^{\frac{\Delta C}{C}} C_{STO}(V_{BG}) \overbrace{\frac{1}{L_{tot} C_{STO}(V_{BG})}}^{\omega_0^2} \tag{5.28}$$

$$= A \times \frac{\Delta C}{C} \left(\frac{1}{L_1} + \frac{1}{L_k(T)} \right) \tag{5.29}$$

$$= G_{STO}(T = 500\text{mK}) + A \times \frac{\Delta C}{C} \frac{1}{L_k(T)} \tag{5.30}$$

The value of A can be determined in the normal state for each gate value (see appendix C). We obtain $A = 100 \times 10^{-12}$ Hz^{-1}. The values of C_{STO} are shown on figure 5.8. At $V_{BG} = 50$ V

$$\Delta C/C = (44\text{pF} - 30\text{pF})/44\text{pF} = 0.32 \tag{5.31}$$

σ_1 is therefore obtained from equation (5.21) after substracting the temperature dependent contribution of G_{STO}.

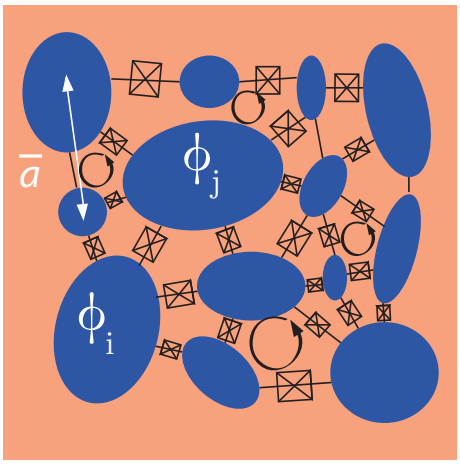

Figure 5.15 – Schematic of the puddles in the overdoped region. $\bar{a}$ is the average distance between puddles. The rounded arrows represents Josephson vortices. The crosses represent Josephson junctions within the RCSJ model. Each puddle has a well defined phase ϕ_i.

Analysis of σ_1 : Figure 5.16 presents the real and imaginary part of the conductance as a function of temperature. A $T = 0$, σ_1 is close to σ_n which is not surprising as we have seen that 98% of the electrons do not condense. It also displays a large peak which maximum value coincides with the jump of the superfluid stiffness at T_{KT}. To explain this behaviour we consider the theory developed in the previous chapter, section 4.3.3. The 2DEG is described by a disorder array of superconducting puddles tightly connected by Josephson effect (see fig. 5.15). In this situation, Josephson vortices take place between puddles and can move from one cell to another. According to equations (4.42), $\sigma_1(\omega, T)$ is maximum when $\epsilon' = \epsilon''$. In this case, we get :

$$\delta_{max}^{-2} = \frac{J}{2d\alpha}\frac{1}{\epsilon''} \tag{5.32}$$

where d is the thickness of the 2DEG and $\alpha = \hbar^2/4e^2\mu_0$. As stated in previous chapter, the dissipation is set by the number of free vortices n_f (eq. (4.42)) and by the vortex diffusion constant D, which in the case of Josephson vortices is fixed by equation (4.50). We thus have

$$\delta_{max}^{-2} = \frac{J}{2d\alpha}\frac{\omega}{Dn_f} \tag{5.33}$$

where $D_v = 2R\bar{a}^2 k_B T/\phi_0^2$ and $\bar{a}$ is the average distance between puddles. Taking $\bar{a} = 10^{-7}$m, $T = 20$mK and $R = 1$kΩ, we find $D_v = 1.310^{-6}$m^2/s. This is much smaller than the electronic diffusion constant $D_e \simeq 10^{-4}$m^2/s. As indicated in the previous chapter, by definition we have $\delta^{-2} = \mu_0\omega\sigma_1$. Using equation (5.33) and the experimental value $\sigma_1^{\max} = 0.02$ S, we find a density of free vortices $n_f = 6\times10^{14}$ m^{-2}, which is consistent with the typical size of the puddles (~ 100 nm). Assuming a thickness of $d = 10$ nm for the 2DEG, one can compute δ corresponding to $\sigma_1^{\max}$. We find $\delta = \frac{1}{\sqrt{\mu_0\omega\sigma_1/d}} \simeq 14.529$ μm which can be compared to r_ω, the distance over which the Josephson vortex move at the probing frequency $r_\omega = \sqrt{\frac{14D}{\omega}} = 97.959$ nm. This value is comparable with the typical distance between puddles which indicate that the RF excitation drives vortices between to neighbouring cells corresponding to energy minima of a disorder egg's box potential. At higher frequency, the vortices would probably dissipate less since they would not even cross one Josephson junction.

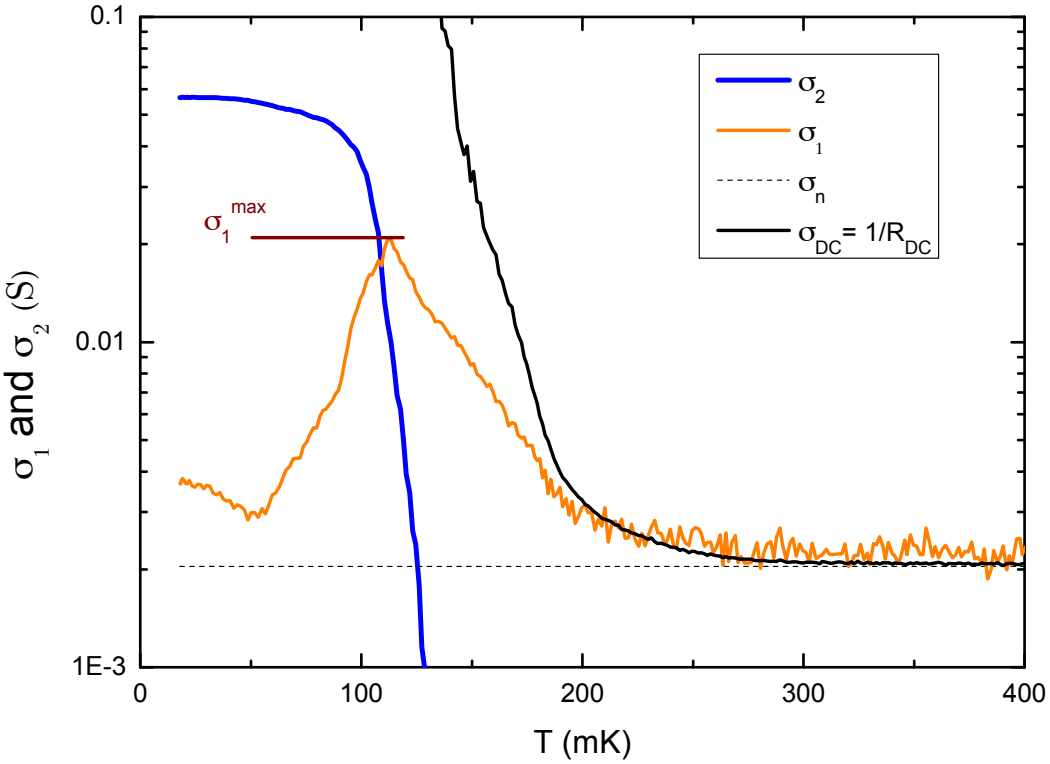

Figure 5.16 – Real and imaginary part of the conductance at $V_{BG} = 50$ V and at $f = 500$ MHz

5.3.3.4 Discussion

Numerical model : In order to get more information on the system, a renormalization group simulation could allow us to fit $\sigma_1(T)$ [7]. An alternative description can be obtained by solving numerically the electrodynamics response of a 2D array of Josephson junctions [141]. Figure 5.17 shows the result of such a simulation performed on a 32×32 JJA. At a frequency approximately ten times lower than the gap energy (upper curve labelled $\omega = 0$), a clear peak is generated in σ_1 at the T_{KT} temperature. This behaviour is similar to the one that we observe in the overdoped region of the LAO/STO interfaces (fig. 5.16). $\sigma_1(T)$ seems to follow two different power laws below and above T_{KT}. This confirms the relevance of the JJA approach to describe this system.

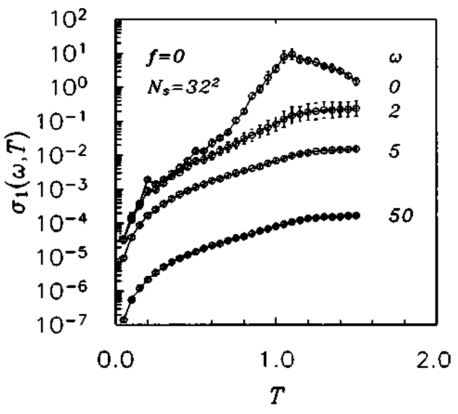

Figure 5.17 – Real part of the conductance of a JJA whose size is 32×32. Temperature is normalized by T_{BKT} and frequency is in unit of $\omega_0 = 2eRI_c/\hbar$ which corresponds to the gap energy. The low frequency conductivity σ_1 (labelled $\omega = 0$) is in fact averaged on frequencies lower than $0.08 \times \omega_0$. From [141]

7. Such analysis is being made at the moment by our collaborator L. Benfatto.

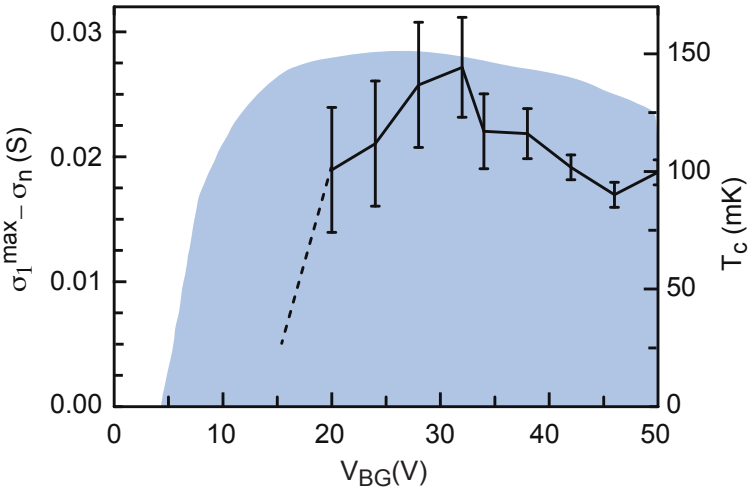

Figure 5.18 – Height of the σ_1 peak as a function of gate voltage. In the underdoped region, a strong decrease of the peak is observed. The superconducting T_c dome is shown in background.

Numerical methods are also powerful to describe the role of inhomogeneities in the superfluid stiffness [142]. According to Josephson junction array scenario, the number of superconducting puddles decreases in the underdoped region. The coupling J_{ij} of the JJA Hamiltonian starts to vary strongly from puddle to puddle depending on their respective size and mutual distance between them. At some point, the connectivity between puddles is strongly reduced and the geometry of the array evolves towards a more filamentary structure corresponding to long percolating paths [76]. Experimentally, we observe a suppression of the dissipation peak in σ_1 (fig. 5.18), which could indicate that in this geometry the vortices can no longer move in the transverse direction or even exist. In collaboration with S. Caprara and M. Grilli, we are now developing a random resistor network model with a complex impedance on each site. By solving numerically this system for different kind of inhomogeneities, we hope to obtain information on the precise evolution of the system in the underdoped region.

Slowing down of vortex motion : Recently Ganguly et al. measured the complex conductance using optical measurement of NbN films at frequencies both in the GHz and the kHz ranges [143]. They found an unusually high peak in σ_1 (fig. 5.19 (a)) which was explained by the effect of inhomogeneities. In order to obtain the right order of magnitude for the dissipation around T_{KT}, the authors assumed a cutoff length ξ_V which affects the vortex mobility μ_V. It corresponds to the typical size of inhomogeneities in NbN films.

5.3.4 Conclusion

In this chapter, we reported on the measurement of the complex conductance of the LAO/STO interface at a fixed frequency. By analyzing $\sigma_2 = \frac{1}{\omega L_k}$ at $T = 0$, we showed that the competition between the superfluid stiffness and the gap energy controls the superconducting T_c in the phase diagram. Whereas a good agreement with the Bardeen-Cooper-Schrieffer (BCS) theory is observed at high carrier doping, our data suggest that the suppression of T_c at low doping is controlled by the loss of macroscopic phase coherence due to strong spatial inhomogeneities. By

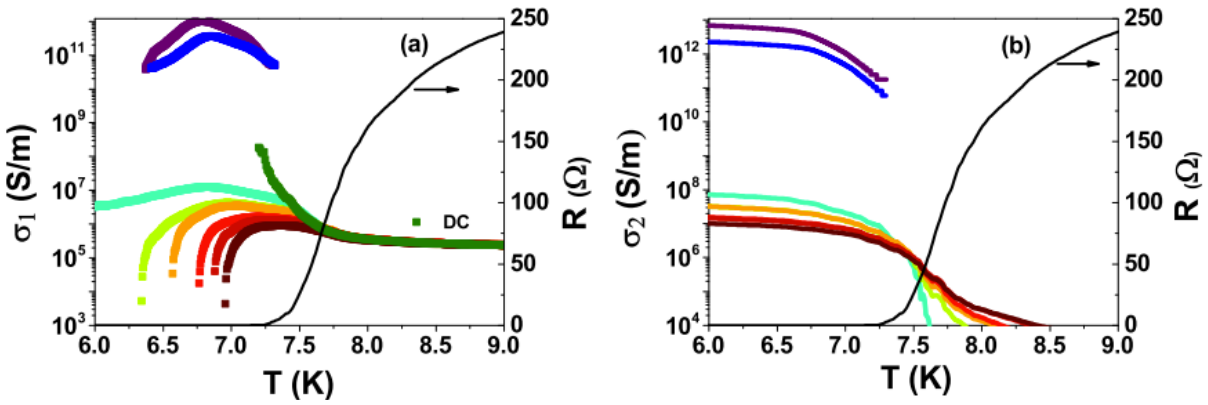

Figure 5.19 – (a),(b) Real and imaginary part of conductivity as a function of temperature for different frequency in a NbN thin films. Figure from [143]

converting J_s into a superfluid density we showed that only a very small fraction of the electrons condense into the superconducting state. We proposed that the emergence of the superconducting phase at low doping could correspond to the weak filling of high-energy $d_{xz/yz}$ bands, which are more prone to host superconductivity as they have a higher density of state and extend deeper into the STO. Finally, we analyzed the temperature dependence of σ_2 and σ_1 by assuming that the 2DEG behaves as a disordered Josephson array. Within this theoretical framework, we qualitatively explained the superfluid jump and the large dissipation peak occurring at T_{KT}.

Chapter 6

Quantum Point Contact

"Si c'était facile, ça aurait déjà été fait il y a longtemps,
à l'époque où c'était difficile"
attributed to Louis Dumoulin

Contents

After describing the effect of top-gating on a large scale, and probing the system with high frequency measurements, we propose to probe it on a short scale by lateral field-effect confinement. Reaching mesoscopic scales has remained a challenge until recently and requires reproducible growth processes and advanced nanofabrication techniques. Here, we report on the fabrication of a Quantum Point Contact (QPC) using split gates to locally deplete the 2DEG and form a quasi-1D conducting channel between two reservoirs. Similar local gating technique has been used in the group of A. Caviglia at Delft university [85] to create Josephson junctions and SQUIDs but at a larger scale. An alternative method to realized 1D structures at the LAO/STO interface using a biased C-AFM tip was proposed in the group of J. Levy at Pitsburg university [144].

In this chapter, we first introduce the main transport properties of a quantum point contact and derive it in the Landauer-Büttiker formalism. In the second part, we present the measurements of quantized conductance as a function of back-gate and top-gate voltages.

6.1 The Landauer-Büttiker Formalism

6.1.1 Conductance in the quantum limit

The conductance G of a homogeneous system is set by its conductivity σ, by its width W and length L

$$G = \sigma \frac{W}{L} \tag{6.1}$$

In a Drude picture, $\sigma = ne^2\tau_e/m^*$ is determined by the elastic scattering time τ_e which is an intrinsic property of each material. As long as the size $\mathcal{L}$ of the system is much larger than mesoscopic lengths as defined in chapter 3, this relation is true. But what happens when the width of the system is so small that it becomes comparable to the intrinsic length of the problem ?

In a simple picture, conduction electrons can be described as plane waves of wavelength λ_F, called the Fermi wavelength. When the size of the system is comparable to λ_F, an analogy with electromagnetic waves in a cavity can be made. Therefore, we can guess the existence of discrete levels due to the confinement like the transverse modes of electromagnetic TEM waves in a rectangular cavity. For a confinement of size L, the energy spacing δE between the discrete levels can be estimated by $\delta E = \hbar v_F/L$. In a quasi 1D geometry, the density of states is $N_{1D} = \frac{2}{2\pi\hbar}\sqrt{2m/(E-E_n)}$ and $v_n(E) = \partial E_n/\partial p_x = \sqrt{(E-E_n)/2m}$ is the electron's velocity along x. E_n is the energy of the bottom of each subband. When a finite bias V_{sd} is applied between the two reservoirs which are connected to the 1D chanel, electrons between E_F and $E_F + eV_{sd}$ contribute to the transport. The number of electrons available in this energy window is given by

$$N_{1D}(E) \times \delta E = N_{1D}(E) \times (eV_{sd}) \tag{6.2}$$

By definition, the total current in one channel reads

$$I_n = n_{1D} \times v = 2e \times N_{1D}(E) \times \delta E \times v_n(E) = \frac{2e^2}{h} V_{sd} \tag{6.3}$$

where the factor 2 reflects the spin degeneracy. The total conductance is therefore quantized by steps of the quantum of conductance for normal electrons $G_0 = 2e^2/h$

$$G_{tot} = \frac{I_{tot}}{V_{sd}} = \frac{2e^2}{h} \times N \tag{6.4}$$

where N is the number of 1D subbands filled in the quasi 1D region. At the end of the 80s, the semi-conductor technology produced 2DEG with a high mobility and a low carrier density, where the Fermi wavelength was approximately $\lambda_F \simeq 40nm$. By confining electrons on a length smaller than λ_F with split gates (field effect depletion with local top gates), Wees et al. measured for the first time discrete values of the conductance [145]. Figure 6.1 shows clearly plateaux every $2e^2/h$ when the gate voltage is decreased. They correspond to additionnal channels opening when the confinement potential becomes wider. Such devices are usualy called Quantum Point Contact (QPC).

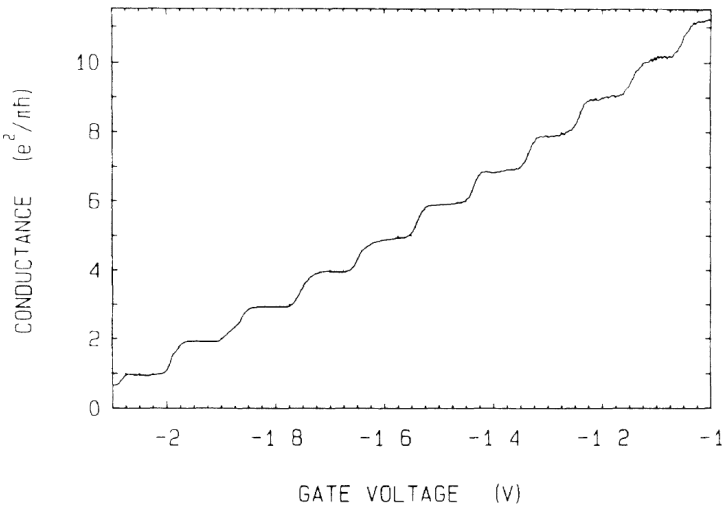

Figure 6.1 – Quantization of conductance in a Quantum Point Contact made in high-mobility $GaAs/Al_{0.33}Ga_{0.67}As$ heterojunction. From [145]

6.1.2 Landauer Formula

We now consider a confined region Ω (see fig. 6.2), connected to the Left and Right reservoirs through balistic 1D leads refered by the index $\alpha = L$ or R. For sake of simplicity, we shall limit ourselves to a single band system, with isotropic dispersion, but this can be easily generalized to multibands systems. In the region of Ω the Hamiltonian can be written

$$H_\alpha = \frac{1}{2m}p_x^2 + \frac{1}{2m}p_y^2 \quad \text{with } x, y \in \Omega \tag{6.5}$$

The eigenstates $\phi^{\pm}_{\alpha nE}(x, y)$ of this Hamiltonian can be written as nearly free electrons in the x direction.

$$\phi^{\pm}_{\alpha nE}(x, \mathbf{r}_\perp) = \frac{1}{\sqrt{\mathcal{L}}}\chi_n(y)e^{\pm ik_x^n(E)x} \quad \text{with } k_x^n(E) = \sqrt{2m(E - E_n)} \tag{6.6}$$

and the transverse mode should match the following boundary conditions

$$\chi_n(y) = 0 \text{ for } y \notin \Omega \tag{6.7}$$

Here $\pm$ represents the electrons moving to the right and to the left. The discrete levels E_n are due to the confinement in the y direction. Let us describe the transport through the confined Ω region by a scattering matrix S which contains all information about the system. We do not need to know the exact shape of the potential in the middle of the QPC; we only need to describe the incoming and outcoming states. These states are linear combinations of the eigenstates $\phi^{\pm}_{\alpha nE}$.

$$\phi_{LnE}(x) = A\phi^+_{LnE}(x) + B\phi^-_{LnE}(x) \quad \text{for } x \in L \tag{6.8}$$

$$\phi_{RnE}(x) = B'\phi^+_{RnE}(x) + A'\phi^-_{RnE}(x) \quad \text{for } x \in R \tag{6.9}$$

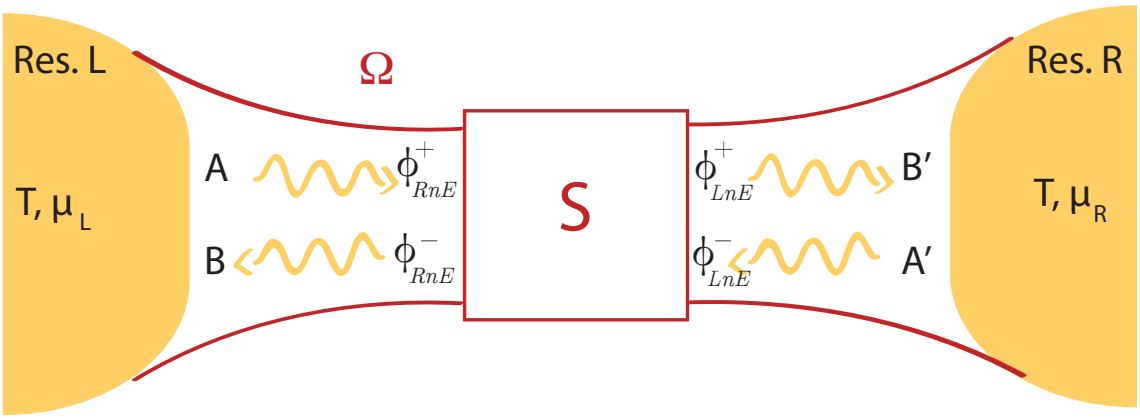

Figure 6.2 – Mesoscopic system

If the leads host only one channel, the scattering matrix S relates the incoming and the outcoming wavefunctions (see fig. 6.2):

$$\begin{pmatrix} B \\ B' \end{pmatrix} = \begin{pmatrix} r & t' \\ t & r' \end{pmatrix} \begin{pmatrix} A \\ A' \end{pmatrix} =_{def} S \begin{pmatrix} A \\ A' \end{pmatrix} \tag{6.10}$$

The scattering matrix is unitary ($S^\dagger S = 1$) as long as charge conservation is imposed. In presence of time reversal symmetry, S is also symmetric ($S^\dagger = S$). The coefficient r, r', t and t' are the amplitude probability to be either reflected or transmitted. This definition is easily generalized to a $2N \times 2N$ scattering matrix with four blocks of $N \times N$ matrices : $\mathbf{r} = r_{nn'}$, $\mathbf{t} = t_{nn'}$, $\mathbf{r}' = r'_{nn'}$ and $\mathbf{t}' = t'_{nn'}$

$$\mathbf{S} = \begin{pmatrix} \mathbf{r}(E) & \mathbf{t}'(E) \\ \mathbf{t}(E) & \mathbf{r}'(E) \end{pmatrix} \tag{6.11}$$

where N is the number of channels that are populated. The transmission and reflection probability associated to each channel is defined as $T_n(E) = |t_{nn}|^2$ and $R_n(E) = |r_{nn}|^2$.

Let us derive the Landauer formula in a heuristic way. For this, we use a basis of scattering states, which implies that the reservoirs do not reflect outgoing electrons (they perfectly absorb the electrons coming from the device). An incoming state from the left ϕ^+_{LnE} having a probability $T_n(E)$ to reach the right side of the system will create a current probability [1] $I_{Lnk} = \frac{\hbar k}{m\mathcal{L}} T_n(E)$. Correspondingly, a scattering state coming from the right creates a current probability $I_{Rnk} = -\frac{\hbar k}{m\mathcal{L}} T_n(E)$ where $\mathcal{L}$ is the size of the leads. Each scattering state is coming from one of the reservoirs at temperature T, with a given distribution function [2] $f_D(E-\mu_\alpha)$ where $\mu_\alpha = \mu - eV_\alpha$ is the chemical potential in each reservoir and V_α the applied source and drain voltage. Summing over all the states, we can compute the total current accross the system

$$I = -2e \sum_{n\alpha k} I_{\alpha nk} f_D(E(k) - \mu_\alpha) \tag{6.12}$$

1. By definition the current probability is given by $I = \frac{\hbar}{j2m}(\Psi^*.\nabla\Psi - \nabla\Psi^*.\Psi)$
2. f_D is the Fermi-Dirac distribution.

Replacing the sum over k by an integral over the energy E, we obtain

$$I = \frac{2e}{\pi\hbar}\sum_n \int_0^\infty dE\,[T_n(E)f_D(E-\mu_L) - T_n(E)f_D(E-\mu_R)] \tag{6.13}$$

$$= \frac{2e}{h}\sum_n \int_0^\infty T_n(E)[f_D(E-\mu+eV_L) - f_D(E-\mu+eV_R)] \tag{6.14}$$

$$\tag{6.15}$$

At low voltage, we can make a first order Taylor expansion around μ and get

$$I(V_L,V_R) = \frac{2e^2}{h}\sum_n \int_0^\infty dE\ \ T_n(E)\overbrace{\left(-\frac{\partial f_D}{\partial E}\right)}^{\simeq\delta(E-\mu)}(V_L-V_R) \tag{6.16}$$

$$= \underbrace{\frac{2e^2}{h}\sum_n T_n(\mu)}_{G(\mu,T=0)}\underbrace{(V_L-V_R)}_{V_{sd}} \tag{6.17}$$

The conductance is given by the sum over the transmission probabilities in units of $G_0 = 2e^2/h$. Here we have assumed that no interaction takes place between electrons. This hypothesis is not always verified as we will see in the following.

6.1.3 Quantum point contact

6.1.3.1 Saddle point

A QPC can be defined using a split gate geometry. Two metallic gates separated by a distance d are deposited above the 2DEG and insulated from it. When a negative voltage is applied, the 2DEG is locally depleted under the gates and the conducting electrons are confined in a region defined by d (see fig. 6.3 (a)).

Assuming a smooth potential along the x direction, one can write the wave function as a product $\psi(x,y) = \sum_n \phi_n(x)\chi_{nx}(y)$ [146]. The transverse modes $\chi_{nx}(y)$ are indexed by n and are solutions of the confinement in the y direction. The potential in the centre can be approximated by an harmonic potential V_{conf}, and the Hamiltonian in the QPC is :

$$H_{QPC} = \frac{1}{2m}p_x^2 + \frac{1}{2m}p_y^2 + V_{conf}(x,y) \tag{6.18}$$

with

$$V_{conf}(x,y) = \frac{1}{2}m\omega_y^2 y^2 - \frac{1}{2}m\omega_x^2 x^2 + V_0 \tag{6.19}$$

V_{conf} has a saddle point shape around V_0 which is tuned by the voltage V_{TG} applied to the split gates. In this particular case, Büttiker calculated the transmission probability which is expressed by [147]

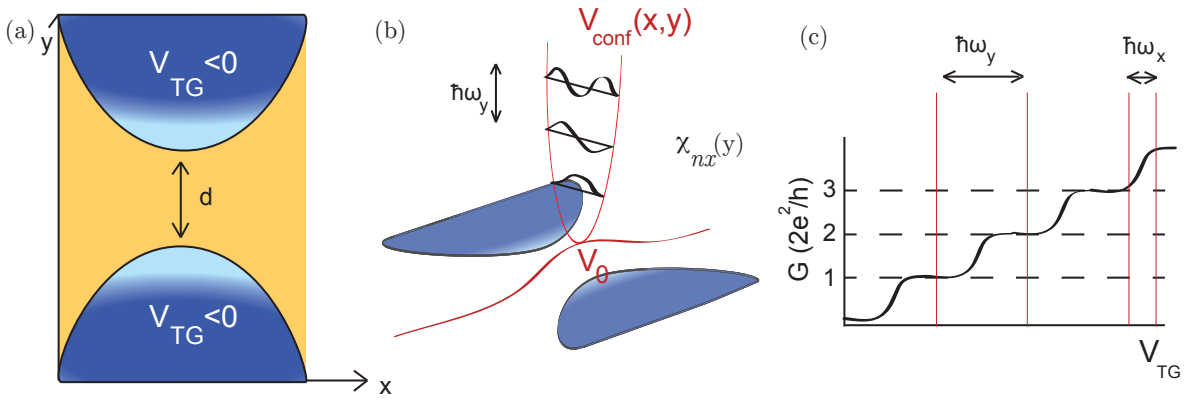

Figure 6.3 – (a) Split gates separated by a distance d seen from the top. The yellow region corresponds to the one where the current flows, the blue region is depleted by the voltage $V_{TG} < 0$ applied between the 2DEG and the gates. (b) Schematic of the confining potential $V_{conf}(x, y)$ near the centre of the QPC (in red). The transverse modes $\chi_{nx}(y)$ are separated by an energy $\hbar\omega_y$. Along the direction of propagation (x direction) the potential reaches its maximum V_0. (c) Corresponding conductance G at $V_{sd} = 0$ V as a function of the top gate voltage V_{TG}.

$$T_n(E) = \frac{1}{1 + \exp[-\pi\varepsilon_n]} \quad \text{with} \quad \varepsilon_n = 2[E - \hbar\omega_y(n + 1/2) - V_0]/\hbar\omega_x \tag{6.20}$$

Figure 6.3 (b) shows this saddle-point potential in a split gate geometry. The distance between energy levels is $\hbar\omega_y$. According to equation (6.20), the confinement in the y direction should be sharper than the potential along the direction of propagation. Therefore, the steps in conductance are clearly visible if $\omega_y > \omega_x$ (see fig. 6.3 (c)). By changing the gate voltage, the spacing between the levels changes, and the number of accessible channels changes the conductance by steps of $2e^2/h$.

6.1.3.2 Non-linear transport

When a source-drain voltage $V_{sd} = V_L - V_R$ is applied, the electrons coming from the left reservoir acquire an energy eV_{sd}. If the bias voltage is small compared to the spliting energy of the 1D levels, the theory derived above is valid (linear transport). If this energy is close to the spacing between the levels, electrons have enough energy to reach the next level : this is the non-linear transport regime. Figure 6.4 shows $G(V_{sd})$ traces for different gate voltages. Clear plateaux appears at $N \times G_0/2$ when $eV_{sd} = \hbar\omega_y$. As a first approximation, one can add the shift in energy due to the bias voltage V_{sd} in equation (6.20) and compute the differential conductance at zero temperature [148]

$$G(\mu, V_{sd}) = \frac{2e^2}{h} \sum_n \frac{1}{1 + \exp(-2\pi[\mu - eV_{sd} - \hbar\omega_y(n + 1/2) - V_0]/\hbar\omega_x)} \tag{6.21}$$

By applying a finite bias on a QPC, one can directly read the energy distance between the confined levels. To make this determination easier, one can plot dG/dV_G as a function of both V_G and V_{sd} in a colorplot.

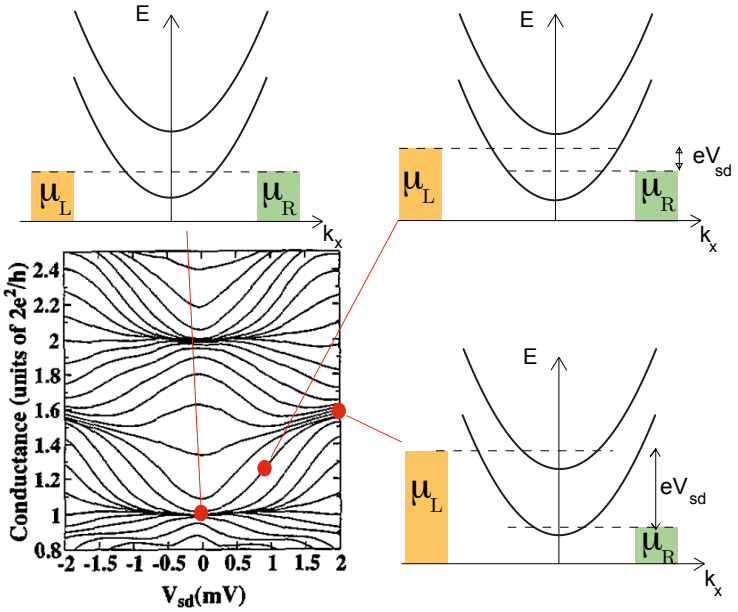

Figure 6.4 – $G(V_{sd})$ traces as a function of gate voltage in a split gate experiment. Schemes represent the 1D dispersion relation of the QPC for three different applied bias voltages V_{sd}. At zero bias, the chemical potentials on the left and right reservoirs are the same $\mu_L = \mu_R = E_F$. A plateau at half the conductance quantum appears when the bias voltage is sufficiently high to allow one electron from the left reservoir to populate the next level which is separated by $\Delta E = \hbar\omega_y$. From [149].

6.1.4 Effect of magnetic field and manybody interactions

In the presence of a magnetic field perpendicular to the xy plane $\mathbf{B} = \nabla \times \mathbf{A}$ (with $\mathbf{A} = -By\mathbf{u}_x$) , the confining potential becomes a magneto-electric potential. The transverse modes are solutions of the following equation (in the limit $\omega_c\tau_e > 1$)[150]

$$\left(V_0 + \frac{p_y^2}{2m} + \frac{1}{2}m\frac{\omega_y^2\omega_c^2}{\omega_{c0}^2}y_k^2 + \frac{1}{2}m\omega_{c0}^2\left[y + \frac{\omega_c^2}{\omega_{c0}^2}y_k\right]^2\right)\chi(y) = E\chi(y) \tag{6.22}$$

where $y_k = \hbar l/eB$, $\omega_c = |e|B/m$ is the cyclotron frequency, and $\omega_{c0}^2 = \omega_c^2 + \omega_y^2$. This equation is a one-dimensional Schrödinger equation which solution is very similar to the one for electric confinement. The first effect of a magnetic field, is to increase the confinement and therefore to further split apart the 1D levels of the QPC.

The magnetic field progressively suppresses back scattering. As shown on figure 6.5 a classical explanation is that the cyclotron orbit forces the electrons to bounce on the potential and move forward without being able to back scatter. Finally, it reduces interferences that may occur because of multiple elastic scattering in the vicinity of the QPC, thanks to the dephasing introduced by the poten-

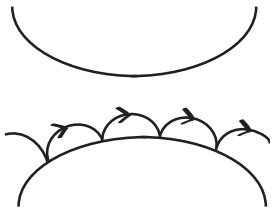

Figure 6.5 – Effect of magnetic field on backscattering.

tial vector along the electron trajectories. If the magnetic field is sufficiently hight, the Zeeman energy lifts the spin degenaracy of the levels and gives rise to quantization of the conductance in $G_0 = e^2/h$.

In general, electron-electron interactions cannot be neglected. Therefore, the regularly spaced steps presented in figure 6.1 are not a universal property of QPC. In particular, the "0.7 anomaly", which appears as a shoulder on the first plateau of conductance is usually assigned to strong electron-electron interactions. The first systematic measurement was done in 1996 [151]. Figure 6.6 shows the evolution of the 0.7 step as a function of in-plane magnetic field which is shifted to $0.5 \times G_0$. Surprisingly, when the temperature is increased, this anomaly is even more pronounced. This behavior shares some similarities with the Kondo effect in quantum dots which take into account interactions between a localized spin and conduction electrons. Recently, it was proposed that in a QPC, a spontaneous charge localization would occur [152]. These questions are still under debate.

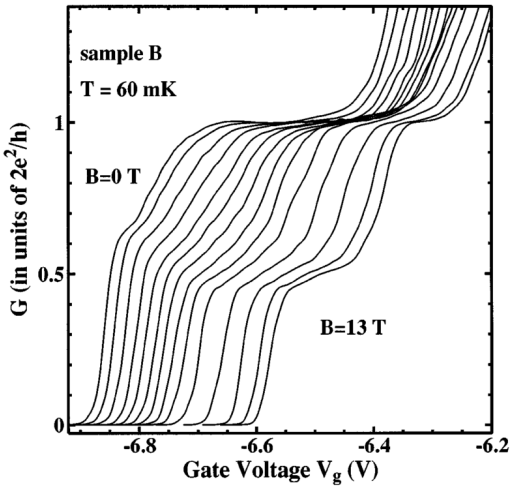

Figure 6.6 – First plateau of conductance in a QPC experiment showing the "0.7 anomaly" and its evolution to $0.5 \times G_0$ in a strong magnetic field. [151]

6.2 Split Gate Experiment

We now report on the experiment performed on sample D described in chapter 2. The split gates were deposited directly on a 14 u.c. thick cristalline LAO Hall bar fabricated by the amorphous template method. The distance between the gates is approximately $d = 26$ nm as shown on figure 2.5 of the SEM image of this device.

6.2.1 Typical scales in LAO/STO

Let us recall the typical lengths at LAO/STO interface. The confinement in the transverse direction is expected to be around ~ 10 nm. In order to be in the quasi-1D limit, we need this confinement to be of the order of the Fermi wavelength $\lambda_F = \frac{2\pi}{k_F}$, where k_F is the Fermi

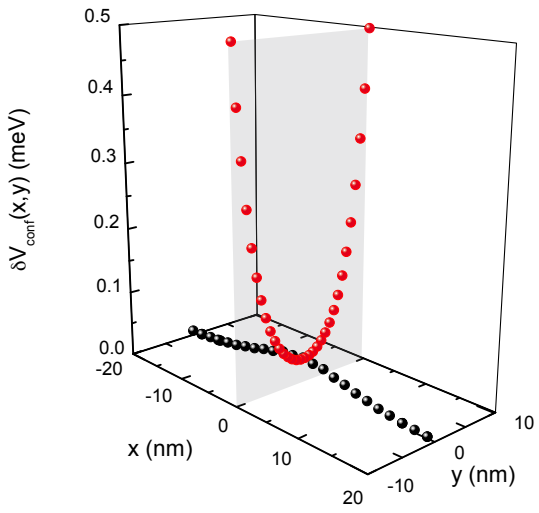

Figure 6.7 – Confining potential $V_{\text{conf}}(x, y)$ of the device obtained via COMSOL simulations.

momentum. In 2D systems, $\hbar k_F = \sqrt{2m(E_F - E^i)}$. The energy difference $\Delta E = E_F - E^i$ can be estimated from the Schrödinger-Poisson simulations. It is typically 100meV, which gives $\lambda_F \sim 10nm$. As the elastic scattering length can be estimated within the same approximation $l_e = v_F \tau_e \sim 20$ nm, the system is therefore expected to be in the quasi-ballistic limit.

The length of the system can be defined as the length $\mathcal{L}$ over which the density is smoothly evolving along the longitudinal direction. A necessary condition to observe quantum interferences is that the size of the system $\mathcal{L}$ should be smaller than the inelastic scattering length l_ϕ ($\mathcal{L} < l_\phi$). The inelastic scattering length $l_\phi = \sqrt{D\tau_\phi}$ was obtained in chapter 3 when measuring the localization corrections to transport in a magnetic field. From the B_ϕ parameter that we extracted, we can estimate $l_\phi \sim 50$ nm. This is the maximum length over which the phase of the electrons is conserved, much bigger than the size of the QPC. It is therefore possible to observe interferences effects in the vicinity of the QPC, as we will see.

6.2.2 Simulations of the device

The goal of this section is to give an order of magnitude for the splitting of the levels created by our split gates. We first compute the electron density $n(x, y)$ created by a negative voltage applied on two split gates using a COMSOL simulation where the 2DEG is described by a metallic plane (perfect screening). The dielectric constant of LAO is $\varepsilon_r = 24$ and its thickness is 5.12 nm. In a metal in the absence of bias voltage, the chemical potential should be constant

$$\mu(x, y) + e\delta V_{conf}(x, y) = \mu_{res} \tag{6.23}$$

where $\mu_{res}(T = 0) = E_F$ is the chemical potential in the reservoir, $\mu(x, y)$ and $\delta V_{conf}(x, y)$ are the local chemical potential and potential change in the top gate region respectively. As a first approximation, we estimate δV_{conf} from the change in carrier density locally induced by the gate voltage on the gates. The variation of the confinement potential is given by $\delta V_{conf} = -1/e \times \partial\mu/\partial n \times \delta n(x, y)$, where $\delta n = n(x, y) - n_{res}$ is the variation with respect

to the carrier density in the reservoirs n_{res}. $\partial\mu/\partial n$ is estimated from our Schrödinger-Poisson calculations of the quantum well that we presented in chapter 1 : $\partial\mu/\partial n \simeq 30$ meV/(10^{13}cm^{-2}). Figure 6.7 shows the variation of the potential in the center of the QPC. Fitting with an harmonic potential in the y direction we find $\frac{1}{2}m\omega_y^2 = 2.7 \times 10^{12}$ eV.m^{-2}. For a mass of $m = 0.7 \times m_e$, this gives a distance between levels of $\hbar\omega_y \simeq 0.7$ meV.

From the plane capacitance formula, we can estimate the voltage needed to fully deplete the 2DEG under the gates. From Hall effect measurements, we know that the 2D carrier density is $n_{2D} \simeq 2 \times 10^{13}$ e$^-$/cm^2. The critical voltage V_c is given by

$$V_c = \frac{-en_{2D}d}{\varepsilon_r\varepsilon_0} \tag{6.24}$$

where d is the thickness of the insulating LAO layer and ε_r its dielectric constant. For a thickness of 5 nm and a dielectric constant $\varepsilon_r = 24$ we find $V_c \simeq -0.7$ V. This numerical application give us an estimated voltage below which the current should stop flowing under the gates, and therefore the QPC behavior be observed.

6.2.3 Preliminary measurements

The sample is cooled down to cryogenic temperatures with both top and back gates at the ground. The resistance shows signs of weak localization but no superconducting transition occurs to the lowest temperature. All the measurement are performed at $T = 100$ mK. A first polarization with a positive back gate ($V_{BG} = 15$ V) is done to avoid any hysteretic behaviour [84]. During this first operation, the top gate was still at $V_{TG} = 0V$. A DC measurement of the sheet resistance was performed as a function of back gate voltage after this first polarization in order to characterize the system without confinement in the centre of the Hall bar (fig. 6.8).

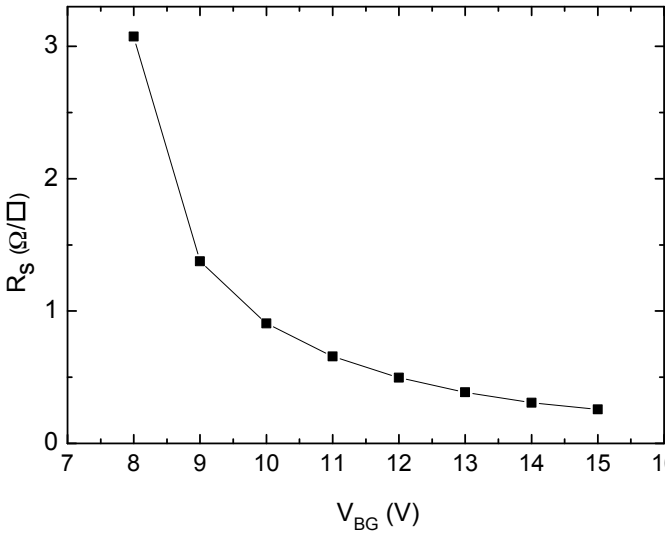

Figure 6.8 – Sheet resistance R_s as a function of back-gate voltage after the first back-gate polarization and before the one with top-gate.

We then go back at maximum back voltage ($V_{BG} = 15$ V) and we do a first polarization with the top gate by applying a positive top-gate voltage ($V_{TG} = 500$ mV), to avoid any further hysteresis, as in the case of back-gating.

6.2.4 Changing the confinement potential

According to the simulations presented in chapter 1, changing the back-gate voltage not only changes the Fermi energy by doping the system, but also it also directly affects the shape of the potential well. We therefore first set the initial carrier density in the 2DEG with a back-gate voltage $V_{BG} = 8.1$ V, in the low doping region (see Figure 6.8). We then vary the top-gate voltage V_{TG} to change the confinement potential, and study the QPC. The negative top-gate voltage will make the confinement stronger and split further appart the levels of the sub-bands.

6.2.4.1 Quantization of the conductance

In this low doping region, we hope, based on the COMSOL simulation, that we can totally deplete the 2DEG below the top gates. By applying a top gate voltage on only one of the split gates, no measurable change of the resistance R_s occurs, as expected since the size of the gate (80 nm) is small as compared to the length of the Hall bar (30 μm). On the contrary, when the voltage is applied on both gates symmetrically, a measurable effect is observed on R_s.

The top-gate voltage V_{TG} is swept down to -200 mV and the conductance $G(V_{TG})$ in the linear regime ($V_{sd} = 0$) is measured at fixed back-gate voltage. The resistance of the reservoirs, that we measure when $V_{TG} = 0$, is subtracted to extract the conductance of the QPC. Figure 6.9 (Left) shows the evolution of $G(V_{TG})$ which clearly exhibits conductance steps of $G_0 = 2e^2/h$.

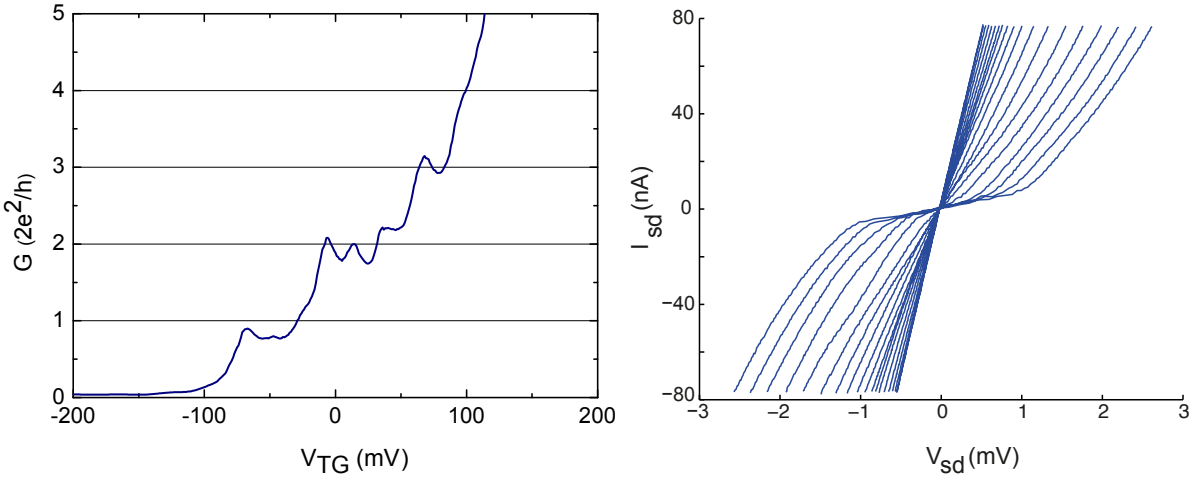

Figure 6.9 – (Left) G_{ac} at $V_{BG} = 8.1$ V and B=0 T. (Right) $I_{sd}(V_{sd})$ for different top-gate voltages.

Few oscillations around plateaux are seen, which are related to interference effects in the QPC [153]. Above $3 \times G_0$, the conductance suddenly increases and the quantization of the conductance disappears. Assuming a Fermi wavelength of around $\lambda_F = 10$ nm, the number of

steps gives us an estimation of the width of the QPC. Indeed, from a classical argument, the conductance of a Sharvin point contact of width W is [145]

$$G_s = \frac{2e^2}{h}\frac{k_F W}{\pi} = \frac{2e^2}{h}\frac{2W}{\lambda_F} \tag{6.25}$$

Therefore, the width is approximately $W \simeq 3 \times \lambda_F/2 = 15$ nm, which is consistent with the distance between our split gates.

6.2.4.2 Non-linear transport

If we now increase the source-drain voltage V_{sd}, a kink appears in the $I_{sd}(V_{sd})$ plot, especially for very negative top-gate voltage (Figure 6.9 (Right)). We enter the non-linear regime presented above. When a bias voltage V_{sd} is applied, the chemical potentials on the left and right side are shifted by eV_{sd}. Hence, electrons coming from the left reservoir are slightly higher in energy than electrons coming from the right. When $eV_{sd} = \hbar\omega_y$, the left movers have enough energy to populate the next unoccupied sub-band. At this point the conductance is half a quantum of conductance $G_0/2$ higher. This can be seen by plotting the conductance G as a function of V_{sd} for different top-gate voltages V_{TG}, as in figure 6.10. For $V_{sd} = 0$ V, we observe an accumulation of curves corresponding to the plateaux at multiples of G_0. At finite V_{sd}, other accumulations of curves can be seen corresponding to $G_O/2$ and $3 \times G_0/2$. This is the signature of level alignements as described above.

A color plot of the transductance dG/dV_{TG} (fig. 6.11) as a function of source-drain voltage and top-gate voltage allows to unveils a clear pattern. Regularly spaced maxima (in yellow) indicate a maximum in the derivative of the conductance. In between, the values of conductance correspond to integer or half-integer values of the conductance quantum G_0. The analysis of this color plot allows us to determine the spacing $\hbar\omega_y$ between the levels. We find $V_{sd} = \pm 0.7$ mV (indicated by a black arrow on fig. 6.11), which is precisely the value expected for a d_{xy} band splitting for a confinement derived from our simulation. On top of this structure, an interference pattern is clearly visible. It gives information on the specific shape of the confinement potential. Further analysis should be made in order to determine the shape of the confinement potential and compare it with the one simulated in section 6.2.2.

6.2.5 Changing the Fermi energy at fixed top gate voltage

Another way of populating the quasi-1D channels formed by the local top gates is to smoothly increase the Fermi energy by changing the back-gate voltage V_{BG}.

6.2.5.1 Linear transport as a function of the back-gate voltage

In the depleted region, the back voltage does not affect strongly the shape of the confining potential in the z direction. Let us assume that increasing V_{BG} simply adds electrons to the 2DEG and therefore shifts the Fermi energy upwards. We now set the top-gate voltage at $V_{TG} = -200$ mV. The shape of the potential will not change from now on and we can compare the

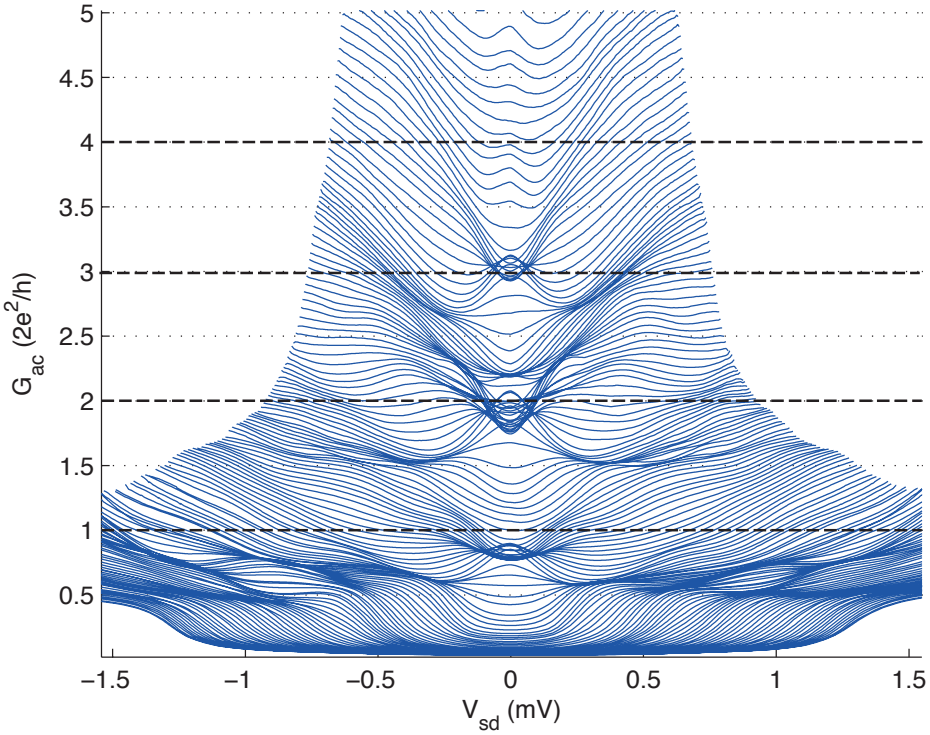

Figure 6.10 – Conductance $G(V_{sd})$ as a function of top gate voltage at $V_{BG} = 8.1$ V.

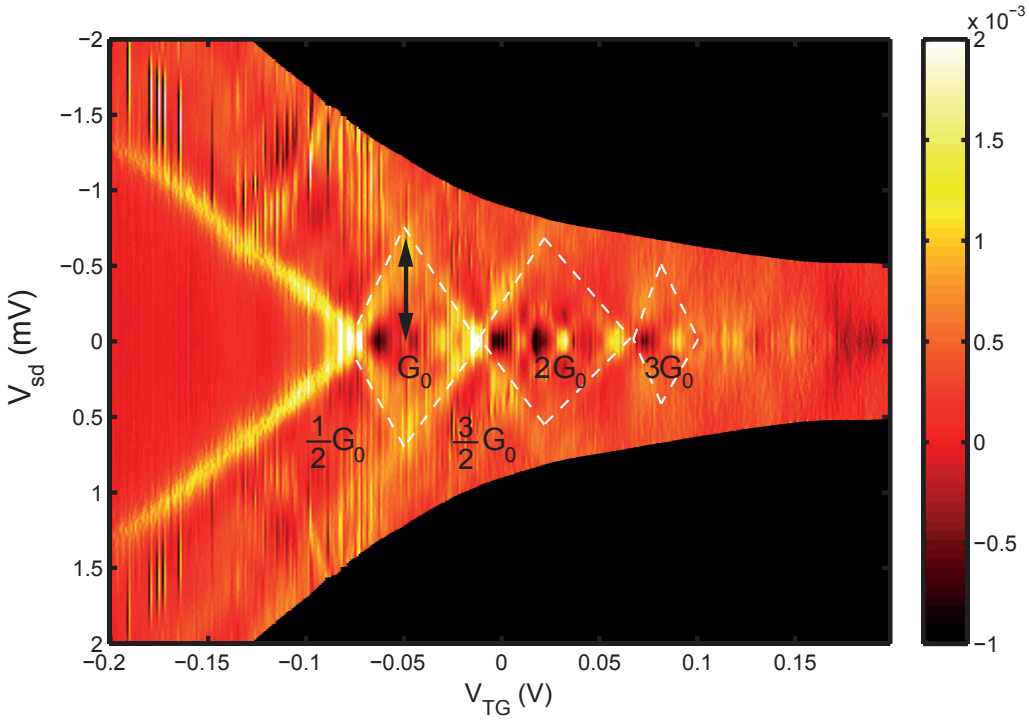

Figure 6.11 – Transductance dG/dV_{TG} as a function of source-drain voltage V_{sd} and top gate voltage V_{TG}

evolution of the chemical potential with respect to V_0 the bottom of the confinement potential. In the insulating region (below $V_{BG} = 8V$), the Fermi energy E_F is lower than V_0 : no electron can jump across the strongly depleted region and $G = 0$. Progressively, the electrons get enough energy to populate the quasi-1D channels. But simultaneously, the conductance of the reservoirs increases. In order to analyze the data, we must substract the conductance of the reservoirs (i.e. the Hall bar) that we measured before the first polarization with the top gate. As the reservoirs and the quantum point contact are in series, we subtract the sheet resistance $R_s(V_{BG})$ from the total dynamical resistance $R_{ac} = 1/G_{ac}$.

$$G_{QPC}(V_{BG}) = \frac{1}{1/G_{ac} - R_s(V_{BG})} \tag{6.26}$$

Data on figure 6.12 (a) present the dynamical conductance G_{QPC} as a function of the back-gate voltage, which presents plateaux at multiple values of G_0. This first plateau is flat, while the second one exhibits an oscillation around $2 \times G_0$. As observed when sweeping the top-gate voltage, the $I_{sd}(V_{sd})$ characteristics is linear at low V_{sd}, while a kink is observed at $V_{sd} = 0.7$ meV for small back-gate voltage. As observed when sweeping the top-gate voltage, the $I_{sd}(V_{sd})$ characteristics is linear at low V_{sd}, while a kink is observed for $V_{sd} = 0.7$ meV for small back-gate voltages.

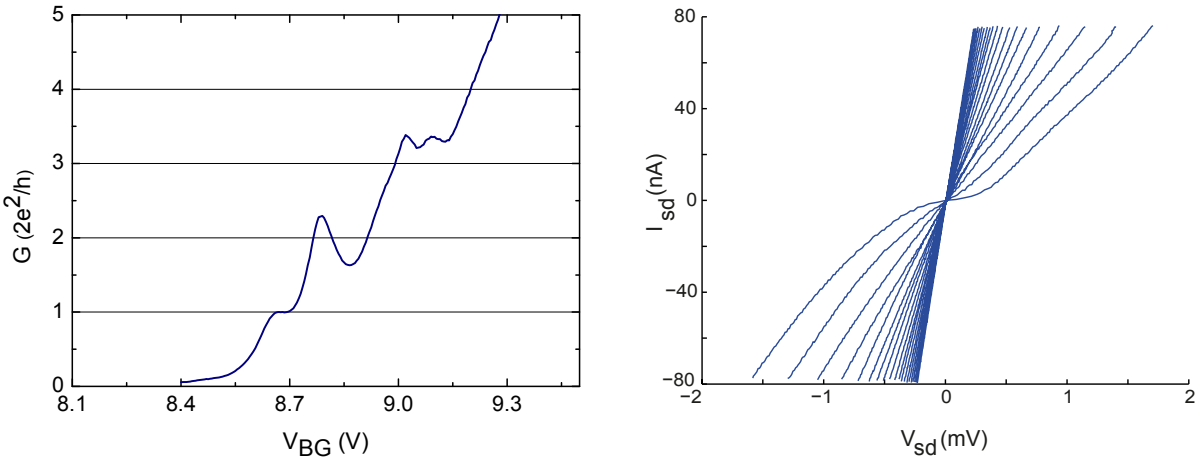

Figure 6.12 – (a) G_{ac} at $V_{TG} = -200$ mV. (b) $I_{sd}(V_{sd})$ characteristics for different back-gate voltages.

6.2.5.2 Non-linear transport

We will now extract the splitting of the levels by the same method based on $G(V_{sd})$ traces. Figure 6.13 shows a set of such traces when the back-gate voltage is increased. The results at first sight are similar to the traces obtained by sweeping the top-gate voltage. Nevertheless, the quantization seems to disappear faster than in the previous experiment.

By analyzing the transductance dG/dV_{BG} in the color plot figure 6.14, the structure presents a well-defined maximum at a value of source-drain voltage which is smaller than in the top-gate

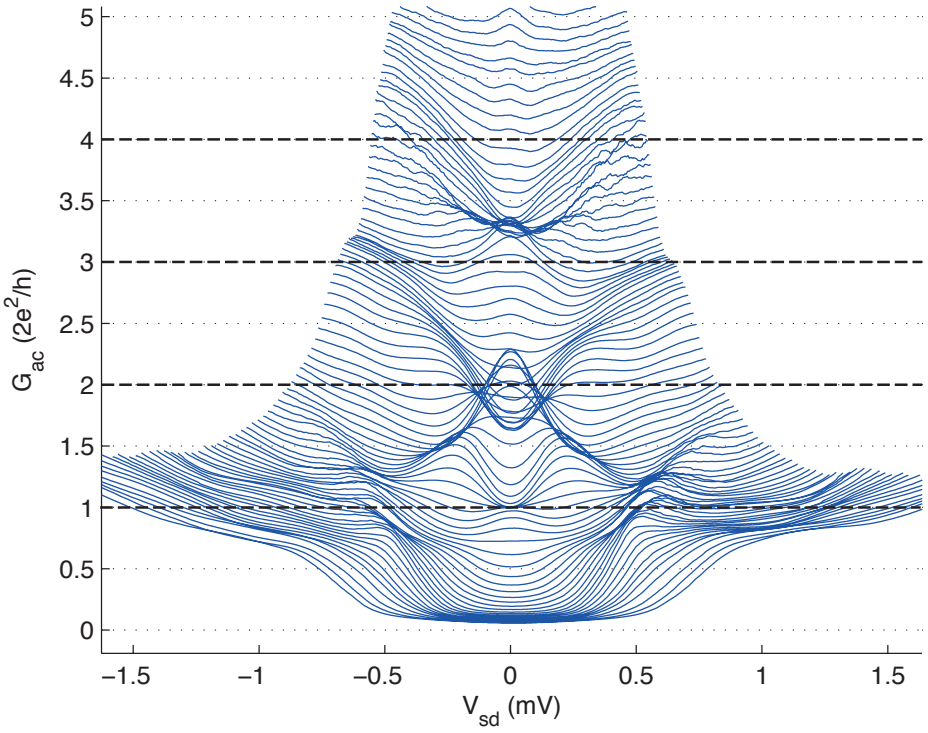

Figure 6.13 – Conductance $G(V_{sd})$ as a function of back-gate voltage at $V_{TG} = -200$ mV and B=0T.

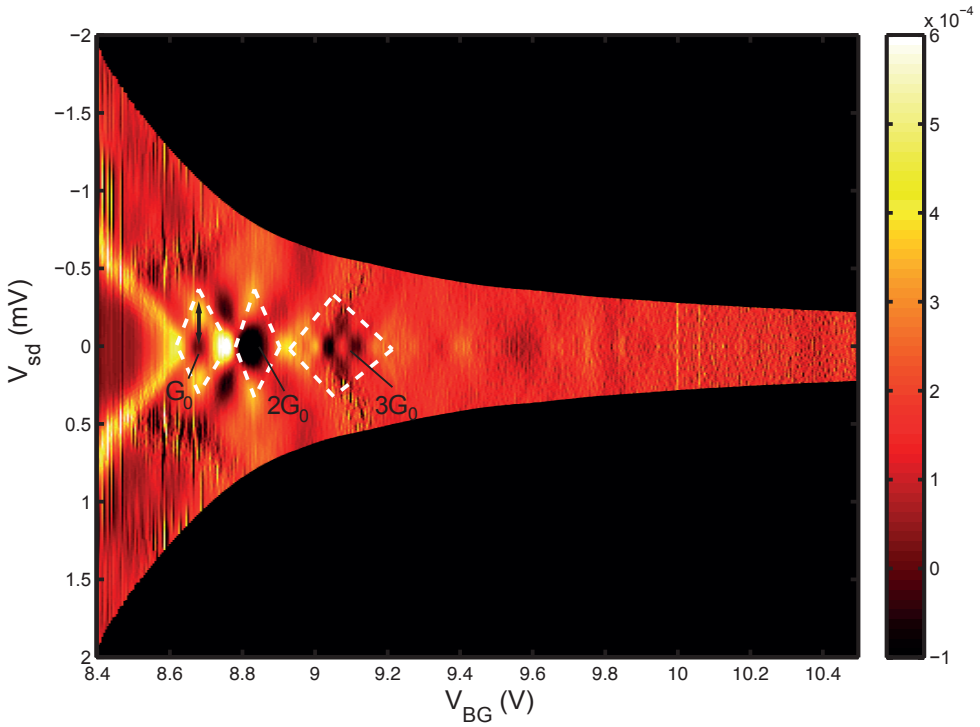

Figure 6.14 – Transductance dG/dV_{BG} as a function of back-gate voltage at $V_{TG} = -200$ mV.

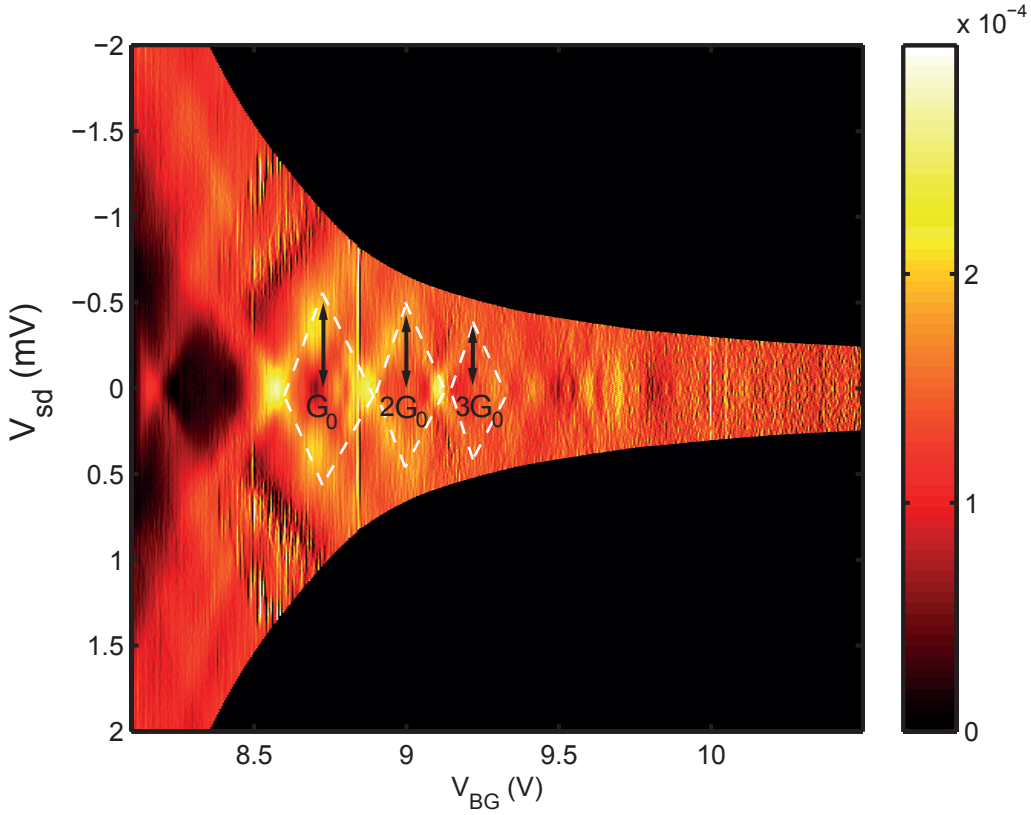

Figure 6.15 – Transductance dG/dV_{BG} as a function of V_{sd} and the back-gate voltage V_{BG} at B=6T.

sweep. This structure occurs at $V_{BG} = 8.7$ V which is higher than the one used in fixed top-gate experiments ($V_{TG} = 8.1$ V). There are more electrons and the chemical potential is higher. We know from the Schrödinger-Poisson resolution of the quantum well, that $\partial\mu/\partial n$ is a sub-linear function of the density (see for example Scopigno et al. [73]). That means that $\partial\mu/\partial n$ is smaller than in the first experiment, and so is δV_{conf}. We therefore expect a smaller level spacing in that case, as observed experimentally. It is difficult to analyze in more detail the data in figure 6.14, because of the interference patterns which are well pronounced and somewhat dominate the color plot. In order to reduce the interference we apply a perpendicular magnetic field.

Figure 6.15 shows a color plot of the transductance dG_{ac}/dV_{BG} as a function of back-gate voltage and bias voltage. The structure is much more simple, since most of the interferences effects have been washed out by the magnetic field which induces dephasing along the electron trajectories. Maxima corresponding to level crossings are clearly visible. As V_{BG} is increased, the V_{sd} of the maxima slightly decreases. This is compatible with the change in $\partial\mu/\partial n$ that we mentioned earlier.

Studying the transport properties of this QPC gives access to spectroscopic features of the LAO/STO interface. A more rigourous modeling of the confinement potential, and additionnal data at different magnetic fields should pave the way of a more precise description of the electronic structure in these heterostructures.

6.2.6 Conclusion

The results presented in this thesis show that standard mesoscopic physics phenomena can be reproduced at oxide interfaces. By pushing the system through higher negative top-gate voltages, we may further increase the confinement and favor the electron-electron interactions. At higher doping with a back gate, the spin-orbit coupling could be much stronger than the splitting energy, which might create exotic 1D electronic states. We are currently analyzing data at $V_{TG} = -450$ mV where unusual behaviour is seen and possible Kondo physics occurs.

Conclusion and perspectives

This thesis was devoted to the study of static and dynamical transport properties of the superconducting two-dimensional electron gas at the $LaAlO_3/SrTiO_3$ interface. Under strong 2D confinement, the degeneracy of the t_{2g} bands of $SrTiO_3$ is lifted, generating a rich and complex band structure. Starting from a free electron model, we derived numerically a self-consistent calculation of the potential well and the band structure (chapter 1). These simulations highlighted the presence of two types of bands (d_{xy} and $d_{xz/yz}$) with very different transport properties, and have guided our analysis all along the way.

First, we investigated the effect of microscopic disorder introduced by Cr doping, on the superconductivity and spin-orbit coupling over a wide range of back-gate doping. The main effect of Cr doping is to induce a stronger scattering potential, leading to the reduction of the elastic scattering time. As a result, superconductivity is suppressed in agreement with the Finkelstein's theory. In addition, by analizing the contribution of spin-orbit coupling to the magnetoconductance, we showed that the spin relaxation occurs according to a D'Yakonov-Perel mechanism. Besides, we demonstrated that the spin-orbit coupling constant increases linearly with the gate tunable interfacial electric field, as expected for a Rashba-type interaction.

We also described the first implementation of a field-effect device where the superconductor-insulator transition could be continuously tuned with a top-gate without any current leakage. The presence of a strong spin-orbit coupling that could be controlled with the top-gate voltage was also demonstrated by analyzing the magneto-transport measurements. The gate dependence of the spin-splitting energy, of the order of a few meV, was found to be consistent with Rashba spin-orbit coupling. Going one step further in nanofabrication, we presented the first realization of a quantum point contact in LAO/STO using split gates. By changing both top and back voltages we were able to tune the number of conducting channels in the normal state and measure the quantization of conductance. Several intringuing features were observed (non-integer steps, splitting of the first quantized step, zero bias anomaly on the forth step...) that are still under investigation at this time. The work on this device will continue in the next months with new experiments. The effect of an in-plane magnetic field will be studied in order to lift the spin degeneracy and unveil the presence of spin-orbit coupling. This investigation could also benefit from the measurement of shot noise associated with the different features.

The possibility to access mesoscopic length scales in $LaAlO_3/SrTiO_3$ devices represents an important step toward the realization of nanostructures where the interaction between supercon-

ductivity and the Rasba Spin-Orbit coupling could give rise to non-conventional electronic states. In particular, it has been shown that a s-wave superconductor in presence of spin-orbit coupling in a quasi-1D channel would realize a topological superconducting phase. Such geometry could be adapted from the QPC device discussed in this thesis, in the presence of superconducting reservoirs.

To go further in the understanding of the $LaAlO_3/SrTiO_3$ interface, we set up a high frequency measurements to assess the dynamical properties of the superconducting gas. The heterostructure was embedded into a resonant circuit formed with SMD components, and placed at the end of a transmission line (chapter 5). We developed an original calibration method that takes advantage of the tunability of the sample impedance offered by electrostatic gating and temperature. This way, we were able to measure the complex conductance $\sigma(\omega)$ of the interface in the range [0.3-0.6 GHz] as a function of gating and temperature. In particular, the imaginary part of σ at $T \simeq 0$ gave us access to the superfluid stiffness and to the gap energy via the BCS theory. We showed that the competition between these two energy scales controls the superconducting Tc in the phase diagram. By analyzing the superfluid density derived from the stiffness, we proposed that the emergence of the superconducting phase at a given doping could correspond to the filling of high-energy $d_{xz/yz}$ bands, which have a higher density of state and extend deeper into the $SrTiO_3$.

We also analyzed the temperature dependence of both the real part and imaginary part of σ, and compared the results with the standard BCS/Mattis-Bardeen theory on one hand, and with the BKT theory on the other hand. We proposed to model the $LaAlO_3/SrTiO_3$ interface by a disordered Josephson junctions array whose properties (coupling, connectivity, strength of superconducting puddles...) can be tuned with the gate. Using this approach, we showed that superconductivity is suppressed by phase fluctuations in the underdoped region. The presence of an unusually large dissipation peak in the real part of sigma was also qualitatively explained by Josephson vortices dynamics.

This method could also be applied to [110] oriented LaAlO3/SrTiO3 interfaces, for which the ordering of the t_{2g} subbands is reversed from that of the [001] orientation, in order to get more insight on the mechanisms behind superconductivity in those interfaces. However, the resonant technique that was used in this thesis only allows measuring the conductance in a limited frequency range around the resonance. In order to perform a direct spectroscopy of the superconducting state, we need to develop a broadband measurement technique in a frequency range spanning above and below the gap frequency ($\sim$ 5GHz). This requires to reduce significantly the thickness of the $SrTiO_3$ substrate in order to minimize both its capacitive contribution and its losses in the total impedance of the sample.

Appendix A

Two-carrier analysis

Elastic and inelastic scattering : In a normal metal or semiconductor, interaction with impurities or with the environment sets a typical length over which electrons can freely propagate before they scatter. Some scattering events preserve the phase while others don't. Elastic processes simply conserve the momentum and phase of the electron's wave function. The mean free path l_e is the typical distance between two elastic scatterings

$$l_e = v_F \tau_e \tag{A.1}$$

where τ_e is the mean time between two elastic processes and v_F the Fermi velocity. In the Drude model the conductivity is given by

$$\sigma = \frac{ne^2\tau_e}{m^*} \tag{A.2}$$

The mobility is defined by

$$\mu = \frac{e\tau}{m} \tag{A.3}$$

Hall measurements in a multiband system : It was shown that in LAO/STO interfaces the Hall voltage is not linear in magnetic field for a large density of carriers ($V_{BG} > 0$) [154]. Biscaras et al. proposed to explain this effect by the presence of two different populations of carriers in the confinement well. They demonstrated that at low doping, the carriers have a low mobility μ_1 and a density n_1. We call them Low Mobility Carriers (LMC). When the carrier density is increased by gate voltage, a second population of carriers (n_2,μ_2) appears with a mobility that continuously increases with gate voltage. We call them High Mobility Carriers (HMC). When measurements are performed at sufficiently high-magnetic field, the densities n_1 and n_2, and the mobilities μ_1 and μ_2 can be extracted by a fit of R_h. [104]

$$R_h = \frac{B}{e} \frac{\frac{n_1\mu_1^2}{1+\mu_1^2B^2} + \frac{n_2\mu_2^2}{1+\mu_2^2B^2}}{\left[\frac{n_1\mu_1}{1+\mu_1^2B^2} + \frac{n_2\mu_2}{1+\mu_2^2B^2}\right]^2 + \left[\frac{n_1\mu_1^2B}{1+\mu_1^2B^2} + \frac{n_2\mu_2^2B}{1+\mu_2^2B^2}\right]^2} \tag{A.4}$$

In addition, it is possible to constrain the fit with the two additionnal equations :

$$n_1 + n_2 = n_{tot} \qquad \text{(from capacitance measurement)} \tag{A.5}$$

$$n_1\mu_1 + n_2\mu_2 = \frac{1}{R_S} \qquad \text{(from DC resistance measurement)} \tag{A.6}$$

where R_s is the sheet resistance and n_{tot} the total carrier density that can be measured by capacitance measurements.

Appendix B

Schrödinger-Poisson simulations

We describe here the numerical resolution of Schrödinger-Poisson semi-classical model including both light d_{xy} bands and heavier $d_{xz/yz}$ bands.

B.1 Schrödinger-Poisson equations

A pure quantum description of the interfacial band structure can be obtained using density functional theory (DFT) calculations [50]. However, as it can only be solved on few unit cells, this approach can not reproduce the system without possible finite size effects. It is also possible to use a tight-binding model with a self-consistent Hartree and random phase approximation as in [51]. One way to tackle this problem numerically on large scales is to adapt simpler strategies initially developped for semiconductors [155].

B.1.1 Numerical solution

As we explained in the first chapter, one way to solve the quantum confinement is to use a semi-classical description. A two-dimensional electron gas confined in the z direction by a potential $e\phi(z)$, can be described by the following set of Schrödinger equations :

$$\frac{d^2\psi_{xy}}{dz^2} + \frac{2m_z^{xy}}{\hbar^2}\left[E^{xy} + e\phi(z)\right]\psi_{xy}(z) = 0 \tag{B.1}$$

$$\frac{d^2\psi_{xz/yz}}{dz^2} + \frac{2m_z^{xz/yz}}{\hbar^2}\left[E^{xz/yz} + e\phi(z)\right]\psi_{xz/yz}(z) = 0 \tag{B.2}$$

where $\psi_{xy}(z)$ and $\psi_{xz/yz}(z)$ are the envelope wave functions for the xy bands and xz/yz bands respectively with $m_z^{xy} = 14 \times m_e$ and $m_z^{xz/yz} = 0.7 \times m_e$. Simultaneously the associated charge density $n_{3D}^{tot}(z)$ and electric field $F(z)$ inside STO have to fulfill the classical Poisson equation :

$$\nabla(\varepsilon_0\varepsilon_r(F(z))\nabla(\phi(z))) = -n_{3D}^{tot}(z) \tag{B.3}$$

$$\varepsilon_r(F) = \varepsilon_r(F=\infty) + \frac{1}{A + B|F|} \tag{B.4}$$

where ε_r is the electric field dependent dielectric constant of STO with $A = 4.907 \times 10^{-5}$ and $B = 4.097 \times 10^{-10}$ m.V^{-1}. A typical electric field can be calculated $F_c = A/B \simeq 10^5$ V.m^{-1}. Above this value, the dielectric constant is close to the value $\varepsilon_r(F = \infty)$. In absence of electric field the dielectric constant reaches the value of bulk STO $\varepsilon_r(F = 0) \simeq \frac{1}{A} \simeq 23000$.

We now describe the procedure used to solve these two equations self-consistently.

— Starting from an initial potential $\phi(z) = \phi_{\text{in}}(z)$ for $z \in [0, L]$ where L is larger than the typical thickness of the potential well, we find the solution $\psi_{xy}(z)$ and $\psi_{xz/yz}(z)$ of Shrödinger equation for the two different masses m_l and m_h numerically by using the Noumerov method (similar to Euler). The different energies E_i^{xy} and $E_i^{xz/yz}$ are found by dichotomy assuming the boundary conditions $\psi_{xy}(0) = \psi_{xz/yz}(0) = 0$ (infinite energy barrier on LAO side).

— The Fermi level is found by dichotomy until the two-dimensional density of carriers $n = \int_0^{E_f} dE N_{2D}(E) = n_{2D}$ where n_{2D} is the carrier density measured experimentally. Here we choose a density of state at T=0 for a 2D free electron gas $N(E) = m_t/\pi\hbar^2$ with $m_t = 0.7 \times m_e$ for d_{xy} bands and $m_t = \sqrt{m_l m_h} = 3.13 \times m_e$ for $d_{xz/yz}$ bands which corresponds to the average density of state for these bands.

— We finally solve (B.3) by including a trapped charges density $N_{trap}(z)$ and the dependence of the dielectric constant of STO. We need first to calculate the electric field at the interface by integrating (B.4) between 0 and L once

$$\varepsilon_{STO}(0)\phi'(0) = -\frac{e(n_s + N_{trap})}{\varepsilon_0} + \varepsilon_{STO}(L)\phi'(L) \tag{B.5}$$

where $\phi'(L) = -V_{BG}/d_{STO}$, is imposed by the back-gate voltage and the thickness of the STO substrate $d_{STO} = 500\mu$m. A fourth order Runge-Kutta method allows to compute the solution $\phi^n_{out}(z)$ starting from the value $\phi'(0)$ obtained in equation B.5.

— The resulting potential ϕ^n_{out} is used to restart from step 1 with a new potential $\phi^{n+1}_{in} = (1-f)\phi^n_{in} + f\phi^n_{out}$, with $f < 1$. The procedure is repeated until the quadratic difference between ϕ_{out} and ϕ_{in} is lower than 10^{-6} eV.

B.1.2 Characteristic parameters of the model

Two-band model : The use of two different bands in the numerical simulations was motivated by experimental and theoretical results [154, 156, 50, 51]. Indeed, it has been proposed that due to the lighter mass $m_z^{xz/yz}$, the $d_{xz/yz}$ band would always be higher in the potential well but also more delocalized. In our simulation, the $d_{xz/yz}$ band start to be filled when a positive back gate voltage is applied. Of course, the precise electronic repartition of the subbands depends on the few free parameters which we describe now.

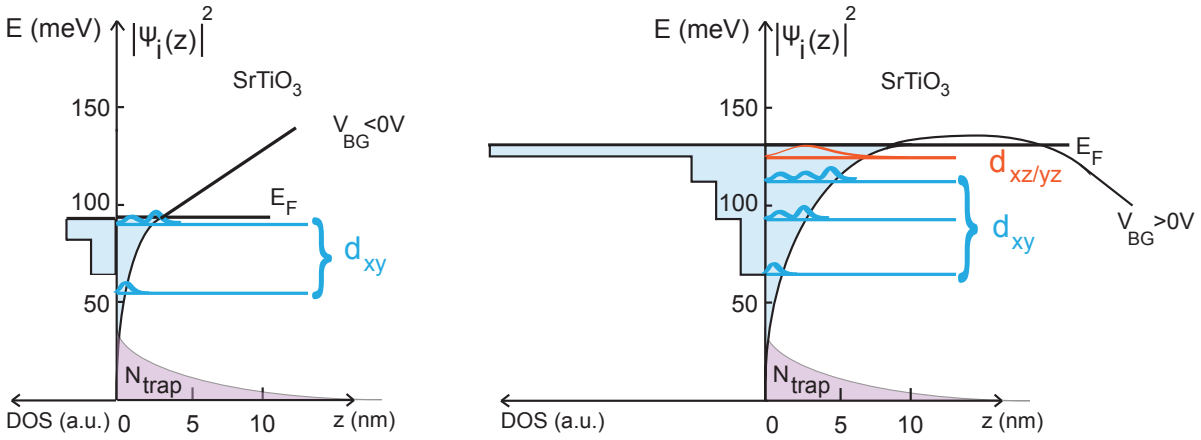

Figure B.1 – The d_{xy} electrons in red are at the bottom of the well and spread on a few nanometres, while the heavier $d_{xz/yz}$ in blue are more delocalized at the top of the potential well. The density of state (DOS), plotted in arbitrary units, is much higher for the latter.

Trapped charges : The presence of trapped charges is crucial to maintain the confinement of the 2DEG, in particular when a positive back-gate voltage is applied. Indeed, in the absence of such charges, the solution of the Schrödinger-Poisson equation would generate an unstable solution where the electrons spread to $z = \infty$ (corresponding to a Fermi energy at the exact top of the quantum well). Although it is now commonly accepted in the community that some trapped charges are located around the QW, their precise number and exact spatial distribution is unknown. In our simulations, an exponentially decreasing distribution $N_{trap}(z) \propto e^{-z/Z_N}$ with a typical length $Z_N \sim 10$ nm was chosen. Z_N should be higher than the typical thickness of the 2DEG $d \sim 5$ nm. We checked that our results were not strongly affected by the choice of N_{trap}.

The density of trapped charges N_{trap} was fixed by the bath tube experiments [84]. When the system is doped by applying a positive gate voltage, the Fermi energy rises until the electrons can thermally escape from the quantum well. After a first positive polarization in gate, we assume that at maximum voltage the Fermi energy lies just below the top of the quantum well (within k_B). N_{trap} is therefore chosen such that the numerical simulations reproduce this situation.

STO dielectric constant : A second important unknown quantity that should be chosen carefully is the dielectric constant of STO under a high electric field ε_∞. In previous work [73, 79], this value was set to $\varepsilon_\infty = 300$. Such a high value allows the 2DEG to extend far into STO, but hinders the influence of the non-linearity of the STO dielectric constant. The precise value of $\varepsilon_r(F = \infty)$ is unknown but it must be carefully chosen. Park and Millis have chosen $\varepsilon_r(F = \infty) = 70$ [51]. We choose this value by default.

B.1.3 Discussion of the results

Fermi Energy and filling of the bands : The carrier densities used for the simulations shown in chapter 1 are those measured in sample A. The Fermi energy obtained varies with the parameters of the system : its typical value is around $E_F \sim 100$ meV. When a negative back gate voltage is applied, only the d_{xy} bands are filled and the electrons are confined close to the interface. When a positive back gate voltage is applied, the system starts to fill $d_{xz/yz}$ bands. As the electrons of these bands have a lower mass in the z direction $m_z^{xz/yz} = 0.7m_0$, they spread more inside bulk STO. At some point these electrons spread into a region where $\varepsilon_{STO}(z)$ is close to the bulk value ~ 23000. Figure B.1 schematically represent the system in the overdoped region. The square modulus of the wavefunctions are in blue and red for the d_{xy} and $d_{xz/yz}$ bands respectively. Thanks to its high density of state (DOS), the $d_{xz/yz}$ band can accommodate a lot of electrons. The d_{xy} bands have a lower DOS, and their level spacing is smaller. The 2DEG extension is typically 10 to 20 nm in the overdoped region when the $d_{xz/yz}$ bands are filled.

Doping with a top gate or a back gate : In the underdoped region the 2DEG has only a few d_{xy} bands that are filled and a low Fermi energy. Figure B.2 (a) shows the square modulus of the electron wave function in red, trapped in a narrow potential well whose slope deep into STO is fixed by the back gate voltage. In figure B.2 (b), the system is maximally doped with a positive back gate voltage. The wave function is much more delocalized and the Fermi energy is close to the top of the potential well.

In the case of top gate doping, the potential well is not directly affected. The hard wall boundary condition chosen at $z = 0$ is justified by the large energy mismatch between the bands of LAO and STO at the interface. Therefore, adding electrons with a top gate corresponds to increasing the number of electrons in the system without changing the boundary conditions. Figure B.2 (c) and (d) show that when more electrons are added to the 2DEG, the electric field at the interface increases

$$F = \frac{e}{\varepsilon_0 \varepsilon_r}(n_s + N_{trap}) \tag{B.6}$$

This enhancement of the electric field pushes the wave function toward the interface.

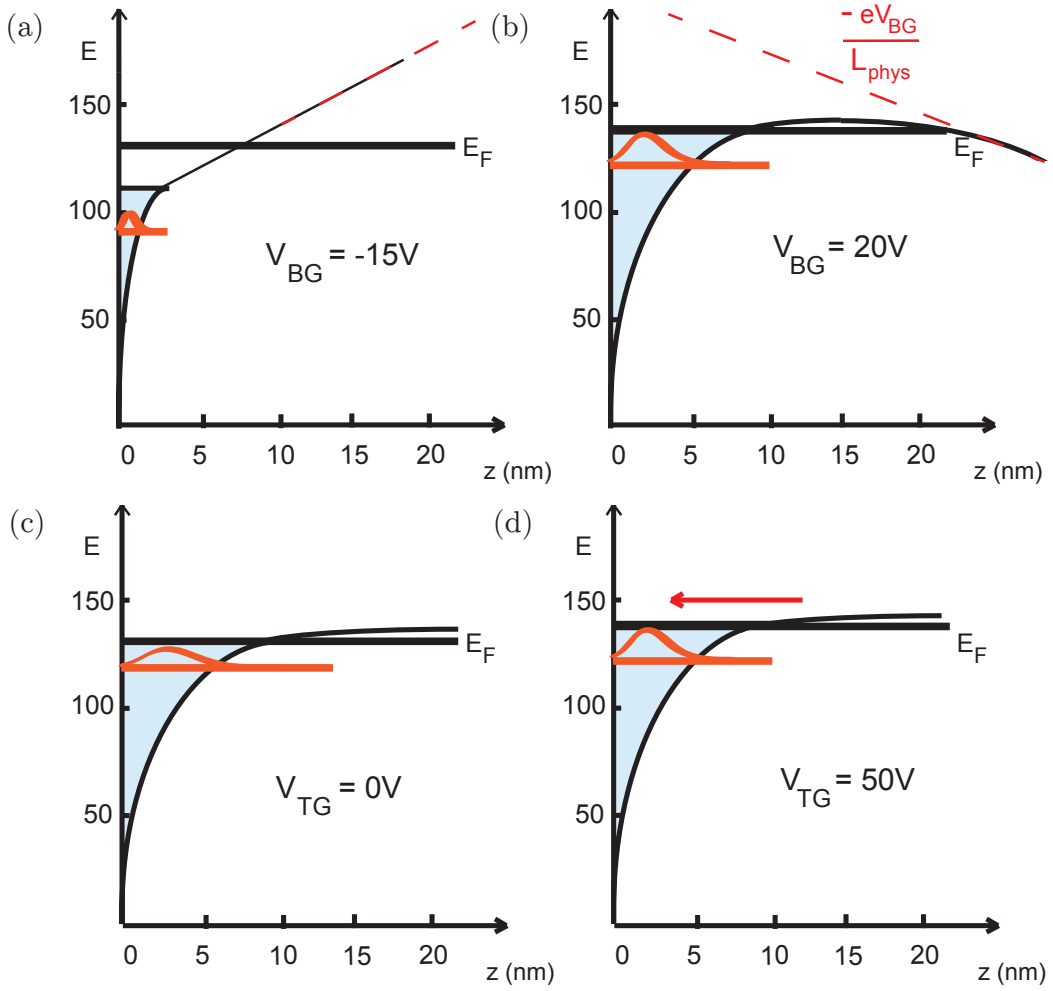

Figure B.2 – (a) Schematic of the 2DEG underdoped with a negative back gate voltage. The Fermi energy is low, the wave function is confined toward the interface. (b) In the overdoped region driven by a positive back gate, the 2DEG is delocalized and the Fermi energy is close to the top of the dome (c,d) The two schematics represent the effect of doping with a top gate. The wave function is more localized at $V_{TG} = 50V$ despite a higher Fermi energy.

Appendix C

Radio Frequency measurements

C.1 Telegrapher equation

The following derivation of the equations in a coaxial cable is taken from [87]. It assumes that the cylinders are perfect conductors. In the cylindrical coordinates, Maxwell equations (5.1) and (5.2) become

$$-\frac{\partial E_\phi}{\partial z}\mathbf{u}_\rho + \frac{\partial E_\rho}{\partial z}\mathbf{u}_\phi + \frac{1}{\rho}\frac{\partial}{\partial \rho}(\rho E_\phi)\mathbf{u}_z = -j\omega\mu(H_\rho \mathbf{u}_\rho + H_\phi \mathbf{u}_\phi) \tag{C.1}$$

$$-\frac{\partial H_\phi}{\partial z}\mathbf{u}_\rho + \frac{\partial H_\rho}{\partial z}\mathbf{u}_\phi + \frac{1}{\rho}\frac{\partial}{\partial \rho}(\rho H_\phi)\mathbf{u}_z = j\omega\epsilon(E_\rho \mathbf{u}_\rho + \phi \mathbf{u}_\phi) \tag{C.2}$$

For a TEM wave between two conducting cylinders of radius a and b, the z components must be zero which means

$$E_\phi = \frac{f(z)}{\rho} \tag{C.3}$$

$$H_\phi = \frac{g(z)}{\rho} \tag{C.4}$$

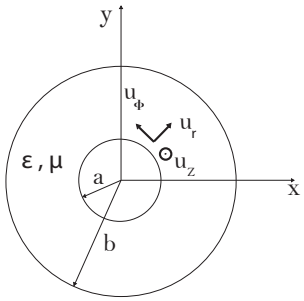

The electric field must be zero in the conducting regions, which set the boundary condition $E_\phi = 0$ at $\rho = a, b$. Using (C.3) and (C.2) we deduce that $E_\phi = 0$ and $H_\rho = 0$ everywhere. The remaining terms of the maxwell equation are then

$$\frac{\partial E_\rho}{\partial z} = -j\omega\mu H_\phi \tag{C.5}$$

$$\frac{\partial H_\phi}{\partial z} = -j\omega\epsilon E_\rho \tag{C.6}$$

From H_ϕ in (C.4) and (C.6), E_ρ must be of the form

$$E_\rho = \frac{h(z)}{\rho} \tag{C.7}$$

Equation (C.5) and (C.6) can then be written as

$$\frac{\partial h(z)}{\partial z} = -j\omega\mu g(z) \tag{C.8}$$

$$\frac{\partial g(z)}{\partial z} = -j\omega\epsilon h(z) \tag{C.9}$$

The voltage drop between the two cylinders is easily computed by integrating the electric field

$$V(z) = \int_{\rho=a}^{b} E_\rho(\rho, z)d\rho = h(z)\int_{\rho=a}^{b} \frac{d\rho}{\rho} = h(z)\ln\frac{b}{a} \tag{C.10}$$

and the total current at $\rho = a$ can be calculated from (C.4)

$$I(z) = \int_{\phi=0}^{2\pi} H_\phi(a, z)ad\phi = 2\pi g(z) \tag{C.11}$$

We finally get the telegrapher equations by using(C.10) and (C.11) in (C.8) and (C.9)

$$\frac{\partial V(z)}{\partial z} = -j\omega L I(z) \quad \text{where} \quad L = \frac{\mu}{2\pi}\ln\frac{b}{a} \tag{C.12}$$

$$\frac{\partial I(z)}{\partial z} = -(G + j\omega C)V(z) \quad \text{where} \quad C = \frac{2\pi\epsilon'}{\ln(b/a)} \text{ and } G = \frac{2\pi\omega\epsilon''}{\ln(b/a)} \tag{C.13}$$

The telegrapher equations lead to the same wave equation as (5.4), except that now the propagation is described along the coaxial cable in terms of voltage and current.

C.2 STO losses

The RF measurement reported in chapter 5 are performed in the frequency range 0.3-0.6GHz where in principle phonons excitations are expected to contribute to losses. However, the literature on STO shows that under the application of an external electric field (gating , the transverse optical phonon modes can generate dissipation at frequency much below the typical phonon frequency [157].

Definition Losses are defined as the ratio $\tan(\delta) = \epsilon''/\epsilon'$, where we recognize the real and imaginary part of the dielectric constant of (5.5). For a plan capacitor, losses due to RF frequency are well described by a conductance G_{STO} in parallel. When a dielectric with a complex dielectric constant ϵ is placed between the two plates of a capacitor its capacitance is generalized as follow $C = \frac{\epsilon C_0}{\epsilon_0}$ [158], where C_0 is the capacitance with the same geometry in the presence of vacuum. Figure C.1 gives a physical meaning to the angle δ between the charging current and the loss current.

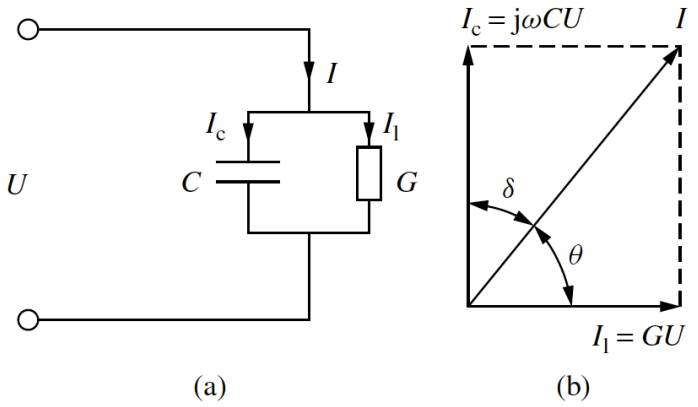

Figure C.1 – Complex impedance of a capacitance with losses : (a) is the equivalent circuit (b) plots the angle δ between the charging current I_c and the loss current I_l (figure taken from [158])

Let us determine the expression of G_{STO} as a function of $\tan(\delta)$

$$I = j\omega CU = j\omega(\epsilon' - j\epsilon'')\frac{C_0}{\epsilon_0}U = j\omega\epsilon'(1 - j\tan(\delta))\frac{C_0}{\epsilon_0}U = (j\omega C_{\mathrm{STO}} + \underbrace{\tan(\delta)\omega C_{\mathrm{STO}}}_{=G_{\mathrm{STO}}})U$$

The conductance that describes the losses is

$$G_{\mathrm{STO}} = \tan(\delta)\omega C_{\mathrm{STO}} \tag{C.14}$$

When there is no loss, G_{STO} is equal to zero. In general losses are due to multiple mechanisms and the total loss tangent is the sum of all contributions [159]

$$\tan(\delta) = \sum_i \tan(\delta_i) \tag{C.15}$$

Since 1962, it is known experimentally that bulk STO undergoes dielectric losses due to the presence of soft phonon modes [160]. The first measurement in the literature for the dependence of the losses with electric field at RF frequency was done by Vendik et al. using $YBa_2Cu_3O_7$ to create a resonant cavity [161]. Very recently, Davidovikj et al. [162] have measured losses as a function of frequency and gate voltage using a resonator deposited on top of a bulk STO sample. They could measure values up to $\tan(\delta) = 10^{-2}$ for high electric field ($E = 3000\text{V/mm}$). Astaview et al. proposed to explain theses losses with the quasi-Debye dissipation mechanism [163]. For low electric field ($< 5000\text{V/mm}$) losses are proportional to ω and to the tunability $n(E) = (\epsilon(0) - \epsilon(E))/\epsilon(0)$ via a coefficient A which is independent of the electric field.

$$\tan(\delta) = A \times \omega \times n(E) \tag{C.16}$$

We see that no loss is expected when no electric field is applied because $n(0) = 0$. Dissipation occurs when the electric field starts to break inversion symmetry. At low temperature, optical phonons become softer [165] creating acoustic wave at RF frequency. This phonons involve titanium atoms which locally create a dipole with the oxygen octahedra. This dipole interacts with the incident electromagnetic field via the electrostriction and inverse piezoelectric effect. This mechanism was validated experimentally by Gevorgian et al. in 2009 [164]. It is responsible for non negligible losses as the external electric field and frequency increase. At higher electric field, losses start to decrease as we can see on figure C.2. This effect is due to the hardening of the polar phonon mode under a bias voltage.

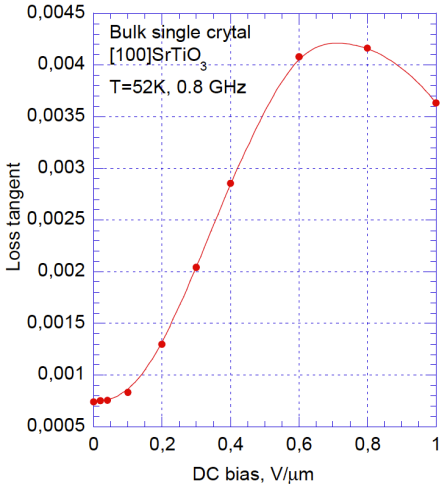

Figure C.2 – Losses as a function of electric field taken from ref. [164]

Using (C.14) and (C.16) it is finally possible to write the contribution of the losses via the parallel conductance G_{STO} as follow

$$G_{\text{STO}}(\omega, E) = A \times n(E) \times C_{\text{STO}}(E) \times \omega^2 \tag{C.17}$$

This formula is used in chapter 5 to extract the normal part of the 2DEG conductance. Note that formally, it has been demonstrated for a plate capacitor geometry where the AC current flows in the direction of the external electric field (gate). In our geometry, we consider an AC current flowing in a direction perpendicular to the external electric field as the gate voltage is applied between the gate and the 2DEG.

C.3 Mattis Bardeen calculations

C.3.1 Sum rule derivation

C.3.1.1 Kramers Kronig

As any analytical function, the conductance σ verifies the Kramers Kronig equation, which will be useful to demonstrate the sum rule.

$$\mathrm{Re}\sigma(\omega) = \frac{1}{\pi}\mathcal{P}\int d\omega' \frac{\mathrm{Im}\sigma(\omega')}{\omega' - \omega} \tag{C.18}$$

$$\mathrm{Im}\sigma(\omega) = -\frac{1}{\pi}\mathcal{P}\int d\omega' \frac{\mathrm{Re}\sigma(\omega')}{\omega' - \omega} \tag{C.19}$$

C.3.1.2 Sum rule

In the presence of disorder one has [118] $\mathrm{Re}\Pi_{\alpha\beta}(\mathbf{q}=0,\omega\to 0) = \frac{n}{m}\delta_{\alpha\beta}$ which leads to

$$\mathrm{Re}\sigma_{\alpha\beta} = \frac{e^2}{\omega}\mathrm{Im}\Pi_{\alpha\beta}(\mathbf{q}=\mathbf{0},\omega) \tag{C.20}$$

Using the Kramers Kronig relation and the relation (C.20), one finds

$$\int_{-\infty}^{\infty}\mathrm{Re}\sigma_{\alpha\beta}(\omega)d\omega = e^2\int_{-\infty}^{\infty}\frac{\mathrm{Im}\Pi_{\alpha\beta}(\mathbf{q}=\mathbf{0},\omega)}{\omega}d\omega = \pi e^2\mathrm{Re}\Pi_{\alpha\beta}(\mathbf{q}=\mathbf{0},\omega) \tag{C.21}$$

C.3.2 Low frequency limit

Let us start from the mattis bardeen formula

$$\frac{\sigma_{1s}}{\sigma_{1n}}(\omega,T) = \frac{\pi n_s}{m\sigma_n}\delta(\omega) + \frac{2}{\omega}\int_{\Delta}^{\infty} dE(f(E) - f(\omega+E))g(E) + \frac{\Theta(\omega-2\Delta)}{\omega}\int_{\Delta-\omega}^{-\Delta} dE(1-2f(\omega+E))g(E) \tag{C.22}$$

$$\frac{\sigma_{2s}}{\sigma_{1n}}(\omega,T) = \frac{1}{\omega}\int_{max(-\Delta,\Delta-\omega)}^{\Delta} dE(1-2f(\omega+E))g(E)\frac{E(E+\omega)+\Delta^2}{\sqrt{\Delta^2-E^2}\sqrt{(E+\omega)^2-\Delta^2}} \tag{C.23}$$

with

$$g(E) = \frac{E(E+\hbar\omega)+\Delta^2}{\sqrt{E^2-\Delta^2}\sqrt{(E+\hbar\omega)^2-\Delta^2}} \tag{C.24}$$

As $\omega\to 0$ the integral in 4.17 can be evaluated as

$$\int_{\Delta-\omega}^{\Delta}[f(-E-\omega)-f(E+\omega)]\frac{E(E+\omega)+\Delta^2}{\sqrt{\Delta^2-E^2}\sqrt{(E+\omega)^2-\Delta^2}} \tag{C.25}$$

$$\simeq \tanh\frac{\beta\Delta}{2}2\Delta^2\int_{\Delta-\omega}^{\Delta} dE\frac{1}{\sqrt{\Delta^2-E^2}\sqrt{(E+\omega)^2-\Delta^2}} \tag{C.26}$$

Indeed $(f(-E-\omega)-f(E+\omega))/2 \to \tanh(\beta\Delta/2)\delta(E-\Delta)$ and we can prove that the rest of the integral is independent of ω. If we write $y = \Delta - E$ in the last part of the integral

$$-\int_{\omega}^{0} dy \frac{1}{\sqrt{y(2\Delta-y)}} \frac{1}{\sqrt{(\omega-y)(\omega+2\Delta-y)}} \simeq \int_{0}^{\omega} dy \frac{1}{2\Delta} \frac{1}{\sqrt{y}} \frac{1}{\sqrt{\omega-y}} \tag{C.27}$$

$$= \frac{1}{2\Delta} 2 \arctan \frac{\sqrt{y}}{\sqrt{\omega-y}}\Big|_{0}^{\omega} = \frac{\pi}{2\Delta} \tag{C.28}$$

Finally, we find

$$\frac{\sigma_2(\omega \to 0, T)}{\sigma_n} = \frac{\pi\Delta}{\omega} \tanh \frac{\beta\Delta(T)}{2} \tag{C.29}$$

C.3.3 Superfluid stiffness in 2D disordered systems

We can express the superfluid stiffness in the dirty limit by using the Mattis Bardeen theory. Equation (4.20) gives

$$J_s = \frac{\hbar^2 n_s^{2D}}{4m} = \frac{R_0}{R_n} \frac{\Delta}{4} \tag{C.30}$$

Where $R_0 = \frac{h}{e^2} = 25.813 k\Omega/\square$. The higher the disorder described by R_n the lower the stiffness will be. In other words, the higher the disorder, the lower the number of electron pairs created below T_c will be. More generally, in a 2D geometry, the superfluid stiffness is defined for transverse conductivity in the limit $\mathbf{q} \to 0$. For a current in the x direction $J_x = -e^2 J_s A_x$ with

$$J_s = \frac{n}{m} + \mathrm{Re}\Pi_{xx}(q_x = 0, q_y \to 0, \omega = 0) \tag{C.31}$$

The real part of the conductivity becomes [129] :

$$\sigma_1(\omega) = e^2 \pi J_s \delta(\omega) - \underbrace{e^2 \frac{\mathrm{Im}\Pi_{xx}(0,\omega)}{\omega}}_{\sigma_{\mathrm{reg}}(\omega)} \tag{C.32}$$

The disorder should contribute to the dissipative part of σ at non-zero frequencies. Hence using the sum rule, it is possible to relate the superconducting stiffness to the spectral weight of σ_1.

$$\int_0^{\infty} d\omega \sigma_1(\omega) = \frac{\pi e^2}{2} J_s + \int_{0^+}^{\infty} \sigma_{\mathrm{reg}}(\omega) = \frac{\pi e^2}{2} \frac{n}{m} \tag{C.33}$$

The contribution from the imaginary part of the current-current correlation σ_{reg} can come from collective modes. As we have seen above, 2D superconductors are dominated by phase fluctuations. Dissipation can therefore occur at finite frequency even below the gap due to phase modes. In order to get insight in the physics of phase fluctuations in 2D, we must let aside the mean field theory and the first order perturbation and use the renormalization group theory.

Appendix D

Fabrication recipes

D.1 General procedure for the amorphous LAO template method

Step 1 : TiO_2 termination

- Cleaning with de-ionised water during 15 minutes in ultra sound bath at 50-60 °C
- Etching with buffered hydrofluoric acid (BHF, ref: BE 7-1 NC1) for 40s
- Annealing in oven for 3 hours at 1000 °C under oxygen pressure PO_2= 1 bar
- Cleaning with de-ionised water for 30 min in ultra sound bath at 50-60 °C
- Drying with nitrogen

Step 2 : amorphous LAO The second step is the deposition of amorphous LAO template.

- Design of a Hall bar by optical lithography using AZ2021 negative resist (2.1μm thick)
- Deposition of amorphous LAO by PLD at room temperature under $PO_2 = 2.10^{-4}$ mbar
- Lift-off in hot acetone

Step 3 : crystalline LAO Up to this stage, no conducting interface is formed because of the amorphous nature of the LAO template. In the third step, the sample is placed in the PLD in order to deposit the crystalline layer

- Heating at 25 C.min^{-1}
- $LaAlO_3$ deposition by PLD at T=650°C under $PO_2 = 2.10^{-4}$ mbar
- Cooling at 25° C.min^{-1} under $PO_2 = 10^{-1}$ mbar
- Annealing at T=500°C during 30min under $PO_2 = 400$ mbar
- Cooling at 25 ° C.min^{-1} down to room temperature
- waiting 30 min with $PO_2 = 400$ mbar before breaking the vacuum

Step 4 : Si_3N_4

- optical lithography with thick AZ2021 negative resist (2.1 μm)
- Si_3N_4 is deposited at LPN-Marcoussis by magnetron sputtering on a target of pure silicium under $P = 1 \times 10^{-2}$mbar of a mixture Ar (67.5%) - N_2 (32.5%), with a radio frequency power of 200W during 5 hours. The temperature was monitored to stay below 80°C.

Step 5 : Top Gate Deposition

— optical lithography with a negative resist (2.1 μm thick) AZ 2021
— evaporation Ti 10nm and Au 200nm on Plassys casing at Paris 7 by e-beam

QPC Fabrication Here is the receipe optimized on this sample :

— A4 PMMA spin coating 4500/4000/30
— Bake 4 min at 100°C
— Deposition of Al layer (20nm) in order to evacuate the electrons easily
— Exposition to e-beam. Dose 1600μC/cm^2 with a current of 500 pA, a resolution 1nm and a step of 1nm
— 2' in a NaOH bath in order to take out Al layer
— Evaporation in plassys casing Ti (3nm)/Au (100nm)
— Lift off with hot trichloroethylene

D.2 Sample fabrication

Sample A : SURF0340 Growth Temperature: 650 °C
P(O2) during growth: 2x10-4 mbar
Fluence: $\sim$ 0.6 J/cm^2
Laser repetition rate: 1 Hz
Thickness: 8 u.c. (grown at 30.9 pulses/u.c.)
Target-substrate distance: 64 mm
Post-annealing: 30 min at 500 Celsius, in about 250-400 mbar of oxygen.
Cool-down in about 400 mbar of oxygen at 20 Celsius/min

Sample B and C Details are given in ref. [95]. The growth parameters are the same for all the samples (B, C0, C1 and C2).

Sample D : SURF0737 Growth Temperature: 650 Celsius
P(O2) during growth: 2x10-4 mbar
Fluence: 0.7-0.8 J/cm^2
Laser repetition rate: 1 Hz
Thickness: 14 u.c. (grown at 23.1 pulses/u.c.)
Target-substrate distance: 64 mm
Post-annealing: 60 min et non 30min at 500 Celsius, in about 250-400mbar of oxygen
Cool-down in about 400 mbar of oxygen at 20 Celsius/min

Sample E : SURF0612 Growth Temperature: 650 Celsius
P(O2) during growth: $2 \times 10{-}4$ mbar

Fluence: ~ 1 J/cm^2
Laser repetition rate: 1 Hz
Thickness: 5 u.c. (grown at 26.2 pulses/u.c.)
Target-substrate distance: 64 mm
Post-annealing: 30 min at 500 Celsius, in about 250-400 mbar of oxygen.
Cool-down in about 400 mbar of oxygen at 20 Celsius/min.

Appendix E

BCS and Josephson effect

E.1 BCS in a nutshell

BCS theory assumes the existence of an attractive potential V between electrons. No matter how small is this energy or what is the underlying pairing mechanism, such interaction creates a complete reorganization of the electronic structure. The simple s-wave singlet pairing hamiltonian in a mean field approximation is :

$$H_{int} = \sum_{\mathbf{k}} \Delta_{\mathbf{k}} c^{\dagger}_{\mathbf{k}\uparrow} c^{\dagger}_{-\mathbf{k}\downarrow} + \Delta^{*}_{\mathbf{k}} c_{-\mathbf{k}\downarrow} c_{\mathbf{k}\uparrow} \tag{E.1}$$

where $\Delta_{\mathbf{k}} = -\sum_l V_{\mathbf{kl}} \langle c_{\mathbf{l}\downarrow} c_{\mathbf{l}\uparrow} \rangle$.

In the particle-hole space, one can rewrite the total hamiltonian as follow :

$$H = H_0 + H_{int} = \sum_{\mathbf{k}} \Psi^{\dagger}_{\mathbf{k}} \begin{pmatrix} \xi_{\mathbf{k}} & \Delta_{\mathbf{k}} \\ \Delta^{*}_{\mathbf{k}} & -\xi_{\mathbf{k}} \end{pmatrix} \Psi_{\mathbf{k}} \quad \text{where} \quad \Psi_{\mathbf{k}} = \begin{pmatrix} c_{\mathbf{k}\uparrow} \\ c^{\dagger}_{-\mathbf{k}\downarrow} \end{pmatrix} \tag{E.2}$$

It gives rise to an exotic ground state $|\phi_0\rangle = \Pi_{\mathbf{k}} (a_{\mathbf{k}} + b_{\mathbf{k}} c^{\dagger}_{n\uparrow} c^{\dagger}_{n\downarrow}) |0\rangle$ where electrons come in pair of opposite momentum and spin. Bardeen Cooper and Schriffer demonstrated that such pairing minimize the total energy. Any excitation requires a minimal energy $E_{\mathbf{k}} = \sqrt{\Delta^2 + \xi^2_{\mathbf{k}}}$ and can be described by a linear combination of particle and hole operators :

$$\gamma^{\dagger}_{\mathbf{k}\uparrow} = u^{*}_{\mathbf{k}} c^{\dagger}_{\mathbf{k}\uparrow} - v^{*}_{\mathbf{k}} c_{\mathbf{k}\downarrow} \tag{E.3}$$

$$\gamma^{\dagger}_{\mathbf{k}\downarrow} = u^{*}_{\mathbf{k}} c^{\dagger}_{-\mathbf{k}\downarrow} + v^{*}_{\mathbf{k}} c_{\mathbf{k}\uparrow} \tag{E.4}$$

where $u_{\mathbf{k}}$ and $v_{\mathbf{k}}$ are found by solving bogolubov equations [166] (see figure E.1(a)). Below the critical temperature T_c, the pairs are formed and behave like bosons. Even in the presence of impurities, such state remain superfluid.

Within this new basis, gap equation becomes

$$\Delta_{\mathbf{k}} = -\sum_{l} V_{\mathbf{kl}} u^{*}_{\mathbf{l}} v_{\mathbf{l}} \langle 1 - \gamma^{*}_{\mathbf{l}\uparrow} \gamma_{\mathbf{l}\uparrow} - \gamma^{*}_{\mathbf{l}\downarrow} \gamma_{\mathbf{l}\downarrow} \rangle \tag{E.5}$$

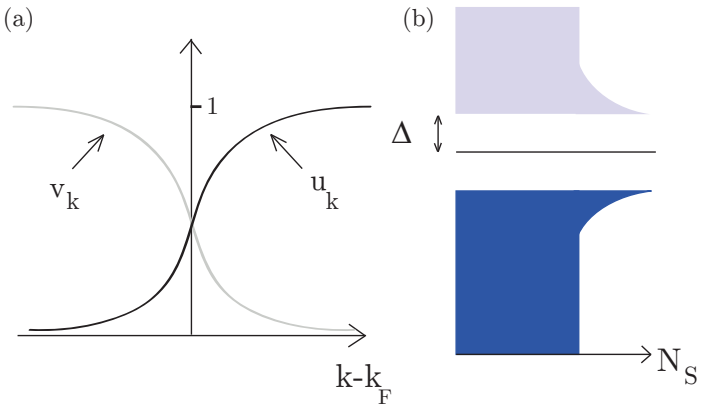

Figure E.1 – (a) $u_{\mathbf{k}}$ and $v_{\mathbf{k}}$ near Fermi level (b) Superfluid density of states in BCS theory

with $2u_{\mathbf{l}}^{*}v_{\mathbf{l}} = \Delta_{\mathbf{l}}/E_{\mathbf{l}}$. Bardeen, Cooper and Schriffer finally assumed that $V_{\mathbf{kl}}$ is constant and equal to $-V$ when $|\xi_{\mathbf{l}}|< \hbar\omega_c$ and 0 elsewhere. At $T = 0$, the gap is given by

$$\Delta = \frac{\hbar\omega_c}{\sinh[1/N(0)V]} \simeq 2\hbar\omega_c e^{-1/N(0)V} \tag{E.6}$$

where N(0) is the density of states at the Fermi energy E_F. The gap energy is related to the critical temperature [115]

$$\Delta(T = 0) = 1.76 k_B T_c \tag{E.7}$$

We see in equation E.6 that the density of states at Fermi energy N(0) and the strength of the attractive electron-electron potential interaction V set a mininimal gap energy Δ. The dynamics of any excited state is non a non trivial combination of particles and holes on top of a completely reorganized ground state with gaped density of states around the Fermi level as plotted in figure E.1(b).

E.2 Josephson effect

Josephson effect is a mechanism that describes the phase coeherent coupling of two superconducting condensates separated by a thin non-superconducting barrier (insulator, normal metal, constriction...). In this section, we first introduce electron tunneling between two metals and then discuss the case where the metals are replaced by superconductors.

E.2.1 Electron tunneling

We consider the situation described by figure E.3 where an electrun tunnel from left to right. The probability $\mathcal{P}_{L\to R}$ to tunnel from left to right

$$P_{L\to R} = \frac{2\pi}{\hbar}|\langle L|\, H_T\, |R\rangle\, |^2 N_R(E)(1 - f(E)) \tag{E.8}$$

where H_T is the tunneling Hamiltonian. The current from left to right is given by

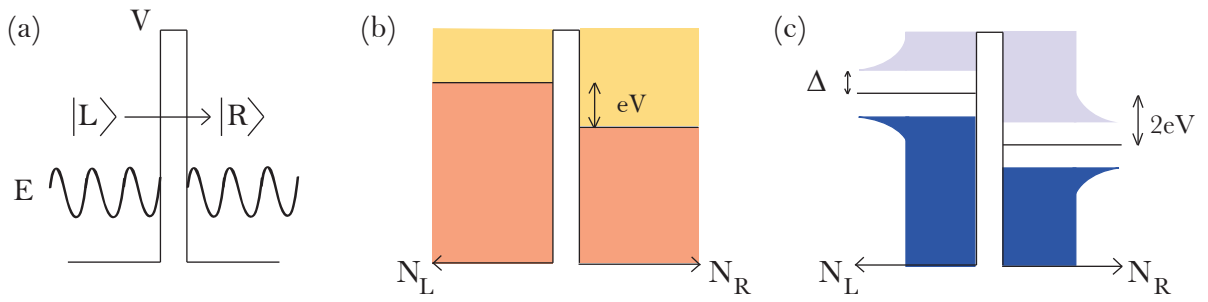

Figure E.2 – (a) Tunnel junction for particle coming from the left with a probability $P_{L\to R}$ to go from state $|L\rangle$ to $|R\rangle$ (b) Electronic tunneling between two metals depending on the density of states of each material and the applied voltage V (c) Tunneling between two superconductors with gap Δ

$$J_{L\to R} = e\int P_{L\to R} N_L(E-eV) f(E-eV) dE \tag{E.9}$$

$$= e\int \frac{2\pi}{\hbar} |\langle L|\, H_T\, |R\rangle\,|^2 N_L(E-eV) f(E-eV) N_R(E)(1-f(E)) dE \tag{E.10}$$

where V is the voltage between both superconductors. The current accross a section of area A is thus the sum of $J_{L\to R}$ and $J_{R\to L}$

$$I = \frac{2\pi e A}{\hbar}|T|^2 \int_{-\infty}^{+\infty} N_L(E-eV) N_R(E)[f(E-eV) f(E)] dE \tag{E.11}$$

Here the current depends on the tunneling amplitude T and on the respective density of states of each metal. We will see now that the situation is much different if we replace the two metals by two superconductors.

E.2.2 Josephson effect simple derivation

A simple derivation of Josephson effect was demonstrated in Feynman's lecture [167]. Let us consider two superconductors seperated by a thin insulating region. If the insulating region is thin enough, there is a finite amplitude t for a cooper pair to tunnel from one side to the other.

$$i\hbar \frac{\partial \psi_1}{\partial t} = E_1 \psi_1 + t\psi_2 \tag{E.12}$$

$$i\hbar \frac{\partial \psi_2}{\partial t} = E_2 \psi_2 + t\psi_1 \tag{E.13}$$

In a superconductor, the energy of the ground state is given by $E = 2\mu$ where μ is the chemical potential. By applying a voltage V between the two superconductors, the difference of energy $E_1 - E_2 = 2eV$. We thus get

$$i\hbar \frac{\partial \psi_1}{\partial t} = -eV\psi_1 + t\psi_2 \tag{E.14}$$

$$i\hbar \frac{\partial \psi_2}{\partial t} = +eV\psi_2 + t\psi_1 \tag{E.15}$$

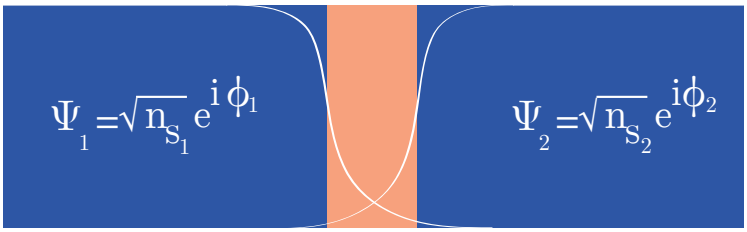

Figure E.3 – Schematic of a Josephson junction from left superconductor with phase ϕ_1 and right superconductor with phase ϕ_2. The barrier can be an insulator or a metal.

By taking real and imaginary part and replacing ψ_1 and ψ_2 by the Ginzburg Landau expression

$$\psi_1 = \sqrt{n_{S_1}} e^{i\phi_1} \qquad \psi_2 = \sqrt{n_{S_2}} e^{i\phi_2} \tag{E.16}$$

We finally get a set a four equations from (E.14) and (E.15)

$$\frac{\partial n_{S_1}}{\partial t} = \frac{2}{\hbar} t n_{S_1} n_{S_2} \sin(\phi) \tag{E.17}$$

$$\frac{\partial n_{S_2}}{\partial t} = -\frac{2}{\hbar} t n_{S_2} n_{S_1} \sin(\phi) \tag{E.18}$$

$$\frac{\partial \phi_1}{\partial t} = \frac{t}{\hbar} \sqrt{\frac{n_{S_1}}{n_{S_2}}} \cos(\phi) + \frac{eV}{\hbar} \tag{E.19}$$

$$\frac{\partial \phi_2}{\partial t} = \frac{t}{\hbar} \sqrt{\frac{n_{S_2}}{n_{S_1}}} \cos(\phi) - \frac{eV}{\hbar} \tag{E.20}$$

The current density $J = \frac{\partial n_{S_1}}{\partial t} = -\frac{\partial n_{S_2}}{\partial t}$ can be integrated on the area of the barrier to obtain the first Josephson equation

$$I = I_c \sin(\phi) \tag{E.21}$$

where I_c is the critical current above which the junction switches in the normal state. This effect is also called the DC Josephson effect.

We can also deduce the second equation which relates ϕ as a function of the applied voltage

$$\frac{\partial \phi}{\partial t} = \frac{2e}{\hbar} V \tag{E.22}$$

This relation is called AC Josephson effect. It means that at a fixed voltage V across the junction, an ac current oscillating at pulsation $\omega_J = 2eV/\hbar$ will be generated. Ambegaokar and Baratoff derived the expression of the critical current as a function of the gap energy Δ and the temperature in the case of a tunnel barrier

$$I_c R_n = \frac{\pi \Delta}{2e} \tanh(\Delta / 2k_B T) \tag{E.23}$$

This simple derivation of the Josephson effect do not take into account some effect which can have a non negligible impact on the dynamical properties of the junction. We will therefore present rapidly the RCSJ model.

E.2.3 RCSJ model

When the barrier between the two superconductors is a metal, the junction should be described by a perfect Josephson element in parallel with a resistor. The junction should be described with a resistance R in parallel. In addition, a capacitor should also be added to account for the possible charging effects on the superconducting electrodes. The total current circulating in the junction is the sum of the three branches of the circuit. Figure E.4 shows the equivalent electrical circuit corresponding to this more realistic description of a Josephson junction. Equation E.21 then becomes

$$I = I_c \sin(\phi) + \frac{V}{R} + C\frac{dV}{dt} \tag{E.24}$$

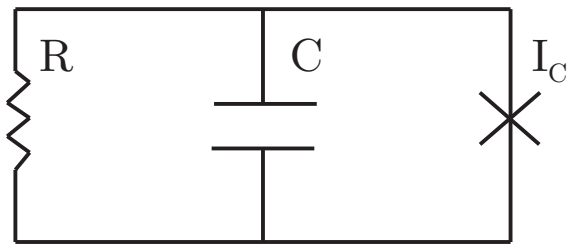

Figure E.4 – RCSJ model equivalent circuit

Using equation E.22 and a normalized current $i = I/I_c$, a normalized time $\tau = \omega_p t$ with $\omega_p = \sqrt{2\pi I_c/\phi_0 C}$, it becomes

$$i = \frac{d^2\phi}{d\tau^2} + \frac{1}{RC\omega_p}\frac{d\phi}{d\tau} + \sin(\phi) \tag{E.25}$$

This equation can be mapped to mecanical problem of a mass m in a washboard potential $U = -\cos(\phi) - i\phi$ with a damping force $-\eta\dot{\phi}$.

$$m\ddot{\phi} + \eta\dot{\phi} + \frac{\partial U}{\partial \phi} = 0 \tag{E.26}$$

with $m = (\phi_0/2\pi)^2 C$ and $\eta = (\phi_0/2\pi)^2/R$. When a current is applied, the washboard potential represented on figure E.5 is tilted. When there is no current in the junction, the phase is trapped in one of the minima. According to the second Josephson equation, no voltage is developped because $V \propto \dot{\phi} = 0$. When the curent reach a critical value I_s, the phase starts to move along the potential. This is called a switching event.

The precise motion of the phase then depends on the mc Cumber parameter

$$\beta_c = \frac{i_c(T) C R_0^2}{\hbar/2e} \tag{E.27}$$

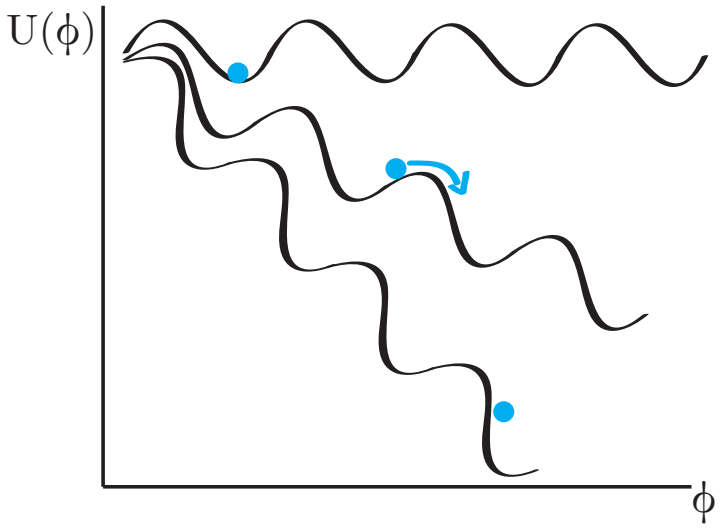

Figure E.5 – Switching event

If $\beta_c << 1$ the capacitance is sufficiently small to be negligible. In this case, the mass in the washboard potential has a small inertia. When the potential is brought back to horizontal (I=0), the phase stops immediately and the return current is equal to the switching current. This situation is called the overdamped situation. On the contrary if $\beta_c >> 1$ the effective mass of the phase is higher and the rettrapping current I_r is lower than I_s.

Bibliography

[1] A. Ohtomo and H. Y. Hwang. A high-mobility electron gas at the LaAlO3/SrTiO3 heterointerface. *Nature*, 427(6973):423–426, jan 2004. URL: https://doi.org/10.1038%2Fnature02308, doi:10.1038/nature02308.

[2] N. Reyren, S. Thiel, A. D. Caviglia, L. F. Kourkoutis, G. Hammerl, C. Richter, C. W. Schneider, T. Kopp, A.-S. Ruetschi, D. Jaccard, M. Gabay, D. A. Muller, J.-M. Triscone, and J. Mannhart. Superconducting interfaces between insulating oxides. *Science*, 317(5842):1196–1199, aug 2007. URL: http://dx.doi.org/10.1126/science.1146006, doi:10.1126/science.1146006.

[3] A. D. Caviglia, S. Gariglio, N. Reyren, D. Jaccard, T. Schneider, M. Gabay, S. Thiel, G. Hammerl, J. Mannhart, and J.-M. Triscone. Electric field control of the LaAlO3/SrTiO3 interface ground state. *Nature*, 456(7222):624–627, dec 2008. URL: http://dx.doi.org/10.1038/nature07576, doi:10.1038/nature07576.

[4] M. Ben Shalom, M. Sachs, D. Rakhmilevitch, A. Palevski, and Y. Dagan. Tuning spin-orbit coupling and superconductivity at the SrTiO 3 / LaAlO 3 interface: A magneto-transport study. *Phys. Rev. Lett.*, 104(12), mar 2010. URL: http://dx.doi.org/10.1103/PhysRevLett.104.126802, doi:10.1103/physrevlett.104.126802.

[5] Lu Li, C. Richter, J. Mannhart, and R. C. Ashoori. Coexistence of magnetic order and two-dimensional superconductivity at LaAlO3/SrTiO3 interfaces. *Nature Physics*, 7(10):762–766, sep 2011. URL: http://dx.doi.org/10.1038/nphys2080, doi:10.1038/nphys2080.

[6] A. von Hippel. Ferroelectricity, domain structure, and phase transitions of barium titanate. *Reviews of Modern Physics*, 22(3):221–237, jul 1950. URL: https://doi.org/10.1103%2Frevmodphys.22.221, doi:10.1103/revmodphys.22.221.

[7] C. Ulrich, G. Khaliullin, S. Okamoto, M. Reehuis, A. Ivanov, H. He, Y. Taguchi, Y. Tokura, and B. Keimer. Magnetic order and dynamics in an orbitally degenerate ferromagnetic insulator. *Physical Review Letters*, 89(16), sep 2002. URL: https://doi.org/10.1103%2Fphysrevlett.89.167202, doi:10.1103/physrevlett.89.167202.

[8] M. Cwik, T. Lorenz, J. Baier, R. Müller, G. André, F. Bourée, F. Lichtenberg, A. Freimuth, R. Schmitz, E. Müller-Hartmann, and M. Braden. Crystal and magnetic structure of LaTiO 3 : Evidence for nondegenerate t 2 g orbitals. *Phys. Rev. B*, 68(6), aug 2003.

URL: http://dx.doi.org/10.1103/PhysRevB.68.060401, doi:10.1103/physrevb.68.060401.

[9] Zhengguo Xiao, Cheng Bi, Yuchuan Shao, Qingfeng Dong, Qi Wang, Yongbo Yuan, Chenggong Wang, Yongli Gao, and Jinsong Huang. Efficient, high yield perovskite photovoltaic devices grown by interdiffusion of solution-processed precursor stacking layers. *Energy & Environmental Science*, 7(8):2619, jun 2014. URL: https://doi.org/10.1039%2Fc4ee01138d, doi:10.1039/c4ee01138d.

[10] Fikadu Alema and Konstantin Pokhodnya. Dielectric properties of BaMg13Nb23o3 doped ba0.45Sr0.55Tio3 thin films for tunable microwave applications. *Journal of Advanced Dielectrics*, 05(04):1550030, dec 2015. URL: https://doi.org/10.1142%2Fs2010135x15500307, doi:10.1142/s2010135x15500307.

[11] A. Ohtomo, D. A. Muller, J. L. Grazul, and H. Y. Hwang. Artificial charge-modulationin atomic-scale perovskite titanate superlattices. *Nature*, 419(6905):378–380, sep 2002. URL: https://doi.org/10.1038%2Fnature00977, doi:10.1038/nature00977.

[12] Etsuro Sawaguchi, Atsushi Kikuchi, and Yoichi Kodera. Microscopic examination of SrTiO3 heterostructures at low temperatures. *Journal of the Physical Society of Japan*, 18(3):459–460, mar 1963. URL: http://dx.doi.org/10.1143/JPSJ.18.459, doi:10.1143/jpsj.18.459.

[13] M. Honig, J. A. Sulpizio, J. Drori, A. Joshua, E. Zeldov, and S. Ilani. Local electrostatic imaging of striped domain order in LaAlO3/SrTiO3. *Nature Materials*, 12(12):1112–1118, nov 2013. URL: http://dx.doi.org/10.1038/nmat3810, doi:10.1038/nmat3810.

[14] K. A. Müller and H. Burkard. SrTi o 3 : An intrinsic quantum paraelectric below 4 K. *Phys. Rev. B*, 19(7):3593–3602, apr 1979. URL: http://dx.doi.org/10.1103/PhysRevB.19.3593, doi:10.1103/physrevb.19.3593.

[15] Farrel W. Lytle. X-ray diffractometry of low-temperature phase transformations in strontium titanate. *J. Appl. Phys.*, 35(7):2212, 1964. URL: http://dx.doi.org/10.1063/1.1702820, doi:10.1063/1.1702820.

[16] Ulrich Aschauer and Nicola A Spaldin. Competition and cooperation between antiferrodistortive and ferroelectric instabilities in the model perovskite SrTiO 3. *Journal of Physics: Condensed Matter*, 26(12):122203, mar 2014. URL: https://doi.org/10.1088%2F0953-8984%2F26%2F12%2F122203, doi:10.1088/0953-8984/26/12/122203.

[17] M. Itoh, R. Wang, Y. Inaguma, T. Yamaguchi, Y-J. Shan, and T. Nakamura. Ferroelectricity induced by oxygen isotope exchange in strontium titanate perovskite. *Physical Review Letters*, 82(17):3540–3543, apr 1999. URL: https://doi.org/10.1103%2Fphysrevlett.82.3540, doi:10.1103/physrevlett.82.3540.

[18] J. G. Bednorz and K. A. Müller. Sr1-xCaxTiO3: AnXYQuantum ferroelectric with transition to randomness. *Physical Review Letters*, 52(25):2289–2292, jun 1984. URL: https://doi.org/10.1103%2Fphysrevlett.52.2289, doi:10.1103/physrevlett.52.2289.

[19] Hiromoto Uwe and Tunetaro Sakudo. Stress-induced ferroelectricity and soft phonon modes in SrTiO3. *Physical Review B*, 13(1):271–286, jan 1976. URL: https://doi.org/10.1103%2Fphysrevb.13.271, doi:10.1103/physrevb.13.271.

[20] R. C. Neville. Permittivity of strontium titanate. *J. Appl. Phys.*, 43(5):2124, 1972. URL: http://dx.doi.org/10.1063/1.1661463, doi:10.1063/1.1661463.

[21] D. E. Grupp. Giant piezoelectric effect in strontium titanate at cryogenic temperatures. *Science*, 276(5311):392–394, apr 1997. URL: http://dx.doi.org/10.1126/science.276.5311.392, doi:10.1126/science.276.5311.392.

[22] L. F. Mattheiss. Energy bands for KNi f 3 , SrTi o 3 , KMo o 3 , and KTa o 3. *Phys. Rev. B*, 6(12):4718–4740, dec 1972. URL: http://dx.doi.org/10.1103/PhysRevB.6.4718, doi:10.1103/physrevb.6.4718.

[23] Jacobus L. M. Van Mechelen. *Charge and Spin electrodynamics of SrTiO3 and EuTiO3 studied by optical spectroscopy*. PhD thesis, Université de Genéve, 2010. ID: unige:11844. URL: http://nbn-resolving.de/urn:nbn:ch:unige-118440, doi:ID:unige:11844.

[24] Adrian G. Swartz, Hisashi Inoue, Tyler A. Merz, Yasuyuki Hikita, Srinivas Raghu, Thomas P. Devereaux, Steven Johnston, and Harold Y. Hwang. Strong polaronic behavior in a weak coupling superconductor. August 2016. arXiv:1608.05621.

[25] D. van der Marel, J. L. M. van Mechelen, and I. I. Mazin. Common fermi-liquid origin ofT2resistivity and superconductivity inn-type SrTiO3. *Physical Review B*, 84(20), nov 2011. URL: https://doi.org/10.1103%2Fphysrevb.84.205111, doi:10.1103/physrevb.84.205111.

[26] W. Meevasana, P. D. C. King, R. H. He, S-K. Mo, M. Hashimoto, A. Tamai, P. Songsiriritthigul, F. Baumberger, and Z-X. Shen. Creation and control of a two-dimensional electron liquid at the bare SrTiO3 surface. *Nature Materials*, 10(2):114–118, jan 2011. URL: http://dx.doi.org/10.1038/nmat2943, doi:10.1038/nmat2943.

[27] M. Kim, C. Bell, Y. Kozuka, M. Kurita, Y. Hikita, and H. Y. Hwang. Fermi surface and superconductivity in low-density high-mobility -doped SrTiO 3. *Phys. Rev. Lett.*, 107(10), aug 2011. URL: http://dx.doi.org/10.1103/PhysRevLett.107.106801, doi:10.1103/physrevlett.107.106801.

[28] H. P. R. Frederikse and W. R. Hosler. Hall mobility in SrTi o 3. *Phys. Rev.*, 161(3):822–827, sep 1967. URL: http://dx.doi.org/10.1103/PhysRev.161.822, doi:10.1103/physrev.161.822.

[29] Xiao Lin, Zengwei Zhu, Benoît Fauqué, and Kamran Behnia. Fermi surface of the most dilute superconductor. *Phys. Rev. X*, 3(2), apr 2013. URL: http://dx.doi.org/10.1103/PhysRevX.3.021002, doi:10.1103/physrevx.3.021002.

[30] C. S. Koonce, Marvin L. Cohen, J. F. Schooley, W. R. Hosler, and E. R. Pfeiffer. Superconducting transition temperatures of semiconducting SrTi o 3. *Phys. Rev.*, 163(2):380–390, nov 1967. URL: http://dx.doi.org/10.1103/PhysRev.163.380, doi:10.1103/physrev.163.380.

[31] D. M. Eagles. Possible pairing without superconductivity at low carrier concentrations in bulk and thin-film superconducting semiconductors. *Physical Review*, 186(2):456–463, oct 1969. URL: https://doi.org/10.1103%2Fphysrev.186.456, doi:10.1103/physrev.186.456.

[32] J. Appel. Soft-mode superconductivity inSrTiO3-x. *Physical Review*, 180(2):508–516, apr 1969. URL: https://doi.org/10.1103%2Fphysrev.180.508, doi:10.1103/physrev.180.508.

[33] K. L. Ngai. Two-phonon deformation potential and superconductivity in degenerate semiconductors. *Physical Review Letters*, 32(5):215–218, feb 1974. URL: https://doi.org/10.1103%2Fphysrevlett.32.215, doi:10.1103/physrevlett.32.215.

[34] E. R. Pfeiffer and J. F. Schooley. Effect of stress on the superconducting transition temperature of SrTiO3. *Journal of Low Temperature Physics*, 2(3-4):333–352, 1970. URL: https://doi.org/10.1007%2Fbf00652506, doi:10.1007/bf00652506.

[35] Yasutami Takada. Theory of superconductivity in polar semiconductors and its application to n-type semiconducting SrTiO 3. *Journal of the Physical Society of Japan*, 49(4):1267–1275, oct 1980. URL: http://dx.doi.org/10.1143/JPSJ.49.1267, doi:10.1143/jpsj.49.1267.

[36] Jonathan Ruhman and Patrick A. Lee. Superconductivity at very low density: The case of strontium titanate. *Physical Review B*, 94(22), dec 2016. URL: https://doi.org/10.1103%2Fphysrevb.94.224515, doi:10.1103/physrevb.94.224515.

[37] Jonathan M. Edge, Yaron Kedem, Ulrich Aschauer, Nicola A. Spaldin, and Alexander V. Balatsky. Quantum critical origin of the superconducting dome inSrTiO3. *Physical Review Letters*, 115(24), dec 2015. URL: https://doi.org/10.1103%2Fphysrevlett.115.247002, doi:10.1103/physrevlett.115.247002.

[38] A. Stucky, G. W. Scheerer, Z. Ren, D. Jaccard, J.-M. Poumirol, C. Barreteau, E. Giannini, and D. van der Marel. Isotope effect in superconducting n-doped SrTiO3. *Scientific Reports*, 6:37582, nov 2016. URL: https://doi.org/10.1038%2Fsrep37582, doi:10.1038/srep37582.

[39] Lev P. Gor'kov. Phonon mechanism in the most dilute superconductorn-type SrTiO3. *Proceedings of the National Academy of Sciences*, 113(17):4646–4651, apr 2016. URL: https://doi.org/10.1073%2Fpnas.1604145113, doi:10.1073/pnas.1604145113.

[40] Seung-Gu Lim, Stas Kriventsov, Thomas N. Jackson, J. H. Haeni, D. G. Schlom, A. M. Balbashov, R. Uecker, P. Reiche, J. L. Freeouf, and G. Lucovsky. Dielectric functions and

optical bandgaps of high-k dielectrics for metal-oxide-semiconductor field-effect transistors by far ultraviolet spectroscopic ellipsometry. *J. Appl. Phys.*, 91(7):4500, 2002. URL: http://dx.doi.org/10.1063/1.1456246, doi:10.1063/1.1456246.

[41] K. A. Müller, W. Berlinger, and F. Waldner. Characteristic structural phase transition in perovskite-type compounds. *Phys. Rev. Lett.*, 21(12):814–817, sep 1968. URL: http://dx.doi.org/10.1103/PhysRevLett.21.814, doi:10.1103/physrevlett.21.814.

[42] Naoyuki Nakagawa, Harold Y. Hwang, and David A. Muller. Why some interfaces cannot be sharp. *Nature Materials*, 5(3):204–209, jan 2006. URL: http://dx.doi.org/10.1038/nmat1569, doi:10.1038/nmat1569.

[43] Pietro Delugas, Vincenzo Fiorentini, and Alessio Filippetti. Dielectric properties and long-wavelength optical modes of the high- oxide LaAlO 3. *Phys. Rev. B*, 71(13), apr 2005. URL: http://dx.doi.org/10.1103/PhysRevB.71.134302, doi:10.1103/physrevb.71.134302.

[44] S. Thiel. Tunable quasi-two-dimensional electron gases in oxide heterostructures. *Science*, 313(5795):1942–1945, sep 2006. URL: http://dx.doi.org/10.1126/science.1131091, doi:10.1126/science.1131091.

[45] Liping Yu and Alex Zunger. A polarity-induced defect mechanism for conductivity and magnetism at polar–nonpolar oxide interfaces. *Nature Communications*, 5:5118, oct 2014. URL: http://dx.doi.org/10.1038/ncomms6118, doi:10.1038/ncomms6118.

[46] G. E. D. K. Prawiroatmodjo, F. Trier, D. V. Christensen, Y. Chen, N. Pryds, and T. S. Jespersen. Evidence of weak superconductivity at the room-temperature grown-LaAlO3/SrTiO3interface. *Physical Review B*, 93(18), may 2016. URL: https://doi.org/10.1103%2Fphysrevb.93.184504, doi:10.1103/physrevb.93.184504.

[47] A. Brinkman, M. Huijben, M. van Zalk, J. Huijben, U. Zeitler, J. C. Maan, W. G. van der Wiel, G. Rijnders, D. H. A. Blank, and H. Hilgenkamp. Magnetic effects at the interface between non-magnetic oxides. *Nature Materials*, 6(7):493–496, jun 2007. URL: http://dx.doi.org/10.1038/nmat1931, doi:10.1038/nmat1931.

[48] M. Basletic, J.-L. Maurice, C. Carrétéro, G. Herranz, O. Copie, M. Bibes, É. Jacquet, K. Bouzehouane, S. Fusil, and A. Barthélémy. Mapping the spatial distribution of charge carriers in LaAlO3/SrTiO3 heterostructures. *Nature Materials*, 7(8):621–625, jun 2008. URL: http://dx.doi.org/10.1038/nmat2223, doi:10.1038/nmat2223.

[49] Takuya Higuchi and Harold Y. Hwang. General considerations of the electrostatic boundary conditions in oxide heterostructures. In *Multifunctional Oxide Heterostructures*, pages 183–213. Oxford University Press (OUP), aug 2012. URL: http://dx.doi.org/10.1093/acprof:oso/9780199584123.003.0007, doi:10.1093/acprof:oso/9780199584123.003.0007.

[50] Zoran S. Popović, Sashi Satpathy, and Richard M. Martin. Origin of the two-dimensional electron gas carrier density at theLaAlO3onsrtio3interface. *Physical Review Letters*, 101(25), dec 2008. URL: https://doi.org/10.1103%2Fphysrevlett.101.256801, doi:10.1103/physrevlett.101.256801.

[51] Se Young Park and Andrew J. Millis. Charge density distribution and optical response of the LaAlO3/SrTiO3interface. *Physical Review B*, 87(20), may 2013. URL: https://doi.org/10.1103%2Fphysrevb.87.205145, doi:10.1103/physrevb.87.205145.

[52] T. Sakudo and H. Unoki. Dielectric properties of SrTiO3at low temperatures. *Physical Review Letters*, 26(14):851–853, apr 1971. URL: https://doi.org/10.1103%2Fphysrevlett.26.851, doi:10.1103/physrevlett.26.851.

[53] Zhicheng Zhong, Anna Tóth, and Karsten Held. Theory of spin-orbit coupling at LaAlO 3 /SrTiO 3 interfaces and SrTiO 3 surfaces. *Phys. Rev. B*, 87(16), apr 2013. URL: http://dx.doi.org/10.1103/PhysRevB.87.161102, doi:10.1103/physrevb.87.161102.

[54] Younghyun Kim, Roman M. Lutchyn, and Chetan Nayak. Origin and transport signatures of spin-orbit interactions in one- and two-dimensional SrTiO 3 -based heterostructures. *Phys. Rev. B*, 87(24), jun 2013. URL: http://dx.doi.org/10.1103/PhysRevB.87.245121, doi:10.1103/physrevb.87.245121.

[55] Guru Khalsa, Byounghak Lee, and A. H. MacDonald. Theory of t 2 g electron-gas rashba interactions. *Phys. Rev. B*, 88(4), jul 2013. URL: http://dx.doi.org/10.1103/PhysRevB.88.041302, doi:10.1103/physrevb.88.041302.

[56] A. D. Caviglia, M. Gabay, S. Gariglio, N. Reyren, C. Cancellieri, and J.-M. Triscone. Tunable rashba spin-orbit interaction at oxide interfaces. *Physical Review Letters*, 104(12), mar 2010. URL: https://doi.org/10.1103%2Fphysrevlett.104.126803, doi:10.1103/physrevlett.104.126803.

[57] E. Lesne, Yu Fu, S. Oyarzun, J. C. Rojas-Sánchez, D. C. Vaz, H. Naganuma, G. Sicoli, J.-P. Attané, M. Jamet, E. Jacquet, J.-M. George, A. Barthélémy, H. Jaffrès, A. Fert, M. Bibes, and L. Vila. Highly efficient and tunable spin-to-charge conversion through rashba coupling at oxide interfaces. *Nature Materials*, 15(12):1261–1266, aug 2016. URL: https://doi.org/10.1038%2Fnmat4726, doi:10.1038/nmat4726.

[58] Tong Zhang, Peng Cheng, Wen-Juan Li, Yu-Jie Sun, Guang Wang, Xie-Gang Zhu, Ke He, Lili Wang, Xucun Ma, Xi Chen, Yayu Wang, Ying Liu, Hai-Qing Lin, Jin-Feng Jia, and Qi-Kun Xue. Superconductivity in one-atomic-layer metal films grown on si(111). *Nat Phys*, 6(2):104–108, jan 2010. URL: http://dx.doi.org/10.1038/nphys1499, doi:10.1038/nphys1499.

[59] Hans Boschker, Christoph Richter, Evangelos Fillis-Tsirakis, Christof W. Schneider, and Jochen Mannhart. Electron—phonon coupling and the superconducting phase diagram of the LaAlO3—SrTiO3 interface. *Sci. Rep.*, 5:12309, jul 2015. URL: http://dx.doi.org/10.1038/srep12309, doi:10.1038/srep12309.

[60] Julie A. Bert, Beena Kalisky, Christopher Bell, Minu Kim, Yasuyuki Hikita, Harold Y. Hwang, and Kathryn A. Moler. Direct imaging of the coexistence of ferromagnetism and superconductivity at the LaAlO3/SrTiO3 interface. *Nature Physics*, 7(10):767–771, sep 2011. URL: http://dx.doi.org/10.1038/nphys2079, doi:10.1038/nphys2079.

[61] D. A. Dikin, M. Mehta, C. W. Bark, C. M. Folkman, C. B. Eom, and V. Chandrasekhar. Coexistence of superconductivity and ferromagnetism in two dimensions. *Physical Review Letters*, 107(5), jul 2011. URL: http://dx.doi.org/10.1103/PhysRevLett.107.056802, doi:10.1103/physrevlett.107.056802.

[62] Karen Michaeli, Andrew C. Potter, and Patrick A. Lee. Superconducting and ferromagnetic phases inSrTiO3/LaAlO3oxide interface structures: Possibility of finite momentum pairing. *Physical Review Letters*, 108(11), mar 2012. URL: https://doi.org/10.1103%2Fphysrevlett.108.117003, doi:10.1103/physrevlett.108.117003.

[63] T. Schneider, A. D. Caviglia, S. Gariglio, N. Reyren, and J.-M. Triscone. Electrostatically-tuned superconductor-metal-insulator quantum transition at the LaAlO 3 / SrTiO 3 interface. *Phys. Rev. B*, 79(18), may 2009. URL: http://dx.doi.org/10.1103/PhysRevB.79.184502, doi:10.1103/physrevb.79.184502.

[64] S. Gariglio, M. Gabay, and J.-M. Triscone. Research update: Conductivity and beyond at the LaAlO3/SrTiO3 interface. *APL Mater.*, 4(6):060701, jun 2016. URL: http://dx.doi.org/10.1063/1.4953822, doi:10.1063/1.4953822.

[65] E. Maniv, M. Ben Shalom, A. Ron, M. Mograbi, A. Palevski, M. Goldstein, and Y. Dagan. Strong correlations elucidate the electronic structure and phase diagram of LaAlO3/SrTiO3 interface. *Nature Communications*, 6:8239, sep 2015. URL: https://doi.org/10.1038%2Fncomms9239, doi:10.1038/ncomms9239.

[66] N. Mohanta and A. Taraphder. Multiband theory of superconductivity at the LaAlO 3 / SrTiO 3 interface. *Phys. Rev. B*, 92(17), nov 2015. URL: http://dx.doi.org/10.1103/PhysRevB.92.174531, doi:10.1103/physrevb.92.174531.

[67] S. N. Klimin, J. Tempere, J. T. Devreese, and D. van der Marel. Interface superconductivity in LaAlO 3 - SrTiO 3 heterostructures. *Physical Review B*, 89(18), may 2014. URL: http://dx.doi.org/10.1103/PhysRevB.89.184514, doi:10.1103/physrevb.89.184514.

[68] S. N. Klimin, J. Tempere, J. T. Devreese, and D. van der Marel. Multiband superconductivity due to the electron–LO–phonon interaction in strontium titanate and on a SrTiO3/LaAlO3 interface. *J Supercond Nov Magn*, aug 2016. URL: http://dx.doi.org/10.1007/s10948-016-3664-2, doi:10.1007/s10948-016-3664-2.

[69] C. Richter, H. Boschker, W. Dietsche, E. Fillis-Tsirakis, R. Jany, F. Loder, L. F. Kourkoutis, D. A. Muller, J. R. Kirtley, C. W. Schneider, and J. Mannhart. Interface superconductor with gap behaviour like a high-temperature superconductor. *Na-*

ture, 502(7472):528–531, oct 2013. URL: http://dx.doi.org/10.1038/nature12494, doi:10.1038/nature12494.

[70] D Bucheli, S Caprara, and M Grilli. Pseudo-gap as a signature of inhomogeneous superconductivity in oxide interfaces. *Superconductor Science and Technology*, 28(4):045004, feb 2015. URL: https://doi.org/10.1088%2F0953-2048%2F28%2F4%2F045004, doi:10.1088/0953-2048/28/4/045004.

[71] Feng Bi, Mengchen Huang, Chung Wung Bark, Sangwoo Ryu, Sanghan Lee, Chang-Beom Eom, Patrick Irvin, and Jeremy Levy. Electro-mechanical response of top-gated laalo3/srtio3 heterostructures. February 2013. arXiv:1302.0204.

[72] Beena Kalisky, Eric M. Spanton, Hilary Noad, John R. Kirtley, Katja C. Nowack, Christopher Bell, Hiroki K. Sato, Masayuki Hosoda, Yanwu Xie, Yasuyuki Hikita, Carsten Woltmann, Georg Pfanzelt, Rainer Jany, Christoph Richter, Harold Y. Hwang, Jochen Mannhart, and Kathryn A. Moler. Locally enhanced conductivity due to the tetragonal domain structure in LaAlO3/SrTiO3 heterointerfaces. *Nature Materials*, 12(12):1091–1095, sep 2013. URL: https://doi.org/10.1038%2Fnmat3753, doi:10.1038/nmat3753.

[73] N. Scopigno, D. Bucheli, S. Caprara, J. Biscaras, N. Bergeal, J. Lesueur, and M. Grilli. Phase separation from electron confinement at oxide interfaces. *Physical Review Letters*, 116(2), jan 2016. URL: https://doi.org/10.1103%2Fphysrevlett.116.026804, doi:10.1103/physrevlett.116.026804.

[74] S. Caprara, F. Peronaci, and M. Grilli. Intrinsic instability of electronic interfaces with strong rashba coupling. *Physical Review Letters*, 109(19), nov 2012. URL: https://doi.org/10.1103%2Fphysrevlett.109.196401, doi:10.1103/physrevlett.109.196401.

[75] L. Benfatto, C. Castellani, and T. Giamarchi. Broadening of the berezinskii-kosterlitz-thouless superconducting transition by inhomogeneity and finite-size effects. *Physical Review B*, 80(21), dec 2009. URL: https://doi.org/10.1103%2Fphysrevb.80.214506, doi:10.1103/physrevb.80.214506.

[76] S. Caprara, J. Biscaras, N. Bergeal, D. Bucheli, S. Hurand, C. Feuillet-Palma, A. Rastogi, R. C. Budhani, J. Lesueur, and M. Grilli. Multiband superconductivity and nanoscale inhomogeneity at oxide interfaces. *Physical Review B*, 88(2), jul 2013. URL: https://doi.org/10.1103%2Fphysrevb.88.020504, doi:10.1103/physrevb.88.020504.

[77] M. V. Feigel'man, L. B. Ioffe, and M. Mézard. Superconductor-insulator transition and energy localization. *Phys. Rev. B*, 82(18), nov 2010. URL: http://dx.doi.org/10.1103/PhysRevB.82.184534, doi:10.1103/physrevb.82.184534.

[78] G. Seibold, L. Benfatto, C. Castellani, and J. Lorenzana. Superfluid density and phase relaxation in superconductors with strong disorder. *Physical Review Letters*, 108(20), may 2012. URL: https://doi.org/10.1103%2Fphysrevlett.108.207004, doi:10.1103/physrevlett.108.207004.

[79] J. Biscaras, N. Bergeal, S. Hurand, C. Feuillet-Palma, A. Rastogi, R. C. Budhani, M. Grilli, S. Caprara, and J. Lesueur. Multiple quantum criticality in a two-dimensional superconductor. *Nature Materials*, 12(6):542–548, apr 2013. URL: http://dx.doi.org/10.1038/nmat3624, doi:10.1038/nmat3624.

[80] S. Hurand. *Contrôle de la supraconductivité à l'interface d'oxydes $LaAlO_3/SrTiO_3$ par effet de champ électrique*. PhD thesis, Université Pierre et Marie Curie - Paris VI, février 2015. URL: https://tel.archives-ouvertes.fr/tel-01132962/document.

[81] A. Ohtomo and H. Y. Hwang. Corrigendum: A high-mobility electron gas at the $LaAlO_3/SrTiO_3$ heterointerface. , 441:120, May 2006. doi:10.1038/nature04773.

[82] Gervasi Herranz, Gyanendra Singh, Nicolas Bergeal, Alexis Jouan, Jérôme Lesueur, Jaume Gázquez, María Varela, Mateusz Scigaj, Nico Dix, Florencio Sánchez, and Josep Fontcuberta. Engineering two-dimensional superconductivity and rashba spin–orbit coupling in LaAlO3/SrTiO3 quantum wells by selective orbital occupancy. *Nature Communications*, 6:6028, jan 2015. URL: http://dx.doi.org/10.1038/ncomms7028, doi:10.1038/ncomms7028.

[83] S. Hurand, A. Jouan, C. Feuillet-Palma, G. Singh, E. Lesne, N. Reyren, A. Barthélémy, M. Bibes, J. E. Villegas, C. Ulysse, M. Pannetier-Lecoeur, M. Malnou, J. Lesueur, and N. Bergeal. Top-gated field-effect LaAlO3/SrTiO3 devices made by ion-irradiation. *Appl. Phys. Lett.*, 108(5):052602, feb 2016. URL: http://dx.doi.org/10.1063/1.4941672, doi:10.1063/1.4941672.

[84] J. Biscaras, S. Hurand, C. Feuillet-Palma, A. Rastogi, R. C. Budhani, N. Reyren, E. Lesne, J. Lesueur, and N. Bergeal. Limit of the electrostatic doping in two-dimensional electron gases of LaXO3(x = al, ti)/SrTiO3. *Sci. Rep.*, 4:6788, oct 2014. URL: http://dx.doi.org/10.1038/srep06788, doi:10.1038/srep06788.

[85] Srijit Goswami, Emre Mulazimoglu, Ana M. R. V. L. Monteiro, Roman Wölbing, Dieter Koelle, Reinhold Kleiner, Ya. M. Blanter, Lieven M. K. Vandersypen, and Andrea D. Caviglia. Quantum interference in an interfacial superconductor. *Nature Nanotechnology*, 11(10):861–865, jul 2016. URL: http://dx.doi.org/10.1038/nnano.2016.112, doi:10.1038/nnano.2016.112.

[86] Frank Pobell. *Matter and Methods at Low Temperatures*. Springer Berlin Heidelberg, 2007. URL: http://www.ebook.de/de/product/20512312/frank_pobell_matter_and_methods_at_low_temperatures.html.

[87] David M. Pozar. *Microwave Engineering*. JOHN WILEY & SONS INC, 2011. URL: http://www.ebook.de/de/product/14948033/david_m_pozar_microwave_engineering.html.

[88] Patrick A. Lee and T. V. Ramakrishnan. Disordered electronic systems. *Reviews of Modern Physics*, 57(2):287–337, apr 1985. URL: http://dx.doi.org/10.1103/RevModPhys.57.287, doi:10.1103/revmodphys.57.287.

[89] A.M. Finkelstein. Suppression of superconductivity in homogeneously disordered systems. *Physica B: Condensed Matter*, 197(1-4):636–648, mar 1994. URL: http://dx.doi.org/10.1016/0921-4526(94)90267-4, doi:10.1016/0921-4526(94)90267-4.

[90] T. Fix, F. Schoofs, J. L. MacManus-Driscoll, and M. G. Blamire. Influence of doping at the nanoscale at LaAlO[sub 3]/SrTiO[sub 3] interfaces. *Appl. Phys. Lett.*, 97(7):072110, 2010. URL: http://dx.doi.org/10.1063/1.3481353, doi:10.1063/1.3481353.

[91] M. E. J. Newman. Random graphs with clustering. *Phys. Rev. Lett.*, 103(5), jul 2009. URL: http://dx.doi.org/10.1103/PhysRevLett.103.058701, doi:10.1103/physrevlett.103.058701.

[92] M. T. Gray, T. D. Sanders, F. J. Wong, A. J. Grutter, U. S. Alaan, C. He, C. A. Jenkins, E. Arenholz, and Y. Suzuki. Quasi-two-dimensional electron gas behavior in doped LaAlO3 thin films on SrTiO3 substrates. *Appl. Phys. Lett.*, 102(13):131601, 2013. URL: http://dx.doi.org/10.1063/1.4800232, doi:10.1063/1.4800232.

[93] T. D. Sanders, M. T. Gray, F. J. Wong, and Y. Suzuki. LaAlO˙3 / SrTiO˙3 interfaces doped with rare-earth ions. *Phys. Rev. B*, 91(20), may 2015. URL: http://dx.doi.org/10.1103/PhysRevB.91.205112, doi:10.1103/physrevb.91.205112.

[94] Andrea De Luca, Jacopo Viti, Leonardo Mazza, and Davide Rossini. Energy transport in heisenberg chains beyond the luttinger liquid paradigm. *Phys. Rev. B*, 90(16), oct 2014. URL: http://dx.doi.org/10.1103/PhysRevB.90.161101, doi:10.1103/physrevb.90.161101.

[95] Pramod Kumar, Anjana Dogra, P P S Bhadauria, Anurag Gupta, K K Maurya, and R C Budhani. Enhanced spin–orbit coupling and charge carrier density suppression in LaAl1-xCrxO3/SrTiO3 hetero-interfaces. *Journal of Physics: Condensed Matter*, 27(12):125007, mar 2015. URL: https://doi.org/10.1088%2F0953-8984%2F27%2F12%2F125007, doi:10.1088/0953-8984/27/12/125007.

[96] T. Okuda, K. Nakanishi, S. Miyasaka, and Y. Tokura. Large thermoelectric response of metallic perovskites:sr1-xLaxTiO3 (0˜x˜0.1). *Physical Review B*, 63(11), mar 2001. URL: https://doi.org/10.1103%2Fphysrevb.63.113104, doi:10.1103/physrevb.63.113104.

[97] J. Biscaras, N. Bergeal, A. Kushwaha, T. Wolf, A. Rastogi, R.C. Budhani, and J. Lesueur. Two-dimensional superconductivity at a mott insulator/band insulator interface LaTiO3/SrTiO3. *Nature Communications*, 1(7):1–5, oct 2010. URL: http://dx.doi.org/10.1038/ncomms1084, doi:10.1038/ncomms1084.

[98] S. Hurand, J. Biscaras, N. Bergeal, C. Feuillet-Palma, G. Singh, A. Jouan, A. Rastogi, A. Dogra, P. Kumar, R. C. Budhani, N. Scopigno, S. Caprara, M. Grilli, and J. Lesueur. Density driven fluctuations in a two-dimensional superconductor. June 2015. arXiv:1506.06874.

[99] Sadamishi Maekawa and Hidetoshi Fukuyama. Localization effects in two-dimensional superconductors. *Journal of the Physical Society of Japan*, 51(5):1380–1385, may 1982. URL: http://dx.doi.org/10.1143/JPSJ.51.1380, doi:10.1143/jpsj.51.1380.

[100] Gilles Montambaux Eric Akkermans. *Mesoscopic Physics of Electrons and Photons*. CAMBRIDGE UNIV PR, 2011. URL: http://www.ebook.de/de/product/15357409/eric_akkermans_gilles_montambaux_mesoscopic_physics_of_electrons_and_photons.html.

[101] Sadamichi Maekawa and Hidetoshi Fukuyama. Magnetoresistance in two-dimensional disordered systems: Effects of zeeman splitting and spin-orbit scattering. *Journal of the Physical Society of Japan*, 50(8):2516–2524, aug 1981. URL: http://dx.doi.org/10.1143/JPSJ.50.2516, doi:10.1143/jpsj.50.2516.

[102] A. V. Germanenko. Spin effects and quantum corrections to the conductivity of two-dimensional systems. *Low Temperature Physics*, 35(1):24, 2009. URL: http://dx.doi.org/10.1063/1.3064887, doi:10.1063/1.3064887.

[103] S. Hikami, A. I. Larkin, and Y. Nagaoka. Spin-orbit interaction and magnetoresistance in the two dimensional random system. *Progress of Theoretical Physics*, 63(2):707–710, feb 1980. URL: http://dx.doi.org/10.1143/PTP.63.707, doi:10.1143/ptp.63.707.

[104] C. M. Hurd. *The Hall Effect in Metals and Alloys*. International Congresses of Quantum Chemistry Series. Plenum Press, 1972.

[105] Roberto Raimondi, Cosimo Gorini, Peter Schwab, and Michael Dzierzawa. Quasiclassical approach to the spin hall effect in the two-dimensional electron gas. *Physical Review B*, 74(3), jul 2006. URL: http://dx.doi.org/10.1103/PhysRevB.74.035340, doi:10.1103/physrevb.74.035340.

[106] Robert A. Smith and Vinay Ambegaokar. Weak-localization correction to the number density of superconducting electrons. *Phys. Rev. B*, 45(5):2463–2473, feb 1992. URL: http://dx.doi.org/10.1103/PhysRevB.45.2463, doi:10.1103/physrevb.45.2463.

[107] L. Li, C. Richter, S. Paetel, T. Kopp, J. Mannhart, and R. C. Ashoori. Very large capacitance enhancement in a two-dimensional electron system. *Science*, 332(6031):825–828, may 2011. URL: https://doi.org/10.1126%2Fscience.1204168, doi:10.1126/science.1204168.

[108] P. D. Eerkes, W. G. van der Wiel, and H. Hilgenkamp. Modulation of conductance and superconductivity by top-gating in LaAlO3/SrTiO3 2-dimensional electron systems. *Applied Physics Letters*, 103(20):201603, nov 2013. URL: https://doi.org/10.1063%2F1.4829555, doi:10.1063/1.4829555.

[109] Zhuoyu Chen, Hongtao Yuan, Yanwu Xie, Di Lu, Hisashi Inoue, Yasuyuki Hikita, Christopher Bell, and Harold Y. Hwang. Dual-gate modulation of carrier density and disorder in an oxide two-dimensional electron system. *Nano Letters*, 16(10):6130–6136, oct

2016. URL: http://dx.doi.org/10.1021/acs.nanolett.6b02348, doi:10.1021/acs.nanolett.6b02348.

[110] Patrick Gallagher, Menyoung Lee, James R. Williams, and David Goldhaber-Gordon. Gate-tunable superconducting weak link and quantum point contact spectroscopy on a strontium titanate surface. *Nature Physics*, aug 2014. URL: http://dx.doi.org/10.1038/nphys3049, doi:10.1038/nphys3049.

[111] S. Hurand, A. Jouan, C. Feuillet-Palma, G. Singh, J. Biscaras, E. Lesne, N. Reyren, A. Barthélémy, M. Bibes, J. E. Villegas, C. Ulysse, X. Lafosse, M. Pannetier-Lecoeur, S. Caprara, M. Grilli, J. Lesueur, and N. Bergeal. Field-effect control of superconductivity and rashba spin-orbit coupling in top-gated LaAlO3/SrTiO3 devices. *Sci. Rep.*, 5:12751, aug 2015. URL: http://dx.doi.org/10.1038/srep12751, doi:10.1038/srep12751.

[112] Matthew P. A. Fisher. Quantum phase transitions in disordered two-dimensional superconductors. *Physical Review Letters*, 65(7):923–926, aug 1990. URL: http://dx.doi.org/10.1103/PhysRevLett.65.923, doi:10.1103/physrevlett.65.923.

[113] B L Altshuler, A G Aronov, and D E Khmelnitsky. Effects of electron-electron collisions with small energy transfers on quantum localisation. *Journal of Physics C: Solid State Physics*, 15(36):7367–7386, dec 1982. URL: http://dx.doi.org/10.1088/0022-3719/15/36/018, doi:10.1088/0022-3719/15/36/018.

[114] F. London and H. London. The electromagnetic equations of the supraconductor. *Proceedings of the Royal Society A: Mathematical, Physical and Engineering Sciences*, 149(866):71–88, mar 1935. URL: https://doi.org/10.1098%2Frspa.1935.0048, doi:10.1098/rspa.1935.0048.

[115] Michael Tinkham. *Introduction to Superconductivity*. DOVER PUBN INC, 2004. URL: http://www.ebook.de/de/product/3429695/michael_tinkham_introduction_to_superconductivity.html.

[116] J. Pearl. CURRENT DISTRIBUTION IN SUPERCONDUCTING FILMS CARRYING QUANTIZED FLUXOIDS. *Applied Physics Letters*, 5(4):65, 1964. URL: http://dx.doi.org/10.1063/1.1754056, doi:10.1063/1.1754056.

[117] Naoto Nagaosa. *Quantum Field Theory in Condensed Matter Physics*. Springer Nature, 1999. URL: https://doi.org/10.1007%2F978-3-662-03774-4, doi:10.1007/978-3-662-03774-4.

[118] L. Benfatto and S. G. Sharapov. Optical-conductivity sum rule in cuprates and unconventional charge density waves: a short review. *Low Temperature Physics*, 32(6):533, 2006. URL: http://dx.doi.org/10.1063/1.2215368, doi:10.1063/1.2215368.

[119] M. Tinkham and R. A. Ferrell. Determination of the superconducting skin depth from the energy gap and sum rule. *Physical Review Letters*, 2(8):331–333, apr 1959. URL: https://doi.org/10.1103%2Fphysrevlett.2.331, doi:10.1103/physrevlett.2.331.

[120] Patrick Lee. *Lecture 8.512 Theory of Solids II*. MIT, 2009.

[121] M. Dressel. Electrodynamics of metallic superconductors. *Advances in Condensed Matter Physics*, 2013:1–25, 2013. URL: http://dx.doi.org/10.1155/2013/104379, doi:10.1155/2013/104379.

[122] D. C. Mattis and J. Bardeen. Theory of the anomalous skin effect in normal and superconducting metals. *Phys. Rev.*, 111(2):412–417, jul 1958. URL: http://dx.doi.org/10.1103/PhysRev.111.412, doi:10.1103/physrev.111.412.

[123] Katrin Steinberg, Marc Scheffler, and Martin Dressel. Quasiparticle response of superconducting aluminum to electromagnetic radiation. *Phys. Rev. B*, 77(21), jun 2008. URL: http://dx.doi.org/10.1103/PhysRevB.77.214517, doi:10.1103/physrevb.77.214517.

[124] P. W. Anderson. Theory of dirty superconductors. *J. Phys. Chm. Solids Pergamon Press*, pages pp 26–30, 1959.

[125] Michael Ma and Patrick A. Lee. Localized superconductors. *Phys. Rev. B*, 32(9):5658–5667, nov 1985. URL: http://dx.doi.org/10.1103/PhysRevB.32.5658, doi:10.1103/physrevb.32.5658.

[126] B. Sacépé, C. Chapelier, T. I. Baturina, V. M. Vinokur, M. R. Baklanov, and M. Sanquer. Disorder-induced inhomogeneities of the superconducting state close to the superconductor-insulator transition. *Phys. Rev. Lett.*, 101(15), oct 2008. URL: http://dx.doi.org/10.1103/PhysRevLett.101.157006, doi:10.1103/physrevlett.101.157006.

[127] Amit Ghosal, Mohit Randeria, and Nandini Trivedi. Inhomogeneous pairing in highly disordered s -wave superconductors. *Physical Review B*, 65(1), nov 2001. URL: http://dx.doi.org/10.1103/PhysRevB.65.014501, doi:10.1103/physrevb.65.014501.

[128] Arun Paramekanti, Nandini Trivedi, and Mohit Randeria. Upper bounds on the superfluid stiffness of disordered systems. *Physical Review B*, 57(18):11639–11647, may 1998. URL: http://dx.doi.org/10.1103/PhysRevB.57.11639, doi:10.1103/physrevb.57.11639.

[129] T. Cea, D. Bucheli, G. Seibold, L. Benfatto, J. Lorenzana, and C. Castellani. Optical excitation of phase modes in strongly disordered superconductors. *Phys. Rev. B*, 89(17), may 2014. URL: http://dx.doi.org/10.1103/PhysRevB.89.174506, doi:10.1103/physrevb.89.174506.

[130] V. J. Emery and S. A. Kivelson. Importance of phase fluctuations in superconductors with small superfluid density. *Nature*, 374(6521):434–437, mar 1995. URL: http://dx.doi.org/10.1038/374434a0, doi:10.1038/374434a0.

[131] J M Kosterlitz and D J Thouless. Ordering, metastability and phase transitions in two-dimensional systems. *Journal of Physics C: Solid State Physics*, 6(7):1181–1203, apr 1973. URL: http://dx.doi.org/10.1088/0022-3719/6/7/010, doi:10.1088/0022-3719/6/7/010.

[132] L. Benfatto. The kosterlitz-thouless transition. Lecture notes, Feb. 2014.

[133] S. Nandy, N. Mohanta, S. Acharya, and A. Taraphder. Anomalous transport near the lifshitz transition at theLaAlO3/SrTiO3interface. *Physical Review B*, 94(15), oct 2016. URL: http://dx.doi.org/10.1103/PhysRevB.94.155103, doi:10.1103/physrevb.94.155103.

[134] Vinay Ambegaokar, B. I. Halperin, David R. Nelson, and Eric D. Siggia. Dynamics of superfluid films. *Physical Review B*, 21(5):1806–1826, mar 1980. URL: http://dx.doi.org/10.1103/PhysRevB.21.1806, doi:10.1103/physrevb.21.1806.

[135] B. I. Halperin and David R. Nelson. Resistive transition in superconducting films. *Journal of Low Temperature Physics*, 36(5-6):599–616, sep 1979. URL: http://dx.doi.org/10.1007/BF00116988, doi:10.1007/bf00116988.

[136] R.S. Newrock, C.J. Lobb, U. Geigenmüller, and M. Octavio. The two-dimensional physics of Josephson junction arrays. In *Solid State Physics*, pages 263–512. Elsevier BV, 2000. URL: http://dx.doi.org/10.1016/S0081-1947(08)60250-7, doi:10.1016/s0081-1947(08)60250-7.

[137] D. J. Resnick, J. C. Garland, J. T. Boyd, S. Shoemaker, and R. S. Newrock. Kosterlitz-thouless transition in proximity-coupled superconducting arrays. *Physical Review Letters*, 47(21):1542–1545, nov 1981. URL: http://dx.doi.org/10.1103/PhysRevLett.47.1542, doi:10.1103/physrevlett.47.1542.

[138] C. J. Lobb, David W. Abraham, and M. Tinkham. Theoretical interpretation of resistive transition data from arrays of superconducting weak links. *Physical Review B*, 27(1):150–157, jan 1983. URL: http://dx.doi.org/10.1103/PhysRevB.27.150, doi:10.1103/physrevb.27.150.

[139] J. A. Bert, K. C. Nowack, B. Kalisky, H. Noad, J. R. Kirtley, C. Bell, H. K. Sato, M. Hosoda, Y. Hikita, H. Y. Hwang, and K. A. Moler. Gate-tuned superfluid density at the superconducting $LaAlO_3/SrTiO_3$ interface. , 86(6):060503, August 2012. doi:10.1103/PhysRevB.86.060503.

[140] Uwe S. Pracht, Nimrod Bachar, Lara Benfatto, Guy Deutscher, Eli Farber, Martin Dressel, and Marc Scheffler. Enhanced cooper pairing versus suppressed phase coherence shaping the superconducting dome in coupled aluminum nanograins. *Phys. Rev. B*, 93(10), mar 2016. URL: http://dx.doi.org/10.1103/PhysRevB.93.100503, doi:10.1103/physrevb.93.100503.

[141] Ing-Jye Hwang and D. Stroud. Vortex noise and fluctuation conductivity in Josephson-junction arrays. *Physical Review B*, 57(10):6036–6045, mar 1998. URL: https://doi.org/10.1103%2Fphysrevb.57.6036, doi:10.1103/physrevb.57.6036.

[142] S. Barabash, D. Stroud, and I.-J. Hwang. Conductivity due to classical phase fluctuations in a model for high-tc superconductors. *Physical Review B*, 61(22):R14924–

R14927, jun 2000. URL: https://doi.org/10.1103%2Fphysrevb.61.r14924, doi:10.1103/physrevb.61.r14924.

[143] Rini Ganguly, Dipanjan Chaudhuri, Pratap Raychaudhuri, and Lara Benfatto. Slowing down of vortex motion at the berezinskii-kosterlitz-thouless transition in ultrathin NbN films. *Physical Review B*, 91(5), feb 2015. URL: http://dx.doi.org/10.1103/PhysRevB.91.054514, doi:10.1103/physrevb.91.054514.

[144] C. Cen, S. Thiel, G. Hammerl, C. W. Schneider, K. E. Andersen, C. S. Hellberg, J. Mannhart, and J. Levy. Nanoscale control of an interfacial metal–insulator transition at room temperature. *Nature Materials*, 7(4):298–302, mar 2008. URL: http://dx.doi.org/10.1038/nmat2136, doi:10.1038/nmat2136.

[145] B. J. van Wees, H. van Houten, C. W. J. Beenakker, J. G. Williamson, L. P. Kouwenhoven, D. van der Marel, and C. T. Foxon. Quantized conductance of point contacts in a two-dimensional electron gas. *Physical Review Letters*, 60(9):848–850, feb 1988. URL: https://doi.org/10.1103%2Fphysrevlett.60.848, doi:10.1103/physrevlett.60.848.

[146] L I Glazman and A V Khaetskii. Quantum conductance of a lateral microconstraint in a magnetic field. *Journal of Physics: Condensed Matter*, 1(30):5005–5011, jul 1989. URL: https://doi.org/10.1088%2F0953-8984%2F1%2F30%2F015, doi:10.1088/0953-8984/1/30/015.

[147] M. Büttiker. Quantized transmission of a saddle-point constriction. *Physical Review B*, 41(11):7906–7909, apr 1990. URL: https://doi.org/10.1103%2Fphysrevb.41.7906, doi:10.1103/physrevb.41.7906.

[148] J. E. F. Frost, K.-F. Berggren, M. Pepper, M. Grimshaw, D. A. Ritchie, A. C. Churchill, and G. A. C. Jones. Analytical model of a one-dimensional constriction with many occupied subbands: Calculation and experiment. *Physical Review B*, 49(16):11500–11503, apr 1994. URL: https://doi.org/10.1103%2Fphysrevb.49.11500, doi:10.1103/physrevb.49.11500.

[149] L Martin-Moreno, J T Nicholls, N K Patel, and M Pepper. Non-linear conductance of a saddle-point constriction. *Journal of Physics: Condensed Matter*, 4(5):1323–1333, feb 1992. URL: https://doi.org/10.1088%2F0953-8984%2F4%2F5%2F012, doi:10.1088/0953-8984/4/5/012.

[150] Supriyo Datta. *Electronic Transport in Mesoscopic Systems*. Cambridge University Press (CUP), 1995. URL: https://doi.org/10.1017%2Fcbo9780511805776, doi:10.1017/cbo9780511805776.

[151] K. J. Thomas, J. T. Nicholls, M. Y. Simmons, M. Pepper, D. R. Mace, and D. A. Ritchie. Possible spin polarization in a one-dimensional electron gas. *Physical Review Letters*, 77(1):135–138, jul 1996. URL: https://doi.org/10.1103%2Fphysrevlett.77.135, doi:10.1103/physrevlett.77.135.

[152] M. J. Iqbal, Roi Levy, E. J. Koop, J. B. Dekker, J. P. de Jong, J. H. M. van der Velde, D. Reuter, A. D. Wieck, Ramón Aguado, Yigal Meir, and C. H. van der Wal. Odd and even kondo effects from emergent localization in quantum point contacts. *Nature*, 501(7465):79–83, aug 2013. URL: https://doi.org/10.1038%2Fnature12491, doi:10.1038/nature12491.

[153] Landolt Börnstein. *Semiconductor Quantum Structures*, volume New Series, Group III, Vol. 34, Subvolume B Pt. 1. Springer, 2001. URL: http://www.springer.com/us/book/9783540633471.

[154] J. Biscaras, N. Bergeal, S. Hurand, C. Grossetête, A. Rastogi, R. C. Budhani, D. LeBoeuf, C. Proust, and J. Lesueur. Two-dimensional superconducting phase in LaTiO 3 / SrTiO 3 Heterostructures induced by high-mobility carrier doping. *Phys. Rev. Lett.*, 108(24), jun 2012. URL: http://dx.doi.org/10.1103/PhysRevLett.108.247004, doi:10.1103/physrevlett.108.247004.

[155] Frank Stern and W. E. Howard. Properties of semiconductor surface inversion layers in the electric quantum limit. *Phys. Rev.*, 163(3):816–835, nov 1967. URL: http://dx.doi.org/10.1103/PhysRev.163.816, doi:10.1103/physrev.163.816.

[156] Arjun Joshua, S. Pecker, J. Ruhman, E. Altman, and S. Ilani. A universal critical density underlying the physics of electrons at the LaAlO3/SrTiO3 interface. *Nature Communications*, 3:1129, oct 2012. URL: https://doi.org/10.1038%2Fncomms2116, doi:10.1038/ncomms2116.

[157] P. A. Fleury and J. M. Worlock. Electric-field-induced raman scattering in SrTi o 3 and KTa o 3. *Physical Review*, 174(2):613–623, oct 1968. URL: http://dx.doi.org/10.1103/PhysRev.174.613, doi:10.1103/physrev.174.613.

[158] L. F. Chen, C. K. Ong, C. P. Neo, V. V. Varadan, and V. K. Varadan. *Microwave Electronics*. Wiley-Blackwell, mar 2004. URL: http://dx.doi.org/10.1002/0470020466, doi:10.1002/0470020466.

[159] A.K. Tagantsev, V.O. Sherman, K.F. Astafiev, J. Venkatesh, and N. Setter. Ferroelectric materials for microwave tunable applications. *Journal of Electroceramics*, 11(1):5–66. URL: http://dx.doi.org/10.1023/B:JECR.0000015661.81386.e6, doi:10.1023/B:JECR.0000015661.81386.e6.

[160] Georg Rupprecht and R. O. Bell. Microwave losses, dielectric properties and elastic constants of SrTiO3. In *First Annual Symposium on the Physics of Failure in Electronics*. Institute of Electrical & Electronics Engineers (IEEE), sep 1962. URL: http://dx.doi.org/10.1109/IRPS.1962.360000, doi:10.1109/irps.1962.360000.

[161] O.G. Vendik, E. Kollberg, S.S. Gevorgian, A.B. Kozyrev, and O.I. Soldatenkov. 1 GHz tunable resonator on bulk single crystal SrTiO3 plated with YBa2Cu3o7-x films. *Electron. Lett.*, 31(8):654, 1995. URL: http://dx.doi.org/10.1049/el:19950427, doi:10.1049/el:19950427.

[162] Dejan Davidovikj, Nicola Manca, Herre S. J. van der Zant, Andrea D. Caviglia, and Gary A. Steele. Quantum paraelectricity probed by superconducting resonators. July 2016. arXiv:1607.08146.

[163] K. F. Astafiev, A. K. Tagantsev, and N. Setter. Quasi-Debye microwave loss as an intrinsic limitation of microwave performance of tunable components based on $SrTiO_3$ and $Ba_xSr_{1-x}TiO_3$ ferroelectrics. *Journal of Applied Physics*, 97(1):014106–014106, January 2005. doi:10.1063/1.1829149.

[164] Spartak Gevorgian. *Ferroelectrics in Microwave Devices, Circuits and Systems*. Springer-Verlag GmbH, 2009. URL: http://www.ebook.de/de/product/8299973/spartak_gevorgian_ferroelectrics_in_microwave_devices_circuits_and_systems.html.

[165] Jan Petzelt, Tetyana Ostapchuk, Ivan Gregora, Susanne Hoffmann, Johannes Lindner, David Rafaja, Stanislav Kamba, Jan Pokorny, Viktor Bovtun, Viktor Porokhonsky, Maxim Savinov, P**r**emysl Van**e**k, Ivan Rychetský, Vratislav Pe**r**ina, and Rainer Waser. Far infrared and raman spectroscopy of ferroelectric soft mode in SrTiO 3 thin films and ceramics. *Integrated Ferroelectrics*, 32(1-4):11–20, jan 2001. URL: http://dx.doi.org/10.1080/10584580108215673, doi:10.1080/10584580108215673.

[166] P. G. de Gennes Pierre-Gilles de Gennes, Pierre-Gilles De Gennes. *Superconductivity of Metals and Alloys*. WESTVIEW PR, 1999. URL: http://www.ebook.de/de/product/3599892/pierre_gilles_de_gennes_pierre_gilles_de_gennes_p_g_de_gennes_superconductivity_of_metals_and_alloys.html.

[167] R. B. Bird. The feynman lectures on physics, richard p. feynman, robert b. leighton, and matthew sands, addison-wesley, reading, mass, volume i, II(1964) volume III(1965). *AIChE Journal*, 10(6):794–794, nov 1964. URL: http://dx.doi.org/10.1002/aic.690100602, doi:10.1002/aic.690100602.

Sujet : Transport DC et AC à l'interface $LaAlO_3/SrTiO_3$ contrôlée par effet de champ

Résumé : Cette thèse est consacrée à l'étude des propriétés de transport statique et dynamique du gaz d'électrons bidimensionnel supraconducteur à l'interface $LaAlO_3/SrTiO_3$. Le confinement des électrons dans un puit quantique lève la dégénérescence des bandes t_{2g} du $SrTiO_3$, ce qui génère une structure de bande riche et complexe. A partir d'un modèle d'électrons libres, nous calculons numériquement la structure de bande et le potentiel de confinement de manière auto-cohérente (chapitre 1). Ces simulations mettent en évidence la présence de deux types de bandes, d_{xy} et $d_{xz/yz}$, ayant des propriétés de transport très différentes. Dans un premier temps, nous étudions l'effet du désordre microscopique induit par le dopage d'atomes de Chrome, sur la supraconductivité et le couplage spin-orbite en fonction de la densité électronique contrôlée par effet de champ (chapitre 3). Nous décrivons également la première réalisation d'un dispositif à effet de champ dans lequel la transition supraconducteur-isolant est obtenue à l'aide d'une grille métallique située au-dessus du gaz. La présence d'un fort couplage spin-orbite (quelques meV) contrôlé par la tension de grille a également été démontrée en analysant les mesures de magnéto-transport. Nous présentons la première réalisation d'un point contact quantique dans $LaAlO_3/SrTiO_3$ par effet de champ (chapitre 6). Pour aller plus loin dans la compréhension de l'interface $LaAlO_3/SrTiO_3$, nous présentons des mesures haute fréquence de la conductivité σ (chapitre 5). Cette mesure nous donne accès à la rigidité de phase et à l'énergie du gap supraconducteur par la théorie BCS. Nous montrons que la compétition entre ces deux échelles d'énergie contrôle la température critique dans le diagramme de phase.

Mot-clefs : Supraconductivité, Couplage Spin-Orbit, Point Contact, Rigidité de Phase

---

Subject : DC and AC transport in field-effect controlled $LaAlO_3/SrTiO_3$ interface

Abstract : This thesis is devoted to the study of static and dynamical transport properties of the superconducting two-dimensional electron gas at the $LaAlO_3/SrTiO_3$ interface. Under strong 2D confinement, the degeneracy of the t_{2g} bands of $SrTiO_3$ is lifted at the interface, generating a rich and complex band structure. Starting from a free electron model, we derive numerically a self-consistent calculation of the potential well and the band structure (chapter 1). These simulations highlight the presence of two types of bands d_{xy} and $d_{xz/yz}$ with very different transport properties. We investigate first the effect of microscopic disorder introduced by Cr doping, on superconductivity and spin-orbit coupling over a wide range of back-gate doping (chapter 3). We also describe the first implementation of a field-effect device where the superconductor-insulator transition could be continuously tuned with a top-gate. The presence of a strong spin-orbit coupling that could be controlled with the top-gate voltage is also demonstrated by analyzing the magneto-transport measurements. The gate dependence of the spin-splitting energy, of the order of a few meV, is found to be consistent with Rashba spin-orbit coupling. Going one step further in nanofabrication, we report on the first realization of a quantum point contact in $LaAlO_3/SrTiO_3$ using split gates (chapter 6). To go further in the understanding of the $LaAlO_3/SrTiO_3$ interface, we present high frequency measurements of the conductivity σ (chapter 5). This measurement gives us access to the superfluid stiffness and to the gap energy via the BCS theory. We show that the competition between these two energy scales controls the superconducting T_c in the phase diagram.

Keywords : Superconductivity, Spin-Orbit Coupling, Quantum Point Contact, Superfluid Stiffness